ABSTRACT

Title of Dissertation: MATERIALS CHARACTERIZATION FOR
SUB-MICRON SUPERCONDUCTING
INTERCONNECTS IN RECIPROCAL
QUANTUM LOGIC CIRCUITS

Cougar Alessandro Tomas Garcia
Doctor of Philosophy, 2022

Dissertation Directed by: Professor Steven M. Anlage
Department of Materials Science and Engineering

Today's server based computing consumes a considerable amount of energy. Reciprocal Quantum Logic (RQL) is a classical logic family within superconducting electronics, and is a candidate for energy efficient computing technologies. Similar to the current complimentary metal-oxide semiconductor technologies, RQL interconnects are responsible for dissipating the majority of the energy. The energy dissipated in RQL interconnects comes from finite resistive losses in the superconducting wires and embedded dielectrics at radio frequencies. Therefore, material properties, processing, and performance are critical to understanding the mechanisms of loss and mitigation of power dissipation in RQL interconnects.

This dissertation presents work on three aspects of materials characterization of RQL interconnects: implementing a method to deconvolve superconducting and dielectric losses, evaluating losses in three generations of RQL fabrication, and understanding the microscopic physics that

determines the performance of RQL interconnects in a temperature and frequency range from 1.5-6 K and 3-12 GHz, respectively.

A novel method to accurately deconvolve superconducting and dielectric losses by exploiting their frequency dependence is described. Furthermore, a finite element modeler is used to accurately extract the losses. This method is termed Dispersive Loss Deconvolution. The designed microstrip transmission line resonators are fabricated in a 0.25 μm RQL fabrication process composed of Nb wires embedded in Tetraethyl orthosilicate (TEOS) dielectric. The Nb and TEOS losses as a function of microstrip width down to 0.25 μm are modeled and measured.

The electrical and physical material properties for 3 RQL processes over 5 wafers are evaluated. The electrical properties were evaluated by characterizing resonators in cryogenic dip probes and a dry system with ± 10 mK temperature control. The physical properties were evaluated using Transmission Electron Microscopy and Energy-Dispersive Spectroscopy. Two of the processes use chemical mechanical polishing (CMP) to planarize the Nb wires, and the other using reactive ion etching (RIE) to define Nb wires.

At 4.2 K, the Nb loss in the 0.25 μm resonators between the 3 processes were surprisingly distinct. The two CMP processes yield Nb losses up to 2 times higher relative to the RIE process, and have a discernible increase in loss by as much as 20% going from 4 to 0.25 μm microstrip widths. For the RIE process, there is no detectable upturn in Nb losses for microstrip widths down to 0.25 μm. Most notably, the RIE process produced 0.25 μm Nb wires with loss reaching the theoretical lower limit of intrinsic surface resistance $R_s = 17$ $\mu \Omega$ at 4.2 K and 10 GHz. The superior RIE process may be linked to the incorporation of thin metal passivation layers protecting the Nb, which prevented Nb oxide from participating in additional loss mechanisms. For all 3 processes and microstrip widths from 0.25-4 μm, the TEOS losses had negligible width

dependence and varied by as much as $\pm 20\%$.

From the electrical characterization at 4.2 K, it was found that the Nb wires are the limiting loss mechanisms in RQL interconnects. As temperature is decreased below 4.2 K, it is well known that Nb loss will exponentially decrease and amorphous dielectrics like TEOS can have loss with a non-monotonic temperature dependence depending on the input power. This offered the opportunity to explore a possible optimum operating temperature to minimize power dissipation by the RQL interconnects. At relatively low input powers, TEOS became the limiting loss mechanism for temperatures below 3 K, and I conclude this can be attributed to losses coming from two-level system tunneling relaxation and resonant absorption processes.

The work in this dissertation describes the development of methods to aid in characterization, design, and fabrication of RQL interconnects, and can be extended to potentially other Single Flux Quantum and Quantum Computing technologies.

MATERIALS CHARACTERIZATION FOR SUB-MICRON SUPERCONDUCTING INTERCONNECTS IN RECIPROCAL QUANTUM LOGIC CIRCUITS

by

Cougar Alessandro Tomas Garcia

Advisory Committee:
     Professor Steven M. Anlage, Chair/Advisor
     Professor Ichiro Takeuchi
     Professor Christopher J. Lobb
     Professor John Cumings
     Professor Christopher J. K. Richardson
Industry Mentor:
     Dr. Vladimir V. Talanov, Northrop Grumman

Dedication

TO MY WIFE, MARLANEA

MY FATHER, MANUEL GARCIA

MY MOTHER, DARA GARCIA

MY GRANDPA & GRANDMA, ORLAN & DIAMANTE HENDRICKSON

AND MY FATHER-IN-LAW, VINCE M. FRANK

Acknowledgments

> "If I have seen further it is by
>
> standing on the shoulders of
>
> Giants".
>
> ———————————————
>
> Sir Isaac Newton stated in a letter
>
> to Robert Hooke in 1675, the same
>
> decade of his pioneering work in
>
> optics and gravity.

First and foremost, I would like to thank my thesis advisor Professor Steven Anlage for his guidance in my journey and his willingness to enlighten my understanding and appreciation of the physical world. In the same light, I thank Dr. Vladimir Talanov, my co-advisor and industry mentor at Northrop Grumman for his his foundational work this thesis was built upon. Additionally, I would like to thank Dr. Nicholas Rizzo for his life and technical mentorship from day one of my scientific career. Thanks also goes to Dr. Elie Track, an influence to many around the world and has played a motivational role on my journey. In like manner, thanks goes to Dr. Joshua Strong, Dr. Anna Herr, Dr. Quentin Herr for their creation of new technologies and their willingness to have me on their team, as it ultimately inaugurated my dissertation work. Special thanks goes to Dr. Daniel Queen for his guidance and fruitful conversations that ultimately helped me understand how low temperature amorphous dielectric properties contributed in Chapters 4

Table of Contents

List of Tables

List of Figures

ix

List of Abbreviations

ABF   Annular Bright Field

AIST   Advanced Industrial Science and Technology

AQFP   Adiabatic Quantum Flux Parametron

BCS   Bardeen, Cooper, and Schrieffer theory

BF   Bright Field

CD   Critical Dimension

CS   Conducting Strip

CVD   Chemical Vapor Deposition

CMOS   Complimentary Metal-Oxide-Semiconductor

CMP   Chemical Mechanical Polishing (or Planarization)

dBm   Decibel-Milliwatts

DC   Direct Current

DLD   Dispersive Loss Deconvolution

EDS   Energy-Dispersive Spectroscopy

eSFQ   Energy Efficient Single Flux Quantum

FEM   Finite Element Modeler

FIB   Focused Ion Beam

GP	Ground Plane
HFSS	High Frequency Structure Simulator
HTS	High Temperature Superconductor
IBM	International Business Machines Corporation
IL	Insertion Loss
IRDS	International Roadmap for Devices and Systems
JJ	Josephson Junction
LL	MIT Lincoln Laboratory
MTL	Microstrip Transmission Line
MUX-MTL	Multiplexed Microstrip Transmission Line
PEC	Perfect Electrical Conductor
PECVD	Plasma-Enhanced Chemical Vapor Deposition
PPW	Parallel Plate Waveguide
PTL	Passive Transmission Line
PVD	Physical Vapor Deposition
QFP	Quantum Flux Parametron
RF	Radio Frequency
RIE	Reactive-Ion Etching
RQL	Reciprocal Quantum Logic
RSFQ	Rapid Single Flux Quantum

SEM   Scanning Electron Microscopy

SFQ   Single Flux Quantum

SIBC   Surface Impedance Boundary Condition

STEM   Scanning Transmission Electron Microscopy

SCE   Superconducting Electronics

TE   Transmitted Electron

TEM   Transmission Electron Microscopy

TEOS   Tetraethyl Orthosilicate

TLS   Two Level System

VNA   Vector Network Analyzer

ZC   Z-Contrast

ZOR   Zeroth-Order Resonator

List of Critical Symbols

$\varepsilon_0 = 8.85 \times 10^{-12}$ vacuum permittivity ($F\ m^{-1}$), Eq. 2.18

$\eta_{wave} = \sqrt{\mu_0/\varepsilon_0} = 120\pi$ intrinsic wave impedance (Ω), Eq. 2.26

$\mu_0 = 4\pi \times 10^{-7}$ vacuum permeability ($N\ A^{-2}$), Eq. 2.3

$c = 3 \times 10^8$ vacuum speed of light ($m\ s^{-1}$), Eq. 2.36

$\hbar = 1.06 \times 10^{-34}$ reduced Planck's constant ($J\ s$), Eq. 2.6

$k_B = 1.38 \times 10^{-23}$ Boltzmann constant ($J\ K^{-1}$), Eq. 2.4

α The transmission line attenuation constant (m^{-1}), Eq. 3.19

α_{db} ultrasonic attenuation (m^{-1} or dB)

β The transmission line phase constant (m^{-1}), Eq. 3.19

Γ_{cm} Transmission line partial geometric factor associated with losses in the m-th conductor (Ω/sq), Eq. 3.6

Γ_{c0} Net conductor geometric factor at reference frequency ω_0, Eq. 3.13

Γ_{c0m} Transmission line partial geometric factor at that frequency associated with loss in the mth conductor, Eq. 3.11

Γ_d Transmission line partial geometric factor associated with losses in that dielectric layer or tube, Eq. 3.41

Γ_{dn} Transmission line partial geometric factor associated with loss in the nth dielectric layer or tube, Eq. 3.6

γ The transmission complex propagation constant

	of a transmission line (m^{-1}), Eq. 2.12
Δ	BCS energy gap of a superconductor (J), Eq. 2.4
$\Delta\varepsilon_{abs}$	The change in dielectric constant due to TLS resonant absorption, Eq. 5.11
ε_r	relative dielectric constant, Eq. 2.26
$\Delta\varepsilon_{rel}$	The change in dielectric constant due to TLS relaxation, Eq. 5.10
λ	magnetic penetration depth (m), Eq. 2.2
λ_{eff}	effective magnetic penetration depth (m), Eq. 2.25
λ_{EM}	the wavelength of the propagating wave (m), Eq. 2.17
λ_L	London penetration depth (m), Eq. 2.2
$n\mu^2$	The permanent dipole coupling of TLSs having a density of states n, Eq. 5.12
$n\mu'^2$	The induced dipole coupling of TLSs having a density of states n, Eq. 5.11
ξ_0	microscopic coherence length of a bulk superconductor (m), Eq. 2.8
$\sigma = \sigma_1 - i\sigma_2$	complex conductivity ($\Omega^{-1}m^{-1}$), Eq. 2.5
σ_n	normal metal conductivity ($\Omega^{-1}m^{-1}$), Eq. 2.5
τ_{rel}	characteristic relaxation time (s), Eq. 2.30
X_{eff}	effective surface reactance (Ω/sq), Eq. 2.23
ω	angular frequency ($rad\ s^{-1}$), Eq. 2.5
a	The TLS material constant, Eq. 5.15

$\bar{M}$ The average TLS coupling energy (eV) Eq. 5.16, Eq. 5.16

n_e total electron density (m^{-3}), Eq. 2.1

n_s superfluid electron density (m^{-3}), Eq. 2.1

P_{in} The incident power at the input of the resonator
after cable attenuation (W), Eq. 5.1

P_r The reflected power to the VNA (W) 5.1

P_{st} The circulating (stored) power in the resonator (W), Eq. 5.4

P_t The transmitted power (W), Eq. 5.1

P_d The power dissipated by the resonator (W), Eq. 5.1

Q_c Partial Q-factor associated with the conductor loss, Eq. 3.1

Q_d Partial Q-factor associated with the dielectric loss, Eq. 3.1

Q_i Internal or intrinsic Q-factor, Eq. 3.1

R Transmission line resistance per unit length ($\Omega\,m^{-1}$), Eq. 3.3

R_{eff} effective surface resistance (Ω/sq), Eq. 2.24

R_s intrinsic surface resistance (Ω/sq), Eq. 2.19

R_{s0} Intrinsic surface resistance at reference frequency ω_0 (Ω/sq), Eq. 3.13

R_{s0m} Transmission line intrinsic resistance
at a reference frequency ω_0 of the m-th conductor (Ω/sq), Eq. 3.11

$\overline{R_{sm}}$ Transmission line effective intrinsic resistance
of the m-th conductor (Ω/sq), Eq. 3.6

$|S_{21}|$ The transmission coefficient magnitude (dB) Eq. 4.2

T temperature (K), Eq. 2.6

Z_{sub} dielectric substrate bulk impedance (Ω/sq), Eq. 2.24

$z(0)$ transformed impedance at film interface normalized to Z_s, Eq. 2.22

$z(d)$ transformed impedance up to the film interface normalized to Z_s, Eq. 2.22

Chapter 1:   Introduction

1.1   Overview

Since the birth of the information age, there has been a relentless need for more computing power. In the 1950s-1970s mainframe computers were only accessible through terminals in close proximity. Today, high performance data centers can be accessed remotely from anywhere around the world. Data centers are now essential to almost every part of the world economy - universities, government institutions, large companies, small companies, and even individuals. Server-based computing is now becoming the primary user for complimentary metal-oxide semiconductor (CMOS) technologies, amounting to considerable energy consumption. Additionally, Moore's Law is expected to flatten by 2025, preventing CMOS from doubling in performance every 2 years [1]. If energy demands continue to evolve across the world as a consequence of the growing usage of available computing power and Moore's law comes to an end, the total energy consumption of data centers across the world is projected to reach 65 GW per year in 2030 ($\approx 70\%$ increase from today) [2], approximately equivalent to the output of 65 power plants, 31 Hoover Dams, or 6.5 billion LED Bulbs.

The power consumption and performance challenges of CMOS need to be addressed, and are being studied by the International Roadmap for Devices and Systems (IRDS) [3]. Logic families within superconducting electronics (SCE) are candidates to address power dissipation.

Reciprocal Quantum Logic (RQL), an SCE digital logic technology, has been reported to be 300 times more energy efficient than CMOS [4], and has demonstrated the largest working circuit to date with $\approx 10^5$ logic units on a single chip [5]. Additionally, RQL has a significant speed advantage over CMOS, where the upper frequency set by the plasma frequency of the Josephson junctions on the order of $f_p \approx 250\ GHz$ [4]. However, RQL is still a young technology as compared to CMOS having consistently $\geq 10^{10}$ logic units per circuit. Several engineering challenges are limiting large scale RQL-based computation.

In particular, superconducting interconnects, which serve as RQL's clocking, power delivery system, and serial data links. Moreover, unlike CMOS where the ground planes only serve as a medium for data propagation and electrical isolation between signals, RQL ground planes are engineered to mitigate magnetic flux being trapped in circuit areas that can reduce operating margins and even catastrophic circuit failure [6, 7]. Material quality and defectivity affect both power dissipation and magnetic flux trapping in RQL circuits, and the focus of this dissertation is the former.

RQL interconnects are composed of superconducting wires down to submicron dimensions embedded in a dielectric. The RQL interconnect performance is governed by the power dissipation in these materials due to radio frequency (RF) resistive losses. The power dissipation in RQL interconnects is orders of magnitude lower than CMOS interconnects, but can dwarf that of the power in RQL logic, and so the superconductor and dielectric RF losses should be minimized.

In CMOS circuits, static and dynamic energy dissipation have become the main limiting factors for further device scaling [8]. Specifically, at maximum scaling and density of CMOS circuits, the clock power becomes the dominant contributor to dynamic power dissipation relative to the logic. Resonator-based clocks in CMOS have been shown to reduce power dissipation

[9]. The 300x higher energy efficiency of RQL relative to CMOS was calculated for only the net power dissipated by the logic alone. Recently, it was found that an RQL circuit with a metamaterial resonator clock yields an energy efficiency of $\eta = P_{RQL}(P_{RQL} + P_{Res})^{-1} \approx 0.3$, where P_{RQL} is the total dynamic power burned by the logic and P_{Res} is the total static power burned by the resonator clock [10]. Therefore, the energy efficiency of RQL relative to CMOS drops down to 90x, significantly reducing its competitive advantage.

Materials science and engineering plays a primary role in creating state-of-the-art computing systems and optimizing their performance. As capabilities increase, so does their complexity, making the analysis and improvement at the single component level more demanding. Grand challenges, such as the ending of Moore's law and the world wide need for more computing power, can be addressed via the materials science tetrahedron [11]. Specifically, RQL interconnect power effeciency can be optimized by examining the materials processing (Fig. 1.1a), structure (Fig. 1.1b), properties (Fig. 1.1c), and performance (Fig. 1.1d). From this perspective, power dissipation in RQL interconnects may be alleviated with a study of fabrication processes, material morphology, electrical properties, and their affect on RQL performance. The information gleaned from such a study can be incorporated into the emerging systems materials engineering triangle [12], enabling system-level planning to facilitate maturation of superconducting electronics (SCE) technologies (e.g. RQL).

This dissertation is focused on characterizing RQL superconductor-dielectric interconnect losses (see Fig. 1.1). This is accomplished by: (i) characterization of the interconnects electrical properties by developing a novel methodology to deconvolve intrinsic RF losses, (ii) evaluating the processing of interconnects using complimentary characterization techniques of the material morphology, and (iii) optimizing the performance by reducing the RF losses in superconducting

3

a) Chemical Mechanical Planarization Processes

b) RQL Interconnect Microstructure

c) RF Resistive Loss Properties

d) Performance of Energy Efficient RQL Metamaterial Clocks
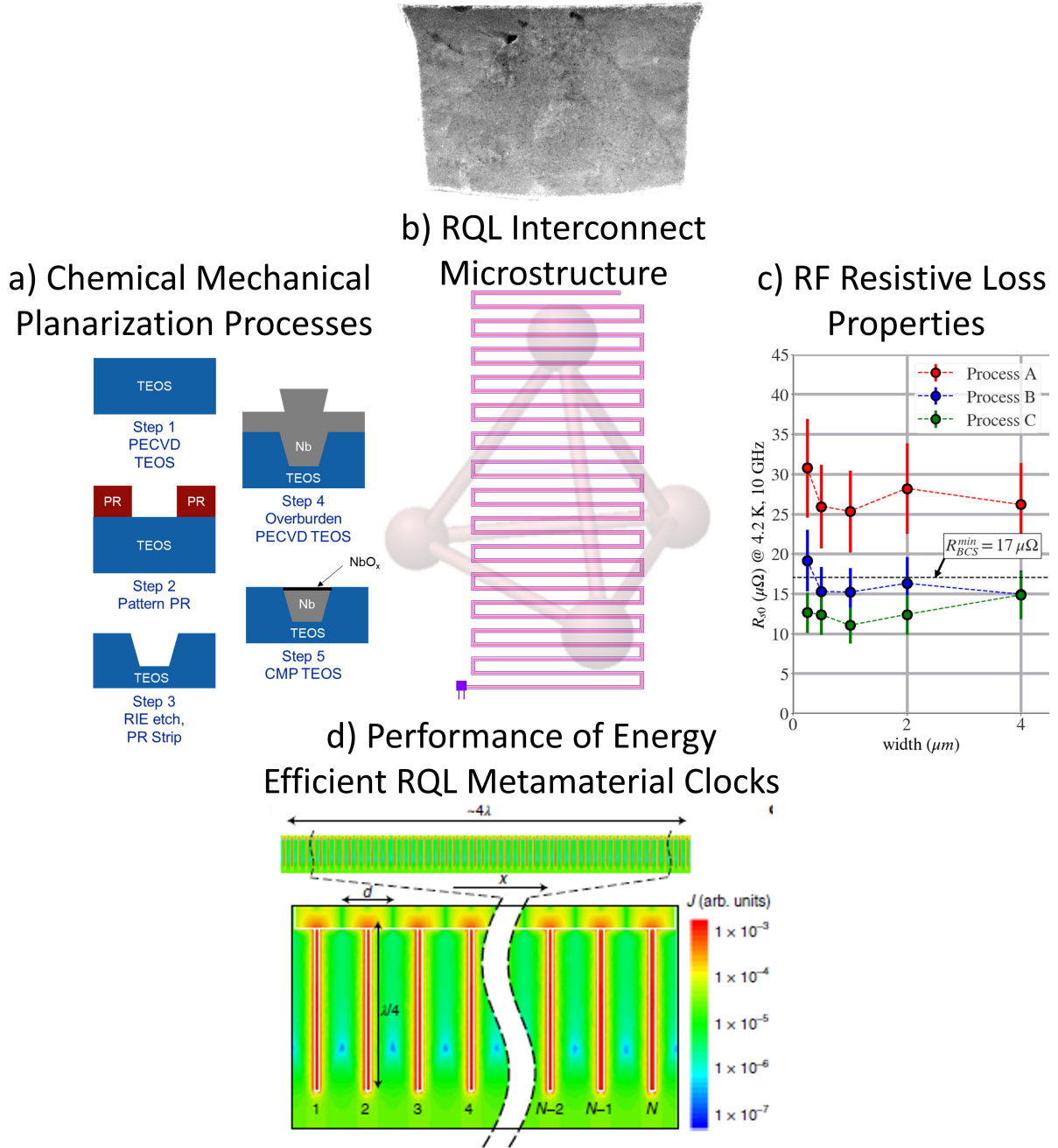
Figure 1.1: Addressing power dissipation with the materials science paradigm (tetrahedron). The submicron microstrip transmission line (MTL) resonator lies at the center of the tetrahedron as the characterization "vehicle". a) Three chemcial mechanical planarization (CMP) processes of RQL MTLs were examined in this work. b) An example of studying the microstructure and morphology an MTL (see Chapter 3) c) MTL resonator measurements to extract the RF resistive loss propoerties of the superconudctor and dielectric materials (see Chapters 4 and 5). d) With new predictive models, improvements in the performance can be applied to increasing the energy efficiency of RQL meta material clock networks (see Chapters 4 and 5)

interconnects.

The dissertation is organized into six chapters. In the remainder of this first chapter, I review the technological challenges of RQL interconnects. In Chapter 2, I discuss the electrodynamics of superconductors and amorphous dielectrics, and RQL fabrication processes. Chapter 3 introduces the non-idealities of RQL interconnects caused by fabrication processes, describes a method to characterize the superconductor and dielectric RF losses independently, and presents a procedure to model superconductors in HFSS in order to extract the RF losses in the superconductor. In Chapter 4, I present a resonator design and measurements of RF losses at 4.2 K in RQL interconnects down to 0.25 μm dimensions. In this chapter, the measured intrinsic losses of the superconductor and dielectric, R_s and $\tan \delta$, will be related back to the morphology analyzed in Chapter 3. In Chapter 5, I explore the temperature dependence of RF losses in Nb and TEOS from 1.5-4.5 K to better understand if temperature plays a role in RQL interconnect performance. Finally, in Chapter 6, I provide a summary of my main results, followed by recommendations for future research.

1.2   Technological Challenges

It was first theorized by Brian Josephson in 1962 that supercurrent could tunnel between two superconducting electrodes if the barrier to tunneling was thin enough [13]. Soon after, Anderson and Rowell measured this tunneling effect [14], followed by John Rowell patenting the use of the Josephson junction (JJ) as a cryogenic logic device [15]. Thus, the birth of Josephson electronics and IBM's thrust to demonstrate a Josephson based computer in the 1960s-1980s. IBMs effort, using Pb based JJs, ended in 1983 due to only a 2.5 times speed improvement

relative to CMOS. The higher reliability of Nb based JJs developed by Gurvitch at Bell Labs [16] allowed for larger scale circuits and complexity, renewing SCE in early 1987. This is around the same time high-temperature superconductivity was discovered. Voltage-state gates were used during this time, where logical 0 (1) is represented by a voltage level of zero (2.5 mV), but requires a large footprint with significant logic power dissipation due to the incorporation of resistors [17]. Miraculously, Josephson microprocessors were functional and demonstrated by Fujitsu Laboratories in Japan [18]. These processors were built one-for-one with CMOS using niobium junctions having a few thousand gates and memory of a few kilobits. Although, memory, processing margins, footprint, and power consumption were the limiting factors preventing from competing with CMOS.

Single flux quantum (SFQ) based logic devices, relying on the current (or phase) state to do computation, can have (i) 1-2 orders of magnitude reduction in power dissipation, (ii) 2-4 times smaller footprint compared to voltage-state Josephson logic [19], and (iii) potential for up to 50 times higher clock rates compared to CMOS [20]. SFQ based logic families are rapid single flux quantum (RSFQ) logic [21], [22], quantum flux parametron (QFP) [23], reciprocal quantum logic (RQL) [4], energy efficient single flux quantum (eSFQ) [24], and adiabatic quantum flux parametron (AQFP) [25]. The biggest advantage for SFQ technologies is computation speed, where greater than 100 GHz data rate has been demonstrated [26, 27]. Additionally, SFQ can be used as the control processor in quantum computing systems [28, 29, 30], and other niché application specific circuits [31]. Recently, scalability and energy efficiency have been reviewed in comparison to CMOS [32, 33]. Without sacrificing computation speed, RQL logic currently has a big advantage in energy efficiency, with the largest JJ count per chip to date (a measure of the scalability) [5]. Superconducting interconnects need to be considered further.

Superconducting microwave transmission line (MTL) are the most common interconnects, supporting low bandwidth signals for clocks and power distribution [34, 35], as well as high bandwidth signals to propagate SFQ pulses that carry bits of information [36]. The latter is called a passive transmission line (PTL). Compared to SiO_2 and Cu at room temperature, PTLs composed of SiO_2 dielectric and Nb at 4.2 K are near lossless. For example, the energy dissipation in CMOS interconnects limits the clock frequency of processors to 4 GHz and forces the amount of transistors that need to be powered off at any given time to prevent the chip temperature from exceeding thermal limits [32].

Fig. 1.2 shows the energy versus delay for CMOS and RQL interconnects, adopted from the International Roadmap For Devices and Systems (IRDS) 2020 edition. Here we are not considering AQFP technology, since it does not use PTL interconnects.

Accounting for the cooling energy to keep circuits at 4 K with $> 10\,W$ cooling power, PTL power dissipation is $1 \times 10^{-16}\,J$ (0.3 μW at 3 GHz) for a 1 mm long PTL ("RQL interconnect" arrow in Fig. 1.2). Therefore, RQL MTL interconnects can have 2-4 orders magnitude lower dissipation relative to CMOS.

As mentioned above, to further scale RQL technology, it is desired to have global clock and power distribution with spatially equal magnitude and phase. Recently, a metamaterial clock resonator has been designed and demonstrated to deliver power to 48k JJs operating at 3.5 GHz supporting uniform power distribution across $3 \times 3\,mm^2$ area at 4.2 K [10]. This clock design is compatible with AC-powered SFQ logic families (e.g. RQL and QFP). Unfortunately, this comes at an energy cost. For the above circuit size, the resonator clock has a best case energy efficiency estimated to be $\eta = P_{RQL}(P_{RQL} + P_{Res})^{-1} \approx 0.3$, where $P_{Res} \approx 18\,\mu W$ is the power burned by the resonator clock, and $P_{RQL} \approx 40\,\mu W$ is the power burned by the logic when all logic units

7
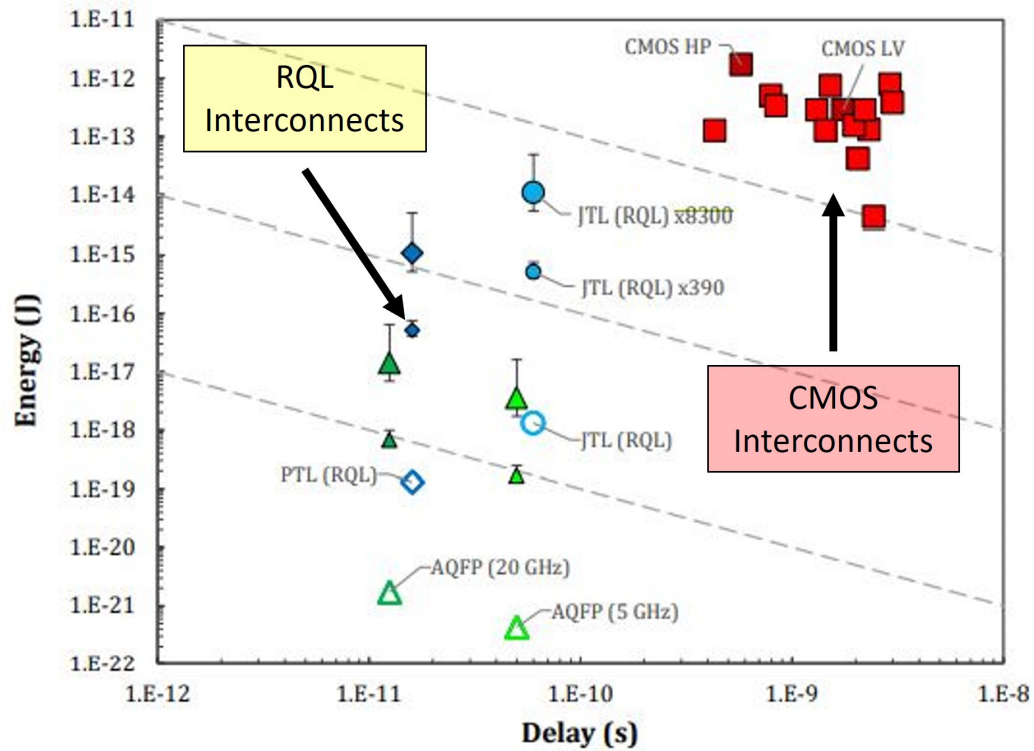
Figure CEQIP-5   Energy versus Delay for Interconnects of 1 mm Length

Note: Superconductor devices (AQFP, RQL) have open symbols (e.g., ○) for operation at ~4 K and solid symbols with whiskers showing ranges including refrigeration power from Table CEQIP-8. Small, solid symbols (e.g., ●) are for large refrigeration systems (>10 W cooling power) and large, solid symbols (e.g., ●) are for small systems (cryocoolers). All other devices are from [391]. Dashed lines show constant energy-delay products.

Figure 1.2:   Adopted from the International Roadmap For Devices and Systems 2020 edition (IRDS) [37]. (Yellow Box) Arrow pointing to the energy dissipated by a RQL 1 mm long passive transmission line (PTL) interconnects. (Red squares) CMOS interconnects energy dissipation and delay for comparison.

are saturated (producing all 1s every clock cycle). This means the resonator clock is now limiting the energy efficiency of RQL, as P_{RQL} is much lower under normal operation of the circuit with only a small percentage of logic gates drawing power from the clock at any given time.

RQL resonator clock interconnects are made of microstrip transmission line (MTL) networks [10]. For a fixed circuit size and damping ratio of the junctions, resonator clock efficiency is related to the intrinsic Q-factor of the resonator by $\eta \propto (1 + Q_i^{-1})^{-1}$ with nominal $Q_i^{-1} = Q_c^{-1} + Q_d^{-1} \approx 4 \times 10^{-3}$ at 10 GHz, where Q_c^{-1} and Q_d^{-1} are proportional to the power dissipated and therefore RF losses in the Nb wires and SiO_2 dielectric, respectively. In RQL fabrication, the SiO_2 is typically made using a chemical vapor deposition process using a tetraethyl Orthosilicate (TEOS) precursor, and so SiO_2 will be referred by its common precursor TEOS throughout this work. The power dissipated in TEOS and Nb are notable and comparable at 4.2 K, which contribute to the low Q_i in RQL clocks. The loss mechanisms and fabrication limitations will be discussed further in Chapter 2.

As a consequence, reducing RF losses in superconductor-dielectric resonant systems is critical for the scaling of RQL and AC-powered SFQ technologies. Furthermore, it is also important to fully characterize power dissipation as a function of frequency (MHz-GHz) and temperature (mK-K) to assure optimum operating points, as non-monotonic functioning are possible. The technological challenge this work will aim to address through materials science is power dissipation in RQL clock interconnects by modeling and characterizing microstrip transmission line resonators.

1.3   Summary

In summary, there is an opportunity to increase the power efficiency of RQL resonator-based interconnects to increase the technology's competitive advantage. This dissertation intends to remedy this state of affairs by providing novel approaches to characterize the microwave losses of Nb and TEOS. I will present techniques that serve as tools to understand both the intrinsic properties and extrinsic effects due to fabrication. These approaches include finite element modeling (e.g. HFSS), physical characterization of the material microstructure, a method to deconvolve the Nb and TEOS loss in a single measurement, and temperature dependent loss spectroscopy. The methods established can be used to predict the power efficiency of RQL interconnects for a given material system, and provide a path for future work.

Chapter 2:   Materials for Superconducting Interconnects

2.1   Overview

In this chapter, I will introduce the intrinsic material properties responsible for power dissipation in RQL interconnects. Each subsection will briefly review the history of superconductors and dielectrics. The superconductor intrinsic resistance R_s and dielectric loss tangent $\tan \delta$ will be defined. Their respective temperature dependence and frequency dependence will also described, supported by models and measurements. The assumptions, concepts, and equations will be used throughout Chapters 3-5.

2.2   Superconductor Electrodynamics

2.2.1   A Brief History

Superconductivity was first discovered in 1911 by Heike Kamerlingh Onnes, the pioneer of helium liquification [38], when he measured a zero resistance on a mercury sample at 4.2 K [39]. In 1934, Gorter and Casimir developed the thermodynamic two-fluid model [40], where the total electron density n_e in a superconductor is split into two parallel channels: a normal electron density n_n and a frictionless electron density n_s. The non-dissipative electron channel n_s is now commonly referred to as the superfluid electron density, coined from the discovery of

superfluidity in ^4He (zero viscosity) by Kapitsa [41] and independently by Allen and Misener [42] in 1937. At absolute zero temperature $T = 0$ the superfluid electron density equals the total electron density $n_s/n_e = 1$. At a thermodynamic critical temperature T_c of a superconductor (e.g. Nb bulk or thin film), the superfluid electron density is equal to zero $n_s/n_e = 0$, having a model temperature dependent form

$$\frac{n_s}{n_e} = 1 - \left(\frac{T}{T_c}\right)^4 \tag{2.1}$$

In 1935, Fritz and Heinz London proposed the two constitutive relations describing the electrodynamics response of a superconductor in an electromagnetic field [43]. The second London equation paired with Ampere's law gives

$$\nabla^2 \mathbf{B} = \frac{1}{\lambda_L^2}\mathbf{B} \tag{2.2}$$

where $\mathbf{B}$ is the vector magnetic field inside the superconductor, and λ_L is the London penetration depth

$$\lambda_L = \sqrt{\frac{mc^2}{4\pi n_e e^2}} \tag{2.3}$$

where μ_0 is the vacuum magnetic permeability, c is the speed of light in vacuum, and m and e are the mass and charge of an electron, respectively. Note, the London penetration depth is traditionally defined in terms of the total electron density, and is not temperature dependent as shown in Eq. 2.1. The temperature dependence of $\lambda_L(T)$ will be reviewed in Section 2.2.2. Eq. 2.2 suggests an applied external magnetic field H_0 decays exponentially inside a superconductor

to a magnetic field of $H = H_0/e$ at a distance into the surface equal to the London penetration depth $\lambda_L \approx 40\ nm$ for bulk Nb, where e is the first power exponential. In normal metals, the decay length is associated with the commonly known skin effect and the corresponding skin depth of Cu is $\approx 700\ nm$ at $\omega/2\pi = 10\ GHz$ [44]. Also note, the skin depth of Cu is infinite at $\omega = 0$ while λ_L is finite.

Jumping ahead, in 1957 the microscopic theory for superconductivity was established by Bardeen, Cooper, and Schrieffer (BCS) theory [45]. In accordance with BCS theory, the superfluid electrons have a bound (e.g. lower energy) state mediated by phonon lattice vibrations. The superfluid state consists of Cooper pairs. Using the simple electrodynamic model description, locally constricting the lattice around one paired electron in a single Cooper pair allows the other paired electron to later travel in the opposite direction with stronger lattice Coulomb interactions. The lowest-energy excitations of the superconduction states requires energy 2Δ, where Δ is the BCS energy gap. At zero temperature $T = 0$, the Nb BCS energy gap, a strongly coupled superconductor, can be estimated as [46]

$$\Delta \approx 1.97 k_B T_c \tag{2.4}$$

where $k_B = 86\ \mu eV/K$ is the Boltzmann constant. A strongly coupled superconductor means there is a strong electron-phonon coupling between the Cooper pairs and the phonon lattice energy $\hbar\omega_{ln}$, where $\hbar$ is the Planck constant. For the measurements in Chapters 4 and 5 of Nb thin films, assuming $T_c \approx 9.2\ K$, the stimulus frequencies $f \approx 10\ GHz$ are much lower than the gap frequency $f \ll 2\Delta/h \approx 750\ GHz$. Estimates of the Nb energy gap from temperature dependent measurements of microstrip transmission line resonators will be presented in Chapter 5 using the

13

dispersive loss deconvolution (DLD) method.

2.2.2 Complex Conductivity

In 1940, Heinz London measured resistive loss in superconducting Sn by means of calorimetry at high frequencies, and proposed it was due to a two-fluid model (interpenetrating mixture of normal and superconducting electrons) [47]. Later in 1947, Sir Brian Pippard measured the surface impedance of superconducting Sn and Hg at 1.2 GHz using a quarter-lambda resonator [48]. I will come back to surface impedance measurements in Section 2.2.3. The above experiments and many more led to the Mattis and Bardeen theory in 1958 that unified the anomalous skin effect for normal and superconducting metals [49].

In weak magnetic fields and in the low frequency limit $\hbar\omega \ll \Delta$, the Mattis and Bardeen expressions for complex conductivity $\sigma = \sigma_1 - i\sigma_2$ of a superconductor can be approximated by [50, 51]

$$\frac{\sigma_1}{\sigma_n} = \frac{2\Delta(T)}{k_B T} \frac{e^{\Delta(T)/k_B T}}{(1+e^{\Delta(T)/k_B T})^2} \ln \frac{\Delta(T)}{k_B T} \tag{2.5}$$

$$\frac{\sigma_2}{\sigma_n} = \frac{\pi\Delta(T)}{\hbar\omega} \tanh \frac{\Delta(T)}{2k_B T} \tag{2.6}$$

where ω is the angular frequency, $\Delta(T)$ is the temperature dependent BCS superconducting gap, σ_n is the normal metal conductivity, and σ_1 and σ_2 are the real and imaginary components of the complex conductivity at temperature T. At absolute zero temperature $T = 0$, the real conductivity is effectively zero $\sigma_1 = 0$. Eq. 2.5 was approximated by Kautz [50] and Eq. 2.6 by Tinkham [51] for all temperatures below $T < T_c$.

Similarly, in weak magnetic fields and in the low frequency limit $\hbar\omega \ll \Delta$, the two-fluid

model yields a complex conductivity of a superconductor

$$\sigma = \sigma_1 - i\sigma_2 \approx \sigma_n(n_n/n_e) - i\mu_0^{-1}\omega^{-1}\lambda^{-2} \tag{2.7}$$

where n_n/n_e is the normal electron density fraction, $\omega = 2\pi f$ is the angular frequency, and σ_n is the normal metal conductivity proportional to the normal electron mean free path $\sigma_n \propto \ell_{mfp}$ [49]. Here, σ_2 is London's conductivity and λ is the resulting magnetic penetration depth of the superconductor that can deviate from the bulk London penetration depth.

Using Pippard's modification to the London theory [52], and assuming the dirty limit where the microscopic (bulk) coherence length ξ_0 is of the same order as the electron mean free path ℓ_{mfp}, the magnetic penetration depth can be approximated as

$$\lambda \approx \lambda_L(\xi_0/\ell_{mfp})^{1/2} \tag{2.8}$$

where ξ_0 is the characteristic coherence length of the superconductor.

Eq. 2.8 suggests the screening length will effectively increase relative to the microscopic London penetration depth as a metal becomes more impure $\lambda > \lambda_L$. Hereby the magnetic penetration depth is sensitive to material defects (e.g. impurities, grain boundaries, dislocations), where higher concentrations of defects increase scattering and therefore decreasing the ℓ_{mfp}. For example, bulk Nb polycrystalline material have $\lambda_L \approx \xi_0 \approx 39\ nm$ with $\ell_{mfp} \gg \xi_0$, whereas nanocrystalline Nb thin films have $\ell_{mfp} \approx 7\ nm$ due to increased defect scattering mechanisms (e.g. grain boundary scattering), and results in a magnetic penetration depth of approximately $\lambda \approx 90\ nm$. This is a good approximation for Nb thin films [53] and patterned submicron wires

[54] described in Chapters 3-5.

Before the now accepted BCS theory, the two-fluid model developed by Gorter and Casimir [40] described the temperature dependent behavior of superconductors by assuming the density fraction of superconducting electrons n_s/n_e would drop to zero at the superconducting critical temperature T_c with dependence

$$\lambda(T) = \lambda(0) \left[1 - (T/T_c)^{\eta}\right]^{-1/2} \tag{2.9}$$

where $\lambda(0)$ is the real (measured) magnetic penetration depth at temperature $T = 0$, and η is an empirical fitting parameter. For low T_c superconductors $\eta \approx 4$ [51] (the approximation used in Eq. 2.1) and for high-temperature superconductors $\eta \approx 2$ [55].

Comparing Eqs. 2.5-2.6 and Eq. 2.7 show a relationship between the superconducting gap Δ and the penentration depth λ. Abiding by the assumption that $\hbar\omega \ll \Delta$, it is assumed here that the penetration depth λ is frequency-independent. Additionally, since all measurement temperatures are $T \ll T_c$ and well below the gap frequency for Nb, it is assumed here that $\sigma_1 \ll \sigma_2$. The complex conductivity is more accurately expressed by the BCS theory but is beyond the scope of this work, and can be found in Ref. [45] and is nicely summarized in Ref. [17]. I will refer back to the complex conductivity in the next section and use it to express the surface impedance of the superconductor. Using the complex conductivity, Nb microstrip transmission lines are modeled in Chapter 3 and simulated parameters are used to deconvolve the intrinsic surface resistance R_s from measurements in Chapters 4 and 5.

2.2.3 Surface Impedance

The ultimate conclusion from this section will relate the complex conductivity σ into an intrinsic surface impedance Z_s to obtain the mechanism of resistive power dissipation coming from the superconductor in RQL interconnect, i.e. intrinsic resistance R_s. Furthermore, the superconducting parallel plate transmission line will be introduced. It will be shown that as the magnetic penetration depth λ becomes comparable to the finite thickness and width dimensions of a superconducting microstrip transmission line, a method is needed to accurately extract R_s to compare RQL interconnects of different dimensions on equal footing and analyze extrinsic effects due to fabrication.

At the end of the 19th century, engineers primarily relied on circuit theory to simplify complex circuit analysis and design without the aid of computers. Discrete components (e.g. transmission line) could be "lumped" and connected into a network only using resistors, inductors, and capacitors. With an an electromagnetic wave applied to a combined circuit or discrete component at radio frequencies (RF), the alternating currents and voltages can be related to the circuit by an intrinsic impedance Z_s introduced by Oliver Lodge in 1889 [56].

First, consider a wave propagating from vacuum to a media as shown in Fig. 2.1 with a relative dielectric constant ε_r or a conductivity σ (real or complex). Fig. 2.1a is an analogy to a transverse electromagnetic (TEM) plane wave propagating along the x-direction into a perfect electrical conductor transmission line with media having a relative dielectric constant $\varepsilon > 1$. Using the coordinate system in Fig. 2.2, the complex voltage V and current I for a wave propagating

17

along the x-axis of a transmission line can be described by the following three equations [57]

$$dV/dx = -ZI \tag{2.10}$$

$$dI/dx = -YV \tag{2.11}$$

$$\gamma = \sqrt{ZY} \tag{2.12}$$

where Z and Y are the distributed series impedance and the distributed shunt admittance of the line, respectively, and γ is the propagation constant of the line. This will be revisited in Chapter 3.

The propagation of plane electromagnetic waves along the x-direction in a lossy medium shown in Fig. 2.1b can be described also by the following three equations

$$d\mathbf{E}/dx = -i\omega\mu\mathbf{H} \tag{2.13}$$

$$d\mathbf{H}/dx = -(\sigma + i\omega\varepsilon)\mathbf{H} \tag{2.14}$$

$$\gamma = \sqrt{i\omega\mu(\sigma + i\omega\varepsilon)} \tag{2.15}$$

where $\mathbf{E}$ is the electric field vector pointing along the y-direction, $\mathbf{H}$ is the magnetic field vector pointing along z-direction, ω is the wave angular frequency, $\varepsilon = \varepsilon_0\varepsilon_r$ is the permittivity of the medium, $\mu = \mu_0\mu_r$ is the permeability of the medium, ε_r is the relative dielectric constant of the medium, μ_r is the relative permeability of the medium, γ is the medium propagation constant, and σ is the conductivity of the medium.

Thus, the impedance term from transmission line theory using V and I could be extended to electromagnetic wave theory $\mathbf{E}$ and $\mathbf{H}$, and the intrinsic impedance takes the general form and
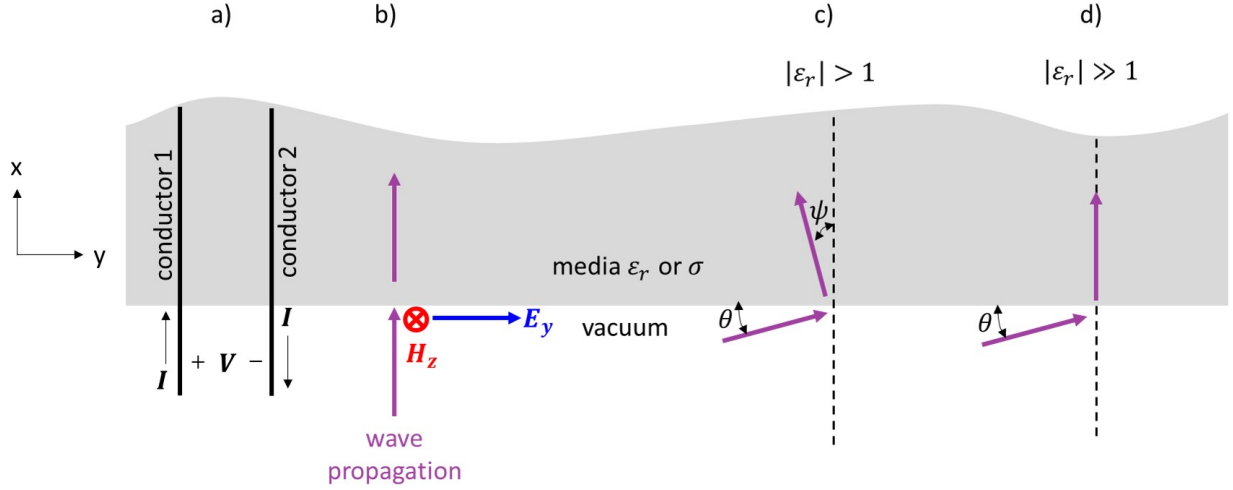
Figure 2.1:   Diagram showing wave propagation from vacuum into media with a relative dielectric constant ε_r or conductivity σ (real or complex). a) Analogy to transmission line with media having a relative dielectric constant $\varepsilon > 1$ showing the Complex voltage V and current I as the wave propagates into media described by Eqs. 2.10-2.12. b) The case for a normal incidence propagating plane wave into media (see Eqs. 2.13-2.15). c) The case for a glancing incidence propagating plane wave for media with $\varepsilon_r > 1$ with refracted angle of $\psi > 0$. In general, the refracted wave is an in-homogeneous wave. This is a wave for which the planes of constant phase are not parallel to the planes of constant amplitude [58]. d) The case for glancing incidence propagating plane wave for media with $\varepsilon_r \gg 1$ with refracted angle of $\psi \approx 0$. Cases c) and d) have been adopted from [58] using Snell's law of refraction in conductive media (see Eq. 2.17).

is related to the media conductivity by

$$Z_s = \frac{E_y}{H_z} = \sqrt{\frac{i\omega\mu}{\sigma + i\omega\varepsilon}} = \frac{\gamma}{\sigma + i\omega\varepsilon} \qquad (2.16)$$

19

Fig. 2.1c and Fig. 2.1d are two cases for a wave propagating at glancing incidence relative to the vacuum-media interface. Using Snell's law of refraction in conductive media [58],

$$\sin \psi \approx \sqrt{\frac{2\omega\varepsilon_0}{\sigma}} \sin \theta \sim k_0 \lambda \sqrt{2} \sin \theta \sim \lambda/\lambda_{EM} \tag{2.17}$$

where θ is the incident angle for wave propagating in vacuum, ψ is the refraction angle for wave propagating in the media, ω is the angular frequency, ε_0 is the vacuum permittivity, μ_0 is the vacuum permeability, σ is the conductivity of the medium the wave is refracted into, $k_0 = \omega\sqrt{\mu_0\varepsilon_0}$ is the vacuum wave number, λ_{EM} is the wavelength of the propagating electromagnetic wave. The left hand side approximation in Eq. 2.17 can be used for case Fig. 2.1c, where the media has an absolute relative dielectric constant greater than 1, $|\varepsilon_r| > 1$. The middle approximation in Eq. 2.17 can be used for case Fig. 2.1d for a superconductor where the relative dielectric constant is negative and its absolute value is much greater than 1 (see Section 3.4.2 where a superconductor is defined as a dielectric with negative permittivity in HFSS). The middle approximation in Eq. 2.17 assumes the conductivity of the superconductor is $\sigma \approx \sigma_2$ from Eq. 2.7 assuming $\sigma_2 \gg \sigma_1$. Assuming a Nb magnetic penetration depth of 40 nm, $\psi \sim 1.2 \times 10^{-5} \, rad$.

Consequently, Eq. 2.17 and Fig. 2.1d exemplify that for a normal or glancing incident wave propagating into a superconductor where $|\varepsilon_r| \gg 1$ the refracted wave will propagate normal to the vacuum-superconductor interface. This is the basis for why a superconducting parallel plate transmission line supports a transverse magnetic (TM) propagation wave and is termed a Swihart wave [59]. In Fig. 2.2, the wave is propagating along the y-direction which is glancing incidence to the two superconductor-dielectric interfaces. At $x = 0$, $E_y = 0$ and at the superconductor

20
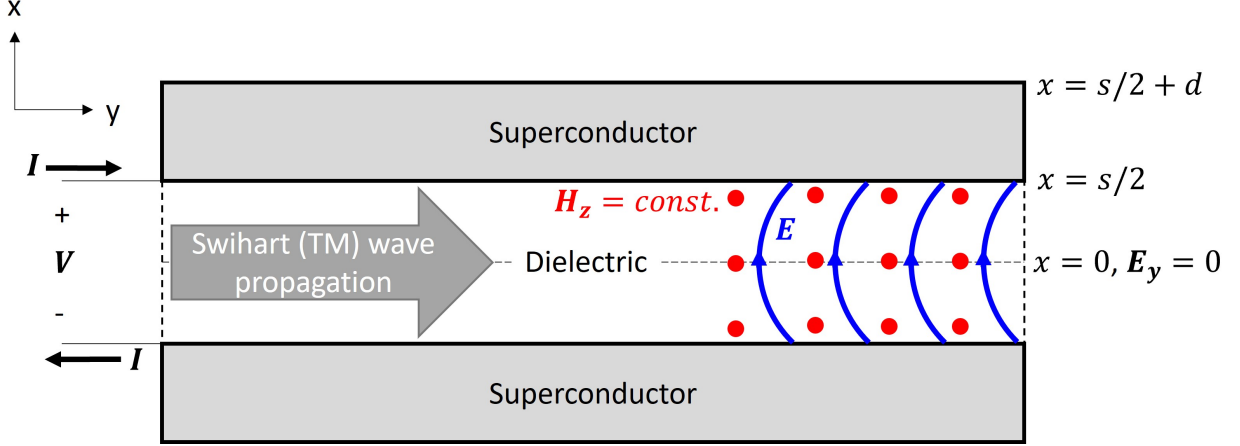
Figure 2.2: Diagram showing a superconducting parallel plate transmission line with a Swihart transverse magnetic (TM) wave [59] propagating along the y-axis, where looking into and out of the page the superconducting plates are infinitely long. The dielectric material between the plates has a thickness s, and each superconducting plate has a thickness d. The propagating wave is transverse magnetic because there is a small, finite y-component to the electric field at the superconductor-dielectric boundaries. The y-component of the electric field is responsible for the curvature of the electric field lines near the boundary (blue).

dielectric interfaces ($x = \pm s/2$), the E_y has a finite magnitude. It can also be seen that Fig. 2.1a and Fig. 2.2 are equivalent and Eqs. 2.10-2.12 can be used. As the dielectric thickness becomes small, and comparable to the magnetic penetration depth λ, E_y becomes significant and can greatly affect the phase velocity v_p (see Appendix Eq. D.7, where $f_n \propto v_p$).

Assuming the superconducting plate thicknesses d and dielectric thickness s in Fig. 2.1 are much larger than the magnetic penetration depth $d \gg \lambda$ and $s \gg \lambda$, respectively, the E_y magnitude is negligible to E_x magnitude, and therefore a surface impedance boundary condition (SIBC) can be enforced.

The Leontovich-Shchukin SIBC approximation is derived by using the following assumptions but in the context of a good superconductor. The wavelength and magnetic penetration depth λ traveling in the media must be small relative to the material dimensions. As a consequence, the

material must be sufficiently thick (bulk) where reflected fields from the back surface/interface are neglected. Furthermore, the EM fields vary slowly on the surface of the medium relative to the wavelength. This constitutes a flat surface, or its smallest radius of curvature must be large relative to the magnetic penetration depth. Assuming the above, and referring to the coordinate system defined in Fig. 2.2, for a wave traveling in the y-direction along a plane surface, i.e. the plane between superconductor plates and dielectric in Fig. 2.2, the complex intrinsic wave impedance is in units of ohms per square and proportional to the ratio of the electric and the magnetic fields by

$$Z_{wave} = \frac{E_y}{H_z}\bigg|_{plane\ wave} = \sqrt{\frac{i\omega\mu}{\sigma + i\omega\varepsilon}}\bigg|_{\sigma \gg \omega\varepsilon} \approx \sqrt{\frac{i\omega\mu}{\sigma}} \tag{2.18}$$

where $\mu = \mu_0\mu_r$ is the permeability of the medium, $\varepsilon = \varepsilon_0\varepsilon_r$ is the permittivity of the medium, E_x is the magnitude of the electric field pointing out-of-plane, H_y is the magnitude of the magnetic field pointing in-plane, and ω is the wave source frequency. The right approximation in Eq. 2.18 holds for good, nonmagnetic conductive media, where the relative permeability μ_r and permittivity ε_r are equal to unity $\mu_r = \varepsilon_r = 1$, and so the permeability and permittivity are that of the vacuum $\mu = \mu_0$ and $\varepsilon = \varepsilon_0$, respectively. As it can be seen, Eq. 2.18 is not dependent on coordinates and assumes the wave impedance is constant over the plane conducting surface. In other words, the intrinsic impedance Z_{wave} connects the electromagnetic response of conducting media with its conductivity function dependent on material properties.

Eq. 2.18 can be used as a surface impedance boundary condition (SIBC), and can greatly simplify complex problems. Today, SIBC are used in finite-element modelers (FEM) to simplify geometries and numerically solve the electromagnetic fields faster. Sergey Yuferev and Nathan

Ida give a good overview of the different SIBCs, their history, and applications [60]. An example of using a SIBC to validate HFSS simulations can be found in Section 3.4.1.

In 1938, the impedance concept was later generalized and applied to engineering applications (e.g. power engineering, transmission lines) by Sergei Schelkunoff [61] who first coined the skin effect term. In this work, assuming a superconducting medium with complex conductivity $\sigma = \sigma_1 - i\sigma_2$ is nonmagnetic with $\mu = \mu_0$ and a good conductor with negligible displacement current $\sigma \gg \omega\varepsilon$, the intrinsic impedance simplifies to

$$Z_s = R_s + iX_s = \sqrt{\frac{i\mu_0\omega}{\sigma_1 - i\sigma_2}} \tag{2.19}$$

where R_s is the intrinsic surface resistance and X_s is the intrinsic surface reactance of the superconducting media. Taking the approximation for the complex conductivity in Eq. 2.7 assuming, $T \ll T_c$, $\sigma_1 \ll \sigma_2$, and $\hbar\omega \ll \Delta$ it can be shown that the two-fluid superconductor intrinsic impedance can be written as

$$Z_s = R_s + iX_s \approx \frac{1}{2}\mu_0^2\omega^2\lambda^3\sigma_1 + i\mu_0\omega\lambda \tag{2.20}$$

where μ_0 is the vacuum magnetic permeability, ω is the stimulus angular frequency, λ is the magnetic penetration depth defined in Eq. 2.8, and σ_1 is the conductivity of the normal electrons. Eq. 2.20 above models a bulk superconductor where the two-fluid model can be assumed. In this work we are concerned with measuring the intrinsic resistance R_s as it determines the power lost due to the superconductor in RQL interconnects. In this context, the intrinsic resistance is that of the effective bulk property of the superconductor and its relation to finite thickness effects will be

discussed later in this section. In normal metals, where $\sigma_1 \gg \sigma_2$, the real and imaginary parts of the intrinsic resistance are equal, and frequency dependence $R_s = X_s \propto \sqrt{\omega}$. For Cu at 10 GHz, the intrinsic resistance is $R_s \approx 26 m\Omega$ and $\approx 2m\Omega$ at temperatures T = 300 and 10 K, respectively. For a superconductor like Nb, assuming a good isotropic superconductor with $\sigma_1 \ll \sigma_2$, Nb has a quadratic frequency dependence of the intrinsic resistance $R_s \propto \omega^2$ [62, 63]. For clean bulk niobium, $R_s \approx 20 - 40 \ \mu\Omega$ at 4.2 K and 10 GHz. Furthermore, for thin film Nb, the BCS R_s can be as low as 17 $\mu\Omega$ at 4.2 K and 10 GHz when σ_1 is at a theoretical optimum for the case $\xi_0/l_{mfp} \approx 4\pi$, where ξ_0 is the microscopic (bulk) coherence length [64]. This means intrinsic resistance can be lower for Nb thin films compared to bulk. To achieve minimum $R_s \approx 17\mu\Omega$ in Nb, the optimal mean free path is $l_{mfp} \approx 10 \ nm$ for $\xi_0 \approx 40 \ nm$. This is conveniently close to typical Nb l_{mfp} values for thin films having thicknesses $d \sim 100 - 200 \ nm$ [53], which is the typical wiring layer thickness in RQL fabrication (see section 2.4). Using Eq. 2.8, assuming $\xi_0 \approx \lambda_L = 40 \ nm$, and $l_{mfp} = 10 \ nm$ yields a magnetic penetration depth of $\lambda = 80 \ nm$. This is within 12% of the measured value of $\lambda = 90 \ nm$ for submicron Nb wires determined from self inductance measurements at T=4.2 K with exceptional hardware-to-model correlation [54, 65].

It is important to note that Eq. 2.20 above describes the impedance of a bulk (infinitely thick) superconductor. Here we deal with finite thin film superconductors that have been patterned into narrow strips, making the above equation incomplete. It is of vital importance in this work to "extract" the intrinsic bulk impedance from an "effective" impedance so we analyze extrinsic effects changing Z_s as the transmission line dimensions shrink. A significant amount of work has been done to modify the impedance definition to account for non-ideal or "non-bulk" situations, and they will be further reviewed and compared to the intrinisic impedance Z_s.

Starting in the 1930s, radio technology facilitated theory development of electromagnetic

wave propagation from a radiating antenna over the Earth's surface. Solutions to the wave propagation can be very complex as the waves can travel in and reflect off of many media including the earth's surface, embedded surfaces, and air over long distances where the curvature of the Earth needs to be considered. To simplify the problem, Leontovich [66, 67] and Shchukin [68] independently proposed an approach where the air region only needs to be considered by making the Earth's surface a surface impedance boundary condition (SIBC).

For the case where the magnetic penetration depth becomes comparable to the material or film-thickness $\lambda \geq 2d$, modifications to the intrinsic impedance Z_s need to be made. The modifications need to be made because unlike the Leontovich-Shchukin SIBC approximation, reflected fields across the bottom surface of the finite thickness superconductor cannot be neglected due to the condition $\lambda \geq 2d$. Furthermore, thin-film superconductors are typically deposited on dielectric substrates, so the electromagnetic fields at the dielectric-superconducting interface as well as into the dielectric need to also be accounted for. In the 1980s high temperature superconductors (HTSs) were discovered. Klein *et al.* came up with the theory for the effective surface impedance Z_{eff} in 1990 to account for finite thickness effects [69] since HTSs have very large magnetic penetration depths relative to the typical thin-film thicknesses $\lambda \geq 2d$. First, assuming an infinitely thick dielectric substrate below the superconducting thin film, the effective surface impedance was calculated by using an impedance transformation method having the form

$$Z_{eff} = z(d)Z_s \tag{2.21}$$

$$z(d) = \frac{z(0) + \tanh(\gamma d)}{1 + z(0)\tanh(\gamma d)} \tag{2.22}$$

where d is the film thickness, Z_s is the intrinsic surface impedance given by Eq. 2.20, $z(0)$ is the

impedance at the film-substrate interface, $z(d)$ is the transformed impedance up to the film surface d, $z(0)$ and $z(d)$ are normalized to Z_s of the film, and $\gamma = \alpha + i\beta$ is the complex propagation constant of the superconductor.

From this and accounting for the dielectric substrate, the effective surface impedance R_{eff} of a superconducting plate can be approximated by [69, 70]

$$Z_{eff} = R_{eff} + iX_{eff} \tag{2.23}$$

$$R_{eff} = R_s \left[\coth(d/\lambda) + \frac{d/\lambda}{\sinh^2(d/\lambda)} \right] + \left(\frac{X_s^2}{Z_{sub}} \right) \frac{d/\lambda}{\sinh^2(d/\lambda)} \tag{2.24}$$

$$X_{eff} = \omega \mu_0 \lambda_{eff} \tag{2.25}$$

$$Z_{sub} = \frac{\eta_0}{\varepsilon_r^{1/2}} \left(1 + i \frac{\tan\delta}{2} \right) \tag{2.26}$$

where R_{eff} is the effective surface resistance, X_{eff} is the effective surface reactance, $\lambda_{eff} = \lambda \coth(d/\lambda)$ is the effective penetration depth, μ_0 is the permeability of free space, Z_{sub} is the bulk impedance of the dielectric substrate, ε_r and $\tan\delta$ are the relative dielectric constant and loss tangent of the substrate, respectively, and $\eta_0 \equiv \sqrt{\mu_0/\varepsilon_0} = 120\pi \ \Omega$ is the intrinsic wave impedance.

It can be inferred from Eqs. 2.23-2.25 that the primary contribution to the enhancement of Z_s is due to the ratio of the film thickness relative to the magnetic penetration depth d/λ. As the film thickness becomes small relative to the magnetic penetration depth $d/\lambda \ll 1$, the effective impedance Z_{eff} dramatically increases as a consequence of the current density increasing inside of the superconducting film by approximately a factor $\coth(d/\lambda)$. Conversely, as $d/\lambda \gg 1$, Eq. 2.23 reduces to Z_s of a bulk superconductor in Eq. 2.20. The second term of R_{eff} is due

26

to power transmission into the dielectric substrate, and decreases in effect as the impedance mismatch between the dielectric substrate and and superconducting film increases $X_s/|Z_{sub}| \ll$ 1 and is independent of the dielectric substrate loss tangent $\tan \delta$, assuming $X_s \gg R_s$ and transmitted power is not reflected back to the film.

Notice in Eq. 2.24, neglecting the substrate contribution, R_{eff} is the intrinsic resistance multiplied by an effective geometric factor in brackets. If one wanted to compare two samples with different film thicknesses, one would need to use Eq. 2.24 to extract the intrinsic (bulk) resistance. The same concept holds for extracting the intrinsic reactance X_s from Eq. 2.25.

2.2.4 Temperature Dependence of Surface Impedance

The temperature dependence of the superconductor bulk intrinsic reactance X_s (magnetic penetration depth λ) from Eq. 2.20 can be approximated by assuming two-fluid model found in Eq. 2.9. The temperature dependence of the intrinsic resistance R_s is better approximated from the temperature dependence of the BCS gap. At temperatures approximately $T \leq T_c/2$ the intrinsic resistance scales exponentially on the ratio of the BCS gap and temperature by $R_s(T) \propto e^{-\Delta(T)/k_B T}$. In this temperature range, the magnetic penetration depth is assumed to be constant, having the value λ found in Eq. 2.9. Below a certain temperature the intrinsic resistance becomes temperature independent having the value R_{res}, and is $T_{res} \approx 1.8\ K$ for thin film Nb [71]. With this, the temperature dependence of the intrinsic impedance Z_{s0} at a reference frequency ω_0 at $T \leq T_c/2$ can be approximated by

$$R_{s0}(T) = R_{s0}(0)\tfrac{1}{T}e^{-\frac{\Delta(T)}{k_B T}} + R_{res0} \approx \tfrac{A}{T}e^{-B(T/T_c)} + C \text{ for } T \leq T_c/2 \qquad (2.27)$$

$$X_{s0}(T) = \omega_0 \mu_0 \lambda(T) \coth\left(d/\lambda(T)\right) \qquad (2.28)$$

$$\lambda(T) = \lambda(0) \left[1 - (T/T_c)^\eta \right]^{-1/2} \tag{2.29}$$

where R_{res0} is the residual intrinsic resistance at a reference frequency ω_0 below $T \approx 1.8\ K$ for thin film Nb, $R_{s0}(0)$ is the BCS zero temperature intrinsic resistance, A is an empirical fitting parameter, $B/T_c = \Delta(0)/k_B T_c$ is the gap ratio fitting parameter, $C = R_{res0}$ is the residual intrinsic resistance fitting parameter, d is the superconductor thin film thickness, and $\lambda(0)$ is the magnetic penetration depth at zero temperature.

Valente-Feliciano *et al.* found $B/T_c = \Delta(0)/k_B T_c \approx 1.89$ for Nb thin films [71], within 5% agreement to approximation of $\Delta(0)/k_B T_c \approx 1.97$ made in Eq. 2.4. The approximation on the right in Eq. 2.27 will be used in Chapter 5 to fit temperature dependent microstrip transmission line (MTL) data having fitted values of $\Delta/k_B T_c \approx 2.1$.

2.2.5 Summary

In summary, to meaningfully compare results for RQL interconnects having different microstrip transmission line (MTL) widths requires the determination of the intrinsic resistance R_s shown in Eq. 2.20. Thin-film superconductors screen electromagnetic fields on the length scale of the magnetic penetration depth λ. Increased defectivity in the material results in an increase in λ, causing the magnetic field penetration to drive further inside of the thin-film or MTL. Furthermore, an increase in the magnetic penetration depth means the RF currents sample defects buried deeper in the wire, and can induce an increase in R_s. The surface impedance boundary condition (SIBC) first introduced by Leontovich and Shchukin simplifies the problem making it easier to account for non-idealities relative to bulk solutions. Klein *et al.* approximated the SIBC condition for an infinitely wide thin film superconductor on a dielectric substrate where

λ is comparable or much larger than the thin film thickness $\lambda \geq 2d$. Although, an additional treatment is needed to account for lossy MTLs where λ also becomes comparable to the dielectric separation thickness s between the conducting strip and the groundplane as well as the MTL width w. With the advancement and maturation of finite element modelers, it is possible to numerically solve the electromagnetic fields and extract the intrinsic impedance Z_s, and the method will be carried out in Chapter 3 to extract R_s from measured data in Chapter 4 and 5.

2.3 Amorphous Dielectrics

Silicon dioxide SiO_2 fabricated via chemical vapor deposition using a tetraethyl orthosilicate (TEOS) precursor is the primary dielectric material used in the microstrip transmission line resonators measured in chapters 3-5. Silicon oxide in this context will be referred to by its precursor TEOS throughout this dissertation. TEOS is deposited on Si wafers and is limited to temperatures $T \leq 150°C$ (see section 2.4.6). Using common plasma-enhanced chemical vapor deposition processes similar to references [72, 73], the kinetics are such that surface diffusion is limited, preventing the growth of a crystalline lattice. The TEOS amorphous structure is confirmed by the presence of a diffuse ring in electron diffraction image similar to reference [74]. The combination of the $T \leq 150°C$ thermal budget and amorphous structure of TEOS limits the lower bound of the loss tangent to approximately $\tan \delta \approx 1 \times 10^{-3}$ at 4.2 K. Comparatively, this is a factor of 3-4 of magnitude higher than thermal oxide grown SiO_2 [75]. Therefore, this gives rise to non-ideal high power dissipation coming from the TEOS dielectric in RQL interconnects and is a motivation of this work to review the fundamental material properties and loss mechanisms.

The typical operating temperatures for classical superconducting logic and quantum computing circuits are $T \leq 4.2\ K$ and $T \ll 1\ K$, respectively. At these temperatures, the power loss from the amorphous (glassy) dielectrics depends strongly on the stimulus energy $\hbar\omega$, where ω is the applied electric field frequency. Therefore, it is important to briefly review the history and explicitly state the temperature and frequency regime carried out in measurements performed in chapters 4 and 5. First, I will introduce the fundamental dielectric loss tangent $\tan\delta$ that describes how energy is dissipated in a dielectric material due to relaxation processes. Then, I will briefly review the history of low temperature measurements of $\tan\delta$. Here, I will focus the review on the difference between crystalline and amorphous dielectrics. I will also incorporate the relative dielectric constant ε_r, as its temperature and frequency dependence are governed by the same mechanisms as $\tan\delta$. For a proper introduction, the two-level system model will be included in the discussion. To conclude this section, I will summarize the historical work that has been done by showing the universality of the $\tan\delta$ temperature dependence and its respective mechanisms, where varying ω more or less shifts the intersection of temperature regimes. Finally, I will explicitly state the mechanism dominating $\tan\delta$ in different temperature and frequency regimes used in the measurements carried out in Chapters 4 and 5.

2.3.1   The Dielectric Loss Tangent $\tan\delta$

A simple RC circuit analogy can be used to describe dielectric relaxation [76]. In a linear system a dielectric material can be modeled having a resistance R due to some Joule losses in the dielectric, and capacitance C capable of holding a charge Q. Here, we assume a series RC circuit with time-independent R and C. For a step-function voltage applied to the dielectric, where the

voltage maximum is $V = V_0$ at time $t = 0$ and zero $V = 0$ for time $t > 0$, the time-dependent discharging can be described as

$$Q = CV_0 e^{-t/\tau_{rel}} \tag{2.30}$$

where Q reaches a fraction $1/e$ after a time τ_{rel}, which is the characteristic relaxation time, or RC time constant equal to $\tau_{rel} = RC$. For a sinusoidal voltage stimulus $V(t) = V_0 e^{i\omega t}$ at angular frequency ω, the charge has both in-phase and quadrature responses, and can be considered complex, and takes the form

$$Q(\omega, t) = CV_0 \left(\frac{1}{1 + \omega^2 \tau_{rel}^2} - i \frac{\omega \tau_{rel}}{1 + \omega^2 \tau_{rel}^2} \right) e^{i\omega t} \tag{2.31}$$

Eq. 2.31 shows a time lag between the charge response Q and applied voltage V. This phase lag can be represented by the tangent of an angle δ as $\tan \delta$. Assuming $\tan \delta << 1$ implies $\delta \approx \omega \tau_{rel}$, where τ_{rel} is the characteristic time lag between Q and V. The time lag induces a dissipation of energy. In other words, if the sinusoidal voltage was turned off, the dielectric charge will "relax" to a lower energy state, and that time lag, or characteristic relaxation time τ_{rel} will dissipate some amount of energy. It can be shown that the energy dissipated W and δ are related by $W \propto \sin \delta$ [76]. For small angles δ, the energy dissipated in the dielectric is directly proportional to δ, hence the commonly used term loss tangent $tan\delta$ and loss angle δ. For a parallel RC circuit, which is more analogous to our circuits here, the loss tangent is related to dielectric relaxation time

$$\tan \delta = 1/\omega \tau_{rel} \tag{2.32}$$

Both the phonon (quantized lattice vibrations) and polarization (charge) can be described with the above RC circuit model. For an acoustic frequency (sound wave) stimulus, the acoustic energy loss is caused by the lattice viscosity, or resistance of the vibrating atoms to displacement. Here, the resistance R is proportional to the viscosity and C is proportional to the stored energy in lattice vibrations. The time lag of lattice displacements induces energy loss.

If a dielectric material can be electrically polarized by a stimulus due to some displacement of charge (e.g. doped dielectric crystals, ionic crystals, amorphous dielectrics), then charge displacement relative to its lattice vibrations under electromagnetic stimuli will induce power dissipation. Hence, phonon vibrational modes and electronic polarization are coupled and dissipate power in dielectric materials.

2.3.2 Dielectric Loss Mechanisms and Phonon Scattering at $T < 10\ K$

As mentioned at the beginning of section 2.3, the TEOS dielectric measured chapters 3-5 is considered amorphous. Therefore, in the context of this work, only amorphous dielectrics will be considered, but it is important to briefly summarize the differentiation between the material properties of glassy and crystalline dielectrics at cryogenic temperatures approximately $T <$ $100\ K$. The surprising difference was seen in heat capacity measurements of vitreous, meaning glassy, silica and crystalline $\alpha-$quartz by Zeller and Pohl in 1971 [77]. At 0.1 K, the specific heat capacity C_D of vitreous silica was 2 orders of magnitude higher than quartz. Crystalline quartz follows the typical Debye dependence $C_D \propto T^3$ below its Debye temperature approximately $T \ll T_D \approx 360\ K$ [78]. At these temperatures, the phonons, or lattice vibrations, can only occupy long wavelength vibrational modes and can be treated as an elastic continuum, and so the

heat capacity is proportional to the thermal conductivity by

$$\kappa_D = \frac{1}{3} C_D v_D \ell_{ph} \tag{2.33}$$

where C_D is the Debye specific heat capacity per volume of the heat carrying phonons, v_D is the phonon velocity, and ℓ_{ph} is the phonon mean free path due to scattering by lattice defects. Referring back to the Zeller and Pohl measurements, it was found that vitreous silica, and universally for amorphous dielectric materials for $T \ll T_D$, have a temperature dependent specific heat and thermal conductivity proportional to $\propto T$ and $\propto T^2$, respectively. Early phenomenological models tried to modify the specific heat capacity alone to account for the $\propto T$ dependence, but were not consistent and are further reviewed in [79]. This led to further experimental evidence that the anomalous thermal properties arise from additional excitations inducing a change in the specific heat and suggests the phonon mean free path has a temperature dependence $\ell_{ph}(T)$.

Similarly to the thermal properties, there is a close relationship between the acoustic and dielectric attenuation/loss properties in amorphous dielectrics at temperatures approximately below 100 K [80]. For example, for amorphous dielectrics there is a quintessential maximum in loss/attenuation at a temperature T_{max}. Anderson and Bommel confirmed this by plotting the temperature of this maximum loss peak as a function of stimulus frequency $\omega/2\pi$ and found exceptional agreement between acoustic and electrical measurements (see Fig. 2.3). An Arrhenius relationship suggests a thermally activated process and will be mentioned briefly later. Notice, Fig. 2.3 shows that T_{max} will increase to higher temperatures as the measurement frequency is increased.

In 1972 Anderson [82] and Phillips [83] proposed a two-level system (TLS) model to
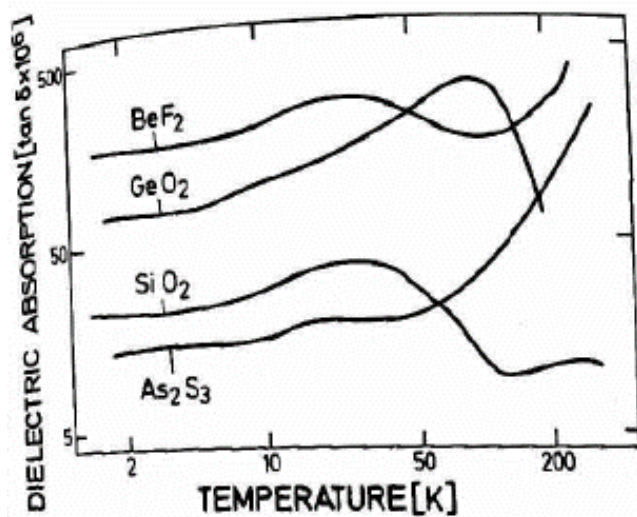
Fig.6.2. Dielectric loss of several glasses below room temperature at 1 kHz (after [6.25,28])
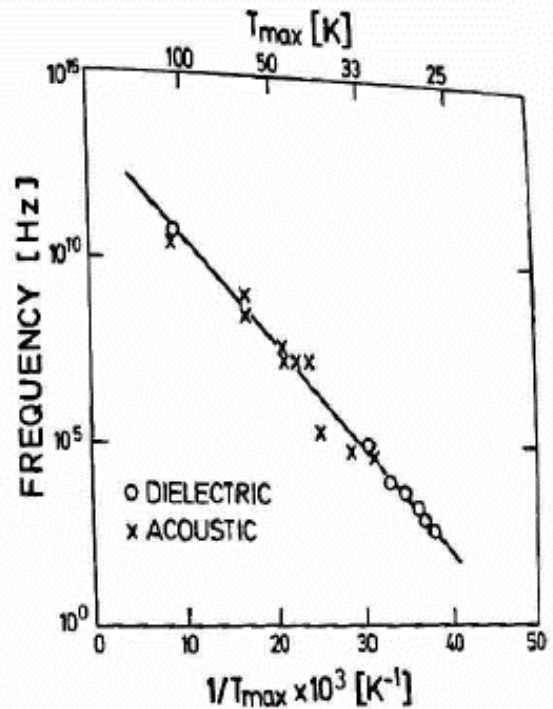
Fig.6.3. Arrhenius plot (frequency versus inverse peak temperature) of the absorption peak observed in vitreous silica in ultrasonic and dielectric measurements

Figure 2.3: This figure is adopted from reference [81] and discussed in reference [80] Fig. 6.2-6.3.

describe the thermal properties of amorphous dielectrics at temperatures below the crystalline Debye temperature T_D. In the TLS model, atoms (or electrons, no one knows) occupy one of two minima capable of tunneling between the two states quantum mechanically. Consequently, the manifestation of tunneling between two energy states scatters phonons, prompting an additional mechanism of dissipated energy (i.e. TLS loss). With this, the TLS model universally explains the temperature dependent specific heat $\propto T$ and thermal conductivity $\propto T^2$ of amorphous dielectrics at temperatures $T < 1\ K$. Effectively, and to support the context of this dissertation, the anomalously low thermal conductivity for amorphous dielectrics at temperatures $T \ll 10\ K$ arrises from low phonon scattering lengths ℓ_{ph} as a result of strong resonant absorption of thermal phonons by the TLSs [80].

Referring back to Fig 2.3, the dissipated loss coming from TLSs have been measured by acoustic attenuation and the dielectric loss tangent, both of which are related. The measured acoustic attenuation α_{db} is proportional to the inverse phonon mean free path $\alpha_{db} \propto \ell_{ph}^{-1}$. Therefore, at temperatures below $T < T_{max}$ and at a given reference frequency ω_0, the temperature dependent dielectric loss tangent and phonon mean free path are approximately proportional $\tan \delta(T, \omega_0) \propto \ell_{ph}^{-1}(T, \omega_0)$ [84]. The frequency dependent proportionality between dieletric loss tangent and ultrasonic absorption is $\tan \delta \propto \alpha_{db}/\omega$. Note, the frequency dependence of α_{db} depends on which temperature below $T < T_{max}$ the measurement is taking place, and will be discussed further.

Since it is established that energy dissipation measured by the loss tangent $\tan \delta$ is coupled to phonon scattering at temperatures $T < 10\ K$, I will focus on the mechanisms causing the temperature and frequency dependence of $\ell_{ph}(T, \omega)$. The TLS loss can be split up into two phonon scattering mechanisms, TLS tunneling due to resonant absorption $\ell_{tun,res}$ and to relaxation

35

$\ell_{tun,rel}$ [79]. Resonant absorption occurs when TLSs are resonant with the applied electric or acoustic fields at particular energies and frequencies. Relaxation of TLSs occur when non-resonant TLSs having a dipole moment are driven out of non-equilibrium in an applied field and scatter phonons as the TLSs "relax" in a decaying oscillatory fashion during redistribution between the energy levels. Schickfus *et al.* was the first to measure the energy dissipation in vitreous silica due to both TLS loss mechanisms below $T \ll 1\ K$ [84] using the 2 cavity test setup [85]. Loss due to resonant absorption manifests in measurements at low applied electric fields, and at higher applied fields the TLSs are saturated and loss is dominated by TLS relaxation.

At higher temperatures in the approximate range $10\ K < T_{max} \approx 100\ K$, "classical" relaxation dominate the phonon scattering process. Contrary to TLS relaxation via tunneling between two energy states, classical relaxation scatters phonons by the dissipation of energy from physical charge displacement (see Eq. 2.32) [76, 86]. The phonon mean free path due to classical relaxation is $\ell_{class,rel}$. Temperatures higher $T > 10\ K$ will not be considered since it is beyond what is measured in chapter 3 and 4, but are mentioned for completeness. Therefore, the three mechanisms contributing to the total phonon free path $l_{ph}(T, \omega)$ at temperatures below $T < 10\ K$ with temperature and frequency dependence are

$$l_{ph}(T, \omega)^{-1} = \ell_{tun,res}^{-1}(T, \omega) + \ell_{tun,rel}^{-1}(T, \omega) + \ell_{class,rel}^{-1}(T, \omega) \tag{2.34}$$

where the phonon scattering mean free path due to TLS resonant tunnelling, TLS tunneling relation, and classical charge (dipole) relaxation are $\ell_{tunn,res}$, $\ell_{tunn,rel}$, and $\ell_{class,rel}$, respectively.

Mentioned previously, the dielectric relaxation is proportional to the ultrasonic attenuation $\tan\delta(T, \omega_0) \propto \alpha_{db}(T, \omega_0)$ [84]. The ultrasonic attenuation is inversely proportional to the phonon

mean free path by $\alpha_{db}(T, \omega_0) \propto l_{ph}^{-1}(T, \omega_0)$ (see [79]). Accordingly, the total dielectric loss tangent $\tan \delta$ can be split up into the three loss mechanisms from Eq. 2.34 in the following way

$$\tan \delta(T, \omega) = \tan \delta_{tun,res}(T, \omega) + \tan \delta_{tun,rel}(T, \omega) + \tan \delta_{class,rel}(T, \omega) \qquad (2.35)$$

where the dissipative loss associated TLS resonant tunnelling, TLS tunneling relaxation, and classical charge (dipole) relaxation are $\tan \delta_{tunn,res}$, $\tan \delta_{tunn,rel}$, and $\tan \delta_{class,rel}$, respectively, and are all temperature and frequency dependent.

2.3.3   Temperature Dependence of $\tan \delta$

Referring to Fig. 2.4 starting from the lowest temperature, depending on the applied electric field strength E, the dielectric loss is dominated by either TLS resonant tunneling (absorption) or TLS relaxation processes. The response of TLSs to applied electric fields is dependent on the coherence between their two eigenfunctions formally treated for solving the problem developed for optical saturation [87] and magnetic resonance [88]. These methods have been applied to TLSs in glasses [89] and a straighforward summary can be found in a review by Phillips *et al.* [79]. The treatment for TLS field strength dependence in the acoustic case can be translated to the electric case and the equations from Schickfus *et al.* for $\tan \delta$ dependence on field strength will be presented in Chapter 5. Essentially, at very low temperatures $T \ll 1\ K$, the critical intensity I_c^{TLS} (in Wm^{-2}) is defined as the cross-over point from TLS resonant absorption (weak field) to TLS relaxation (strong field) and can be written as [79]

$$I_c^{TLS} = \frac{3\hbar^2 \varepsilon_r \varepsilon_0 c}{2p_0^2 T_1 T_2} \qquad (2.36)$$

37

where ε_r is the relative dielectric constant, p_0 is the electric dipole moment (in Cm), c is the speed of light, and T_1 and T_2 are the TLS relaxation and dephasing times, respectively. For electric field intensities greater than the critical intensity $I^{TLS} \gg I_c^{TLS}$, TLS resonant absorption is saturated and relaxation processes will dominate. For electric field intensities less than the critical intensity $I^{TLS} \ll I_c^{TLS}$, TLS resonant absorption processes will dominate.

Referring again to Fig. 2.4, below $\widetilde{T}$ and for weak electric fields, $\tan \delta$ is dominated by TLS resonant absorption processes and is proportional to the inverse of the phonon mean free path with temperature dependence $\tan \delta_{res,tun}(\omega_0) \propto \ell_{res,tun}^{-1}(\omega_0) \propto \tan \hbar \omega_0 / k_B T$. Below $\widetilde{T}$, for strong electric fields, and for long relaxation minimum TLS relaxation times $\omega \tau_{min} \gg 1$, $\tan \delta$ is dominated by TLS relaxation and so called "one-phonon" processes having temperature dependence $\tan \delta_{rel,tun}(\omega_0) \propto \ell_{rel,tun}^{-1}(\omega_0) \propto T^3$ [86]. Above $\widetilde{T}$, where relaxation times begin to decrease due to thermal excitation $\omega \tau_{min} \ll 1$, TLS relaxation still dominates but a "plateau" is reached for a long range of temperatures yielding $\tan \delta_{rel,tun}(\omega_0) \propto \ell_{rel,tun}^{-1}(\omega_0) = const.$ Here, it is important to note that I am not reviewing or incorporating the soft potential model first proposed by Karpov *et al.* and thoroughly reviewed in references [90, 91]. Essentially, the soft potential model can explain the "plateau"' and other features in the data for measurements at higher frequency ($\approx$ THz) by incorporating the existence of soft localized modes accounting for anharmonicity. For the measurements carried out in chapters 3 and 4, the temperature ranges are below $\widetilde{T}$ in the frequency range $\omega / 2\pi = 1 - 20$ GHz. Above T^*, classical relaxation processes dominate where charge "hopping" dominates with temperature dependence $\tan \delta_{rel,class}(\omega_0) \propto \ell_{rel,class}^{-1}(\omega_0) \propto T$ [76, 79, 86]. At T_{max}, the thermal energy is equal to the "hopping" barrier height and thermal vibrations now dominate the system above this temperature where static spin polarizations are negligible [86].
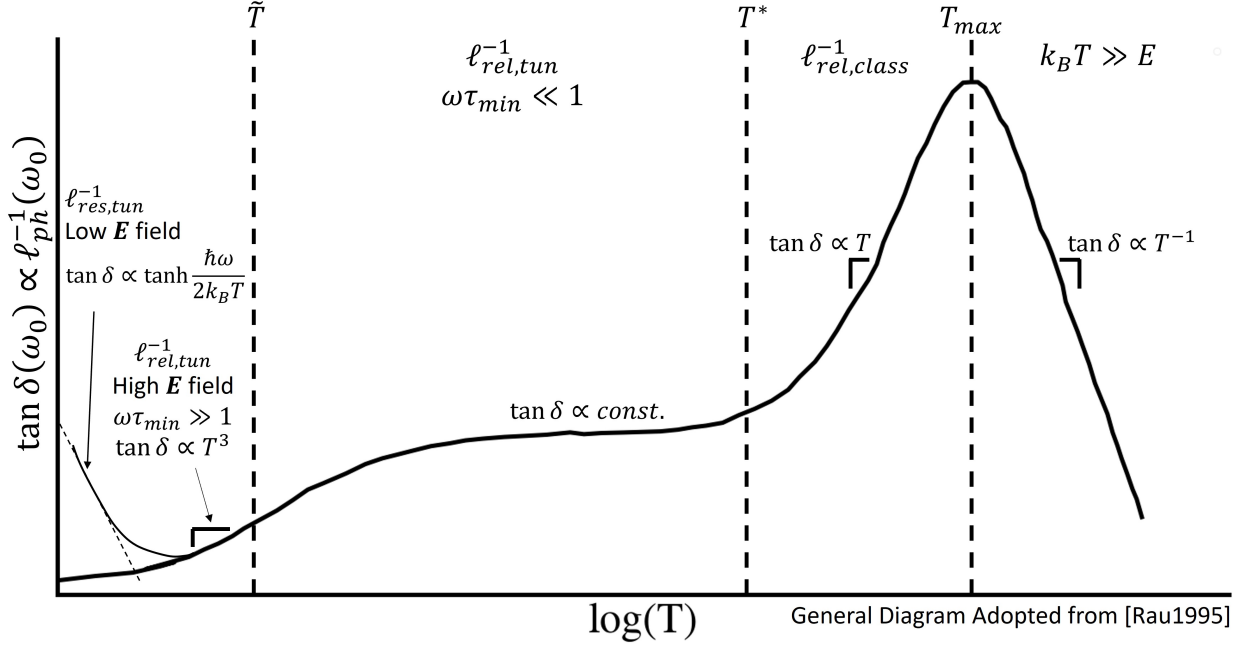
Figure 2.4: Diagram depicting the regimes of mechanisms dominating the temperature dependent $\tan\delta$. The general diagram was adopted from reference [86] for dependence of ℓ_{ph} and modified to include the TLS absorption regime at the lowest temperatures and lowest applied **E** fields, which is the most widely used and understood regime today. The loss tangent and inverse mean free path at a reference frequency ω_0 have temperature dependent proportionality $\tan\delta \propto \ell_{ph}^{-1}$ The majority of the notations are adopted from references [90, 91, 92] that thoroughly review all of the mechanisms relating to energy dissipation, but the soft potential model is not included or reviewed here. The y-axis is plotted as the inverse quality factor or internal friction Q^{-1} from acoustic measurements, which is proportional to the loss tangent $\tan\delta$, the ultrasonic attenuation α_{db} typically measured in dB/cm, and the inverse phonon mean free path ℓ_{ph} by $Q^{-1} \propto \tan\delta \propto \alpha_{db} \propto \ell_{ph}^{-1}$. The critical temperatures $\tilde{T}$, T^*, and T_{max} are the transition temperature regimes are dominated by TLS resonant tunneling, TLS relaxation, classical relaxation processes as temperature is increased. Note, this entire plot can shift to the left in or regions can squeeze/widen in temperature depending on the relative energy scales of the various processes to the thermal energy k_BT, applied frequency ω.

Note that the general trend in Fig 2.4 can shift left/right, or regions can squeeze/widen, in temperature depending on the relative energy scales of the various processes unique to the material such as (i) the thermal energy $k_B T$, and (ii) applied frequency ω. As an example, internal friction data was taken from reference [93] and re-plotted to estimate $\widetilde{T}$ in Fig. 2.5. Note, the inverse acoustic internal friction Q-factor is proportional to the loss tangent $Q^{-1} \propto \tan \delta$. These plots clearly show a frequency dependence of $\widetilde{T}$. This is analogous to the frequency dependence of T_{max} mentioned and confirmed by Anderson and Bommel shown in Fig. 2.3. It can be estimated that $\widetilde{T} \approx 22\,K$ at a measurement (stimulus) frequency of 10 GHz for $\alpha - SiO_2$. This serves as an initial estimate for measurements performed here at temperatures below 10 K and applied frequencies of 10 GHz suggesting the dominant mechanism contributing to loss is the TLS relaxation processes in Chapters 4 and 5.

It is interesting to note that below $\widetilde{T}$, the temperature power law dependence of $\tan \delta$ is $T^{2.3}$, which is less than T^3 for the 43 MHz measurement in Fig. 2.5. Schickfus and Hunklinger measured a $\tan \delta$ temperature dependence of $T^{2.4}$ from 2-8 K in the TLS relaxation regime at 10 GHz [84]. Furthermore, Strom *et al.* measured a $\tan \delta \propto T^{2.4}$ dependence in the relaxation regime for Na β-alumina at 11.5 GHz with the transition temperature between TLS absorption and relaxation at 5 K [94]. Therefore, deviations from $\tan \delta \propto T^3$ dependence in the TLS relaxation regime is not uncommon. This is most likely due to the measurements taking place at temperatures near $\widetilde{T}$ or near the TLS resonant absorption regimes.

Here I assume TLS relaxation processes dominate dielectric loss $\tan \delta$ in measurements carried out in this work. I will not treat losses due to TLS absorption processes since measurements here are carried out above $T > 1\,K$ and all TLSs are saturated above this temperature. Although, the temperature dependent data in chapter 4 suggests we see the onset of TLS absorption regime.
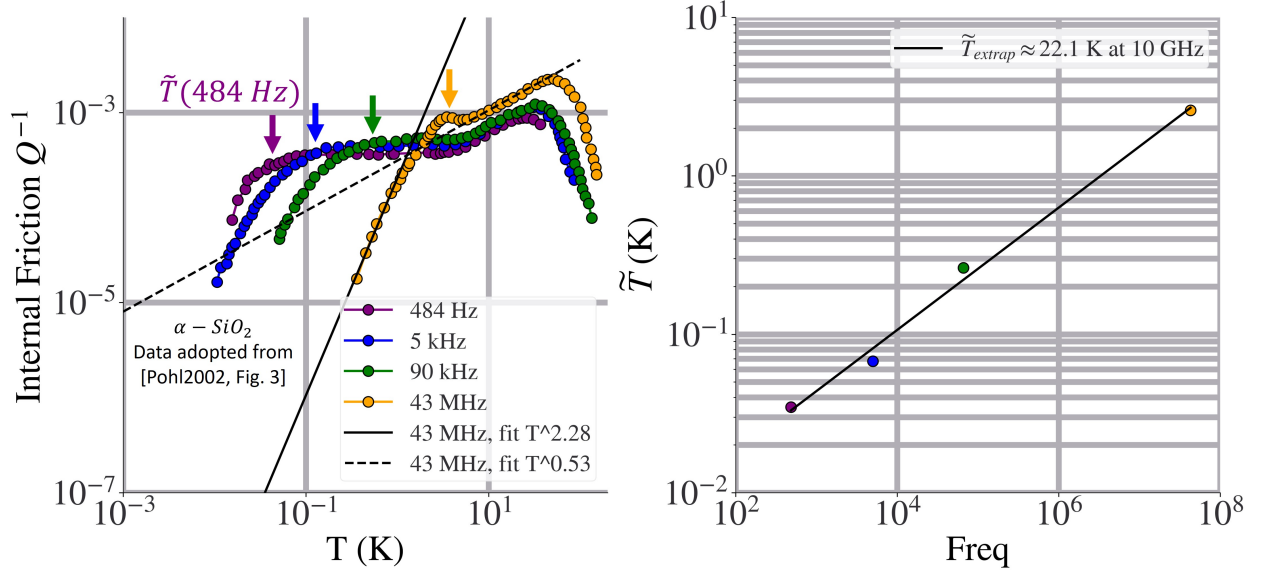
Figure 2.5: The (left) plot is data re-plotted from reference [93] Fig. 3. In this plot, i fit the low temperature regime (TLS relaxation) and the higher temperature regime (classical relaxation) of the 43 MHz data (yellow). The (right) plot is estimated $\widetilde{T}$ temperatures taken at the arrows shown in (left) plot. At 10 GHz, the extrapolated temperature is $\widetilde{T} \approx 22\ K$.

With that, the model used here for the $\tan\delta$ temperature dependence is

$$\tan\delta(T,\omega) \approx \tan\delta_{tun,rel}(T,\omega) \propto T^3 \tag{2.37}$$

2.3.4 Frequency Dependence of $\tan\delta$

Considering only loss due to TLS relaxation with $\omega\tau_{min} \gg 1$ and $T < \widetilde{T}$, the phonon scattering length $\ell_{ph} \approx \ell_{tun,rel}$ is constant as a function of frequency (see Eq. 2.34). In this temperature regime, the loss tangent has a frequency dependence

$$\tan\delta \propto \omega^{-1},\ T < \widetilde{T},\ \text{strong E field} \tag{2.38}$$

41

Although, specifically in the amorphous dielectric TLS community, the frequency dependence of $\tan \delta$ in Eq. 2.38 is rarely measured or has possibly never been explicitly confirmed experimentally.

For comparison, the frequency dependence of $\tan \delta$ in the temperature regime where TLS absorption dominates, the loss tangent is frequency independent by

$$\tan \delta(\omega) = constant, \; T \ll \widetilde{T}, \; \text{weak E field} \tag{2.39}$$

In parallel communities the frequency dependence of dielectrics with finite electrical conductivity have been measured suggesting universality due to many body interactions. The electrical conductivity is related to the dielectric loss tangent by [95]

$$\tan \delta = \frac{\omega \epsilon'' + \sigma}{\omega \epsilon'} \tag{2.40}$$

where ω is the angular frequency, ϵ' and ϵ'' are the real and imaginary part of the complex dielectric constant, respectively, and σ is the finite electrical conductivity in the dielectric.

In 1961, Pollak *et al.* observed a frequency dependence of the conductivity ω in n-type Si at temperatures $T \leq 4.2 \; K$ having the form [96]

$$\sigma = A_s \omega^b \tag{2.41}$$

where A_s and b are empirical fitting parameters. Pollak *et al.* found that $b \approx 0.8$ fit for a range of temperatures below 10 K. The model described by Pollak *et al.* explaining the frequency power dependence requires low concentrations of localized conduction states allowing electron (charge)

to "hop" between states giving rise to an increase in conductivity. With the application of a steady state alternating current, charge will be displaced by the ionized group-3 and group-5 impurities systematically incorporated into the Si by Pollak *et al.* experiment. The "hopping" time of the charge is analogous to a relaxation time having some phase lag relative to the applied electric field (refer back to Eq. 2.31 and discussion). Therefore, energy can be dissipated through this mechanism and witnessed by measurements of the loss tangent $\tan \delta$.

A host of studies found a similar frequency dependence in materials with low conductivity, predominantly dielectrics, that satisfy the presence of non-interacting dipoles free to rotate or displace in a medium. In 1977 Jonscher [97], and later updated by Ngai *et al.* in 1979 [98], presented the universality of dielectric frequency dependent response supported by half a century worth of data. The universal power law proposed have the forms [97]

$$\tan \delta \propto \omega^{b-1}, 0 < b < 1 \tag{2.42}$$

$$\sigma \propto \omega^b, 0 < b < 1 \tag{2.43}$$

Ngai *et al.* refers specifically to TLS as a possible electron-phonon mechanism adhering to the power dependent universality [98]. Although, the TLS and the universal dielectric power law were not explicitly connected.

Kaiser *et al.* argues that measurements using lumped element resonators at 4.2 K of amorphous thin film dielectrics, TLS relaxation processes dominate the measured $\tan \delta$ [99]. Assuming non-interacting dipoles with equal relaxation times τ_{rel} at GHz frequencies, Kaiser *et al.* makes the power exponent a free fitting parameter b to fit to Eq. 2.43 [97, 98]. Kaiser *et al.* suggests the parameter b_d depends on the coupling of TLSs to each other, where $b_d = 0$ is

43

non-interacting (Debye-like), $b_d = 0.5$ nearest neighbor interactions, and $b_d > 0.6$ is attributed to many-body interactions [98]. Although outside of the scope of this work, it is still worth noting that amorphous and crystalline metals can exhibit similar exponents with $b_d \approx 0.8$ in Pollak's experiments of n-type Si as an example mentioned earlier. This is worth exploring further in experimentation building off the work presented in Chapters 3-5.

Considering both the (i) proposed universal frequency dependence in Eq. 2.43, and (ii) TLS relaxation frequency dependence in Eq. 2.38 assuming $\omega\tau_{min} \gg 1$ and $T < \tilde{T}$, the empirical frequency dependence of the dielectric loss tangent can be fit to

$$\tan\delta = B_d\omega^{b-1}, \; 0 < b < 1 \tag{2.44}$$

where B_d and b are power law free fitting parameters. For $b = 0$, the frequency dependence simplifies to that expected for TLS relaxation. For $0 < b < 1$ the frequency dependence follows universal scaling supported by measurements at 4.2 K [99].

2.3.5 Summary

In this work, the dielectric studied is tetraethyl orthosilicate (TEOS). The thin film TEOS material fabricated (see Section 2.4 and 3.2) and measured (see Chapters 4 and 5) is considered to be an amorphous (glassy) dielectric.

The resonator measurements carried out here (see Chapters 4 and 5) were done in the temperature and frequency range 1.5-10 K, 1-15 GHz, respectively, in an electric field regime between strong and weak. In this range, I assume two-level system (TLS) relaxation processes are dominating $\tan\delta$.

In Chapter 4, for the dielectric loss tangent $\tan\delta$, we will assume both non-dispersive ($\tan\delta = constant$) [100] and dispersive ($\tan\delta \propto \omega^{b-1}$) [79, 97, 98, 99, 101] loss tangent models over a frequency range $\omega/2\pi \approx 1 - 12\ GHz$ at $T = 4.2\ K$. In Chapter 5, I will attempt to fit the frequency dependence of $\tan\delta$ as a function of temperature, and compare $\tan\delta$ temperature dependence to the expected $\propto T^3$ for TLS relaxation processes [84]. Furthermore, I will claim the non-monotonic temperature dependence of $\tan\delta$ is due to TLS relaxation and resonant absorption loss and leads to TEOS being the dominate loss mechanism in RQL interconnects below 4 K.

2.4 Fabrication Processes for RQL Interconnects

2.4.1 Brief Background of CMOS Technologies

Both CMOS and superconducting electronics (SCE) technologies have similar interconnect fabrication challenges, one of them being planarization. In CMOS, to achieve higher performance and lower cost per chip for successive technology generations, there is an approximate linear increase in number of devices leading to a quadratic increase in the number of interconnects required [102]. This demand is met by reducing the pitch between wires or increasing the total number of interconnect layers. This increase in density has a negative effect on performance, and has been solved by qualitative improvements of the fabrication processes. Planarization of each successive layer is paramount when increasing density, as the minimum feature sizes and pitch are set by the depth of focus in the lithography process [103].

To fabricate interconnects, current CMOS technologies use some form of a damascene Cu electroplating process for on-chip metalization [104]. The damascene process will be explained below. Electroplating is the ideal process to conformally fill high-aspect ratio dielectric trenches

Example Electroplated Cu Damascene Process for CMOS Interconnects

1.4 AR   1.8 AR   1.9 AR   2.5 AR

350 nm   285 nm   260 nm   200 nm

a)

500 nm

Cu

500 nm

Magnetron Sputtered Nb Damascene Process for RQL Interconnects

306.7 nm

b)

198.0 nm

Nb

500 nm   253.2 nm

0.86 AR
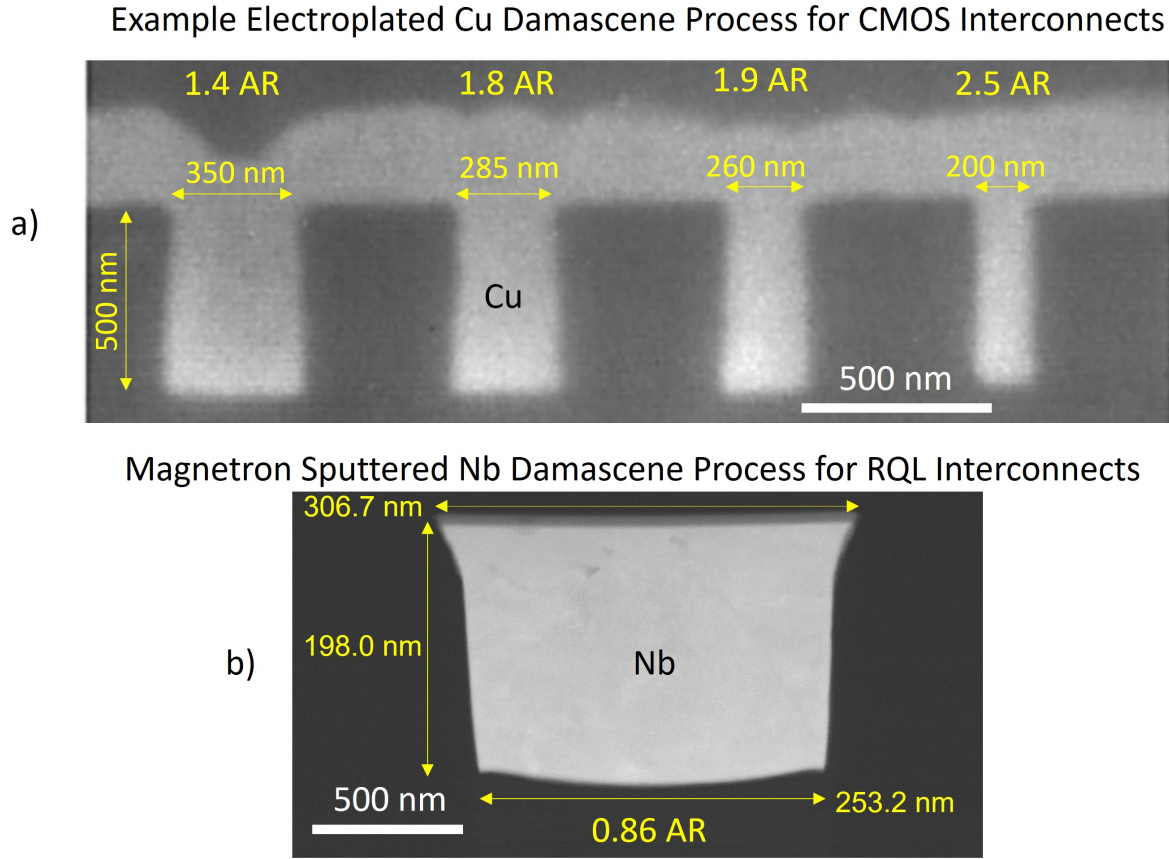
Figure 2.6:   a) SEM image adopted from reference [105] as an example of high aspect ratio trench filling using Cu electroplating in a CMOS damascene process (before metal planarization). b) RQL damascene process after planarization showing a Nb interconnect deposited using magnetron sputting at $T \leq 150°$ as an example of low aspect ratio trench filling.   More characterization on this in Chapter 3.

with Cu. SCE technologies are currently limited to trench aspect ratios of < 1 and resort to less conformal sputtering processes. Fig. 2.6 exemplifies the low aspect ratio filling of RQL interconnects relative to common CMOS electroplating technologies [105, 106, 107, 108, 109].

In CMOS, the push for higher density of submicron interconnects increases the overall resistivity of the Cu. This increase in resistivity induces an increase in energy dissipation and Joule heating. RQL interconnects can provide advantage over this, and was discussed in Section 1.2.

2.4.2 SCE Fabrication Technologies

Currently, the following companies have advanced fabrication processes producing SCE logic circuits: SEEQC [110, 111, 112], National Institute of Advanced Industrial Science and Technology (AIST) in Japan [113, 114]; D-Wave Systems Inc. using Cypress semiconductor foundry in Minnesota (proprietary process unpublished, reviewed here [115]); and MIT Lincoln Laboratory (LL) in Massachusetts [115]. Parallel to semiconductor microelectronic scaling, interconnect wire width, pitch, and total number of layers determine the scalability of SFQ circuits. The LL process currently has eight wiring layers with minimum wire width and spacing (pitch) of 0.35 and 0.5 μm, respectively [115]. Unlike CMOS where minimum dimensions are defined by the transistors, the interconnects in SCE have comparable or larger minimum dimensions relative to the logic units (Josephson junctions), therefore determining current scaling of the technology. Niobium is the most commonly used metal in SCE, as it has a relatively short penetration depth λ and long coherence length [53, 54], relatively low RF losses [71], and can be consistently fabricated having high critical current densities [54]. Silicon dioxide SiO_2 is the most common interlayer dielectric used in SCE and is adopted from semiconductor technologies [116]. These dielectrics provide isolation between metal layers, and the dielectric synthesis and quality can have an impact on the metal layer performance (inductance, RF loss) as well as determining the speed and dispersion of data propagation [36], governed by the relative dielectric constant ε_r and loss tangent $\tan \delta$, respectively.

2.4.3 Chemical Mechanical Planarization (CMP)

For both CMOS and SFQ based planarized processes (e.g. [115]), interconnect fabrication cannot be made without chemical-mechanical planarization (CMP) [117, 118, 119, 120]. Pioneered at IBM, CMP is a technique to remove material with undesired topography by abrasive action in a chemical etching environment. The physical abrasion is done using a rotating polishing pad in contact with the wafer mediated by a chemical alumina slurry. There is also a pad conditioner to remove residual contaminants to maintain constant abrasion on the wafer (i.e. "sandpaperness"). Furthermore, there are different types of endpoint detection methods to determine when the metal/dielectric has been planarized. The two most common *in-situ* endpoint detection methods are: $ISRM^{TM}$ (interferometry based) [121, 122] developed by AMAT [123], and eddy current based techniques [124]. There are also many other techniques to perform endpoint detection [125, 126]. This process can achieve a planar surfaces to sub nm levels over a 200 mm wafer, but due to the coupled physical-chemical nature of this technique, induced material defects are of primary concern. The two primary planarized processes are the cloisonné and damascene process. In regard to availability, these planarization processes enable both high metal densities per layer (approximately 50-95%) and many layers to be used as interconnects. Although, for superconducting interconnects, as wire dimensions decrease so does the electron mean free path giving rise to higher surface resistance R_s and power dissipation (see Eq. 2.20 and Sections 2.2.2-2.2.3).
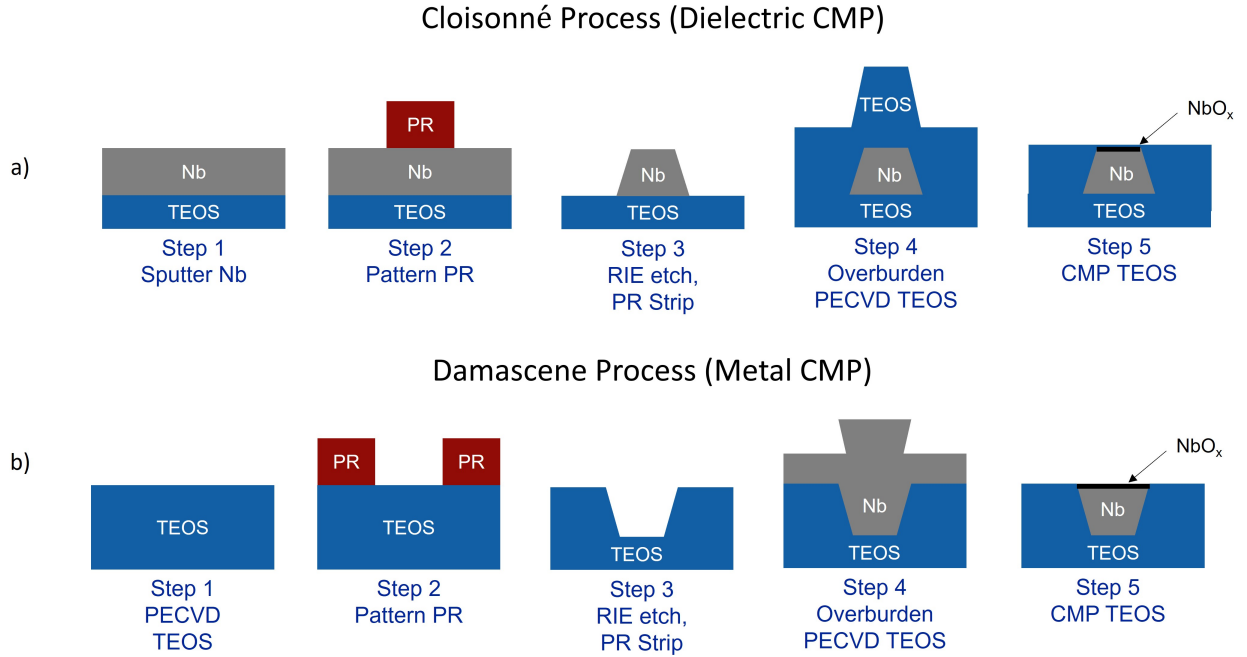
Figure 2.7: Superconducting Electronics (SCE) fabrication processes showing the generalized a) cloisonné process involving a metal etch followed by a dielectric CMP, and b) the damscene processes involving a dielectric etch followed by a metal fill and CMP. Here, the dielectric Tetraethyl orthosilicate (TEOS) and metal niobium (Nb) were used to fabricate (MTL) interconnects with both the cloisonné and damascene process. Samples from *Process A* and *B* were fabricated using a damascene process. Samples from *Process C* were fabricated using a cloisonné process. Physical characterization of the MTLs can be found in Section 3.2. Electrical characterization of the MTLs can be found in Chapter 4 and Chapter 5.

2.4.4 Cloisonné Process (Dielectric CMP)

Arguably, the first metal-dielectric fabrication process was Cloisonné, which is the ancient art originating from Egypt of decorating objects with intricate metal designs encapsulated in insulating enamel to give a colorful finish. The resulting surface of the object is rough after the firing step to adhere the enamel onto the metal and is sanded down to give it a smooth finish. In microelectronics fabrication, the Cloisonné process is started by depositing the interconnect metal (Cu, Nb) with physical vapor deposition (PVD). After the dense metal (e.g. Cu, Nb) interconnect design has been defined by photo-lithography and patterned using reactive-ion etching (RIE), the metal is embedded with insulating dielectric (e.g. SiO_2, SiN_x) using chemical-vapor-deposition (CVD) processes [127]. Since CVD deposits conformally over the metal, the resulting surface is planarized to make the surface planar and smooth. See Fig. 2.7. PVD and RIE processes are relatively inexpensive and produce excellent metal thickness uniformity (between 1-10%). Additionally, RIE is more scalable than the liftoff process [118]. Although, the cloisonné process is unable to produce higher density (small wire pitch) interconnects. The RIE etch selectivity at corners of the photoresist and high metal density areas, which ultimately limit the metal thickness and induced metal sidewall angle. Typically in practice, CMOS resorts to a damascene (metal CMP) process to achieve the highest metal densities. Fortunately, there are many "knobs" that can be turned turned in CMOS/SCE to get the cloisonné process to meet desired requirements.

2.4.5 Damascene Process (Metal CMP)

In constrast to cloisonné, the damascene process [119, 120] starts with a uniform dielectric deposited on a planarized wafer followed by patterning the dielectric "trenches" using photolithography

and oxide RIE. Metal is then deposited to fill the troughs, over filled (over burdened), and then metal is CMPed down to the dielectric surface, leaving behind only recessed metal wire. See Fig. 2.7. This process is the primary planarization process producing the highest yield and largest processing window. A large processing window means the performance of the device or product being fabricated is not sensitive to small changes in the fabrication process (e.g. small changes in temperature during metal deposition). In general, dielectrics are amiable to the process (lithography, RIE). As a consequence, this technique suffers from the poor trench filling qualities of refractory metals. Magnetron Sputtering techniques, although optimal in many ways (e.g. high deposition rates, process control, thickness uniformity), do not uniformly fill trenches because the flux concentration of atoms towards the recessed areas is hard to control [128]. Additionally, uniform coverage inside the trench facilitated by surface diffusion of adsorbed atoms is almost is extremely difficult due to magnetron sputter energy scales [129]. Because of this, trench filling at corners is especially difficult and commonly causes voiding inside of the trench due to metal deposited on the upper edge surface eventually blocking incoming flux. At the same time, this blocks atoms/plasma from leaving the trench. As one can expect, this process can induce a plethora of defects on the metal (contaminants, residual stress, voids, etc) due to trench filling and CMP.

Both cloisonné and damascene processes used in CMOS/SCE technologies give a planarized interconnect balanced by performance trade-offs. Changes in the process parameters have been shown to mitigate short comings of each process [102, 120]. For example, depsition parameters (e.g. deposition pressure, RF/DC bias, substrate temperature) have been tuned to achieve optimal adatom energies for uniform filling of trenches. Thin protective layers (e.g. Ti, Al, Ta) have been used as diffusion barriers. Trade-offs can be further mitigated to enhance performance by

advances in the fundamental understanding of the materials and their response to fabrication changes.

2.4.6 Thermal Budget

Somewhat analogous to atomic mobility through self-diffusion in Al based wiring in CMOS due to fabrication temperatures reaching 40% of the Al melting temperature [102], the thermal budget in SFQ technologies is primarily set by the activation temperature of oxygen migration into Nb interconnects and intermixing at Josephson junction oxide interfaces. The latter could be alleviated by having the Jospehson junction integration at the end of the fabrication process. Therefore Nb interconnects are the thermal budget limiting factor where fabrication temperatures do not typically exceed $T \leq 150°C$. As a reference, 0.1 and 1 at. % of oxygen in Nb reduces the superconducting critical temperature by approximately 0.2 and 1 K, respectively [130]. In addition, the normal state resistivity at 4.2 K has been shown to increase by a factor of 30 for 0.5 at. % oxygen in Nb. An increase in normal state resistivity will decrease the electron mean free path ℓ and increase the magnetic penetration depth λ (see Eq. 2.8). With this, low deposition temperatures make it difficult to fabricate high quality SiO_2 and Nb thin film material. For CMOS fabrication, the typical deposition temperature is $T \approx 350°C$ for SiO_2 using a TEOS precursor, which is approximately 1/3 the melting temperature of Cu. An increased thermal budget would allow for higher substrate (wafer) deposition temperatures, facilitating ideal growth kinetics of metals/dielectrics for high quality materials.

2.5   Summary

In summary, the fabrication process has a significant impact on RQL interconnect morphology of Nb wires and the low temperature thermal budget invokes the TEOS dielectric to be amorphous in character. Consequently, the intrinsic microwave losses need to be monitored for changes in the process and the mechanisms causing extrinsic loss should be mitigated. Models of the microwave losses will be presented in Chapter 3 and demonstrated in Chapter 4 at 4.2 K. The morphology will be further explored in Chapter 3, and then compared to RF characterization in Chapter 4. Temperature dependent models will be presented and demonstrated in Chapter 5.

Chapter 3: Modeling Lossy 3D Superconductor-Dielectric 2-Port Networks

3.1 Introduction

A resonator remains the only practical way to accurately measure intrinsic resistance R_s [62, 131] and loss tangent $\tan\delta$ [100, 132] at microwave frequencies. The resonator internal Q-factor is related to the partial Q-factors associated with the conductor loss Q_c and the dielectric loss Q_d by $Q_i^{-1} = Q_c^{-1} + Q_d^{-1}$. There will be more discussion on the measurement techniques in Chapter 4.

For an MTL embedded in a single dielectric material, the loss tangent is related to the partial dielectric Q-factor by $\tan\delta = Q_d^{-1}$ and is independent of the MTL geometry. To extract the intrinsic resistance from measurements of Q_c, one needs to accurately solve the geometric factor Γ, where $R_s \equiv \Gamma/Q_c$. The geometric factor can be solved analytically for simple geometries or numerically for more complex geometries.

The analytical modeling work to account for Z_s (and Γ) contribution on transmission line characteristics are accurate only when the current distributions are known and/or geometries are such that the conducting strip width w is greater than the dielectric thickness s: $w/s > 1$ (see Table 3.1) [133, 134, 135, 136, 137]. Sheen *et al.* describes the limitations in detail, presents a new method accounting for current distributions, and numerically solves for the lossy stripline parameters (e.g. Γ) using a proprietary Finite Element Modeler (FEM) [138].

Recently, commercially available FEM products have been used to simulate superconducting transmission lines. Analytical work applied to a variety of lossless transmission line geometries (microstrip, stripline, etc.) has been compared to a commercially available software [65], and is in good agreement with SQUID based inductance measurements [54]. Other FEM implementations have been used to simulate MTLs with lossless superconductor properties by using plane sheets with user-defined surface impedance, but is only accurate for MTLs with $w \gg \lambda$ [139], [140]. Piccinini *et al.* simulated lossy normal metal CPWs for CMOS Quantum Computing systems using HFSS similar to our method for superconducting MTLs but did not *solve inside* the normal metal due to its negligible skin depth at microwave frequencies [141, 142]. Additionally, the superconducting microwave losses and current distributions of coplanar waveguides with strip widths down to 50 nm have been simulated and compared with measured data [143, 144]. In the Quantum Computing community, Comsol 2D simulations are used to calculate the participation ratios of varying thin dielectrics contributing to two-level system (TLS) loss and are generally not concerned with simulating the negligible superconductor loss at mK temperatures [145, 146].

In addition to the need for numerical solutions when one is dealing with nonuniform current distributions, no analytical theory can account for the common fabrication effects impacting the MTL - sidewall trench tilt, rounded edges of wires, in-homogeneous superconductor or dielectric materials due to intermixing at material interfaces, cross-sectional thickness miss-targeting, etc. Furthermore, to maintain a desired metal density $\approx 50\%$ for each layer in the damascene planarization process, small superconducting fill strips on the order of $0.5 \times 3 \mu m$ need to be included above, below and beside MTLs running perpendicular or parallel to conducting strip, which again is almost impossible to account for in the analytical calculations.

The expected nonuniform current distribution cannot be solved analytically for our 0.25-

micron fabrication process (similar to [115]), where the dielectric separation thickness s, superconductor thickness d, conducting strip cross-section width w, and magnetic penetration depth are all comparable: $s \approx d \approx w \approx \lambda \leq 0.25~\mu m$. Furthermore, to extract an accurate R_s, the exact cross-sectional geometry should be measured by Scanning Electron Microscopy (SEM) or Transmission Electron Microscopy (TEM). Therefore, in this chapter, to extract R_s from measurements, we will numerically solve for Γ using HFSS coupled with TEM measurements.

3.2   Materials Characterization of Interconnect Morphology

The damascene fabrication process is the desired planarization process for interconnects to scale a technology. As mentioned in Section 2.4, it is a challenge to fill dielectric trenches with refractory metals (like Nb) using magnetron sputtering [128]. This creates non-ideal morphology in the metal interconnect. In this section, the morphology of damascened Nb-TEOS fabrication processes will be examined with scanning transmission electron microscopy (STEM) coupled with energy-dispersive x-ray spectroscopy (EDS). The sample preparation and measurements will be briefly presented with the focus on the primary results that can affect RF losses in the Nb and TEOS. This analysis will be referred to in Chapters 4 and 5 to help explain physical mechanisms of RF loss measured by RF electrical characterization.

Reviews on STEM can be found in the following references [147, 148, 149, 150, 151] D'Alfonso *et al.*, later confirmed by Chu *et al.*, were the first to do spatial atomic mapping using EDS with a STEM [152, 153]. A review on this technique can be found in reference [147, 154].

3.2.1 Scanning Transmission Electron Microscopy (STEM)

To accurately calculate the Γ from HFSS, the cross sectional geometry of an MTL needs to be accurately known. With Γ, the intrinsic resistance R_s can be extracted from measurements of Q_c (see Eq. 3.13). Focused Ion Beam Microscopy (FIB) (see Appendix A), and Scanning Transmission Electron Microscopy (STEM) were used to measure the MTL down to sub-nm accuracy.

The STEM imaging was done as a service by EAG Laboratories [155]. First a carbon protective coating was applied prior to Focused Ion Beam (FIB) milling of the structure. A cross-section was prepared using an FEI Helios 660 Dual Beam FIB/SEM and thinned to electron transparency. Reviews on specimen preparation for TEM using FIB can be found in the following references [156, 157] Samples were imaged using Hitachi 2700 Aberration Corrected Scanning Tunnelling Electron Microscope (ACSTEM) with an accelerating voltage of 200 kV and a nominal probe size of $\approx 0.1 - 1nm$. The focused probe is scanned across the sample surface, and transmitted electrons are imaged. Transmitted Electron (TE) STEM images form from electrons transmitted through the samples that are un-scattered or scattered to low angles and are similar to and commonly referred to as Bright Field (BF) images (Fig. 3.15a,c). Transmitted electron (TE) is the first and standard imaging method. Annular bright field (ABF) imaging is analagous to TE, but with enhanced contrast from weakly scattered electrons from light elements by using a "preventing disk" (see Fig 1 in [158] and reference [149]). Atomic Contrast (or Z-contrast) STEM images are formed by electrons transmitted through the sample that have scattered out to higher angles (Fig. 3.15b). These are acquired using annular dark-field (ADF) detectors. If the electrons scatter to high enough angles the image intensity is roughly proportional to the square of

the atomic number (Z^2), hence these are termed Z-contrast (ZC) images [159, 160]. In summary,

TE images are most useful in this section to analyze the dielectric material (e.g. density, porosity)

while ZC images are useful to analyze the morphology of the metal wires (see Figs. 3.1 and 3.3).

Below, in Table 3.1 summarizes the measured cross sectional critical dimensions. The

measurements were taken from the STEM images found from Fig. 3.1 and Fig. 3.2.

Table 3.1: STEM Results Summary table for all three processes measured in this work. The
"mean width" column reports the minimum/max width, pertaining to the top and bottom width
of the wire (see Fig. 3.1 and Fig. 3.2). All measurements were done at EAG Laboratories [155]

Process	Nb/TEOS CMP	Ground Plane	Nominal Wire Width [nm]	Wire Width [nm] (Mean Width)	Ground Plane Thickness [nm] (% from Nominal)	Wire Thickness [nm] (% from Nominal)	Dielectric Thickness [nm] (% from Nominal)
A	Nb	Above Wire	250	253.2, 306.7 (280)	114 (-43%)	198 (-1%)	140 (-7%)
A	Nb	Above Wire	1000	979.0, 1053.0 (1016)	109 (-46%)	199 (<1%)	144 (-4%)
B	Nb	Below Wire	250	211.2, 316.5 (264)	216.1 (8%)	210.1 (5%)	138.4 (-7%)
C	TEOS	Below Wire	250	280.3, 353.5 (317)	205 (3%)	202.8 (1%)	139 (-7%)
C	TEOS	Below Wire	1000	972, 1061 (1017)	207 (4%)	201.1 (1%)	136 (-9%)

In Fig. 3.1 and 3.2, the bottom of all images are closest to the wafer substrate. The top

of all images are closest to dielectric-air interface. For process A and C, the ground plane is

below the wire, or conducting strip (CS). For process B, the ground plane is above the CS. The

CS (wire) in Process A and B have an inverted trapazoid shape from the damascene process

described in Section 2.4. In process C, the CS has a trapazoid shape from the cloisonné process

(see Section 2.4). The bottom metal in Fig. 3.2(a) and top metal in Fig. 3.2(b) are 6x0.4 μm fill

metal strips with 0.3 μm spacing, and will be discussed in Section 3.6.

Aside from geometries, information about the morphologies can be analyzed from STEM

images. Fig. 3.3 highlights the primary features that can have an impact on the Nb and TEOS
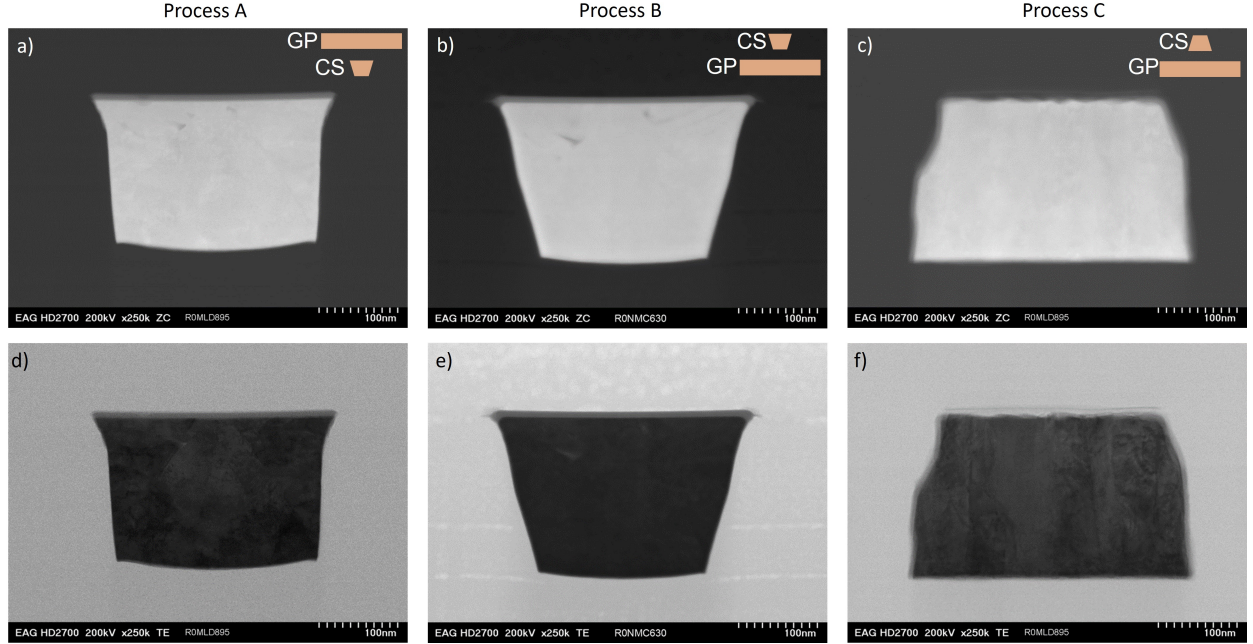
Figure 3.1: STEM images taken from representative samples of $0.25 \ \mu m$ MTLs fabricated by Process a) A, b) B, and c) C. The top row of images (a-c) are ZC, where bright is high Z and dark is low Z. The bottom row are TE images. The bottom of all images are closest to the wafer substrate. The top of the images are closest to dielectric-air interface. Process A and C have the ground plane (GP) below the wire (or conducting strip CS). Process B has the GP above the CS. All measurements were done at EAG Laboratories [155].

RF losses. Namely, damascene processes A and B show distinct lower metal density lines going diagonally inward from from the bottom edges of the CS. This is primarily caused during trench filling process when two growth directions (trench bottom, side wall) meet. This also gives rise to the voids, or very low density metal, found along the intersection lines (see features 1 (yellow) and 2 (orange) in Fig. 3.3). For the cloisonné process C, the Nb CS has a relatively continuous columnar grain structure, typical for sputtered Nb. The missing metal at the top and left edges of the 0.25-um CS is from the "undercut" during RIE (see Fig. 3.3(b) feature 6).

From the ZC images, a 8-10 nm NbO_x layer can be seen at the top of the planarized trench in damascene processes A and B. For process B only, there are lower density regions in the dielectric and can be see in Fig. 3.3(d). Both of these oxide features will be discussed further

a)   Process A   b)   Process C

GP

CS

EAG HD2700 200kV x100k TE   R0MLD895   300nm

CS

GP

EAG HD2700 200kV x90.0k TE   R0MLD895   300nm
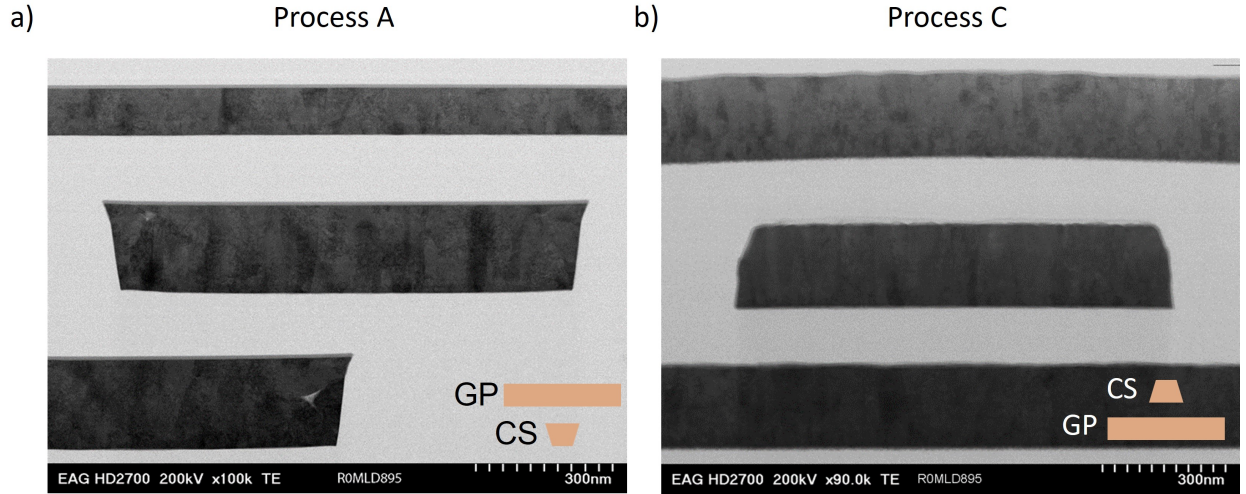
Figure 3.2:   STEM images taken from representative samples of $1~\mu m$ MTLs fabricated by Process a) A and b) B. Both images are TE images. The bottom of all images are closest to the wafer substrate. The top of the images are closest to dielectric-air interface. Process A and C have the ground plane (GP) below the wire (or conducting strip CS). Process B has the GP above the CS. The bottom metal in a) and top metal in b) are 6x0.4 μm fill metal strips with 0.3 μm spacing, and will be discussed in Section 3.6. All measurements were done at EAG Laboratories [155].

in Section 3.2.2.

At 0.25-micron dimensions, the electronmagnetic fringing fields become a significant fraction in cross section [134]. Additionally, the current distribution will be nonuniform taking up a significant fraction of the cross sectional area. Furthermore, the location of defects relative to the current density concentrations in cross section can have a significant impact on the Nb and TEOS RF losses, and will be discussed in detail in Section 4.5 Hence, the motivation to model the electromagnetic fields around and inside the Nb layers, as well as numerically solving Γ (see Section 3.4).
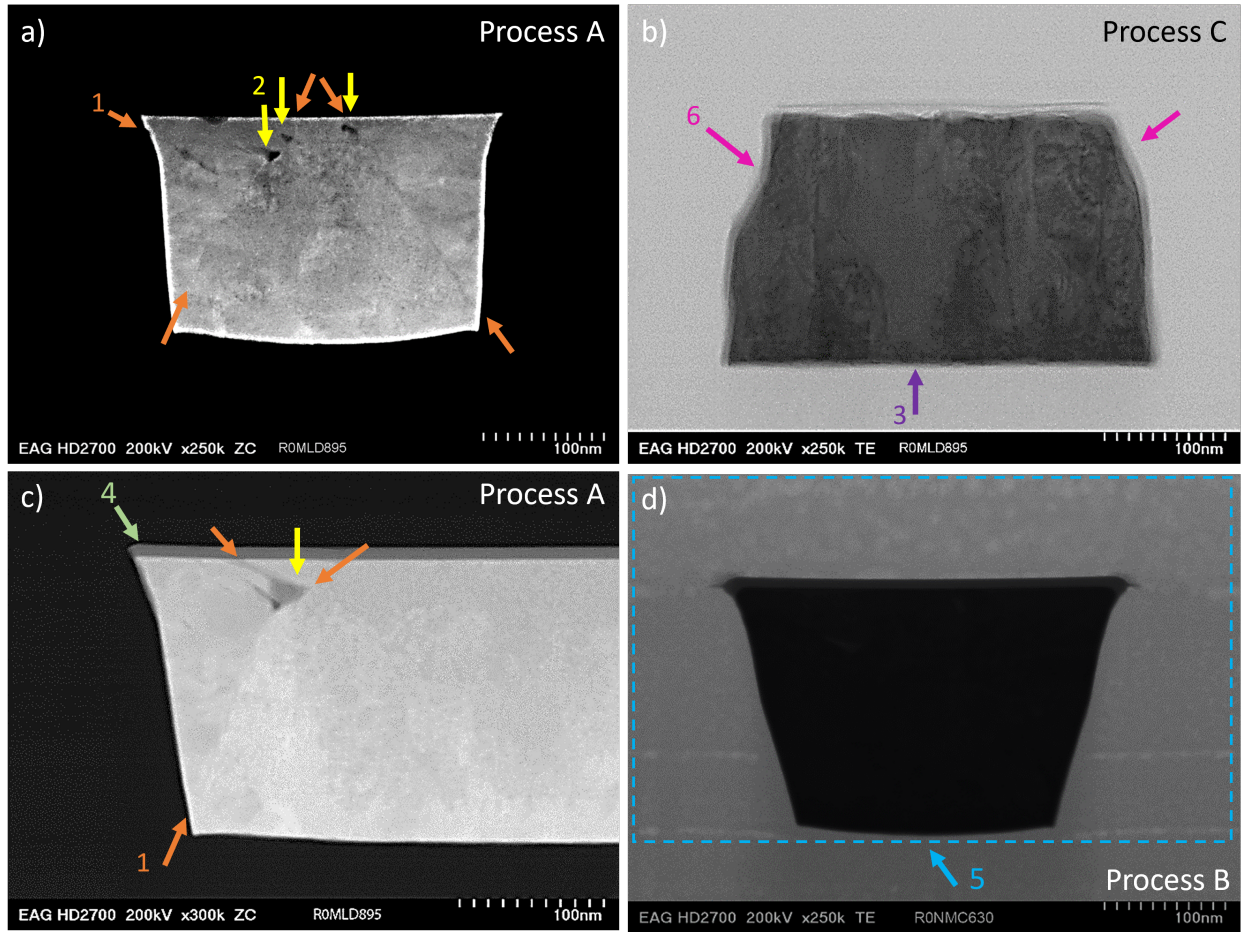
Figure 3.3: Highlighted Morphology features from STEM images for Processes A, B and C. Note, image contrast has been enhanced to highlight features. a) Feature 1 (orange) highlights the intersection between two grain orientations. Feature 2 (yellow) highlights voids or areas of low metal concentration. b) Feature 3 (purple) highlights a continuous Nb columnar grain. Feature 6 (pink) highlights the "undercut" of the Nb during RIE. c) Feature 4 (green) highlights the NbO_x layer found in Process A and B. d) Feature 5 (blue) highlights the lower density areas (bubbling and streaks) found in Process B only. All measurements were done at EAG Laboratories [155].

3.2.2 Energy-Dispersive Spectroscopy (EDS)

Energy Dispersive X-Ray Spectroscopy (EDS) will be used to survey the spatial concentration of elements with a detection limit of $> 1at\%$ (for elements Li-Pb). Although, the measurements here were standardless, and therefore accuracy down to 1at% cannot be claimed. Rather, the analysis will only qualitatively compare between samples and processes. This tool will help

understand the oxide compositions, and possible contamination of elements in the Nb layers.

EDS mapping was done immediately after STEM, as it only requires a different detector inside the system. A 0.1-1 nm diameter electron beam is scanned across the sample surface as X-rays are detected.

Fig. 3.4 shows a detectable amount of Ar content ($\leq 1at\%$) in damascene process A and B. The larger amount of noise for Process A signal in Fig. 3.4(d) is due to an overall lower number of counts relative to Process B measurement. Additionally, the Process A sample is most likely more electron transparent (thinner). Hence the reason why Process A and B are plotted together normalized to their respective Nb signal. The sputtering pressure during trench filling is typically increased for more "conformal" coverage of the trench [161]. The mechanism is an increased Ar pressures induces higher net columnated flux of metal ions depositing into the trench. As a result, there is also higher concentration of Ar plasma able to get trapped inside the trench/Nb. Ar content was not detected in EDS measurements of Process C.

Fig. 3.5 shows the EDS maps spatial maps of Nb, Si, and O for damascene Process B. The top down line scan in Fig. 3.5(a) starts with the TEOS layer at position 0 nm and suggests a stoichiometry close to SiO. This insert of Fig. 3.5(a) zooms into the TEOS-Nb oxide interface. There is a plateau of the Nb signal from 23-27 nm and then a gradualy increase (decrease) of the Nb (O) signal from 27-33 nm. The overall NbO_x 10 nm (greater than a typical niobium native oxide layer), and there is a stable oxide layer of 5 nm with a stoichiometry somewhere between $NbO - NbO_2$.

Fig. 3.6(a) shows the O/Nb ratio at the niobium oxide interface for both damscene Process A and B. The abscence of a plateau suggests Process B does not have a stable oxide layer. Oxygen content decreases to zero over the same exact length scale as Process A of 10 nm. Fig. 3.6(b)
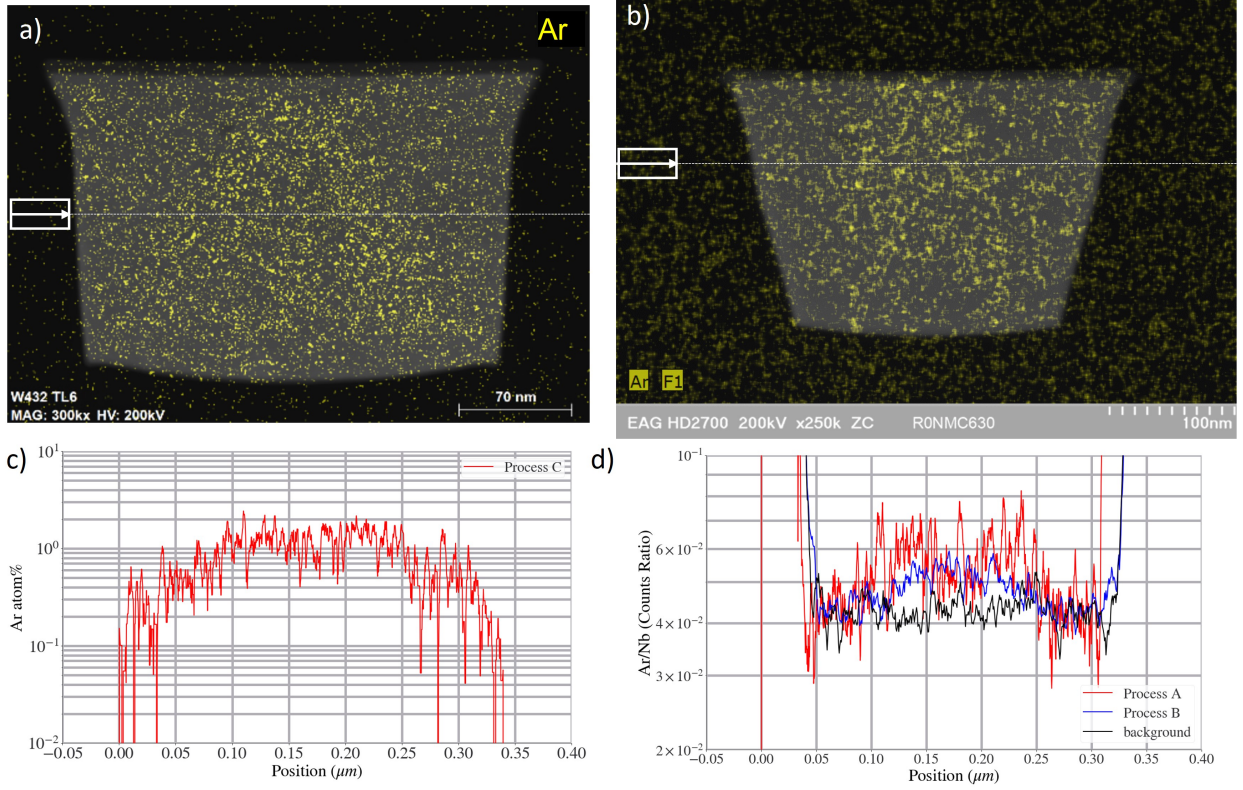
Figure 3.4: EDS measurement of Ar content in damascene process A and B. EDS map of Ar signal superimposed on the STEM image for damascene process a) A and b) B. The white dashed lines signify the EDS line scans plotted in c) and d). c) The semi-quantitative atomic percent of Ar in Process A, showing there is a detectable amount of Ar. d) The Ar signal normalized to the Nb to compare process A and B. The background signal is there for reference. All measurements were done at EAG Laboratories [155]

is the Tc dependence of O/Nb ratio for bulk cast alloys of niobium and oxygen adopted from Hulm *et al.* [162]. It can be inferred that a bulk alloy of niobium and 60% oxygen would have a $T_c \approx 7\ K$. A thin film of Nb, especially at 5 nm, will have a significantly suppressed T_c, suggesting the 5 nm, 60% rich niobium oxide may be a normal conductor as opposed to a stable oxide like Nb_2O_5 at these temperatures.

Fig. 3.7 shows an Al and SiNx passivation layer was introduced into Process C. This Al/SiNx prevented a NbO_x layer from forming.
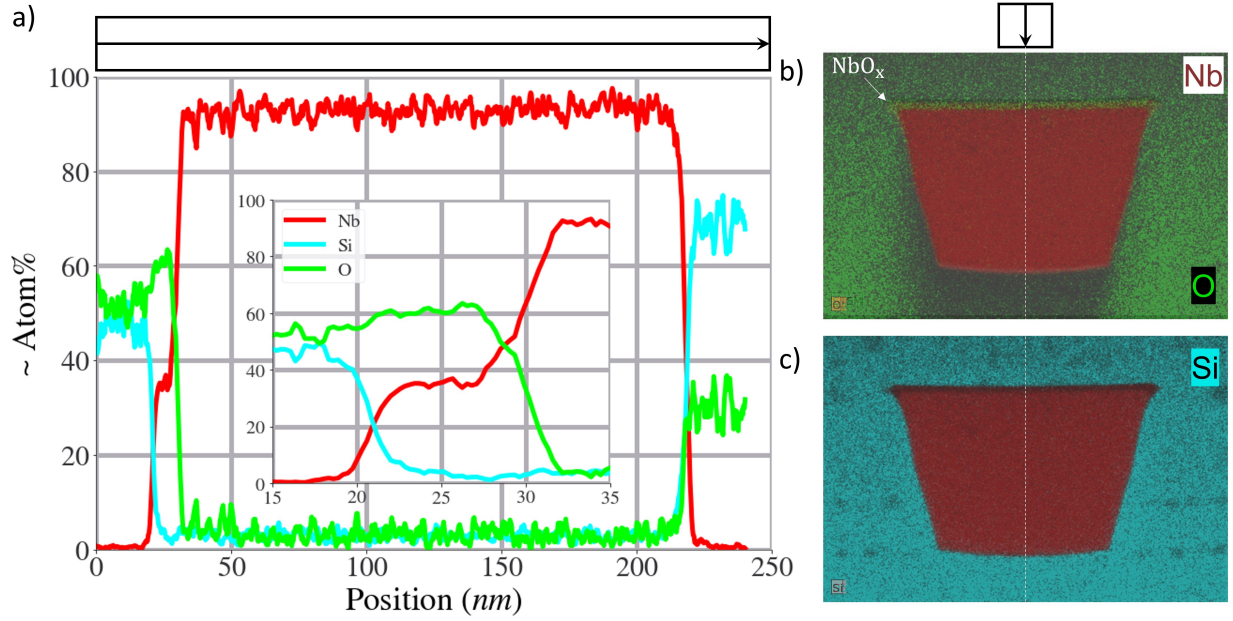
Figure 3.5: EDS data on damascene process B 0.25-micron MTL showing a) semi-quatitative plot of O, Si, and Nb atomic% in a top-down line scan. b) A STEM image with two superimposed EDS maps (Nb and O) showing spatial variation and NbO_x layer. c) A STEM image with a Si EDS map superimposed, showing areas with low Si concentrations.
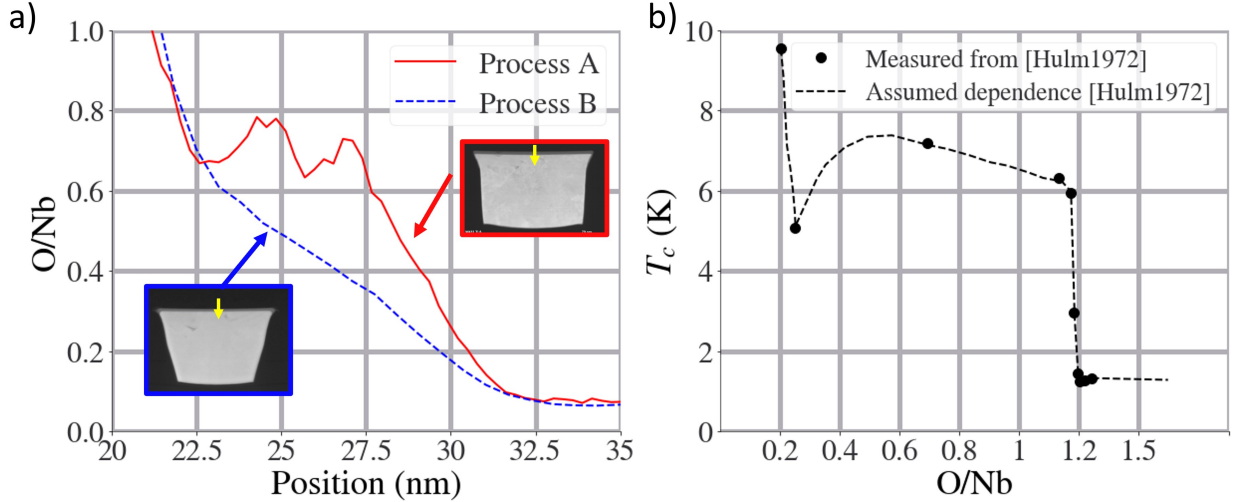
Figure 3.6: Plots of a) EDS top-down line scan showing calculated respective O/Nb ratios vs position for damascene Process A and B. b) Replotted Tc vs O/Nb ratio from [Hulm1972] [162]
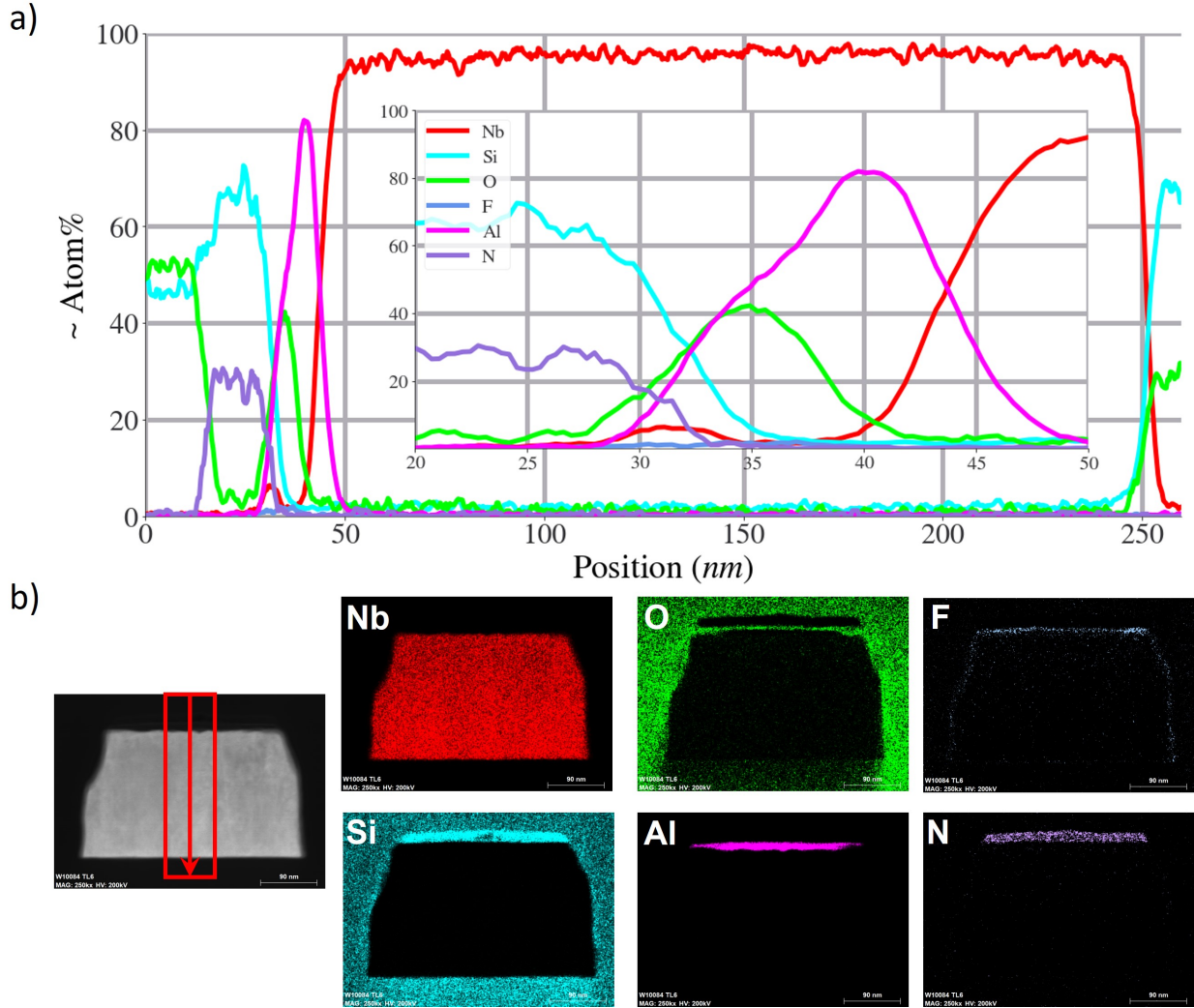
Figure 3.7: EDS data on Process C 0.25-micron MTL showing a) semi-quatitative plot of atomic% in a top-down line scan. b) EDS maps for each element.

3.3 Theory and Method

The method to deconvolve superconductor and dielectric losses will be described in this section, and is termed the Dispersive Loss Deconvolution (DLD) method. The method described here will be demonstrated in Chapters 4 and 5.

3.3.1 $RLGC$ Telegrapher's equations

The internal Q-factor of a superconducting transmission line resonator can be expressed as [95]

$$\frac{1}{Q_\mathrm{i}} = \frac{1}{Q_\mathrm{c}} + \frac{1}{Q_\mathrm{d}} = \frac{R}{\omega L} + \frac{G}{\omega C} \tag{3.1}$$

where Q_c is the partial Q-factor associated with the conductor loss, Q_d is the partial Q-factor associated with the dielectric loss, R, L, G, and C are the transmission line resistance, inductance, conductance, and capacitance per unit length, respectively, $\omega = 2\pi f$ is the angular resonant frequency, and the radiation loss is ignored as justified in Appendix B [163]. The telegrapher's expressions for R, L, G, and C of a superconducting transmission line, assuming $\sigma_1 \ll \sigma_2$, embedded in an interlayer dielectric are [95, 138, 164],

$$R = \frac{2}{|I|^2} \int_\mathrm{S} R_s \lambda |\mathbf{J}|^2 \mathrm{d}s \tag{3.2}$$

$$L = \frac{\mu_0}{|I|^2} \int_\mathrm{S} (|\mathbf{H}|^2 + \lambda^2 |\mathbf{J}|^2) \mathrm{d}s \tag{3.3}$$

$$G = \frac{\omega \varepsilon_0}{|V|^2} \int_\mathrm{S} \varepsilon_r \tan \delta |\mathbf{E}|^2 \mathrm{d}s \tag{3.4}$$

$$C = \frac{\varepsilon_0}{|V|^2} \int_\mathrm{S} \varepsilon_r |\mathbf{E}|^2 \mathrm{d}s \tag{3.5}$$

where I is the line current, V is the potential difference between the strip and ground plane, $\mathbf{J}$ is the vector (longitudinal) current density, $\mathbf{H}$ is the (transverse) magnetic field vector, μ_0 is the permeability of free space, ε_0 is the permittivity of free space, R_s, λ, $\tan \delta$, and ε_r are the

spatially dependent superconductor intrinsic resistance, magnetic penetration depth, dielectric loss tangent, and relative dielectric constant, respectively, in the lateral plane and this treatment assumes everything is homogeneous in the longitudinal direction. The integrals are over the entire cross-sectional area S of the line.

3.3.2 Geometric Factors in Inhomogeneous Transmission Line

Inserting Eqs. 3.2-3.5 into Eq. 3.1 yields

$$\frac{1}{Q_i} = \sum_m \frac{\overline{R_{sm}}}{\Gamma_{cm}} + \sum_n \frac{\overline{\tan \delta_n}}{\Gamma_{dn}} \tag{3.6}$$

where $\overline{R_{sm}}$ is the effective intrinsic resistance of the m-th conductor, Γ_{cm} is the partial geometric factor associated with losses in that conductor, $\overline{\tan \delta_n}$ is the effective loss tangent of the n-th dielectric layer or tube, and Γ_{dn} is the partial geometric factor associated with losses in that dielectric layer or tube. These are defined as follows

$$\overline{R_{sm}} = \frac{\int \int_{S_m} R_s \lambda |\mathbf{J}|^2 \mathrm{ds}}{\int \int_{S_m} \lambda |\mathbf{J}|^2 \mathrm{ds}} \tag{3.7}$$

$$\overline{\tan \delta_n} = \frac{\int \int_{S_n} \varepsilon_r \tan \delta |\mathbf{E}|^2 \mathrm{ds}}{\int \int_{S_n} \varepsilon_r |\mathbf{E}|^2 \mathrm{ds}} \tag{3.8}$$

$$\Gamma_{cm} = \mu_0 \omega \frac{\int \int_S (|\mathbf{H}|^2 + \lambda^2 |\mathbf{J}|^2) \mathrm{ds}}{2 \int \int_{S_m} \lambda |\mathbf{J}|^2 \mathrm{ds}} \tag{3.9}$$

$$\Gamma_{dn} = \frac{\int \int_S \varepsilon_r |\mathbf{E}|^2 \mathrm{ds}}{\int \int_{S_n} \varepsilon_r |\mathbf{E}|^2 \mathrm{ds}} \tag{3.10}$$

where S_m and S_n are the cross-sectional areas of the mth wire and n^{th} dielectric layer or tube, respectively.

It shall be noted that Γ_{cm} defined by Eq. 3.9 differs from the cavity geometric factor definition for conductor loss ($Q_c = R_s/\Gamma^{cavity}$) where $\Gamma^{cavity} = \mu_0\omega \int_V |\mathbf{H}|^2 \, \mathrm{d}v / \int_S |\mathbf{H}_\tau|^2 \, \mathrm{d}s$ defined as the ratio of the volume integral due to magnetic energy stored inside the cavity to the surface integral due to energy loss into the cavity walls [63, 131] associated with the tangential fields on the conductor. In Eq. 3.9, the first addend under the numerator integral includes resonant energy stored in the magnetic field penetrating the superconductor, while the second addend is due to resonant energy stored in the kinetic energy of the superconducting carriers [138]. The Γ^{cavity} does not account for them because in voluminous high-Q superconducting resonators [70, 165, 166] those energies can be ignored due to the penetration depth (typically, nm to um) being much smaller than the resonator characteristic size (mm to m). Also, unlike Γ^{cavity} that depends on the mode index, Eq. 3.7 effectively defines Γ_{cm} per unit length of transmission line because a transmission line resonator only supports a quasi-TEM mode, making it independent of the mode index. Likewise, Γ_{dn} defined in Eq. 3.10 is the cross-sectional fractional electric field energy stored in the n-th dielectric and is equivalent to the reciprocal of both (i) the electrical energy volume filling factor described by Krupka *et al.* [132] and (ii) the participation ratio definition used by the Quantum Computing community [145], [146].

Due to the assumption $\sigma_1 \ll \sigma_2$ for isotropic superconductors, low transition temperature s-wave superconductors (e.g. Nb) exhibit intrinsic resistance R_s with quadratic frequency dependence [63], which per Eq. 3.6) and Eqs. 3.7-3.10 leads to a $Q_c \propto \omega^{-1}$ dependence [100]. At the same time, at GHz frequencies and above, amorphous dielectrics commonly exhibit a universal frequency dependence $\tan\delta \propto \omega^{b-1}$, with $b = 0.6-1$ [97, 98]. Thus, inserting $R_s = R_{s0}(\omega/\omega_0)^2$ and $\tan\delta = \tan\delta_0(\omega/\omega_0)^{b-1}$ into Eq. 3.6 and assuming frequency-independent Γ_{dn}, allows one

68

to factor out the frequency as follows

$$\frac{1}{Q_i} = \frac{\omega}{\omega_0} \sum_{m=1}^{M} \frac{R_{s0m}}{\Gamma_{c0m}} + \left(\frac{\omega}{\omega_0}\right)^{b-1} \sum_{n=1}^{N} \frac{\tan \delta_{0n}}{\Gamma_{dn}} \tag{3.11}$$

where R_{s0m} and $\tan \delta_{0n}$ are the intrinsic resistance and the loss tangent at a reference frequency ω_0, Γ_{c0m} is the partial geometric factor at that frequency associated with loss in the mth conductor, and Γ_{dn} is the partial geometric factor associated with loss in the nth dielectric.

3.3.3 Geometric Factors in Homogeneous Transmission Line

Consequently, Eq. 3.11 implies that the experimental dependence of Q_i^{-1} on the resonant frequency $\omega_n = 2\pi f_n$ of a multi-mode transmission line resonator, with $n = 1, 2, 3 \ldots$ being the mode index, can be fit to

$$Q_i^{-1} = A\omega + B\omega^{b-1} \tag{3.12}$$

where the first term corresponds to the superconductor loss $A = \omega_0^{-1} \sum_m R_{s0m} \Gamma_{c0m}^{-1}$, while the second term corresponds to the dielectric loss $B = \omega_0^{1-b} \sum_n \tan \delta_{0n} \Gamma_{dn}^{-1}$.

Generally, thin film fabrication methods may cause the ground plane and conducting strip to have dissimilar superconducting properties, especially for submicron width strips [72]. Similarly, the stack may involve multiple dielectrics. In a basic case of a homogeneous superconducting resonator formed by MTL embedded into non-dispersive dielectric ($\Gamma_{dn} = 1$, $\omega = \omega_0$, $b = 1$)

Eq. 3.11 reduces to

$$\frac{1}{Q_i} = \frac{\omega}{\omega_0}\frac{R_{s0}}{\Gamma_{c0}} + \tan\delta \tag{3.13}$$

where the net conductor geometric factor Γ_{c0} is

$$\Gamma_{c0} = \frac{\Gamma_{0GP}\Gamma_{0CS}}{\Gamma_{0GP} + \Gamma_{0CS}} = \omega_0\mu_0\frac{\int_S(|\mathbf{H}|^2 + \lambda^2|\mathbf{J}|^2)\mathrm{ds}}{2\int_S \lambda|\mathbf{J}|^2\mathrm{ds}} \tag{3.14}$$

Here Γ_{0GP} and Γ_{0CS} are the partial geometric factors of the ground plane (GP) and conducting strip (CS), respectively. We choose $\omega_0/2\pi = 10\,GHz$ because it is commonly used for scaling and comparison of the surface resistance obtained by different superconducting resonators, and is also a convenient frequency to perform HFSS simulations. Per Eq. 3.13 the experimental dependence of Q_i^{-1} on the resonant frequency can be fit with

$$Q_i^{-1} = A\omega + B \tag{3.15}$$

where the fit y-intercept immediately yields the dielectric loss tangent as $\tan\delta = B$ [100], while the fit slope coefficient A corresponds to the intrinsic resistance as follows

$$R_{s0} = A\omega_0\Gamma_{c0} \tag{3.16}$$

where Γ_{c0} is found either from Eq. 3.14 if the fields and currents are known, or from the HFSS simulation, as described in Section 3.4. A linear fit of Eq. 3.15 enables easy analysis of large data sets and is advantageous for engineering. Moreover, the fit y-intercept yields $\tan\delta$ even for

the loaded Q-factor data since the capacitive coupling loss becomes zero at zero frequency. On the other hand, a dispersive model per Eq. 3.12 accounts for fundamental physical properties of dielectric material. Initially, the data will be fit to the non-dispersive loss tangent model using 3.15 and Eq. 3.16 in Chapter 4. Then, the linear model will be tested against the dispersive model and results from reference [99].

To provide a simple analytical limiting case for Eq. 3.14 where fringing fields are not a factor, consider a resonator formed by a parallel-plate waveguide with identical superconducting plates of the width w and thickness d, separated by the dielectric layer of thickness s. This geometry approximates MTL with $w \gg s$ where the fringing fields can be ignored. The geometric factor is

$$\Gamma_{PP}(\omega) = \omega\mu_0 \frac{s + 2\lambda\coth(d/\lambda)}{2[\coth(d/\lambda) + (d/\lambda)\text{csch}^2(d/\lambda)]} \tag{3.17}$$

utilizing the expression for the effective surface resistance of thin superconducting films, and by $R_{eff} \approx R_s[\coth(d/\lambda) + (d/\lambda)\text{csch}^2(d/\lambda)]$ that ignores transmission loss through the superconducting films [69]. In the thick film limit the geometric factor reduces to $\Gamma_{PP} = \frac{1}{2}\omega\mu_0(s + 2\lambda)$ and the geometric factor is no longer dependent on the superconductor plate thicknesses d. For the thin film limit where $\lambda \gg d$ the full expression needs to be used in Eq. D.11 and a term including the dielectric substrate impedance may be needed [70].

Eq. 3.14 implies the resonator optimized for characterization of both losses calls for a geometric factor $\Gamma_{c0}^* = R_s/\tan\delta$. For $R_s \approx 17\,\mu\Omega$ representative of high quality Nb at 4.2 K, 10 GHz [138], and $\tan\delta \approx 10^{-3}$ [99], the optimal geometric factor is $\Gamma_{c0}^* \approx 17\,m\Omega$. At the same time, applying Eq. D.11 to our fabrication stack in Fig. 4.1(b) yields $\Gamma_{PP} \approx 12\,m\Omega$, which is

close to Γ^*_{c0}. Incidentally, this affords us the opportunity to design an MTL resonator capable of deconvolving the superconducting and dielectric losses at GHz frequencies.

3.3.4 $RLGC$ and Q-Factors From Impedance Matrix $[Z]$

In the last section, it was established that the net conductor geometric factor Γ_{c0} needs to be known to extract accurate values from measured data using Eq. 3.16. The net conductor geometric factor can be approximated analytically using Eq. D.11 if a parallel plate waveguide geometry can be assumed. The right hand side of Eq. 3.14 can be solved numerically using finite element solvers like HFSS [142]. This section will describe the method to extract $RLGC$ parameters and Q-factors from the output impedance matrix $[Z_{ij}]$ from HFSS, where i and j refer to the i-th row and j-th column in the impedance matrix. The geometric factors can then be found from these extracted parameters and will be shown in Section 3.5.

The $ABCD$ matrix for a generalized, linear transmission line is [95]

$$\begin{pmatrix} A & B \\ C & D \end{pmatrix} = \begin{pmatrix} \cosh(\gamma l) & Z_0 \sinh(\gamma l) \\ \sinh(\gamma l)/Z_0 & \cosh(\gamma l) \end{pmatrix} \approx \begin{pmatrix} 1 + (\gamma l)^2/2 & Z_0 \gamma l \\ \gamma l/Z_0 & 1 + (\gamma l)^2/2 \end{pmatrix} \tag{3.18}$$

where γ is the propagation constant, l is the length of transmission line, and Z_0 is the characteristic impedance. The approximation on the right holds for electrically short line $\beta l \ll 1$ using the quadratic Taylor series expansion for hyperbolic functions. The propogation constant and characteristic impedance of a general transmission line are [57]

$$\gamma = \alpha + i\beta = \sqrt{ZY} \tag{3.19}$$

$$Z_0 = \sqrt{Z/Y} \tag{3.20}$$

where Z and Y are the series impedance and shunt admittance per unit length of the line. Inserting Eq. 3.19 and Eq. 3.20 into approximation Eq. 3.18 and assuming the two-port network is reciprocal yields

$$\begin{pmatrix} A & B \\ C & D \end{pmatrix} = \begin{pmatrix} 1 + ZYl^2/2 & Zl \\ Yl & 1 + ZYl^2/2 \end{pmatrix} \tag{3.21}$$

$$[Z_{ij}] = \begin{pmatrix} (Yl)^{-1} + (Zl)/2 & (Yl)^{-1} \\ (Yl)^{-1} & (Yl)^{-1} + (Zl)/2 \end{pmatrix} \tag{3.22}$$

$$Z = 2(Z_{11} - Z_{12})/l \tag{3.23}$$

$$Y = (Z_{12}l)^{-1} \tag{3.24}$$

where $[Z_{ij}]$ is the 2×2 impedance matrix. See Fig. 3.8 for the simplified diagram representations of the 2-port network parameters.

Without assuming a reciprocal two-port network, the series impedance and shunt admittance per unit length of the transmission line can also be found from HFSS solved $[Z_{ij}]$ using a very simple yet intuitive differential voltage method in the following way [57]. The propagation constant can be solved in terms of series impedance Z and shunt admittance Y per unit length of the line $\gamma \equiv \sqrt{ZY}$ by taking advantage of the current at each end of the ports being approximately equal for an electrically short line. The current at one end (port 1) is equal and the opposite polarity to the current at the other end (port 2) $I = I_1 = -I_2$. In a two-port network the relationship between current and voltage using the impedance matrix $[Z]$ is

$$\begin{pmatrix} V_1 \\ V_2 \end{pmatrix} = \begin{pmatrix} Z_{11} & Z_{12} \\ Z_{21} & Z_{22} \end{pmatrix} \begin{pmatrix} I \\ -I \end{pmatrix} \tag{3.25}$$
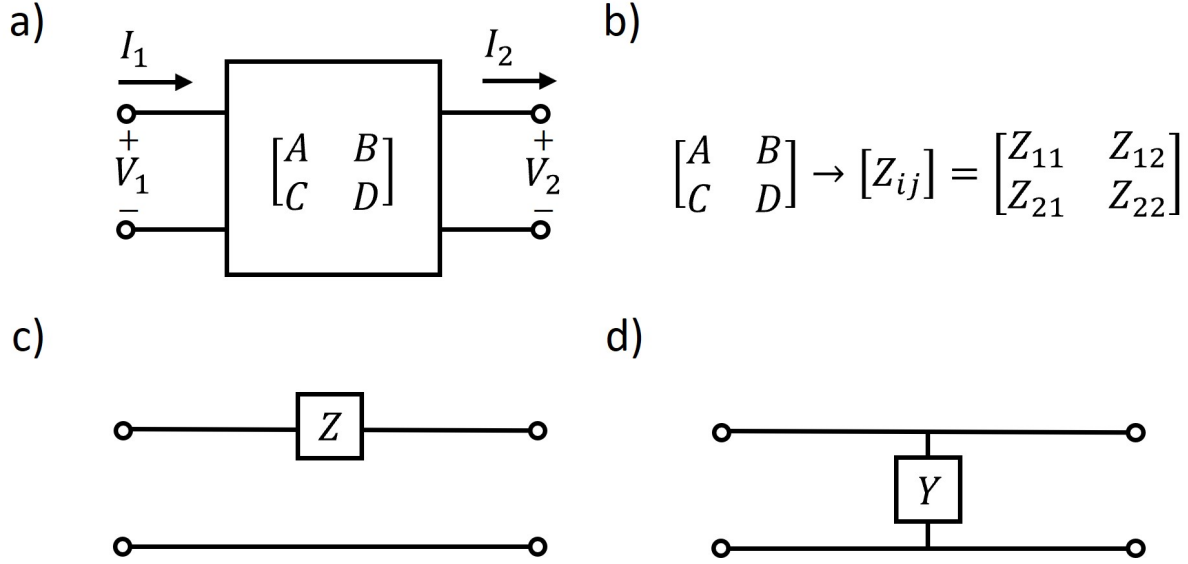
Figure 3.8: Block diagrams of 2-port network parameters showing (a) $ABCD$ block diagram (Eq. 3.21), (b) $ABCD$ can be transformed into the impedance matrix $[Z_{ij}]$ (Eq. 3.22), and the 2-port network can be represented as a single series impedance Z (Eq. 3.23) or shunt admittance Y (Eq. 3.24) [95].

The differential voltage between the two ports is equal to [57]

$$\delta V = V_1 - V_2 = ZI \tag{3.26}$$

From Eq. 3.25 and Eq. 3.26, Z can be written as

$$Z = R + i\omega L \approx (Z_{11} - Z_{12} - Z_{21} + Z_{22})/l \tag{3.27}$$

where Z_{ij} are the elements of the impedance matrix, and R and L are the series resistance and series inductance per unit length, respectively. Equivalently, by utilizing $I = I_1 = -I_2$, the

differential current being equal to the admittance and voltage product [57]

$$\delta I = I_1 - I_2 = YV \tag{3.28}$$

and the relationship between current and voltage using the admittance matrix $[Y]$

$$\begin{pmatrix} I_1 \\ I_2 \end{pmatrix} = \begin{pmatrix} Y_{11} & Y_{12} \\ Y_{21} & Y_{22} \end{pmatrix} \begin{pmatrix} V \\ -V \end{pmatrix} \tag{3.29}$$

the admittance can be expressed as

$$Y = G + i\omega C \approx (Y_{11} + Y_{12} + Y_{21} + Y_{22})/l \tag{3.30}$$

where Y_{ij} are the elements of the admittance matrix, G and C are the shunt conductance and shunt capacitance of the network per unit length, respectively. Now with expressions for both Z and Y, $RLGC$ can be separated and analyzed separately in two-port HFSS simulations. Eqs. 3.23 and 3.24 assume a reciprocal 2-port network, and Eqs. 3.27 and 3.30 do not.

For $Q_i \equiv \frac{1}{2}\beta\alpha^{-1}$ [95], inserting Eq. 3.23 and Eq. 3.24 into Eq. 3.19 and Eq. 3.20, and utilizing the identity $Im[\sqrt{z}]/Re[\sqrt{z}] = \tan\left[(\arg z)/2\right]$ for a reciprocal 2-port network, one can simplify Q_i in terms of the impedance matrix Eq. 3.22 by

$$Q_i = \frac{1}{2}\tan\left[\frac{1}{2}\arg(2Z_{21}^{-1}(Z_{11} - Z_{21}))\right] \tag{3.31}$$

Eqs. 3.27, 3.30, and 3.31 will be used in Section 3.5 to extract numerically solved geometric factors of microstrip transmission line resonators measured in Chapters 4 and 5. The above

75

method can be applied to any electrically short, 2-port transmission line geometry.

3.4   HFSS Modeling

In this section I describe how to model superconductors embedded in dielectrics by using impedance boundary conditions or by a *Solve-Inside* method. These distinctly different model types to be simulated are shown in Fig. 3.9, and are evaluated here to show (i) the limitations of Fig. 3.9(a) due to assuming boundary conditions, and (ii) the capability of the *Solve-Inside* method Fig. 3.9(b) to extract geometric factors analytically for any arbitrary geometry. Here we start by modeling a parallel plate waveguide with superconducting impedance boundary conditions. This is how superconductors have been defined in finite element modelers in the past [139, 140]. A microstrip transmission line (MTL) will be modeled using the *solve-inside* approach described here. From HFSS solved telegrapher's expressions ($RLGC$) described above, the superconducting and dielectric net geometric factors Γ_{c0} and Γ_{d0}, respectively, are calculated.

Analytically solving these factors can be difficult as dimensions become comparable to λ and geometries increase in complexity. Here we utilize this method to extract the intrinsic resistance R_s, and determine $RLGC$ and Γ sensitivities to fabrication variation.

Modeling dielectric loss tangent $\tan \delta$ comes standard in HFSS and is straight forward. The critical differences in modeling a superconductor in HFSS as opposed to a normal conductor are (i) the definition of the superconducting material with a real conductivity σ_1 and a negative real permittivity $\varepsilon_r < 1$ ($\sigma = \sigma_1 - i\sigma_2$ or $Z_s = R_s + i\omega\mu_0\lambda$ cannot be defined directly for 3D material [142]), (ii) the use of *Perfect Electrical Conductor* material to connect superconductor materials to a wave port due to wave ports not being able to handle materials with $\varepsilon_r < 1$ (see Fig. 3.12),

76

and (iii) selecting the *solve-inside* option for the defined 3D lossy superconducting material due to a real conductivity much smaller than normal conductors. The first critical difference will be discussed in detail, followed by the process of converting the HFSS impedance matrix into useful parameters, and results validation.

This method can be used for any linear 2-port electrically short transmission line geometry, as long as the ratio of largest to smallest dimensions defined in the simulation are less than a factor of 10^4. Other possible geometries that can be simulated include coplanar waveguides (CPWs) and striplines.

3.4.1   Parallel Plate Waveguide

A method to simulate a superconductor in HFSS is by defining the superconductor as impedance boundary conditions [140, 141, 167, 168]. To demonstrate this, a parallel plate waveguide (PPW) will be modeled and validated against analytical equations. A range of superconductor thicknesses d and penetration depths λ are simulated to show HFSS yields proper solutions for the bulk, thin film, and intermediate limits.

As described in Section 2.2, the complex surface impedance of a parallel plate waveguide (or resonator) can be modeled using Eq. 2.24 and Eq. 2.25 [70]. The expressions in brackets in Eq. 2.24 and the term $\coth{(d/\lambda)}$ in Eq. 2.25 are modifications to the intrinsic impedance to account for superconducting plate thicknesses on the order or less than the penetration depths $d \leq \lambda$. For a system composed of bulk superconductor with thicknesses $d \gg \lambda$, the intrinsic impedance of each conductor simplifies to $Z_{s0} = R_{s0}(\frac{\omega}{\omega_0})^2 + i\mu_0\omega_0\lambda$, where R_{s0} is the intrinsic resistance at reference frequency ω_0. Here, a PPW system has been enforced, and we are
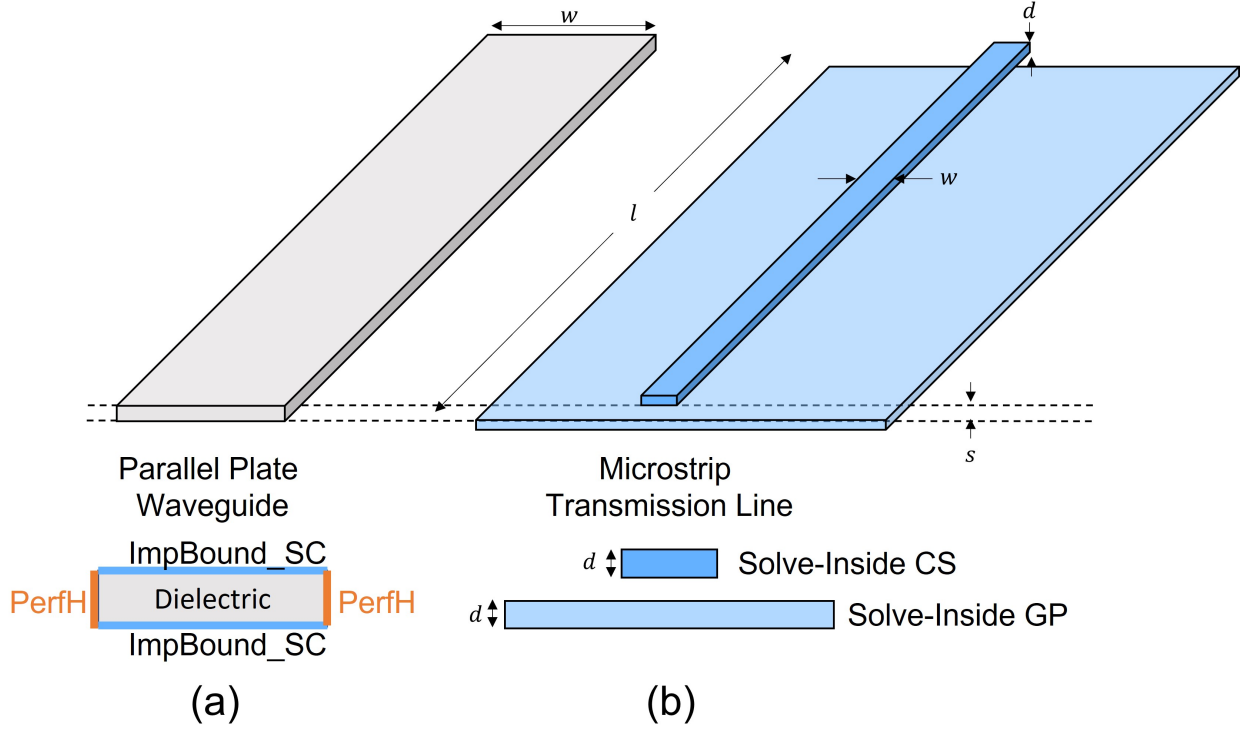
Figure 3.9: A diagram showing the different HFSS model geometries simulated in this section: a) Parallel Plate Waveguide (PPW) with superconducting complex impedance boundary conditions on the top and bottom faces labeled "ImpBound SC" and *PerfH* boundary conditions on the side faces. b) Microstrip Transmission Line (MTL) with *Solve-Inside* ground plane (GP) and conducting strip (CS). The conducting strip has width w. These models have superconductor thickness d and interlayer dielectric thickness s. The nominal HFSS simulation frequency is set to 10 GHz and simulated lengths ranging from 10-100 μm. For all Ls, Cs, and l simulated here meet electrically short condition $\beta l \ll 1$.

interested in the resulting transverse electromagnetic (TEM) mode propagating along the longitudinal length l in the x direction (see Fig. 3.10). The accuracy of HFSS solutions will be tested using the following equations for $RLGC$ by inserting the superconducting impedance definitions Eq. 2.24 and Eq. 2.25 into PPW analytical solutions [95]

$$R = \frac{2R_{eff}}{w} \tag{3.32}$$

$$L = \mu_0 \frac{s + 2\lambda \coth(d/\lambda)}{w} \tag{3.33}$$

$$G = \omega \varepsilon_0 \varepsilon_r \tan \delta \frac{w}{s} \tag{3.34}$$

$$C = \varepsilon_0 \varepsilon_r \frac{w}{s} \tag{3.35}$$

where μ_0 is the vacuum permeability, ε_0 is the vacuum permittivity, ω is the angular frequency, w is the PPW width, s is the plate separation dielectric thickness, R_{eff} is the effective resistance defined in Eq. 2.24, and $\tan \delta$ is the dielectric loss tangent. The $RLGC$ are the series resistance, series inductance, shunt conductance, and shunt capacitance per unit length of a generalized transmission line defined in Eq. 3.2-Eq. 3.5 in Section 3.3.

Using Eq. 3.1, the partial conductor and dielectric Q-factors for a PPW, $Q_c = \omega L/R$ and $Q_d = \omega C/G$, respectively, are

$$Q_c = \omega \mu_0 \frac{s + 2\lambda \coth (d/\lambda)}{2R_{eff}} \tag{3.36}$$

$$Q_d = 1/\tan \delta \tag{3.37}$$

Notice, the PPW width w drops out in Q_c, and ω drops out in Q_d with no geometry dependence. Then, the only parameters needed to model the superconducting PPW, analytically and with HFSS impedance boundaries, are s, d, ω, λ, R_s, and $\tan \delta$.

The HFSS *Driven Modal network analysis* design will be used [142] to model the PPW. The top and bottom faces of the rectangular PPW are defined as impedance boundary conditions (see Fig. 3.10). To ensure no fringing fields, the two sides are defined with *Perfect H* boundary conditions. When defining the HFSS *wave ports*, a new line of integration needs to be defined to explicitly set the expected electric field **E** direction for the propagating mode 1. For the PPW case, the direction is defined to be normal to the impedance boundary plates. In this section, we

are concerned with the first mode of propagation only, where the electric field is exactly normal to the conducting plates (impedance planes). Take note, this is enforced with the integration line, allowing HFSS to converge to the correct solution IF and ONLY IF mode 1 is the only mode present in the model defined. If other modes are present for a given geometry and simulation frequency $\omega/2\pi$, then phenomena such as mode conversion, the presence of non-propogating evanescent modes, and parasitic reflections of higher-order modes can cause HFSS to converge to non-realistic (bad) results [169]. This is true when modeling any material as complex impedance boundary conditions.

To facilitate proper convergence of transmission line parameters (e.g. $RLGC$), the default settings are the following:

(a) *maximum number of passes* is set to 40

(b) *maximum delta S* is set to 0.001

(c) *output variables $RLGC$* are set to a 1% convergence criteria

(d) *lambda refinement* and *initial mesh operations* are not used

(e) *maximum refinement per pass* of mesh is set to 50%

(f) *solution options* are set to mixed order with *relative residual* of 1×10^{-4}

(g) *maximum delta Z_0* set to 2% in the *port options*.

To aid HFSS in converging to accurate solutions quickly, the simulation geometry used in Fig. 3.10 and Fig. 3.11 will be set to $l = 1\ \mu m$, $w = 0.5\ \mu m$, and nominal $s = 150\ nm$. For impedance definitions, the nominal $\lambda = 90\ nm$, $R_s = 20\ \mu\Omega$, $\tan\delta = 1 \times 10^{-3}$, and simulation frequency $\omega/2\pi = 20\ GHz$.
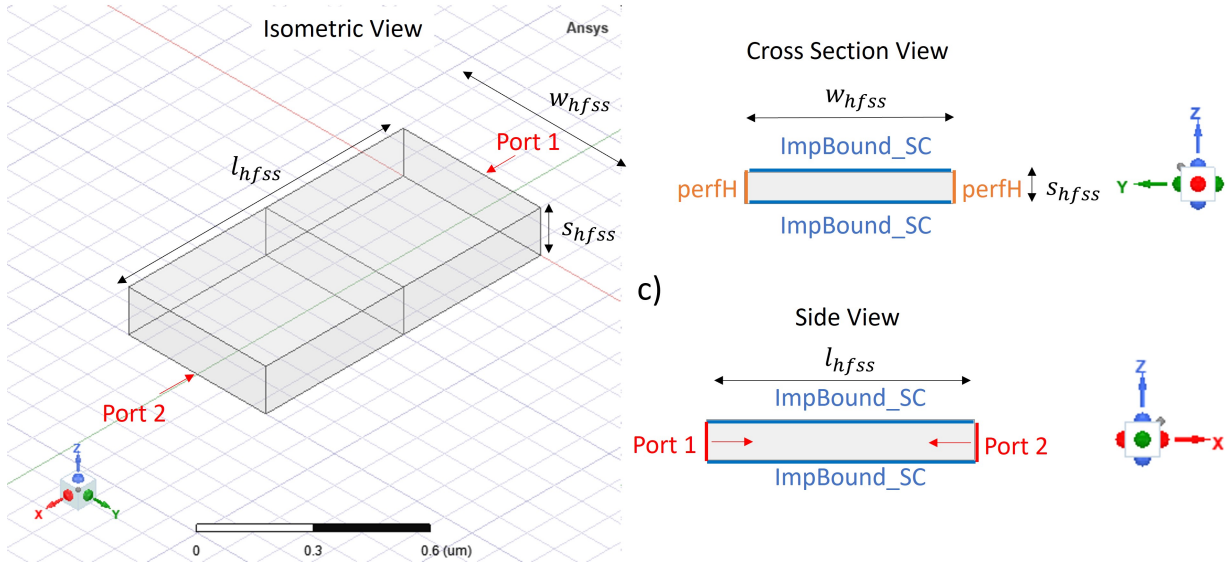
Figure 3.10: Model of parallel plate waveguide (PPW) in HFSS using a *Driven Model* solution type. The model a) isometric view, b) cross section view along x-axis, and c) cross section view along y-axis. The top and bottom faces (z-axis) of the simulation box are the superconducting plates defined as impedance boundary conditions using Eq. 2.24 and Eq. 2.25. The side faces (y-axis) are *Perfect H* boundaries. The PPW length, width, and plate separation thickness are $l - 1\ \mu m$, $w - 0.5\ \mu m$, and $s = 0.15\ \mu m$, respectively. The nominal simulation frequency is $\omega/2\pi = 20\ GHz$.

For a wide range of d and λ, the $RLGC$ and partial Q-factor errors from HFSS solutions relative to Eq. D.3-Eq. D.6 are plotted in Fig. 3.11. The $d = 1\ \mu m$ (pink) at minimum $\lambda = 1\ nm$ represents the bulk case ($d \gg \lambda$), whereas the $d = 10\ nm$ (red) at maximum $\lambda = 1\ \mu m$ represents the thin film limit ($d \ll \lambda$). Everything in between is considered the intermediate regime. A positive (negative) error corresponds to HFSS converging to a larger (smaller) results relative to Eq. D.3-Eq. D.6. It can be seen the errors in all parameters do not exceed 0.35% over the bulk limit, thin film limit, and intermediate regime. This validates HFSS is converging to the expected results.

Modeling superconductors as impedance boundary conditions has been used in the community and has been further validated in HFSS for a parallel plate waveguide (PPW) here. Although, this
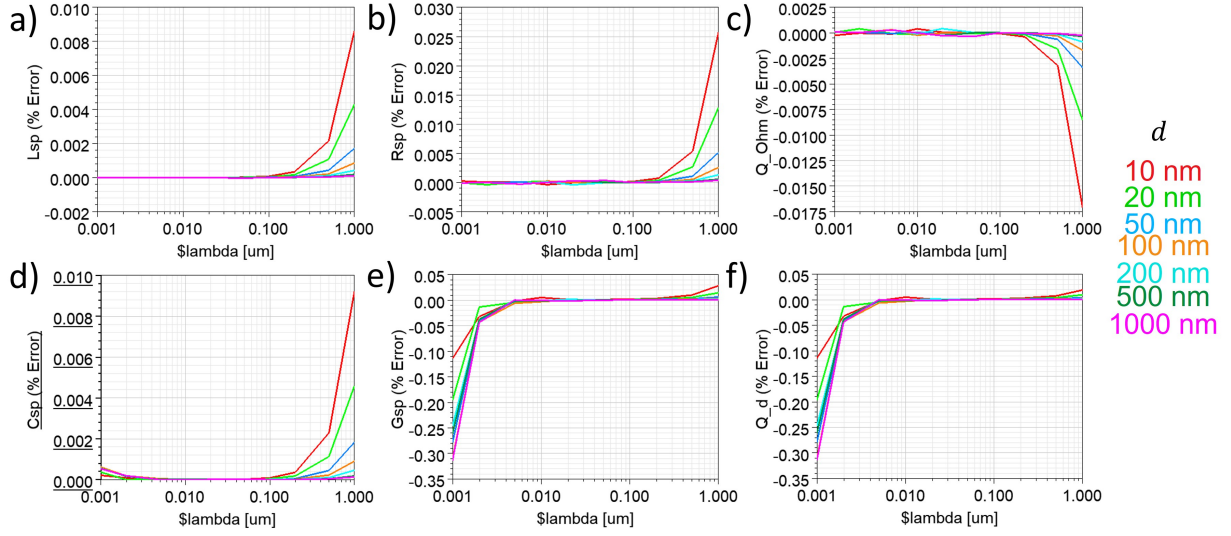
Figure 3.11: HFSS results of a PPW using geometry in Fig. 3.10. The (a) series inductance L, (b) series resistance R, (c) partial conductor Q-factor Q_{c0}, (d) shunt capacitance C, (e) shunt conductance G, and (f) dielectric partial Q-factor Q_d error relative to parallel plate analytical Eq. D.3-Eq. D.6 as a function of penetration depth λ and effective plate thickness d. In HFSS the penetration depth λ (with name \$lambda on the x-axis) and plate thickness d are parameterized variables. The error was calculated using the equation $X^{error} = 100 \times (X^{HFSS} - X^{PP})/X^{PP}$, where X_{HFSS} is solved value by HFSS simulation and X_{PP} is the calculated value from parallel plate model analytical Eq. D.3-Eq. D.6. The simulation frequency was $\omega/2\pi = 20\,GHz$.

is only a good approximation under the assumptions of (i) fringing fields can be ignored and (ii) current distributions inside the superconductor are known. If this cannot be assumed and a two-fluid model can still be used [40, 43], then one must resort to numerically solving inside a 3D superconductor.

3.4.2 Defining *Solve-Inside* Superconductor

A good, isotropic superconductor ($\sigma_1 \ll \sigma_2$) can be defined as a material with bulk conductivity σ_1 and negative relative permittivity [170]. Inserting the superconductor current-field constitutive relationship $\mathbf{J} = (\sigma_1 - i\sigma_2)\mathbf{E}$ into Maxwell's curlH equation in phasor form

yields

$$\nabla \times \mathbf{H} = \sigma_1 \mathbf{E} + i\omega\varepsilon_0(\varepsilon_r - \frac{\sigma_2}{\varepsilon_0\omega})\mathbf{E} \tag{3.38}$$

where $\varepsilon_{sc} = \varepsilon_r - \sigma_2/\varepsilon_0\omega$ can be seen as the superconductor real relative permittivity, with ε_r being the ordinary dielectric constant associated with displacement current. The ε_r value can be estimated by approximating a superconductor as a collisionless neutral plasma with Langmuir frequency $\omega_p = c/\lambda$ and dielectric function $\varepsilon_p = 1 - \frac{\omega_p^2}{\omega^2} = 1 - (\omega\lambda/c)^{-2}$, where c is the speed of light [171]. Comparison of ε_{sc} and ε_p implies that $\varepsilon_r = 1$ is the superconductor permittivity in the limit $\omega \gg \omega_p$ (approached from below), and $\sigma_2 = (\omega\mu_0\lambda^2)^{-1}$ is the London conductivity applicable at frequencies well below the gap and temperatures not too close to T_c. Therefore, a superconductor can be defined in HFSS as a material with real relative permittivity $\varepsilon_{sc}^{HFSS} = 1 - \sigma_2(T,\omega)\varepsilon_0^{-1}\omega^{-1}$ and real conductivity $\sigma_1^{HFSS} = \sigma_1(T,\omega)$, which is applicable over the entire range of temperatures and frequencies considered in this work. At frequencies below the gap, and temperatures below T_c, a superconductor relative permittivity is substantially negative [172]. According to Eq. 3.38, the superconductor complex permittivity is $\epsilon_{sc} = \varepsilon_0(1 - \frac{\sigma_2}{\varepsilon_0\omega} - \frac{i\sigma_1}{\varepsilon_0\omega})$, where the three addends are associated with displacement, superconducting, and normal current, respectively. Due to the fact that $\sigma/\varepsilon_0\omega \gg 1$ the displacement current is negligibly small, and the intrinsic impedance generally defined as $\sqrt{\mu_0/\epsilon_{sc}}$ reduces to a value much smaller than the vacuum wave impedance $Z_s = \sqrt{i\omega\mu_0/\sigma} \ll \sqrt{\mu_0/\epsilon_0} = 120\pi \ \Omega$.

Generally, σ_1 and σ_2 can be calculated from the Mattis-Bardeen theory [49] and the respective $\sigma_1^{HFSS}(\omega)$ and $\varepsilon^{HFSS}(\omega)$ are tabulated and implemented in HFSS as *datasets* [49]. To meet the assumption $\sigma_1 \ll \sigma_2$ made in Sections 2.2.2 and 3.3, I will model σ_1 as a Drude-like

conductivity, which is related to the experimental intrinsic resistance found in Eq. 3.16 via

$\sigma_1^{HFSS} = 2R_{s0}\mu_0^{-2}\omega_0^{-2}\lambda^{-3}$ [138]. Likewise, we will model σ_2 as the London conductivity which

gives $\varepsilon^{HFSS} = -(\omega\lambda/c)^{-2}$. Such an approach allows one to implement σ_1^{HFSS} and ε^{HFSS}

analytically. Forcing HFSS to solve inside the superconductor overcomes the limitations of an

impedance boundary approximation [140], [167].

3.4.3 *Solve-Inside* Model Setup

When simulating electromagnetic fields inside highly conductive materials with $\sigma/\varepsilon_0\omega \gg$

1, a proper modeler setup is vital for accurate results. The HFSS model and setup were optimized

for accuracy (meeting condition $\beta l^{HFSS} \ll 1$) and simulation time, in order to complete parametric

sweeps on the order of 100 simulations in a few hours for sensitivity analysis and MTL design

optimization. The *network analysis driven terminal* solution type was used [142] to simulate 2-

port MTLs with nominal lengths $l^{HFSS} = 10-50\mu m$, cross-section geometry shown in Fig. 3.12,

simulation frequencies $f_{HFSS} = 10 - 100\ GHz$, and perfect electrical conductor port length

$l_{PEC} = 1\ \mu m$ (see Fig. 3.12) [36]. The MTL is surrounded by a radiation bounding box with

walls sufficiently spaced to avoid impinging magnetic and electric fields shown in Fig. 3.13. Ports

were de-embedded by a length l_{PEC} to calculate only the network parameters pertaining to the

superconductor MTL. After defining a superconducting material with negative real permittivity

ε^{HFSS} and real conductivity σ_1^{HFSS} described in last section, the *solve inside* option is selected,

to override HFSS default to solving inside when real conductivity $\sigma_1 < 10^5\ S/m$. All geometries

and material properties were parametrized and the *Optimetrics* option was used for sweeps and

sensitivity analysis. To allow for fast and accurate convergence, the analysis setup was set to

Maximum Delta S of 0.001 and 0.1-1 % convergence criteria for $RLGC$ output variables.

3.4.4   Microstrip Transmission Line (MTL)

The (embedded) microstrip transmission line (MTL) geometry is the one measured in Chapter 4 and Chapter 5. The MTL geometry simulated here consists of a ground plane (GP) and a conducting strip (CS) embedded in a dielectric having thickness d, and separated by a thickness s (see Fig. 3.12). The GP and CS are defined as *solve-inside* superconductors as explained above. To stay within the assumption $\beta l \ll 1$, the simulated MTL simulation lengths and frequencies are $l < 100\ \mu m$ and $\omega/2\pi < 100\ GHz$, respectively. Unless otherwise specified, the nominal conductor and separation thicknesses are $d = 200\ nm$ and $s = 150\ nm$, respectively. The GP width is nominally 20 μm when simulating CS $w \leq 4\mu m$, to be sufficiently far from the electromagnetic fringing fields. Similarly, the simulation box height separation from the GP and CS is roughly 5-10s to be sufficiently far from electromagnetic fields. The perfect electrical conductor (PEC) strips (yellow) connecting the GP and CS to the waveports are $l_{pec} = 1\ \mu m$. The wave ports are surrounding the CS cross section and only touch the corner of the GP to properly act as references. Extending the wave port into the cross section of the GP will induce an error and HFSS will not be able to solve. Additionally, the GP cannot touch the edges of the simulation, as this will effectively cause a short. Lastly, all faces of the simulation box are defined as *Radiation Boundary* conditions.

Two-port *driven terminal* simulations for MTL widths $w = 0.25 - 4\ \mu m$ were done and magnetic field profiles in cross section can be seen in Fig. 3.13. Up to this point, the lossy telegraph's R and G for an MTL at these dimensions and λ have not yet been reported. For

the 4 μm MTL, the magnitude of the magnetic fields (H) at the edge (fringing fields) are only a small fraction relative to the H fields underneath the CS. Therefore, a parallel plate model is a good approximation for this width (assuming $w >> s$). For the 0.25 μm MTL, the fringing fields become a significant fraction. It can also be seen from Fig. 3.13 for there is a transition in fringing field character between 0.5 and 1 μm. At 0.5 μm, the fringing fields on each side begin to overlap. At 0.25 μm, a significant fraction of the CS is penetrated by magnetic field, but the current is not yet uniform, making it difficult to analytically model. When considering the GP, the fraction of fields inside reduce significantly relative to the CS. This will be discussed further in the next section. Chang *et al.* analytically solved telegraph's L and C acounting for a fringing factor for microstrip widths $w \geq 1$ μm [134].
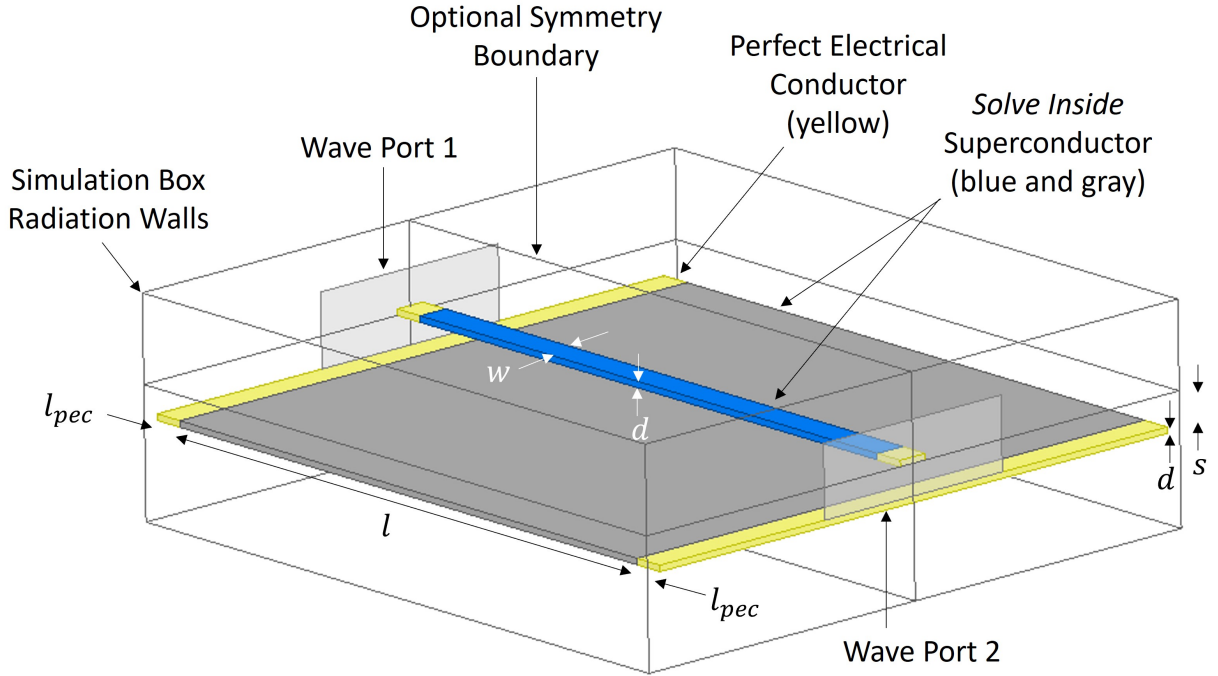
Figure 3.12: MTL geometry modeled in HFSS. The MTL conducting strip (blue) has width w and a dielectric separation thickness s from the ground plane (gray). Both the strip and ground plane have thickness d and simulation length l. In HFSS, the MTL is surrounded by a simulation box with all six faces defined with *Radiation* boundaries. To properly launch waves into a superconductor with negative real permittivity, small lengths of Perfect Electrical Conductors $l_{pec} \approx 1\ \mu m$ (yellow) are used to connect the superconducting ground plane and conducting strip to the wave ports. To cut down on simulation time and reduce the simulation size in half, one can utilize a *Symmetry* boundary condition.
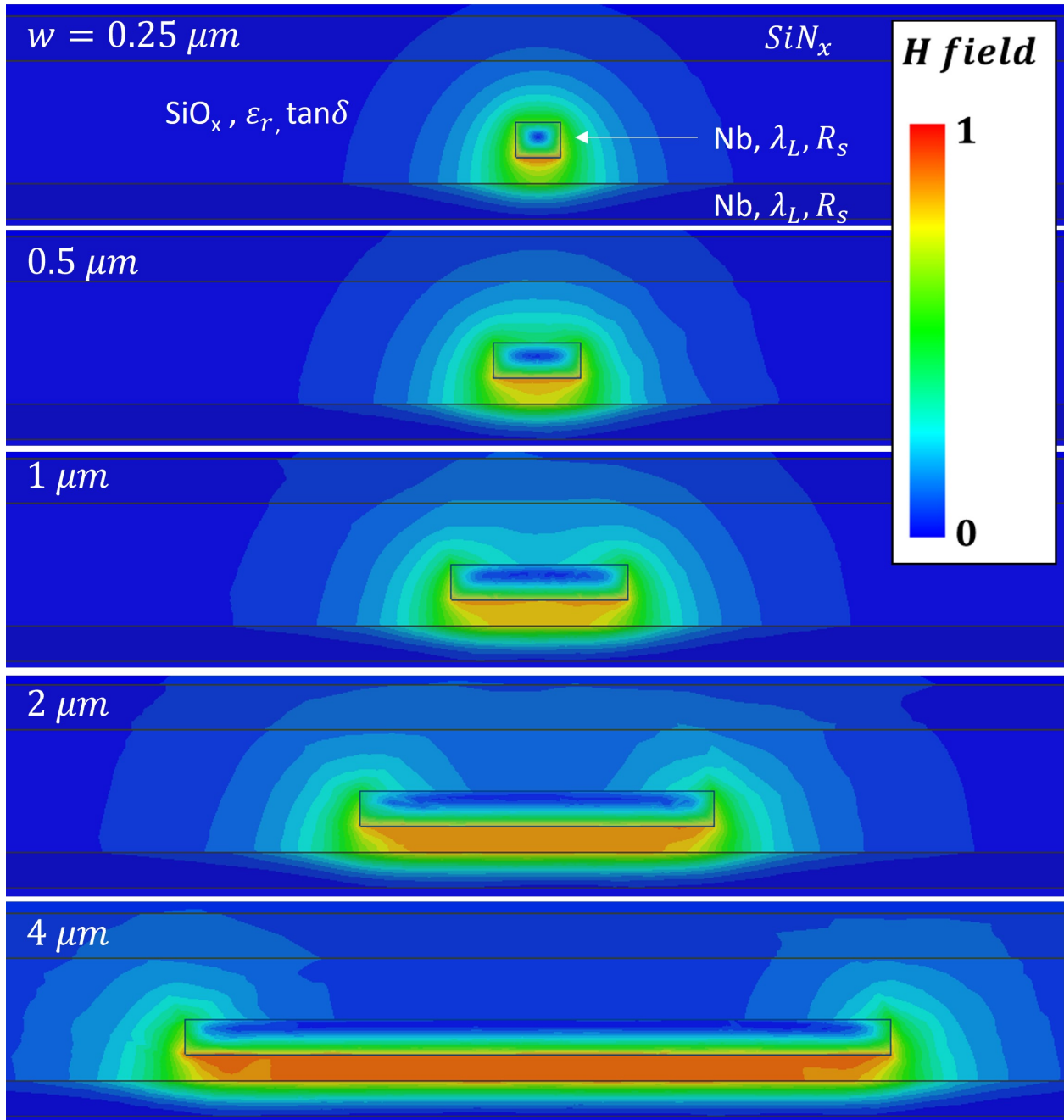
Figure 3.13: Cross section MTLs simulated using HFSS and geometry shown in Fig. 3.12. The dielectric thickness is $s = 150\,nm$. The ground plane and conducting strip thicknesses are both $d = 200\,nm$. The MTL width varied from $0.25 - 4\,\mu m$ going from top to bottom. The inputted intrinsic resistance $R_s = 20\,\mu\Omega$, TEOS loss tangent $\tan\delta = 1 \times 10^{-3}$, and the SiNx loss tangent $\tan\delta = 1 \times 10^{-4}$. The magnetic penetration depth was set to $\lambda = 90\,nm$. The relative dielectric constant of TEOS and SiNx relative dielectric constant were set to $\varepsilon_r^{TEOS} = 4.5$ and $\varepsilon_r^{SiNx} = 7.5$, respectively. The simulation frequency was set to $\omega/2\pi = 10\,GHz$.

3.5 MTL Geometric Factor Γ Extraction

For an electrically short transmission line $\beta l \ll 1$, the propagation constant of a general transmission line $\gamma = \alpha + i\beta = \sqrt{ZY}$ [57], and the internal Q-factor of a transmission line resonator is $Q_i = \frac{1}{2}\beta\alpha^{-1}$ [95] This can be expressed in terms of the series impedance Z and shunt admittance Y per unit length yielding $Q_i = \frac{1}{2}Im(\sqrt{ZY})/Re(\sqrt{ZY})$. Inserting here $Z \approx 2l^{-1}(Z_{11}-Z_{21})$ and $Y \approx (Z_{12}l)^{-1}$ found in Section 3.3.4, and using an identity $Im(\sqrt{z})/Re(\sqrt{z}) = \tan[\mathrm{Arg}(z)/2]$, yields

$$Q_i = \frac{1}{2}\tan\left[\frac{1}{2}\mathrm{Arg}\left(\frac{2(Z_{11}-Z_{21})}{Z_{21}}\right)\right] \tag{3.39}$$

where $\mathrm{Arg}(z)$ is the argument of a complex variable z, and Z_{ij} are the respective elements of the model Z matrix solved by HFSS. For a model of arbitrary length, one shall resort to a general solution for propagation factor $e^{-\gamma l}$ of a transmission line with mismatched ports [36].

Setting the dielectric loss to zero, $\tan\delta = 0$ throughout the entire HFSS model leads to $Q_i = Q_c$. Then, the conductor geometric factor Γ_{c0} can be computed as

$$\Gamma_{c0} = R_s^{HFSS}Q_c^{HFSS} \tag{3.40}$$

where R_{s0}^{HFSS} is the superconductor intrinsic resistance defined in the HFSS model, and Q_c^{HFSS} is the quality factor found from the HFSS solution using Eq. 3.39, and the simulations are done at a reference frequency $\omega_0/2\pi$. Here Γ_{c0} is independent of intrinsic resistance and the product $Q_c^{HFSS}R_s^{HFSS}$ of each cross-sectional geometry can be found from a single simulation

at any intrinsic resistance value meeting $R_s^{HFSS} \ll \omega_0 \mu_0 \lambda$. This simplifies the experimental data analysis by removing the need to simulate Q_c as a function of R_s for every MTL width.

Similarly, by setting the superconductor intrinsic resistance to zero throughout the entire HFSS model leads to $Q_i = Q_d$. Then the dielectric geometric factor Γ_d can be computed as

$$\Gamma_d = \tan \delta^{HFSS} Q_d^{HFSS} \tag{3.41}$$

where $\tan \delta^{HFSS}$ is the dielectric loss tangent defined in the HFSS model, and Q_d^{HFSS} is the quality factor associated with the dielectric loss.

The HFSS results can be validated by comparing the HFSS solved geometric factors Γ_{c0} using Eq. 3.40 to the analytical parallel plate model using Eq. D.11 for MTL widths much larger than the dielectric thickness $w/s \gg 1$. For $w_{HFSS} = 4 \, \mu m$ the partial Q-factor associated with the conductor loss solved by HFSS $Q_{c0}^{HFSS}(4 \, \mu m) = 586$ using Eq. 3.13 and an input value of $R_{s0}^{HFSS} = 20 \, \mu\Omega$. Using the parallel plate model, the partial Q-factor is found to be $Q_{c0}^{PP} = 584$, yielding agreement within 0.34%. This can also be seen directly in Fig. 3.13, where Γ_{c0}^{tot} (green solid line) approaches Γ_{c0}^{PP} (dashed line) for $w_{HFSS} \geq 1 \mu m$. Intuitively this can be understood by looking at Fig. 3.14. The fringing fields at MTL left/right edges of cross-section begin to overlap for $w_{HFSS} \leq 1 \, \mu m$, making the parallel plate model inapplicable as it does not account for field fringing, concentration at the edges, and penetration above the conducting strip. Furthermore, it is important to note the geometric factors calculated from HFSS solutions were independent of the input value $R_s^{HFSS} = 0.1 - 100 \, \mu\Omega$.
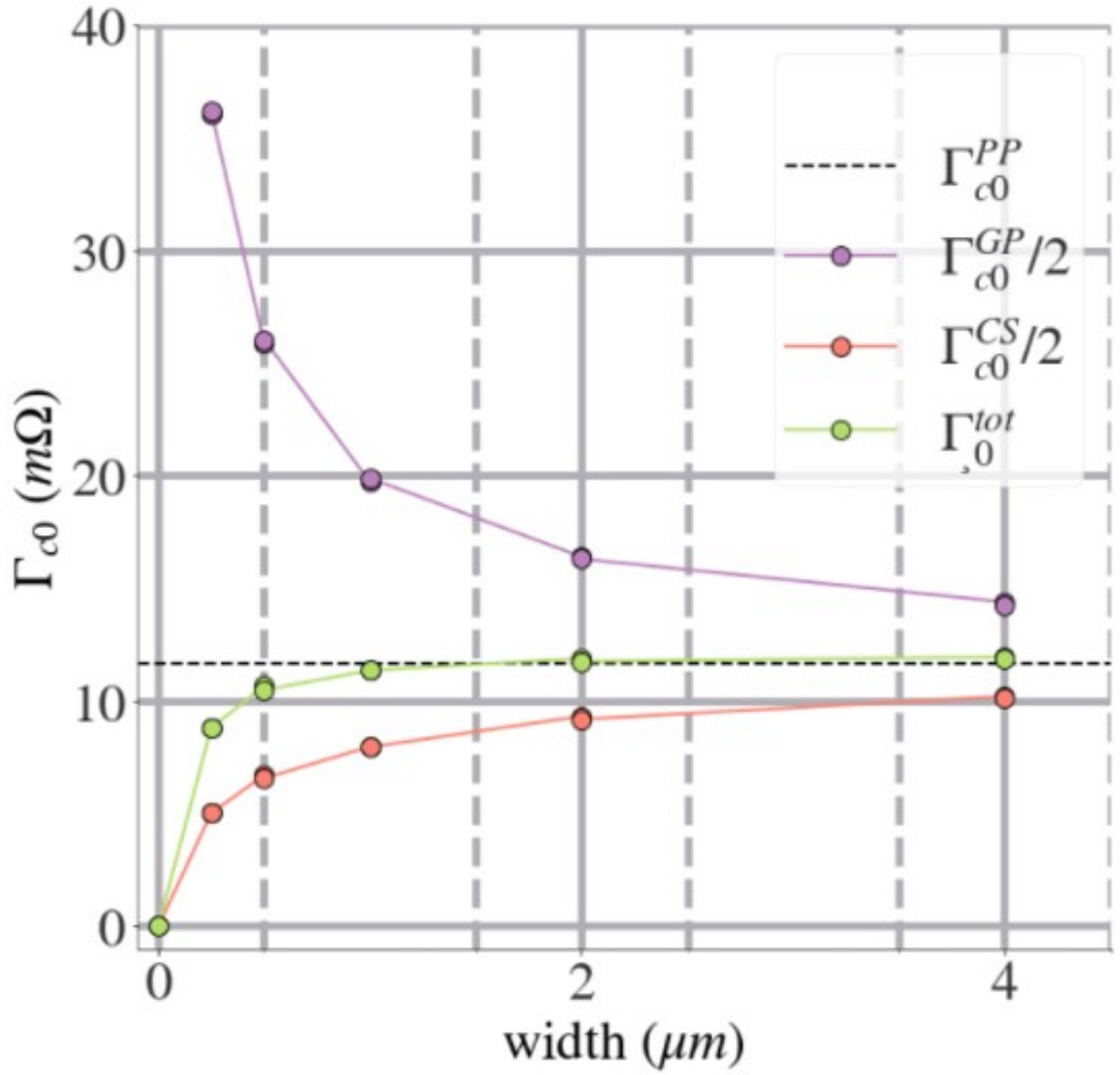
Figure 3.14: Geometric factors for the conducting strip Γ_{c0}^{CS}, ground plane Γ_{c0}^{GP}, and Γ_{c0}^{tot}. This is assuming $R_{s0}^{GP} = R_{s0}^{CS}$ from Eq. 3.14 for all MTL widths. The parallel plate analytical calculation Γ_{c0}^{PP} is compared (see Eq. D.11).

3.6 MTL $RLGC$ and Γ Sensitivity to Fill

Spatially dense areas of metal polishes (etches) faster than lower density areas in the damascene CMP process. Floating fill patterns (metal strips) are used to maintain a certain metal density, achieving uniformity across the chip and wafer, mitigating dishing effects [54].

Fig. 3.15 shows the MTL strip below the ground plane and surrounded by floating fill patterns length (left to right) and width (into the page) $\approx 1.5\ \mu m$ and $\approx 0.5\ \mu m$, respectively, to reach minimum density requirements of $\approx 65\%$.
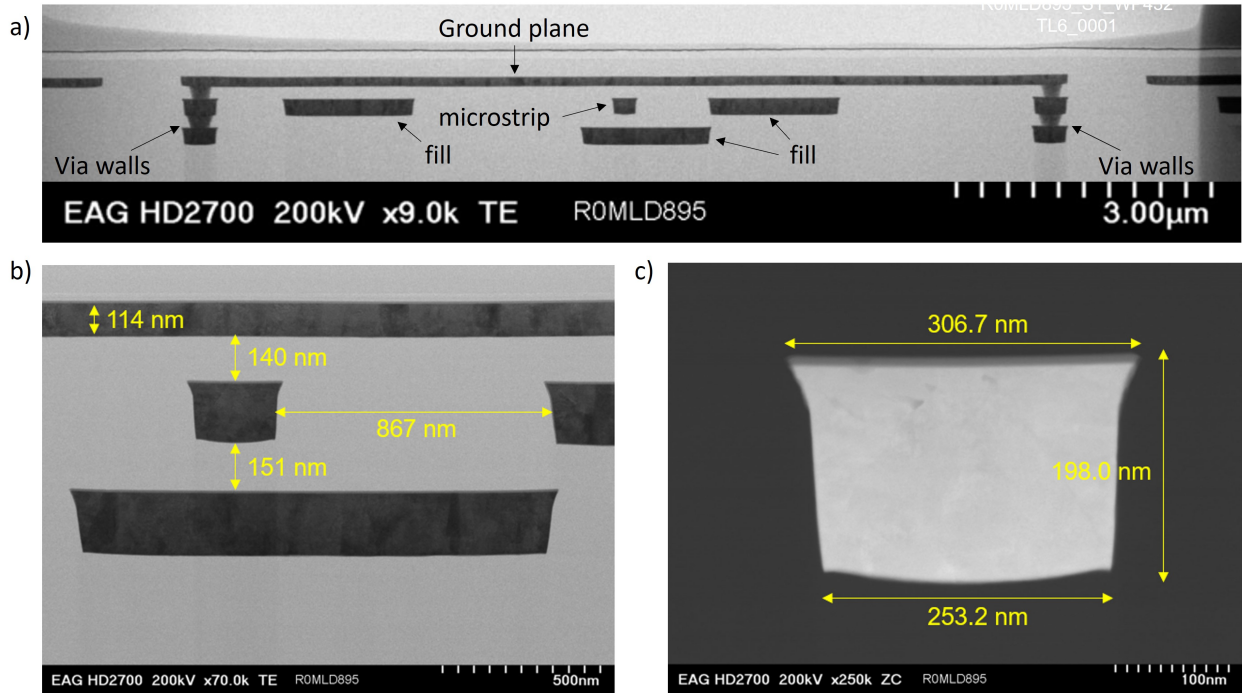
Figure 3.15: STEM images of (a) full MTL showing the via walls and surrounding fill, (b) measurements of fill proximity to conducting strip (CS), and (c) is a zoom in of the conducting strip showing the resulting inverted trapezoid geometry.

Using the measurements in Fig. 3.15, three HFSS simulations were run and compared (see Fig. 3.16 and Table 3.2). The top row in Fig. 3.16 is the nominal cross sectional geometry. The middle row is the actual cross-sectional geometry of the MTL without surrounding fill. Note, the

sidewall angle was introduced in the HFSS simulation to model the damascene Process A. The bottom row is the same as the middle row but with the additional Nb fill to reflect the geometry shown in Fig. 3.15(b).
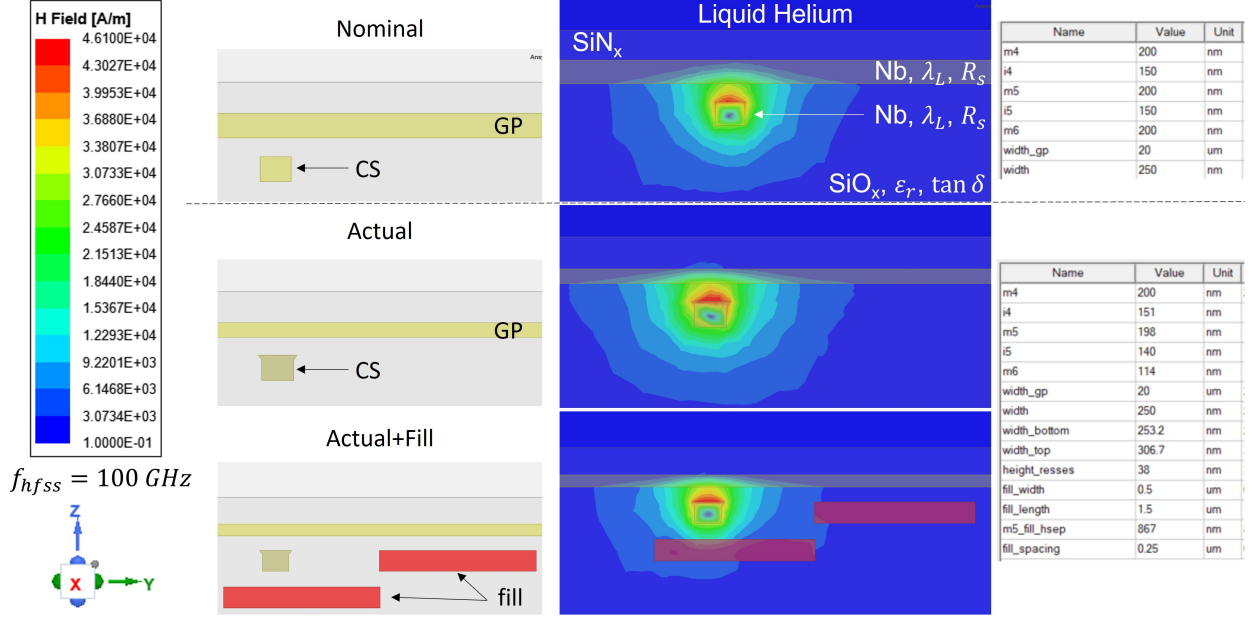
Figure 3.16: Cross sections of three different HFSS simulations, where the (top) is the nominal designed geometry of the 250 nm wide conducting strip (CS) underneath the ground plane (GP). The (middle) row is the actual cross section geometry as measured by TEM data for wp432-TL6 with CS shaped more like a Reeses Cup. The (Bottom) row is the same MTL geometry as (middle) but with added and repeated superconducting strip fill patterns.

Table 3.2 summarizes the results from simulations shown in Fig. 3.16. The $RLCG$ values were calculated as described in Section 3.3.4. The partial geometric factors associated to the ground plane (GP), conducting strip (CS), TEOS dielectric layer, and SiN_x dielectric passivation layer are calculated based off of geometry shown in Fig. 3.16.

Immediately, it is important to point out that Fig. 3.15 shows the CS is in the layer below the GP (also shown in Fig. 3.1 and summarized in Table 3.1). Therefore the electric fields are masked from the SiN_x. This is confirmed in Fig. 3.2, showing Γ_{SiN_x} is a factor of 10 larger than Γ_{TEOS}, and is not participating. This is also true for Process A and B where the GP is below the CS. Referencing Fig. 3.13, only a small fraction of the fields of significant magnitude reach the SiN_x layer (magnetic field is shown, but electric field profile is almost identical outside of the CS

and GP). Therefore, for MTL widths and process geometries, $\Gamma_{\mathrm{SiN_x}} \gg \Gamma_{\mathrm{TEOS}}$, and therefore is ignored in the remainder of this work.

Table 3.2 shows the effective geometric factor Γ_{c0} decreased 5% for actual geometry and further decreased by 2% when floating fill was introduced. This change is primarily due to the large change in geometry of the GP (Γ_{GP}) having thickness half of nominal and the dielectric thickness $\approx 8\%$ thinner whereas the CS geometric factor Γ_{CS} was almost unchanged.

Due to $\approx 8\%$ change in dielectric separation thickness both G and C changed by $\approx 8-10\%$. When fill was introduced, both G and C increased by $\approx 36-38\%$, due to the removal of dielectric replaced by metal fill. Both G and C changed the same way and therefore the dielectric geometric factor Γ_{d0} was almost unchanged. Although, the notable increase in C by about 36% and almost no change in L will considerable decrease the data propagation velocity by about 15% where $v_p \propto (LC)^{-1/2}$. This result is relevant for synchronous clock timing designs where the interconnect inductance and capacitance across long distances need to be meet required values, and fill patterns around the interconnect can have a notable affect.

Table 3.2: Table of $RLCG$ for three different HFSS simulations shown in Fig. 3.16 using geometry measured from Fig. 3.15 fabricated using *Process A* (see Table 4.1). The material properties used for all three simulations are $R_{s0} = 20\mu\Omega$, $\lambda = 90\,nm$, $\varepsilon_{TEOS} = 4.5$, $\tan \delta_{TEOS} = 1 \times 10^{-3}$, $\varepsilon_{SiNx} = 7.5$, and $\tan \delta_{SiNx} = 1 \times 10^{-4}$.

Process A, w=250 nm	Nominal	Actual	Actual+Fill	Actual % Difference From Nominal	Actual+Fill % Difference From Actual
R (kΩ/m)	8.47	8.69	8.80	-2.62	-1.30
L (nH/m)	585.60	574.60	571.60	1.88	0.53
G (mS/m)	143.65	155.50	214.13	-8.25	-37.71
C (pF/m)	205.60	225.60	307.00	-9.73	-36.08
Γ_{GP} (mΩ)	65.90	48.17	48.20	26.90	-0.07
Γ_{CS} (mΩ)	9.93	9.95	9.72	-0.23	2.27
Γ_{c0} (mΩ)	8.63	8.25	8.09	4.41	1.88
Γ_{TEOS}	0.90	0.90	0.90	-0.74	0.45
Γ_{SiN_x}	8.75	9.43	9.05	-7.85	4.04
Γ_{d0}	0.81	0.83	0.82	-1.37	0.77

Overall, measuring $RLGC$ sensitivities to fill showed that geometric factors are fairly insensitive and can be approximately ignored. However, propagation velocity is sensitive to fill placement and geometry and should be taken into consideration. The method described here can be used to check the change in propogation velocity for a given fill geometry. Most importantly, the largest changes in $RLGC$ and Γ were seen in the difference between nominal (expected) cross sectional geometry and as fabricated (measured by STEM). In the next section, we will do a sensitivity analysis on MTL geometries.

3.7 MTL Γ Sensitivity to RQL Fabrication

This section will discuss how $RLGC$ parameters (see Eq. 3.2-Eq. 3.5) and resonator geometric factors (see Eq. 3.9-Eq. 3.10) in MTLs vary at parametric corners of the fabrication process (see Fig. 4.1). A simple sensitivity analysis will be presented to get a sense of (i) the precision of extracted R_{s0} from measurements in Chapter 4 (ii) the application of this method to determine sensitivity to fabrication variation. This procedure can be used for any arbitrary two port transmission line cross-sectional geometry (e.g. coplanar wave guide, strip line, etc).

Table 3.3(a) shows the nominal parameters for the fabrication of samples from *Process A*, *B*, and *C* (see STEM summary table Fig. 3.1). Table 3.3(b) are the assumed minimum to maximum variations of the fabrication/material parameters. These parameters were inserted into HFSS as parametric variables to calculate variations in Γ and $RLGC$ using methods described in Section 3.3.4 and Section 3.5.

Table 3.3: Tables showing a) the nominal material properties and simulation lengths, and b) the minimum, nominal, and maximum values chosen as the parametric corners based off fabrication variation worst case scenario.

Nominal Material Properties & HFSS Static Inputs

a)

R_{s0}^{CS}, R_{s0}^{GP} ($\mu\Omega$)	$\lambda_L^{CS}, \lambda_L^{GP}$ (μm)	TEOS ε_r	SiN$_x$ ε_r	TEOS $tan\delta$	SiN$_x$ $tan\delta$	l_{hfss} (μm)	l_{pec} (μm)	f_{HFSS} (GHz)
20	0.09	4.5	7.5	1.00E-03	1.00E-03	5	1	10

MTL Cross-Sectional Geometry Nominals & Parametric Corners

b)

Parameter	w (μm)	λ_L^{CS} (μm)	λ_L^{GP} (μm)	d^{CS} (μm)	d^{GP} (μm)	s (um)
Min	-0.1	0.08	0.08	0.17	0.17	0.12
Nominal	0.25, 0.5, 1, 2, 4	0.09	0.09	0.20	0.20	0.15
Max	+0.1	0.12	0.12	0.23	0.23	0.18

Fig. 3.17 shows the percent variation of the geometric factor Γ_{c0} is roughly $\pm 20\%$ for

all CS widths shown. The 0.25 μm has an additional $\pm 2\%$ variation. These are conservative estimates for *Process A*, *B*, and *C* based off worst case geometry variations shown in Table 3.3(b). Aside from the ground plane thickness offset in *Process A*, the summary Table 3.1 from STEM measurement show the variations in thicknesses do not exceed 10%. Although, these are critical dimension (CD) measurements on single chips and are not representative of the whole wafer or lot of wafers. Thickness uniformity and line width targeting at minimum feature sizes are one of the many challenges in fabrication. Therefore, a worst case 20% variation in Γ_{c0} will be incorporated as error in our extraction of R_s from measurements in Chapter 4.
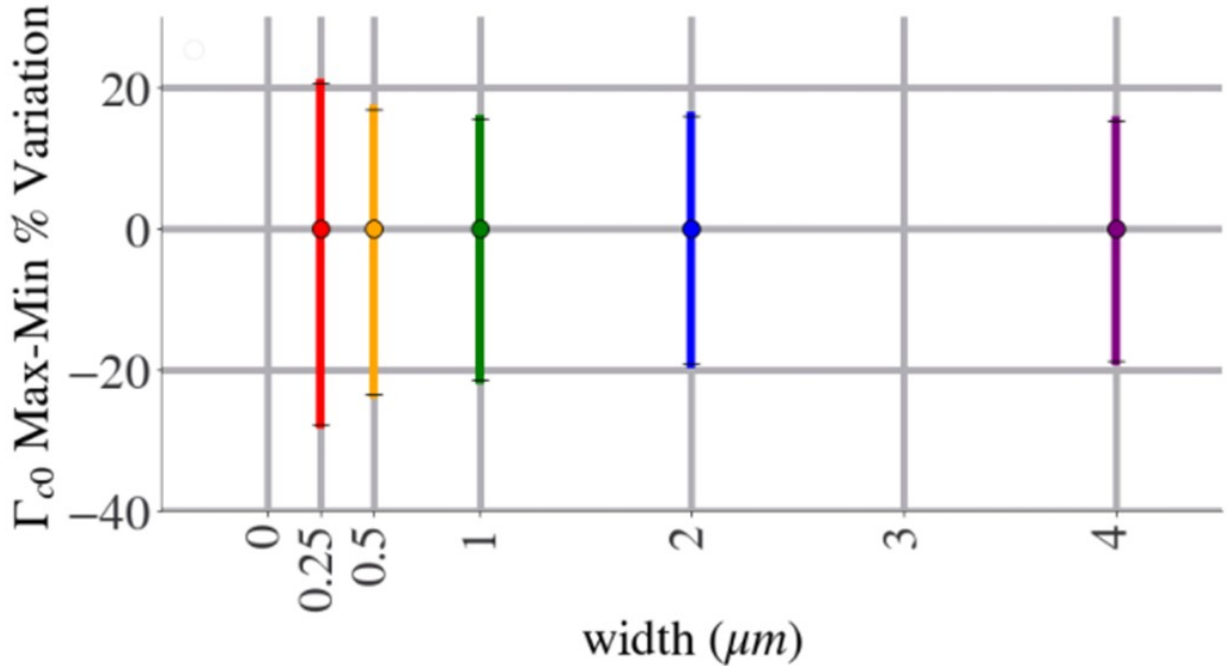
Figure 3.17: Parametric Corners to show worst case max/min error in Γ_{c0} for MTL widths $0.25 - 4\,\mu m$. This is assuming nominal geometry from Table 3.3(a) and worst case cross section geometric variation in Table 3.3(b), based off fabrication tolerances.

The variation in Γ, or Q_c assuming a constant R_s, can be further scrutinized by doing a sensitivity analysis on each parameter contributing to changes in $RLGC$. Fig. 3.18 shows $RLGC$ % change as a function of the parameter % change for a 0.25 μm MTL starting at

nominal geometry Table 3.3(a). Note, R_s and $\tan \delta$ were held constant in Fig. 3.18 shows $RLGC$, and therefore any variations in Q_c or Q_d are variations in the geometric factors exclusively. Immediately, it can be seen from Fig. 3.18(f) that Γ_d is insensitive to all parameter variations. This is expected for an MTL embedded in a homogeneous dielectric, as the material property $\tan \delta$ is geometry independent. If phase velocity sensitivity to fabrication variation is desired ($v_p \propto (LC)^{-1/2}$), then the L and C sensitivities can be simply multiplied from Fig. 3.18(a)-(b). Here, the discussion will be focused on Γ_c sensitivity to fabrication variation.

The conducting strip (CS) magnetic penetration depth λ_{CS} varies L and R by as much as $\pm 10\%$, but change in the same way and therefore Γ_c (Q_c with constant R_s) is insensitive to λ_{CS}. Interestingly, Γ_c can change by 3% for -30% change in λ_{GP}. This is most likely due to magnetic field becoming more concentrated in and around the CS (see Fig. 3.13). Evidently, this suggests Γ_c is relatively insensitive to changes in λ.

The most surprising result is Γ_c is most sensitive to thickness variations in the conducting strip d_{CS}. The L maximum change is $\pm 6\%$, whereas the R can change by as much as $\pm 12\%$. The lower L sensitivity to d_{CS} is most likely due to the internal inductance term only being one of two contributions to the total inductance (see 3.3). Whereas R is completely defined by λ (current distribution inside wire), and is greatly affected when the CS (or film) thickness is on the order of the $\lambda \approx d_{CS}$, i.e. $\lambda_{eff} = \lambda \coth (d/\lambda)$. This argument can also explain Γ_c secondary sensitivity to MTL widths w_{bottom} and w_{top}. Although, Γ_c has a slightly lower sensitivity to w_{bottom} relative to w_{top}. The dielectric separation thickness s can vary Γ_c by $\pm 5\%$, as this can significantly change the current distribution and fringing fields.

Using HFSS simulations and the methods described here, it has been determined Γ_c can vary as much as $\pm 20\%$ for MTL widths $0.25 - 4 \ \mu m$. A sensitivity analysis on a 0.25 μm
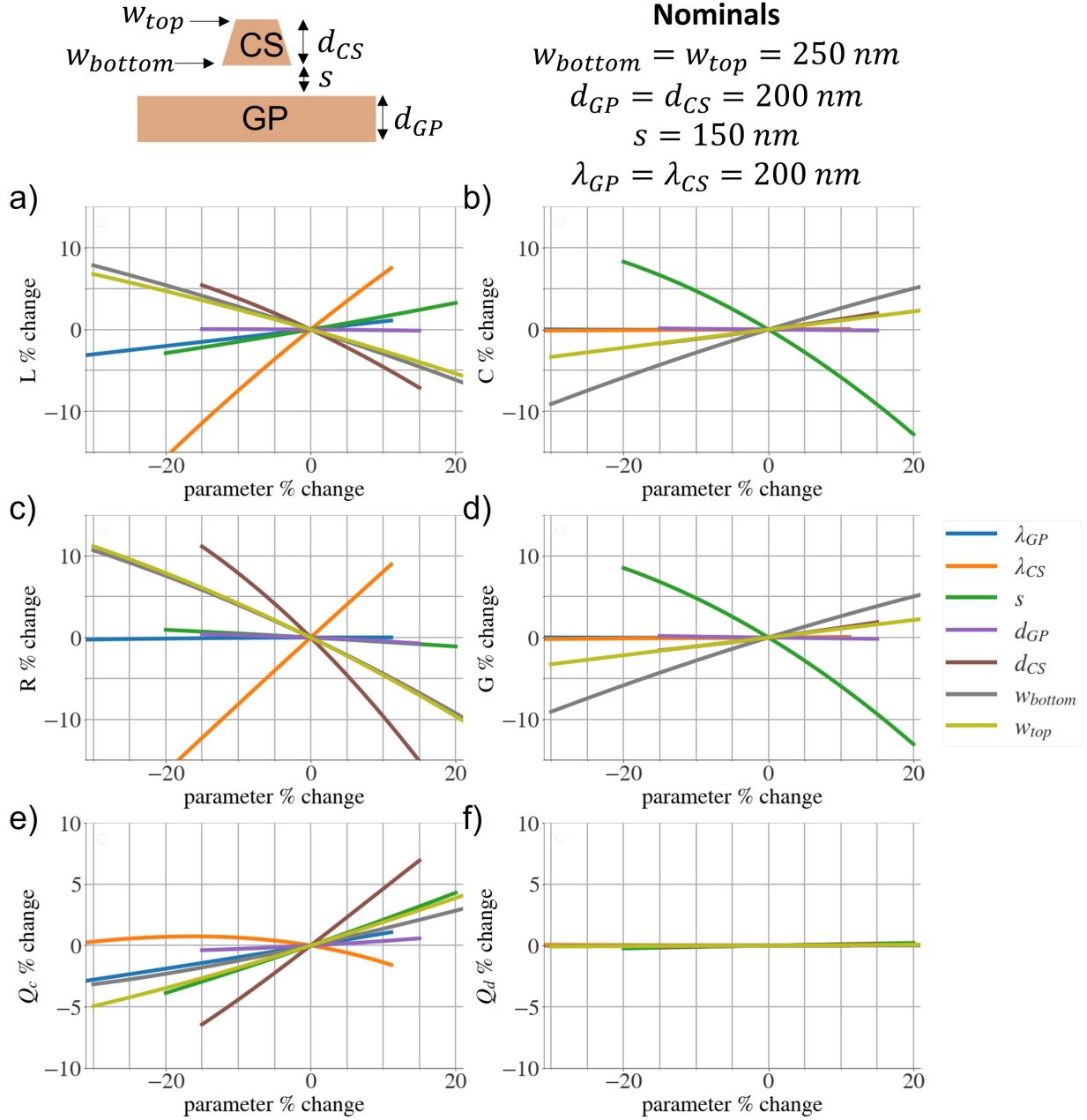
Figure 3.18: $RLGC$ Sensitivity Analysis on MTL minimum width $0.25\ \mu m$ as well as the % change in Q_c and Q_d (see Eq. 3.1 and Eqs. 3.2-3.5). The Nominal geometry shown in Fig. 3.12, where w_{bottom} and w_{top} are the dimension closest and furthest from the ground plane (GP), respectively. The absolute parameter ranges can be found in Table 3.3.

with trapezoidal geometry suggests Γ_c is most sensitive to the conducting strip thickness d_{CS}, s, w_{bottom}, and w_{top}. This analysis affords us the ability to bound our error in extracted R_s from measurement in Chapter 4 and Chapter 5.

100

3.8 Summary

In this chapter, I discussed the importance of numerically solving inside a lossy superconductor, and reviewed the work that has been done thus far. I presented a method to extract the intrinsic superconductor and dielectric RF losses coupled with HFSS modeling.

I discussed the morphologies (non-idealities) in Nb-TEOS 0.25 μm and 1 μm MTLs from *Process A*, *B*, and *C* were study using STEM and EDS. For the damascene *Process A* and *B*, line defects and voiding occur at the edge of the fill trenches, quintessential to the sputtered fill step in damascene processes. These defects occur in a region of highest magnetic field (current density) concentration for *Process A*. For *Process A* and *B*, up to 1at% Ar was detected inside of the conducting strips. No Ar was detected in MTLs from *Process C*. *Process A* shows a total Nb oxide layer approximately 10 nm with 5 nm layer of $NbO - NbO_2$. *Process B* shows the same total Nb oxide thickness of approximately 10 nm, but no stable oxide was detected. *Process C* shows no detectable Nb oxide layer due to the incorporated SiNx/Al passivation layer.

I presented a method to deconvolve the partial Q factors $Q_c \equiv \Gamma/R_s$ from the superconductor and $Q_d = 1/\tan\delta$ from the dielectric by relying on their respective dispersion relationships. To extract the intrinsic resistance R_s from Q_c, I presented a procedure using HFSS to calculate the geometric factors Γ numerically. The HFSS procedure was validated by comparing to analytical models and other work. The geometric factor is insensitive to the surrounding fill patterns used in *Process A*, *B*, and *C*. The geometric factor is notably sensitive to primarily the conducting strip thickness, interlayer dielectric thickness, and the conducting strip width, but is not sensitive to the magnetic penetration depth. The conservative error in Γ_c will be bounded to $\pm 20\%$.

Chapter 4:   Characterization of Microwave Loss in RQL Interconnects at 4.2 K

In the previous chapter, non-idealities in the morphology were measured in TEM/EDS, and could be causing added extrinsic resistive losses in Nb interconnects. The geometric factor methodology and solving numerically in HFSS was established as a means to accurately extract the intrinsic resistance R_s from measurements of the partial conductor Q-factor Q_c. This enables the ability to compare R_s across processes A, B, and C for all MTL widths.

In this chapter, a brief history on Q-factor measurements in different systems and assumptions will be presented in the introduction. The MTL resonator design will then be described, followed by the measurement and fitting method to measure the internal Q-factor Q_i. The Q_i can then be deconvolved in the dielectric Q_d and conducting Q_c partial Q-factors by relying on their respective dispersive relationships. The analysis of data will be presented using two different models. The non-dispersive model and analysis will show a clear difference in R_s between the three processes and a nearly constant $\tan \delta$ for all samples measured. The dispersive model is difficult to confirm or deny, but there is some agreement found with previously measured results and fundamentals expectations. In the discussion section, the morphology characterization and HFSS simulations will then be reference to help explain the difference between the three processes.

4.1 Introduction

As said before, resonator remains the only practical way to accurately measure R_s [131], [62] and $\tan\delta$ [100, 132] at microwave frequencies. Because Q_c^{-1} and Q_d^{-1} are additive, the two losses are inseparable. Hence, existing resonant measurement techniques exploit regimes where the net Q-factor is dominated by either the superconductor or dielectric loss. The former case with $Q_c \ll Q_d$, favors the measurements of R_s. The latter case with $Q_c \gg Q_d$, favors the measurement of $\tan\delta$. Tuckerman *et al.* take advantage of the condition $Q_c \gg Q_d$ to measure $\tan\delta$ of Nb-polyimide flexible transmission line tapes at 2 K [100]. Dielectric measurements by Krupka *et al.* optimize their resonant cavity design to satisfy the condition $Q_c \gg Q_d$ and measure the dielectric loss tangent [132],[173]. Oates *et al.* Q-factor measurements on Nb-SiO$_2$ sub-micron stripline resonators show they are limited by dielectric loss except for the narrowest strips, but they do not report measurements of $\tan\delta$ or R_s [174]. Superconducting cavities measure R_s under circumstances where $Q_c \ll Q_d$ [165], [175]. Taber overcomes the above limitations by varying the geometric factor (dielectric thickness) of the parallel plate resonator [136], [70], and extracts both R_s and $\tan\delta$, but his approach is impractical for characterization of superconducting integrated circuits if one wants to deconvolve losses in a single structure and measurement. To measure the frequency dependence of $\tan\delta$ of thin film dielectrics commonly used as Josephson Junction barriers, Kaiser *et al.* neglects the metal loss by making use of lumped element LC resonators satisfying the condition $Q_c \gg Q_d$.

In contrast with most prior work, to measure R_s and $\tan\delta$, I designed and tested microstrip transmission line (MTL) resonators having comparable superconductor and dielectric losses such that $Q_c \approx Q_d \approx 1000$. To be sensitive to Q_c and Q_d, the MTL was designed into fabrication

Process A, *B*, and *C* with multiple resonances and sensitive to intrinsic Q-factor Q_i. In this chapter, I compare the extract R_s and $\tan \delta$ from measurements of the frequency dependent internal Q-factor $Q_i(\omega)$ for MTL widths 0.25-4 μm. I was most interested in analyzing R_s MTL width dependence and difference between *Process A*, *B*, and *C*, and seeing how R_s correlated with morphology measured by STEM and EDS in Chapter 3.

4.2 Resonator Design

To implement the proposed concept, we designed a chip with five open-ended half-lambda MTL resonators shown in Fig. 4.1. The conducting strip width varies from 0.25 to 4 μm. Each 15 mm long resonator was folded into meander shape to preserve space. Each resonator is reactively coupled to a 50 Ω feedline via a coupling capacitor C_c. Via walls were placed about ten dielectric thicknesses ($\approx 10s$) away from the edge of the conducting strip, to reduce cross-talk between two adjacent resonator meander sections (see STEM cross-section in 3.15).

The method to deconvolve $\tan \delta$ and R_{s0} can be found in Section 3.3. In this section, deconvolution will be demonstrated by comparing extracted RF losses for two damascened *Process A* and *Process B*) and a cloisonné *Process C*. Results are summarized in Table 4.1).

4.2.1 Resonant Frequency

MTL resonators support a TM_{00n} [59] mode with the eigen frequency

$$f_n = \frac{n}{2l_{res}\sqrt{LC}} \approx \frac{nc}{2l_{res}\sqrt{\varepsilon_r}\sqrt{1 + 2\lambda \coth(d/\lambda)/s}} \tag{4.1}$$

Table 4.1: Results summary of Extracted R_s and $\tan\delta$ from *Process A*, *B*, and *C*. The MTL resonator measurements were done at 4.2 K and are shown in Fig. 4.5. A homogeneous MTL, with $\lambda = 90\ nm$, and a non-dispersive $\tan\delta$ were assumed.

Process	Nb/TEOS CMP	Ground Plane	Geometry	Number of Wafers Measured	Number of Chips Measured	R_{s0} $(\mu\Omega)$ $w = 0.25\ \mu m$ $\Gamma_{c0}^{PP}/\Gamma_{c0}^{MTL}$	$\tan\delta$ $w = 0.25\ \mu m$	λ $\lambda_{GP} = \lambda_{CS}$
A	Nb	Above Wire	GP / CS	1	7	40/30 $\pm 20\%$	1.2×10^{-3}	90
B	Nb	Below Wire	CS / GP	2	6	25/20 $\pm 20\%$	1.2×10^{-3}	90
C	TEOS	Below Wire	CS / GP	2	9	17/14 $\pm 20\%$	1.2×10^{-3}	90
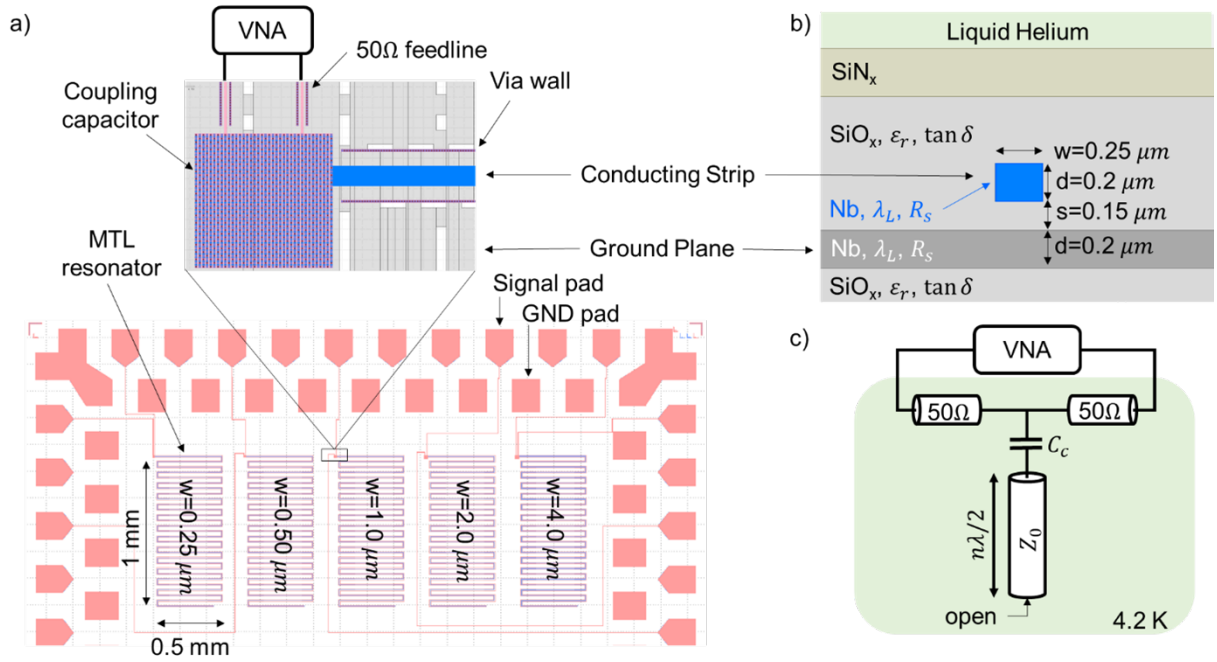
Figure 4.1: a) Physical layout of five MTL resonators of varying widths w showing (bottom) contact pad arrangement, feedline wiring to C_c, and resonator meander geometry taking up chip area $\approx 0.5 \times 1mm^2$. The (Top) of a) is a zoom in of how the VNA makes connections to the feedline, followed by the coupling capacitor C_c connection to the MTL. This also shows the via walls that serve as isolation for the feedlines and MTL conducting strips. b) A cross-section of fabrication process showing the nominal critical dimensions of a two metal layer process: the ground plane (dark gray), conductiong strip (blue), surrounding TEOS dielectric (light gray), and SiNx passivation layer (gold). c) Representative diagram of the open ended MTL resonator connected to C_c, 50 Ω feedline and VNA

where $n = 1, 2, 3\ldots$ is the mode index, l_{res} is the geometrical length of the resonator, and L and C are the conducting strip series inductance and shunt capacitance per unit length defined by Eq. 3.3 and 3.5. The approximation on the right in Eq. 4.1 holds for a wide MTL where the width is much greater than the dielectric thickness ($w \gg s$) [70], where c is the speed of light, and ε_r is the dielectric constant. The resonator frequency was designed based upon the nominal material properties (ε_r, λ) and the fabrication process thicknesses (s, d). The selection of l_{res} was a trade-off between placing many resonators on a single $5 \times 5 \, mm^2$ chip, and a convenient frequency range to measure multiple resonant modes using a vector network analyzer (VNA) while avoiding the standing-wave ripple due to impedance mismatch. For a resonator length of $l_{res} = 15 \, mm$ the fundamental mode resonant frequency $f_1 \approx 3.27 \, GHz$. The average mode 1 index resonant frequency for *Process C* $w = 4 \, \mu m$ resonators $f_1 = 3.2 \pm 0.07$ GHz and is within 0.8% of wide MTL estimate using Eq.. 4.1, and this agreement supports our nominal $\lambda \approx 90 \, nm$ [54] and $\varepsilon_r \approx 4.2$ [73].

4.2.2 Critical Coupling

To overcome parasitic ripple seen in the transmission coefficient $|S_{21}|$ in Fig. 4.4(a), which is caused by inevitable impedance mismatch within the dip probe, we tune the coupling between the resonator and feedline to provide about $6 \, dB$ insertion loss (IL) at the resonant frequency. For a reactively coupled resonator this corresponds to critical coupling, $Q_i = Q_e$, where Q_e is the external (coupling) Q-factor.

The feedline is directly connected to the top plate of the coupling capacitor while the MTL resonator is directly connected to the bottom plate. The C_c value is tuned to reach a critical

coupling g=1 using the following equation [176]

$$g = \frac{R}{2Z_0} = \frac{1 - |S_{21}|}{|S_{21}|} = \frac{Q_i}{Q_e} = 1 \qquad (4.2)$$

where g is the coupling factor, R and Z_0 are the series resistance and characteristic impedance of the MTL resonator, $|S_{21}| = 10^{-IL/20}$ with IL being the insertion loss at resonance in dB, Q_i is the resonator internal (or intrinsic) Q-factor, and Q_e is the resonator external (or coupling) Q-factor. The input impedance Z_{in} looking into a coupling capacitor towards a resonator is [95]

$$Z_{in} = \frac{\pi Z_0}{2Q_i b_c^2}; b_c = \omega C_c Z_0 \qquad (4.3)$$

where ω is the angular frequency. Converting the $ABCD$ transmission matrix for a shunt admittance $Y = Z_{in}^{-1}$ into respective S_{21} gives [95]

$$S_{21} = \frac{2Z_{in}}{2Z_{in} + Z_{feed}} \qquad (4.4)$$

where Z_{feed} is the feedline characteristic impedance. Assuming a parallel plate geometry ($w \gg s$) and thick plates ($d \gg \lambda$), the MTL characteristic impedance can be estimated $Z_0 = \sqrt{L/C} \approx \sqrt{\mu_0(s + 2\lambda_{eff})/(\varepsilon_0\varepsilon_r s)}$. Eq. 4.4 can be used to calculate the C_c needed to achieve the desired coupling factor g to a resonator with a given Q_i, characteristic impedance Z_0, and resonant frequency f_0 [95]

$$C_c = \left(\frac{1}{2\pi f_0}\right) \sqrt{\frac{2\pi g}{Z_{feed}Q_i Z_0}} \qquad (4.5)$$

Using Eq. 4.5 and the following parameters expected for a 4 μm conducting strip resonator $f_0 = 3$ GHz, $Q_i = 685$, $Z_0 = 8.6$ Ω, and $Z_{feed} = 50$ Ω gives a $C_c = 245 fF$ to critically couple the resonator and achieve an $IL \approx 6$ dB. The measured $IL \approx 6$ dB for this geometry giving $g \approx 0.7$, which means the resonator is under coupled and the measurement is sensitive to material losses. Error is most likely due to variations in the feedline and resoantor characteristic impedance due to fabrication. Fig. 4.2 shows four different coupling strengths for a 0.25 μm MTL resonator. Each color is data averaged over 2 wafers and 9 chips (see Table 4.1. Each symbol is a different mode index of the MTL resonator (see Fig 4.4). Fig. 4.2(a) shows the extracted Q_i for each coupling design (colors) overlay fairly well with the 12 GHz modes having the most spread. Fig. 4.2(b) shows Q_i for calculated coupling factor g from measurement of IL (see Eq. 4.2). Similar calculations are found when taking the ratio of Q_i/Q_e within 15%. This data suggests the extracted Q_i for all coupling designs are equal with error from wafer spread, and confirms our extraction method is valid and is fairly insensitive to coupling strength up to $g = 3$.

Hence, the coupling capacitor design targets the following value

$$C_{crit} = \frac{1}{2\pi f_1} \sqrt{\frac{2\pi}{Z_{feed} Q_i Z_0}} \tag{4.6}$$

where f_1 is the fundamental resonant frequency given by Eq. 4.1, $Z_{feed} = 50\Omega$ is the characteristic impedance of the feedline, Q_i is the internal quality factor of the resonator that can be estimated from Eq. D.11, and Z_0 is the characteristic impedance of the MTL resonator. The characteristic impedance can be estimated using Eq. D.8 assuming a parallel plate transmission line geometry or simulated in HFSS as described in Chapter 3. In this MTL design, the C_c varies from $50 - 250 fF$
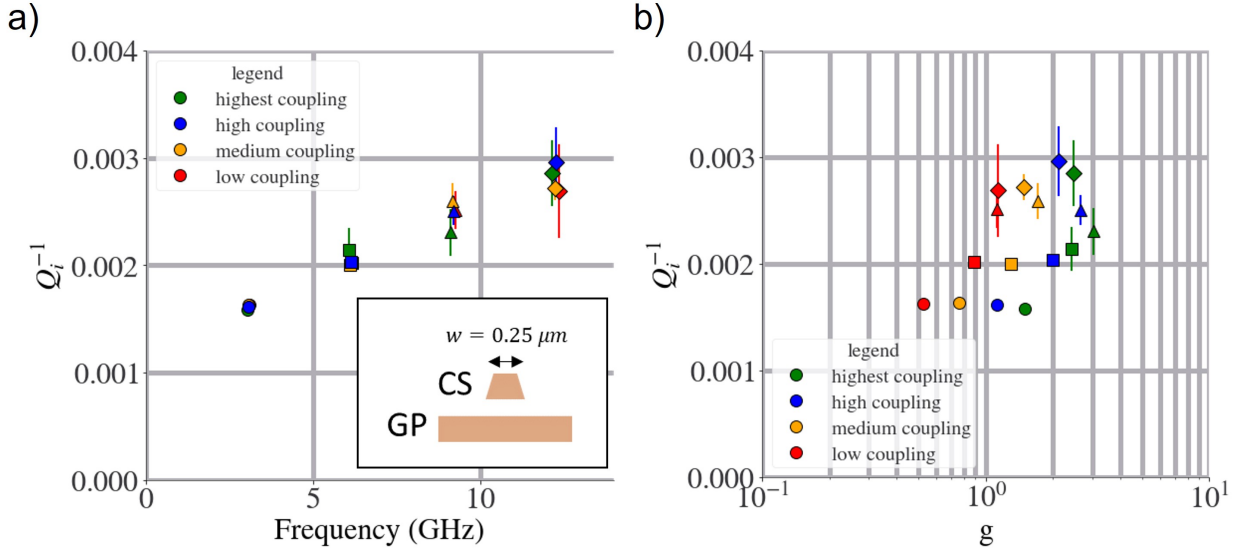
Figure 4.2: Demonstration of the coupling design on a 0.25 μm MTL resonator design showing fitted Q_i on four resonant modes for four different couplings as a function of a) resonant frequency (or mode index), and b) the coupling factor g (see Eq. 4.2). The measurement method is described in Section 4.3. Representative $S_{21}(\omega)$ data and Q_i fitting can be seen in Fig. 4.4. These measurements are on samples fabricated using *Process C* taken at 4.2 K

for MTL $w = 0.25 - 4 \ \mu m$, respectively.

A plaid capacitor design (see Fig. 4.1(a)) was used for the coupling capacitors. This capacitor design enabled the fabrication of large capacitors in a damascene process, where wide metal patches are disallowed to minimize under (over) etching of low (high) metal density during CMP. The capacitor is composed of multiple parallel lines (with minimum allowed spacing) in one metal layer and many more in adjacent metal layer, running perpendicular to the lines in the first layer. The two metal layers are separated by TEOS of thickness s. Every other line in each layer are connected with vias thus creating two interwoven (plaid) electrodes. While the structure complies with design rules that limit wire width and metal density it exhibits electrical performance of a parallel plate capacitor; it has low parasitic inductance and approximately the same capacitance (within $\approx 30\%$) per unit area.

4.3 Measurement

Chips were selected within the inner 80 mm diameter of 150 mm wafers (see Fig. 4.3). The number of chips and wafers measured from each *Process* can be found in summary Table 4.1. Measurements were taken at $4.2\ K$ with a cryogenic, RF dip probe outfitted with a 32 pin (contact pad) test fixture. The same test fixutre was used in previous works [35], [34], [36], [10]. To achieve RF signal integrity and avoid wire bonding for fast sample chip exchanges, a non-magnetic Cu/Au flip chip press contact technology is used. The fixture PCB connects the flip-chip bump pads to the probe .047 inch semi-rigid coaxial cables. The chip and roughly $30\ cm$ of the cables are submerged in L-He bath during measurements. The temperature was monitored with a calibrated Lakeshore Cernox sensor. The resonators were measured by 2-port S-parameters using a Keysight N5222A vector network analyzer (VNA). The network analyzer was calibrated up to the top of the probe.

Typical measurements were taken over $2-14\ GHz$ frequency span with $200\ kHz$ spacing with input power $\approx -20\ dBm$ to minimize possibility of non-linear effects. The probe usable bandwidth accommodates resonant modes up to $n = 4$. Measurements above $14\ GHz$ are dismissed due to the standing-wave Q-factor becoming comparable to the resonance Q-factor. Fig. 4.4(a) shows the first four resonant modes for each MTL width w. From the complex S-matrix circle fits (see Fig. 4.4(b), the Q_i, Q_e, and f_n are found using the methodologies described in [177, 178], where the Q-factors are related to the loaded Q-factor by $Q_L^{-1} = Q_i^{-1} + Q_e^{-1}$ in the complex plane. The first mode fitting for each width is shown in Fig. 4.4. Measurements shown in Fig. 4.4 were taken across 4 wafers and a total of 22 chips (5 MTLs per chip). All resonances from 2-14 GHz were detected, fitted, and analyzed using a custom Python script.
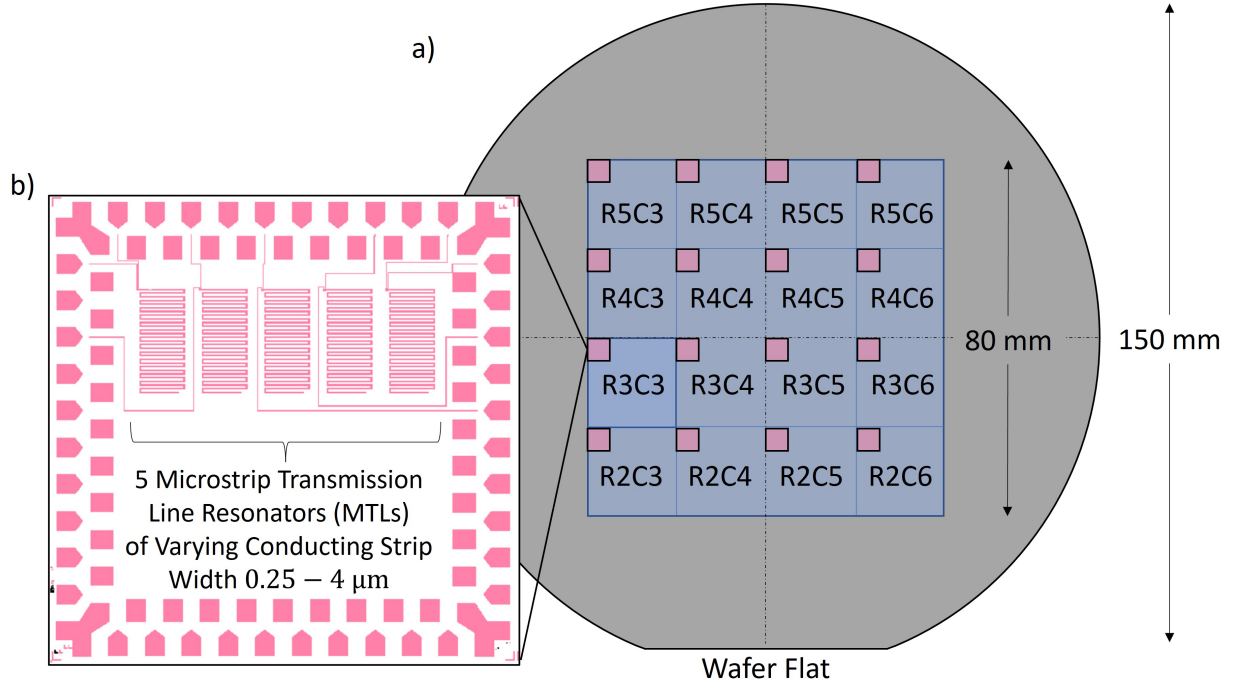
Figure 4.3: Wafer Map Diagram used for all three *Processes* showing (a) the 16 mask reticles (blue) and the chip (pink) fabricated with the resonator chips. (b) A zoom in of the MTL resonators chip (see Fig. 4.1) for more details on chip layout and design. All measured chips from *Process A*,*B*, and *C* were picked from the inner 80 mm diameter of 150 mm wafers shown here.

4.4 Method Demonstration

The statistical mean and standard deviation for all modes, conducting strip widths, and fabrication processes are shown in Fig. 4.5. The increased spread in Q_i^{-1} for $n = 3, 4$ is due to the fitting error due to standing wave ripples and reduced measurement repeatability. A separate gauge study was performed by installing, testing, and re-installing the same chip 4 times and yielded max percent variations in extracted Q_i and f_n to be $< 10\%$ and $< 0.1\%$, respectively.

From Fig. 4.5, it can immediately be seen that *Process A* has larger slopes for all conducting strip widths relative to *Process B* and *Process C*, and most convinently seen in Fig. 4.5(f). Using Eq. 3.16, a larger slope A yields an approximately larger intrinsic resistance assuming the slope is

111
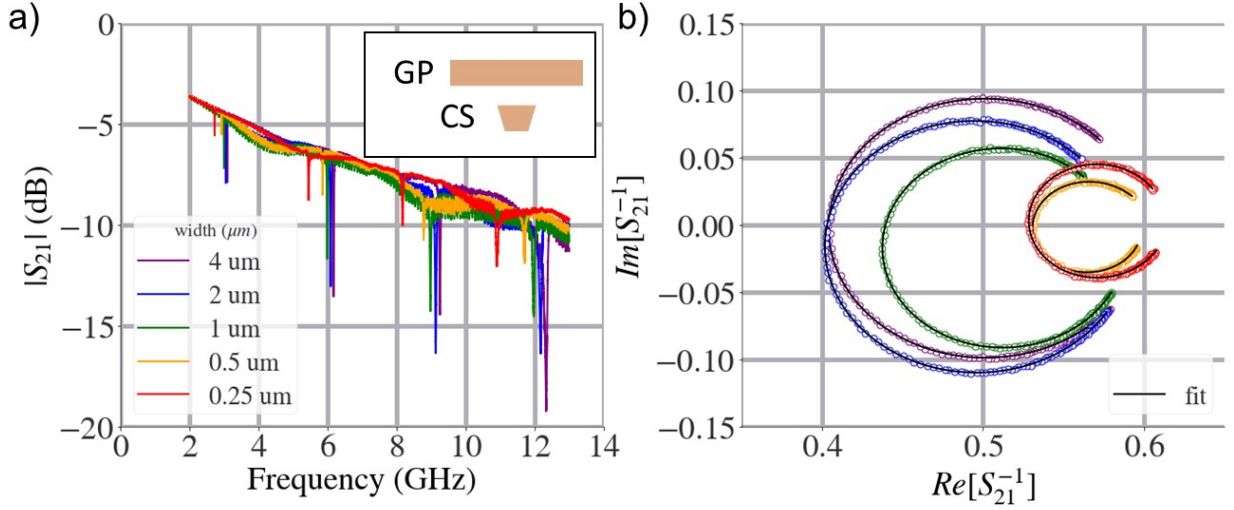
Figure 4.4: Data for a chip from center of the wafer fabricated using process *Process A*. (a) Insertion loss versus frequency for modes $n = 1 - 4$ on MTL widths $0.25 - 4\,\mu m$ at 4.2 K. (b) Complex circle fitting of the fundamental mode resonant peaks from (a) using methodology from [177, 178].

exclusively and the equal geometric factors between each process. The linear dependence of Q_i with frequency ω in Fig. 4.5 supports the inclination that Eq. 3.15 is valid, but will be scrutinized in section 4.4.2. At the the same time, for lines $1\,\mu m$ and narrower *Process B* has relatively higher R_s relative to *Process C*, while for the 2 and $4\,\mu m$ lines *Process B* and *Process C* have nearly the same superconductor loss. It is also evident from Fig. 4.5 that all MTL widths and processes yield roughly the same linear y-intercept, which is related to the dielectric loss $\tan\delta \approx 10^{-3}$. Although, this is all assuming the ground plane and conducting strip have the same intrinsic resistance R_s, a non-dispersive $\tan\delta$, and the same geometric factors between each process.

The fitted linear slope using Eq. 3.15 from Fig. 4.5 as a function of process and MTL width is shown in Fig 4.6. For reference, the analytical geometric factor assuming a parallel plate model Γ_{PP} (solid black line) is also shown calculated using Eq. 3.16 with nominal dimensions shown in the parallel plate MTL diagram. Primarily for processes A and B, the slope A is approximately
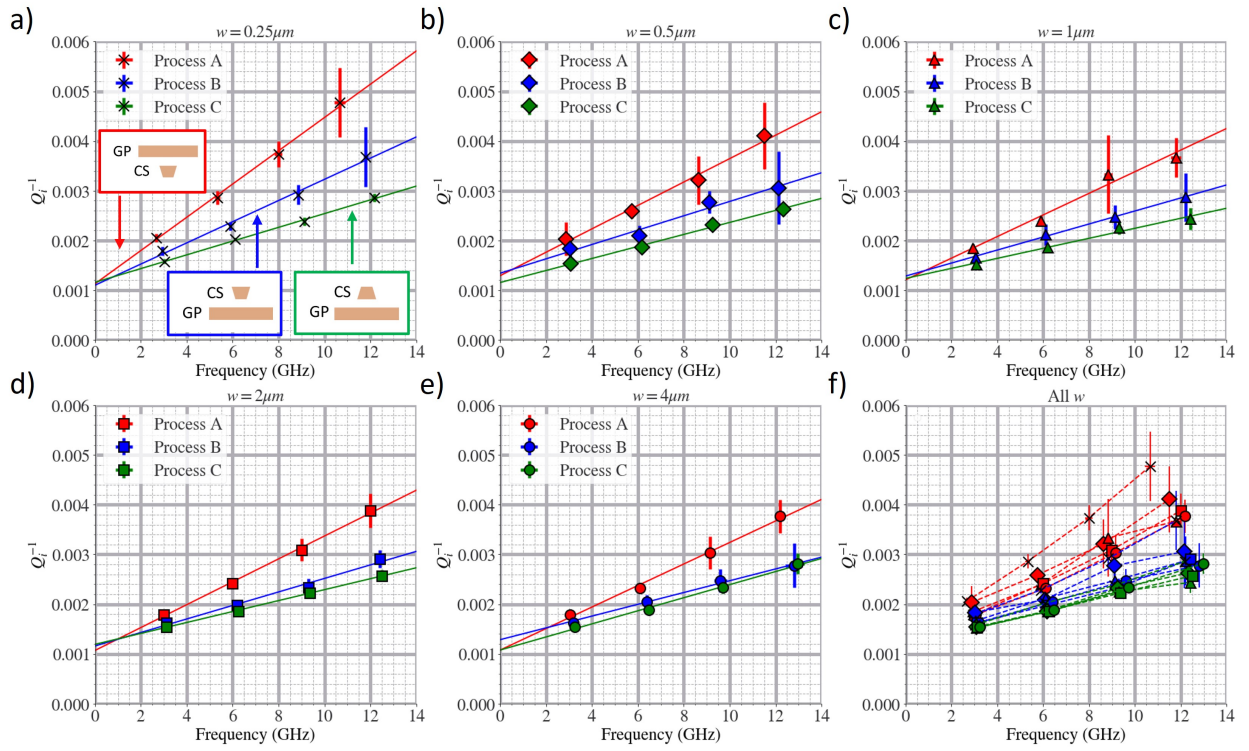
Figure 4.5: The reciprocal internal Q-factor Q_i^{-1} at 4.2 K as a function of the resonant frequency for each of the five MTL widths and for three fabrication processes. The bottom right graph is five linewidths and processes plotted together.

constant for MTL widths $1 - 4\ \mu m$. A noticeable upturn in A can be seen for MTL widths 0.25 and $0.5\ \mu m$ for processes A and B. Additionally, the y-offset of $\approx 1.5 \times 10^{-14}\ Hz^{-1}$ between process A and B is a strong indication the intrinsic resistance is larger for process A with respect to process B. Furthermore, process C has a near MTL width independent slope A and $\approx 1 \times 10^{-14}\ Hz^{-1}$ lower A at MTL width $0.25 \mu m$ with respect to process B. Empirically, it can be concluded that process C has a lowest conductive loss and does not have a width dependence. Although, accurate conclusions about the intrinsic resistance R_s cannot be drawn due to the convoluted width dependence of MTL geometric factor Γ_{c0} found from HFSS simulations in Chapter 3. As an example of the worst case scenario, without knowing the cross-section of the MTL fabricated it can be conceivable the differences between process B and C are completely due to geometry differences as opposed to the intrinsic resistance R_s.

Utilizing the methods and procedures described in Chapter 3 as well as the measurements of cross-section dimensions from TEM and FIB, the geometric factors were numerically solved in HFSS and are plotted in Fig. 4.7. Similar to Fig. 3.14 for nominal cross-sectional geometries, Fig. 4.7(a) shows Γ_{c0} solved for the as measured cross-sections. The solid black line is referenced for the nominal geometries. Errors are calculated between measured relative to nominal and can be seen in Fig. 4.7(b). Process A and B have percent errors increasing from of approximately 3-6% as the MTL width is reduced from 4 to 0.25 μm, respectively. Process C has an almost consistent error for MTL widths 0.5-4 μm of -2%, but increase up to 6% for 0.25 μm (delta of 8%). Referring to the STEM summary Table 3.1, maximum error (variation) of 8% in Γ_{c0} correlates fairly well to the maximum dimension variation of approximately 7-9% of the dielectric thickness. From an engineering and fabrication perspective where targeting consistent critical dimensions is important, 8% variation is manageable and is a good result confirmed by HFSS.
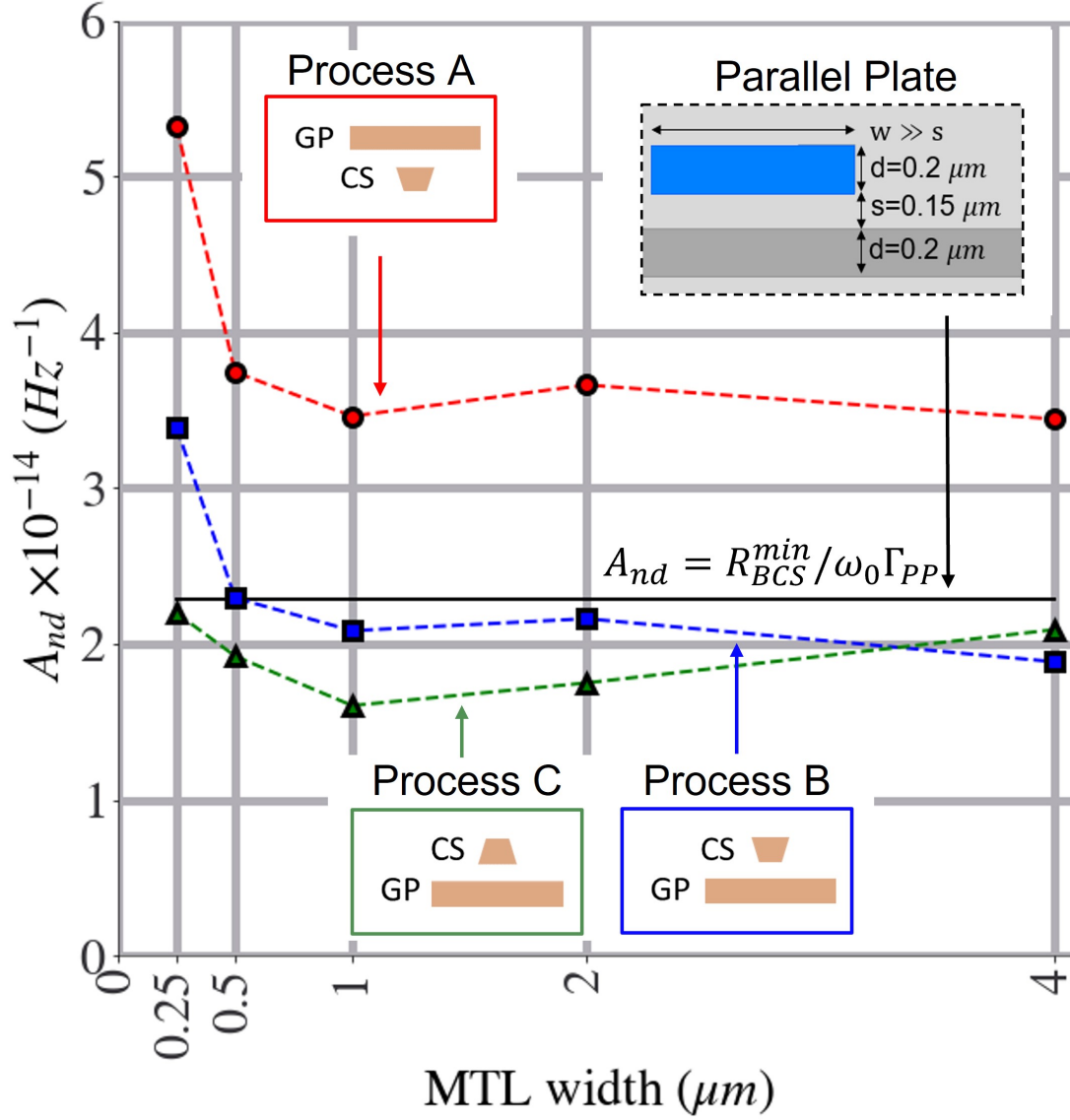
Figure 4.6: Plots showing the fit slope A as a function of MTL width for all three processes (assuming non-dispersive model). (solid black line) The predicted slope A using Eq. 3.16 assuming the minimum BCS intrinsic resistance R_{BCS}^{min} and geometric factor for a parallel plate MTL (very wide conducting strip) using Eq. D.11 at 10 GHz and 4.2 K.

In other words, an 8% variation in dielectric constant only varies the Γ_{c0} by roughly the same amount. This affords a two-fold understanding: (1) the Q-factor of the MTL resonator (RQL interconnect) related to power dissipation is fairly resilient to fabrication variation geometrically and (2) any variations in Q-factor above the fabricated geometric variation can be attributed to extrinsic loss variation (i.e. R_s and $\tan \delta$).

Deconvolving the geometric factor further, the partial geometric factors of the conducting strip Γ_{0CS} and Γ_{0GP} are plotted in Fig. 4.7(c) and Fig. 4.7(d), respectively. For the conducting strip, there is about a 5% variation between all three processes at $4\mu m$ MTL width. Surprisingly, as the MTL width is reduced, Γ_{0CS} becomes comparable for all widths and almost equal at $0.25\mu m$ MTL width. The total MTL geometric factors for all processes are also equal at $0.25\ \mu m$ MTL shown in Fig. 4.7(a). Note, the microstrip geometries are notably different and diagrams are shown on the right of Fig. 4.7(b) and better seen in Fig. 3.1. This is an important conclusion as any changes of the partial Q-factor associated to the conductor Q_c, or Q_i since $\tan \delta$ is geometry independent, can be attributed to changes in the intrinsic resistance R_s and dielectric loss tangent $\tan \delta$.

Referring back to STEM summary Table 3.1 on the large discrepancy in ground plane thickness of 50% in process A, the partial geometric factor of the ground plane Γ_{0GP} has a marginal 10% maximum difference. This is most likely due to the ground plane thickness not falling below the estimated penetration depth of $\lambda \approx 90\ nm$. Referring to Fig. 3.13, the magnetic fields are penetration the $4\ \mu m$ MTL an approximate distance of λ. If process A ground plane thickness d_{GP} to magnetic penetration depth ratio becomes much less than one $d_{GP}/\lambda \ll 1$, then significant change would be seen in Γ_{GP} (see Eq. 2.24). Conversely, for a $0.25\ \mu m$ MTL, the magnetic fields (currents) are more concentrated in the conducting strip (Fig. 3.13), so $d_{GP}/\lambda \ll$

1 will have less of an effect, but an effect to keep track of nonetheless.

The next two sections will extract R_s and $\tan\delta$ more accurately by assuming one of three models: (i) non-dispersive $\tan\delta$ and homogeneous superconductor, (ii) non-dispersive $\tan\delta$ and in-homogeneous superconductor, and (iii) dispersive $\tan\delta$ and homogeneous superconductor.

4.4.1   Non-Dispersive $\tan\delta$ Model

In this subsection, the non-dispersive $\tan\delta$ model will be assumed throughout unless otherwise specified using Eq. 3.13-3.16 and assumptions therein.

Taking the MTL geomtric factors solved by HFSS in Fig. 4.7, the intrinsic resistance R_s from process A is extracted from the fitted slopes A as a function of MTL width in Fig. 4.6. The red data set extracts R_s assuming a parallel plate model with $\Gamma_{PP} \approx 12\ m\Omega$ (see dashed black line in Fig. 4.7(a)). The blue data set extracts R_s assuming a homogeneous MTL where $R_{s0GP} = R_{s0CS}$ and solved Γ_{c0} in Fig. 4.7(a). The black data set (overlapping the blue data set) extracts R_{s0} assuming a non-homogeneous MTL where $R_{s0GP} \neq R_{s0CS}$ for MTL widths less than $4\ \mu m$.

Immediately it can be seen that the parallel plate model (red data set) has approximately 25% high R_s for 0.25 μm MTL relative to the homogeneous model using HFSS solve geometric factors. This means that if one was to use the parallel plate analytical model alone, the extracted R_s would be an upper bound of the actual intrinsic resistance. As MTL width dimensions shrink below $0.25\mu m$ the induced error in extracted intrinsic resistance will also increase. This makes it difficult to distinguish whether changes in Q-factor or intrinsic resistance R_s are due to extrinsic effects caused by processing as the conducting strip goes to minimum dimensions or
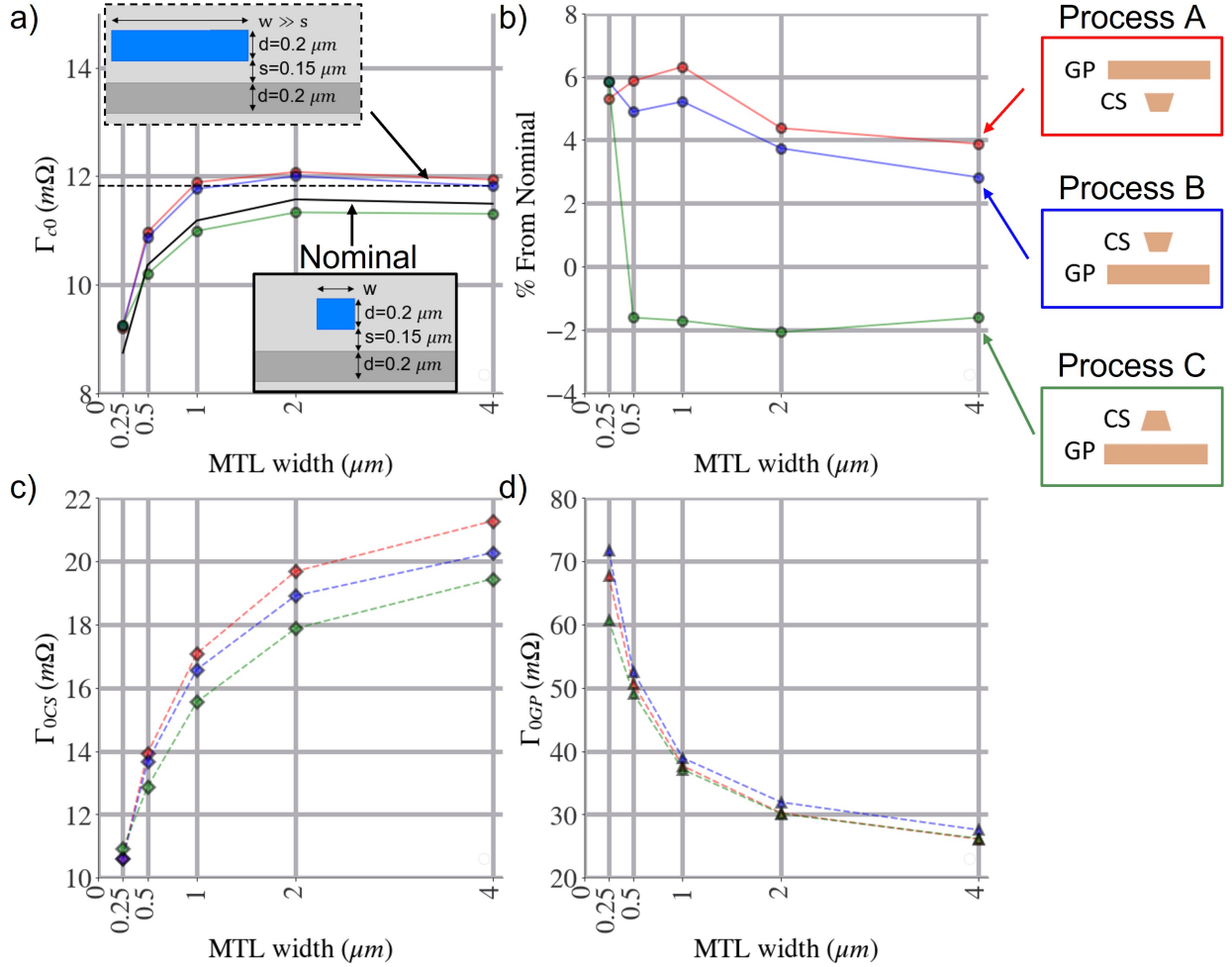
Figure 4.7: Plots showing the calculated geometric factors Γ from HFSS using STEM/FIB measurements. a) The total MTL geometric factor calculated by HFSS from measured MTL geometries versus MTL width. These will be used to extract R_s from the slope A found in Fig. 4.5 b) The % difference (or error) of Γ_{c0} from measured geometry versus assuming nominal cross section dimensions. c) The partial conductor geometric factor Γ_{0CS} as a function of MTL width calculated by HFSS. d) The partial ground plane geometric factor Γ_{0GP} as a function of MTL width calculated by HFSS. HFSS simulations and method can be found in Chapter 3. STEM measurements can be found in Section 3.2. FIB cross section measurements can be found in Appendix A

if its completely due to geometrical effects. Going a step further, if one wants to monitor the process of the conducting strip alone and the intrinsic resistance of the ground plane R_{s0GP} is known with some certainty and can be assumed to not be changing, then one can employ the homogeneous model with the following equation

$$R_{s0CS} = (A\omega_0 - R_{s0GP}/\Gamma_{0GP})\Gamma_{0CS} \tag{4.7}$$

where R_{s0CS} is the intrinsic resistance of the conducting strip, R_{s0GP} is the intrinsic resistance of the conducting strip, A is the fit slope from Fig. 4.6 and Eq. 3.15, Γ_{0GP} is the partial geometric factor of the ground plane, Γ_{0CS} is the partial geometric factor of the conducting strip, and $\omega_0/2\pi = 10\,GHz$ is the reference frequency.

Here, for the in-homogeneous model, it is assumed at $4\,\mu m$ MTL width the ground plane and conducting strip have equal intrinsic resistances $R_{s0CS} = R_{s0GP}$. The coinciding of the homogeneous (blue data) and in-homgeneous (black data) for all MTL widths suggests that the R_{s0CS} is not significantly larger than the R_{s0GP}. Although, as the MTL width decreases, the geometric factor of the conducting strip Γ_{0CS} decreases and therefore dominates the conductive loss. The geometric factor can be looked at as a participation ratio similar to methods shown in the quantum community to determine which interface dielectric losses participate more [145, 146]. In this case, a large partial geometric factor for the m-th conductor Γ_{0m}, its respective intrinsic resistance R_s will participate less in the overall Q-factor dissipating less power and vice versa. For 0.25 μm MTLs, $\Gamma_{0GP} \approx 10\Gamma_{0CS}$ so the loss in the conducting strip is dominating the microstrip conductor loss.

Referring now to Fig. 4.9, to compare the power loss in the MTL resonators (MTL interconnects)
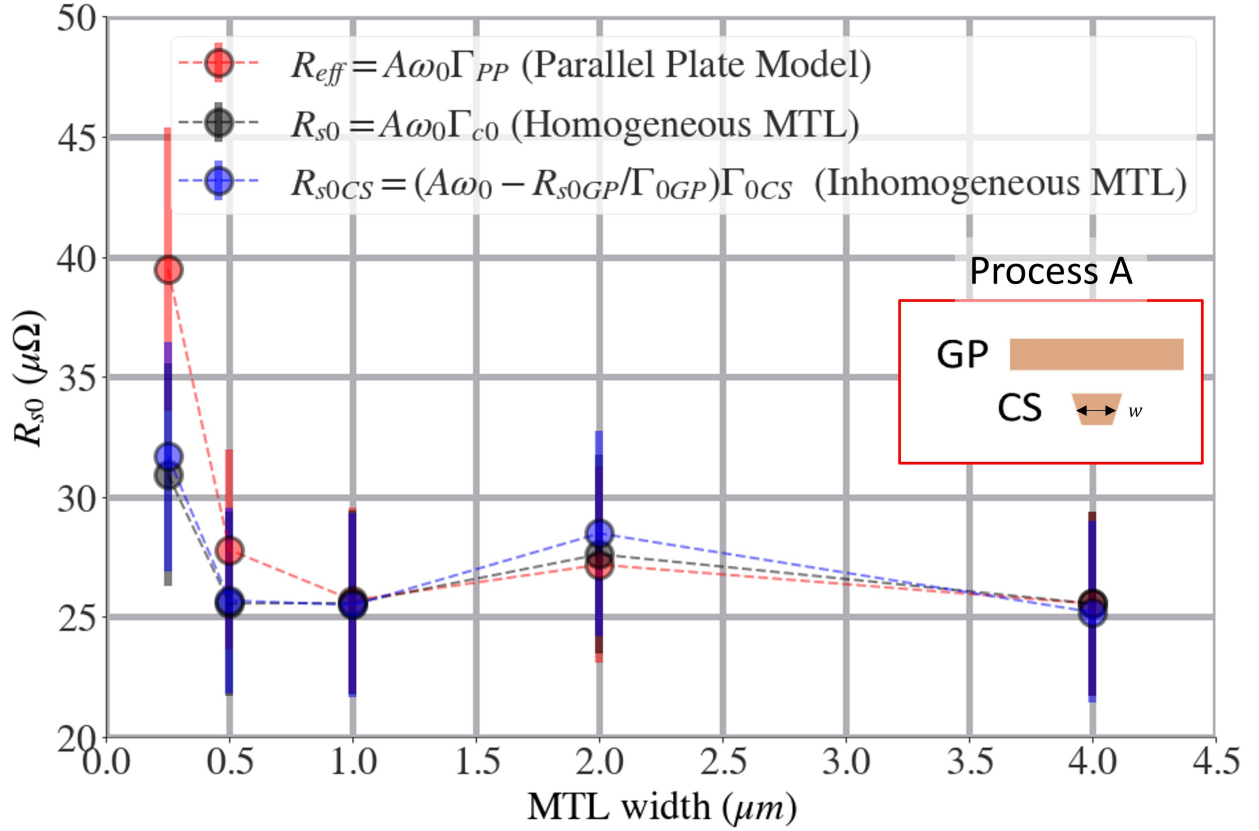
Figure 4.8: (red) Extracted effective resistance R_{eff} from Q_c assuming Eq. D.11 for a parallel plate. (black) Extracted intrinsic resistance R_{s0} from Q_c using Γ_{c0} calculated from HFSS at each MTL width. (blue) Extracted intrinsic resistance of the conducting strip R_{s0CS} assuming $R_{s0CS}(4\,\mu m) = R_{s0CS}(4\,\mu m)$ using calculated Γ_{cGP} and Γ_{cGP} from HFSS at each MTL width (see Fig. 3.14). The reference frequency is $\omega_0/2\pi = 10\,GHz$. The cross section geometries of each MTL was measured in TEM (see Section 3.2).

for each fabrication process, the homogeneous model with a non-dispersive loss tangent is assumed from Eq. 3.13-3.16 using the HFSS solved MTL geometric factors $\Gamma_{c0}(w)$. Fig. 4.9(a) and Fig. 4.9(b) show the extracted intrinsic resistance R_{s0} of Nb at reference frequency $\omega/2\pi = 10\ GHz$ and assumed frequency independent $\tan\delta$ of TEOS as a function of MTL width at 4.2 K, respectively. The error bars are $\pm 20\%$ as worst case error of 20% variation in geometric factor across a 150 mm wafer (see Fig. 4.3). The black dashed line is the BCS minimum intrinsic resistance R_{BCS}^{min} as measured by Benvenuti *et al.* [64] for thin film Nb samples at 4.2 K and scaled to 10 GHz using quadratic frequency scaling [62]. Since a $4\ \mu m$ MTL resonator can be approximated as a parallel plate resonator, the R_{s0} can be compared to parallel plate resonator measurements at 4.2 K and 10 GHz. The intrinsic resistances for a $4\ \mu m$ MTL width ranges from $R_{s0} \approx 15 - 25$, and is in good agreement with $R_{s0} \approx 20$ measured by Taber [136] using his parallel plate resonator technique. To get accurate measurements of R_{s0}, Taber varied the dielectric spacer thickness in the parallel plate resonator, which requires about 1-2 days worth of measurements. Here, we extracted R_{s0} in a single measurement by relying in the frequency dependence of Q_c and assuming a non-dispersive loss tangent.

The data will now be compared between processes in Fig. 4.9. Process A, R_{s0} is relatively high for all MTL widths relative to process B and C. This was also inferred in Fig. 4.6 and discussion. There might be a noticeable upturn in R_{s0} as the MTL width goes down to 0.25 μm, but cant be claimed with the large error bars. Recall, process A has an inverted MTL geometry where the ground plane is above the microstrip and will be discussed further in the discussion section (see Fig. 3.2 and summary Table 3.1). Process B, a damascene CMP process, has an $R_{s0} \approx 15\ \mu\Omega$ for MTL widths $0.5 - 4\ \mu m$ and an upturn in $R_{s0} \approx 20\ \mu\Omega$ for 0.25 μm MTL. Process B falls below the BCS minimum intrinsic resistance measured by Benvenuti *et al.* for

MTL widths $0.5 - 4\ \mu m$ within some error. This is an outstanding result for a damascene CMP processed RQL interconnect at submicron dimensions and demonstrates its possible to fabricate Nb submicron lines with the theoretically lowest power dissipation. Based on process C results for R_{s0} and small error bars, a cloisonné process with a metal etch and dielectric CMP, it can be argued that Nb $0.25\ \mu m$ wires can have R_{s0} below what has been measured before. For all processes, especially process C, a dip (or minimum) in R_{s0} at about $1\ \mu m$ can be seen. At this time, a robust model of this minimum at $1\ \mu m$ has not been developed and still needs to be looked into further. Although, it is worth noting that from Fig. 3.13, the magnetic fields begin to overlap on-top of the conducting strip and a redistribution of magnetic field circulating at the top of the strip rather than be concentrated at the bottom edges may induce lower loss. Due to the uncertainty in R_{s0} from the assumed worst case error bars, it can be inferred that process C R_{s0} does not have a width dependence for MTL widths $0.25 - 4\ \mu m$.

Now focusing on the power dissipation in the TEOS dielectric, Fig. 4.9(b) shows all three processes have approximately the same loss tangent $\tan\delta \approx 1.2 \pm 0.1 \times 10^{-3}$ and virtually no MTL width dependence. This is not surprising as the deposition parameters of the TEOS were unchanged for all three processes and $\tan\delta$ is ideally geometry independent. In spite of this, it is plausible that the presence of a $\mathrm{NbO_x}$ layer in process A and B (or lack thereof in process C) could participate as an additional loss mechanism if the $\mathrm{NbO_x}$ was a dielectric. Also, the TEOS RIE etch process in processes A and B could affect $\tan\delta$ differently relative to the TEOS CMP process using chemical mechanical polishing in process C (reduce or increase loss). In retrospect, this is an compelling result that TEOS is not sensitive to small changes in the process and therefore has a desirably large processing window (see Section 2.4).
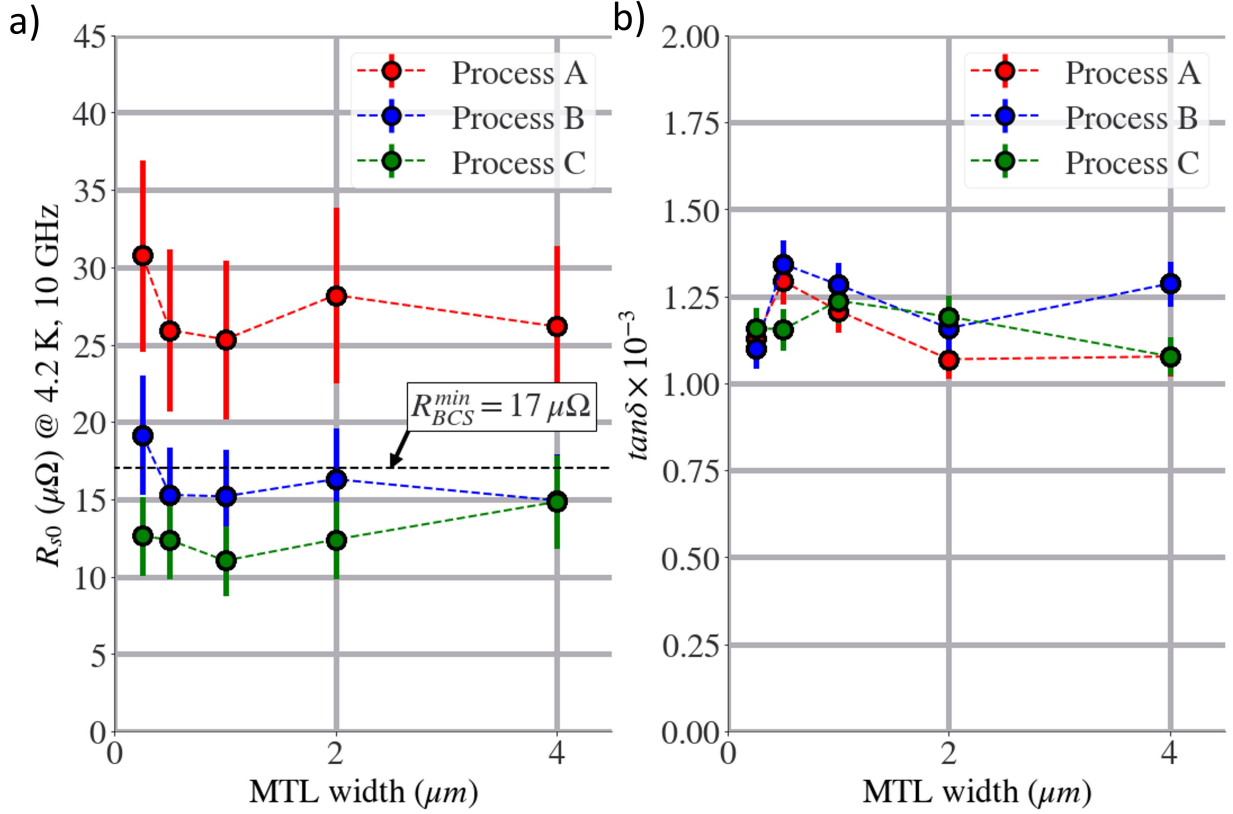
Figure 4.9: (a) Extracted intrinsic resistance R_{s0} at $\omega_0/2\pi = 10\,GHz$, and (right) $\tan\delta$ at 4.2 K as a function of MTL conducting strip width w and fabrication process recipe. The R_{s0} from slope A (see Fig. 4.6) HFSS calculated Γ_{c0} (see Fig. 4.7). The R_{s0} error bars are the worst-case scenario of +/-20% using the parametric corners results in Fig. 3.17. These are conservative error bars relative to measurement error, fitting error, and linear fitting errors in Fig. 4.5. The black dashed reference on the left is the known BCS limit of the intrinsic resistance at 4.2 K and 10 GHz. The BCS R_s can be calculated using [179]. The minimum BCS R_s has been measured at 4.2 K for Nb thin films [64]. This may be the first time it has been reported for sub-micron Nb wires.

4.4.2   Homogeneous Superconductor, Dispersive $\tan \delta$ Model

In the last section, we assumed the loss tangent $\tan \delta$ was constant in the frequency range $\approx 1 - 15 GHz$. It was found that *Process C* produces MTLs having an intrinsic resistance R_s near or below BCS limit of $17\,\mu\Omega$ at temperature T=4.2 K and $\omega_0/2\pi = 10$ GHz reference frequency. It was also found that the frequency dependence for Q_i scaled approximately linear. This affords the opportunity to assume a model for Q_c^{-1} and subtract it from Q_i^{-1} in order to analyze the frequency dependence of $Q_d^{-1} \equiv \tan \delta$. Assuming $Q_c^{-1} \propto \omega$ frequency dependence, $R_{s0} = 17\mu\Omega$ at 10 GHz and 4.2 K, and a nominal geometric factor for 4 μm MTL $\Gamma_{c0}(4\ \mu m) = 11.5\ m\Omega$, the superconductor loss slope can be calculated to be $A = 2.35 \times 10^{-14}\ Hz^{-1}$ (see second term in Eq. 4.8). In Fig. 4.10(a) below, the black solid line is the model for $Q_c^{-1} = \frac{\omega}{\omega_0}\frac{R_{c0}}{\Gamma_{c0}}$ just described and agrees nicely for 4 μm MTL (purple) with a constant loss tangent $\tan \delta = 9 \times 10^{-4}$. This is more validation the method described here fits the data well. Although, it is interesting to note the 4 μm , 3 GHz (purple) data point does not coincide with the black line, suggesting some non-linearity. To further analyze this, and compare with Kaiser *et al.* [99], utilizing Eq. 3.13, the frequency dependent loss tangent $\tan \delta(\omega)$ can be inferred from Fig. 4.10(a) by

$$\tan \delta(\omega) = Q_i(\omega) - \frac{\omega}{\omega_0}\frac{R_{c0}}{\Gamma_{c0}} \tag{4.8}$$

where the subtracted term is the partial Q-factor associated to the conductor $Q_c = \frac{\omega}{\omega_0}\frac{R_{c0}}{\Gamma_{c0}}$. Using Eq. 4.8, Q_c was subtracted from the Q_i data and can be seen in Fig. 4.10(b). The data measured here is compared with Kaiser *et al.* measurements of $\tan \delta(\omega)$ for Nb_2O_5 and SiO_2 amorphous dielectrics (dashed lines), the dielectrics most closely related or involved in our system. For
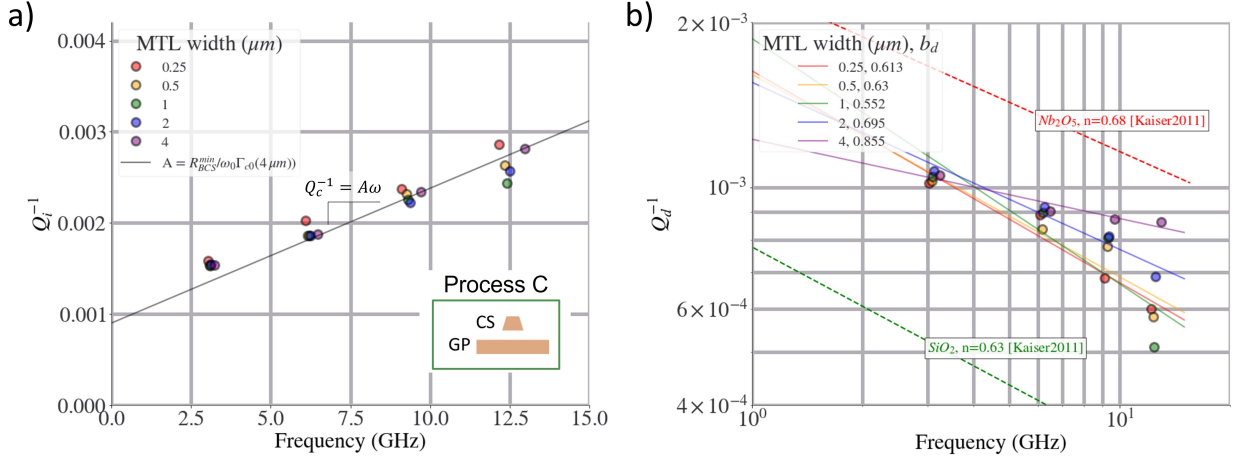
Figure 4.10: a) Inverse internal Q-factor Q_i versus frequency for Process C taken from Fig. 4.5. The black solid line is assuming $R_{s0} = 17\mu\Omega$ at 10 GHz and 4.2 K, and nominal $\Gamma_{c0}(4\,\mu m)$ calculated by HFSS b) $Q_d \equiv \tan\delta$ inferred using Eq. 4.8 and compared to Kaiser *et al.* data [99].

TEOS fabricated here is non-ideal as the deposition temperature is limited to 150 C, preventing crystal like growth kinetics and the presence of voiding (see Fig. 3.3(d) feature 5). Therefore, it is expected the loss tangent of TEOS is 1-2 orders of magnitude higher than Kaiser *et al.* SiO_2.

The *Process C* inferred $\tan\delta(\omega)$ for all MTL widths in Fig. 4.10(b) agree well and fall in between Nb_2O_5 and SiO_2 loss tangents measured by Kaiser *et al.*. From 3 to 10 GHz, the inferred $\tan\delta(\omega)$ decreases by a factor of 2 for $0.25\,\mu m$ MTL, and only decreases by about 10% for the 4 μm MTL. In comparison, the Q_c increases by a factor of 2 from 3 to 10 GHz for all MTL widths.

Using Eq. 2.44, the loss tangent data is fit to a power law and plotted as a function of MTL width in Fig. 4.11(a). The fit parameter b_d agrees well with Kaiser for $0.25 - 2\,\mu m$ MTLs in the regime of 0.5-0.75. The $4\,\mu m$ MTL has a relatively higher $b_d = 0.86$, giving a loss tangent frequency dependence of $\tan\delta \propto \omega^{-0.14}$.

It can be argued that the $4\,\mu m$ MTL, at low frequencies ω, is the most sensitive to $\tan\delta$, as Γ_{c0} is the largest at this width (see Fig. 4.7 and Eq. 3.13). This could explain the non-linearity in Fig. 4.10(a) mentioned earier, and can also be seen in Fig. 4.10(b) (purple data). Additionally,
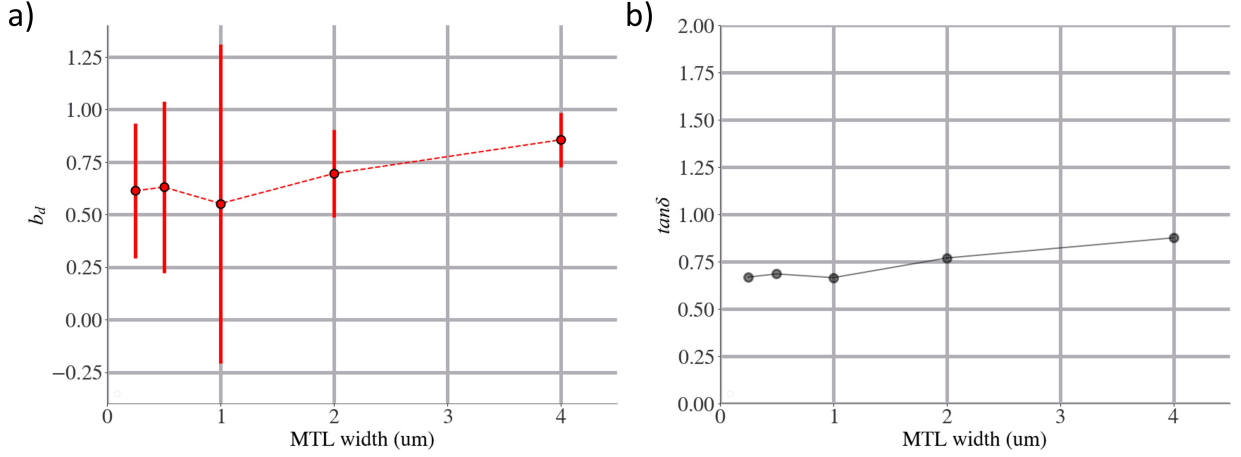
Figure 4.11: Results plotted from Fig. 4.10 showing the following as a function of MTL width: a) fitted exponent b_d from Eq. 3.12 and 1 standard deviation error and b) fitted loss tangent $\tan \delta$ at 10 GHz. Kaiser *et al.* measured $b_d \approx 0.6$ and $\tan \delta \approx 3 \times 10^{-4}$ for SiO_2 at 10 GHz.

the first mode for $4\ \mu m$ MTL falls on top of all other MTL widths, but then deviates at higher frequencies.

From the dispersive fits in Fig. 4.10(b), the loss tangent $\tan \delta$ at $\omega/2\pi = 10GHz$ reference frequency as a function of MTL width is plotted in Fig. 4.11(b). In comparison to extracted non-dispersive loss tangents in Fig. 4.9, the dispersive loss tangent is approximately 20-60% lower at 10 GHz.

The agreement with Kaiser *et al.* of $\tan \delta$ magnitude and power dependence as a function of frequency for similar dielectrics is a good first indication that there is dispersion the TEOS dielectrics measured here at 4.2 K. Yet, we had to assume an R_{s0} and geometric factor Γ_{c0}.

To scrutinize the dispersion relationship further and demonstrate the superconductor and dielectric loss deconvolution method described here, I used Eq. 3.12 to fit the $Q_i(\omega)$ data to 3 free fitting parameters shown in Fig. 4.12. Except the process A $1\ \mu m$ MTL, all fits (dashed lines) fall in between the error bars, which are one standard deviation of Q_i variation across the wafer.

An interesting visual result can be seen in Fig. 4.12(e) for the $4\,\mu m$ MTL, which is the most sensitive to the loss tangent, shows process B is concave down and process A and C are concave up. In other light, process B and process C $4\,\mu m$ MTLs have almost the same mode 1 and mode 4 Q_i^{-1}, but modes 2 and 3 in process B are higher. This discrepancy and false concave down character in process B may just be due to the error bar for mode 4 in process B. Other than the fits for 1 μm MTLs and process B 4 μm MTL, all of the fits show a minimum in Q_i somewhere below 2 GHz. If $\tan\delta$ is expected to decrease as a function of frequency and the inverse partial conductor Q-factor Q_c^{-1} is proportional to frequency, then a minimum in Q_i^{-1} is expected. This minimum in the internal Q-factor $Q_i^{min}(\omega_m in)$ is a useful parameter for application, as it is the optimum frequency to operate RQL interconnects in terms of minimum power dissipation. Using $\tan\delta(\omega)$ for SiO_2 measured by Kaiser *et al.* (Fig. 4.10(b)), and assuming minimum $Q_c(\omega)$ with $R_{BCS}^{min} = 17\mu\Omega$ and $\Gamma_{c0} = 11.5m\Omega$ (Fig. 4.10(a)), the frequency for mimum power dissipation can be estimated to be $\omega_{min}/2\pi \approx 1GHz$. In a future MTL design, the fundamental mode should be decreased to ideally below 1 GHz to see if there is a minimum in Q_i^{-1}.

The dispersive fitting parameters A_d, B_d, and b_d as a function of process and MTL width are shown in Fig. 4.13(d-f), where $A = A_d$ is the slope associated to the conductor loss, $B = B_d$ is "non-dispersive" $\tan\delta$ if $b = 1$, and $b = b_d$ is the dispersive power exponent (see Eq. 3.12). The non-dispersive fitting parameters $A = A_{nd}$, $B = B_{nd}$, and $b = b_{nd}$ are shown in the first row for reference. For a 3 parameter fit on only data points, this system is nearly over-determined and could explain a lot of the scatter in Fig. 4.13(d-f) and Fig. 4.13. Similarly said before, other than 1 μm MTLs and process B 4 μm MTL, all dispersive exponents are less than 1 $b = b_d < 1$. This is a notable result, as a $0.5 < b < 1$ fitted from 3 fitting parameters without assuming loss in the superconductor is in agreement in Kaiser *et al.*. Thus, to first approximations, this demonstration

127
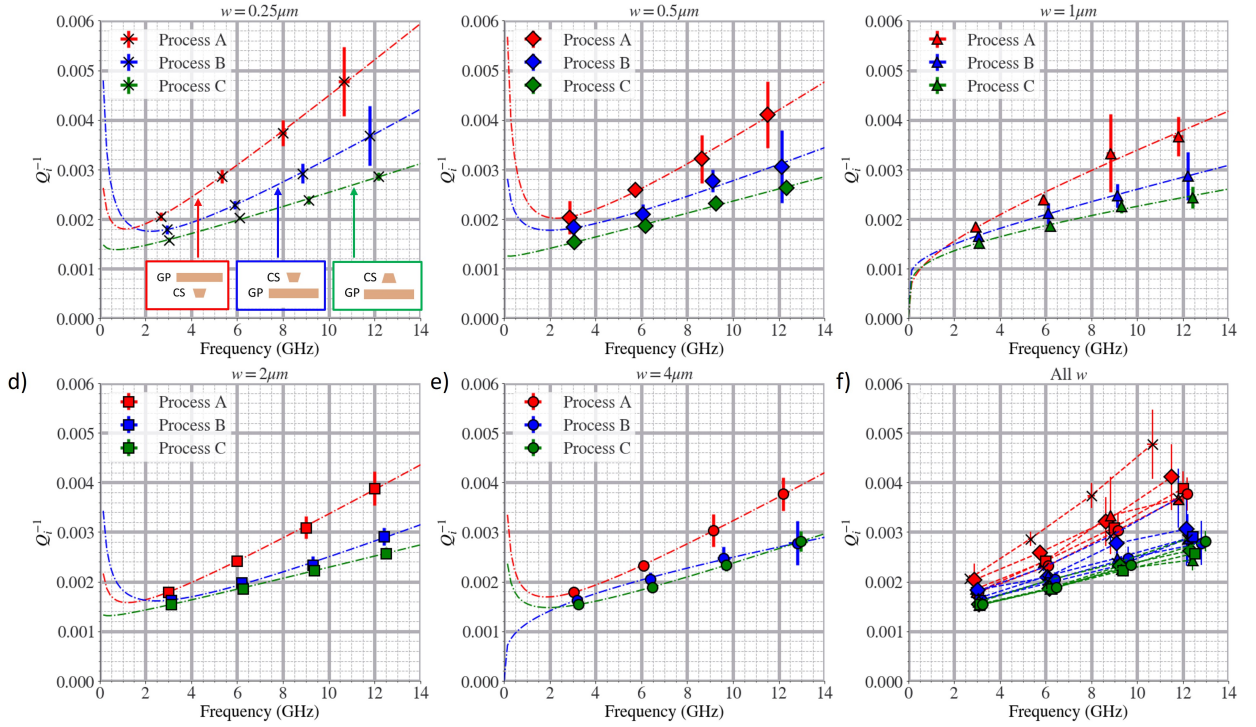
Figure 4.12: Internal Q-factor $Q_i(\omega)$ for Processes A (red), B (blue), and C (green) for MTL widths a) $0.25\,\mu m$ (crosses), b) $0.5\,\mu m$ (diamonds), c) $1\,\mu m$ (triangles), d) $2\,\mu m$ (squares), e) $4\,\mu m$ (circles) and f) all plotted together. The 3-parameter dispersive $\tan\delta$ fits (dahsed lines) use Eq. 3.12. Diagrams of the MTL geometry for each process are shown in a) for convenience.
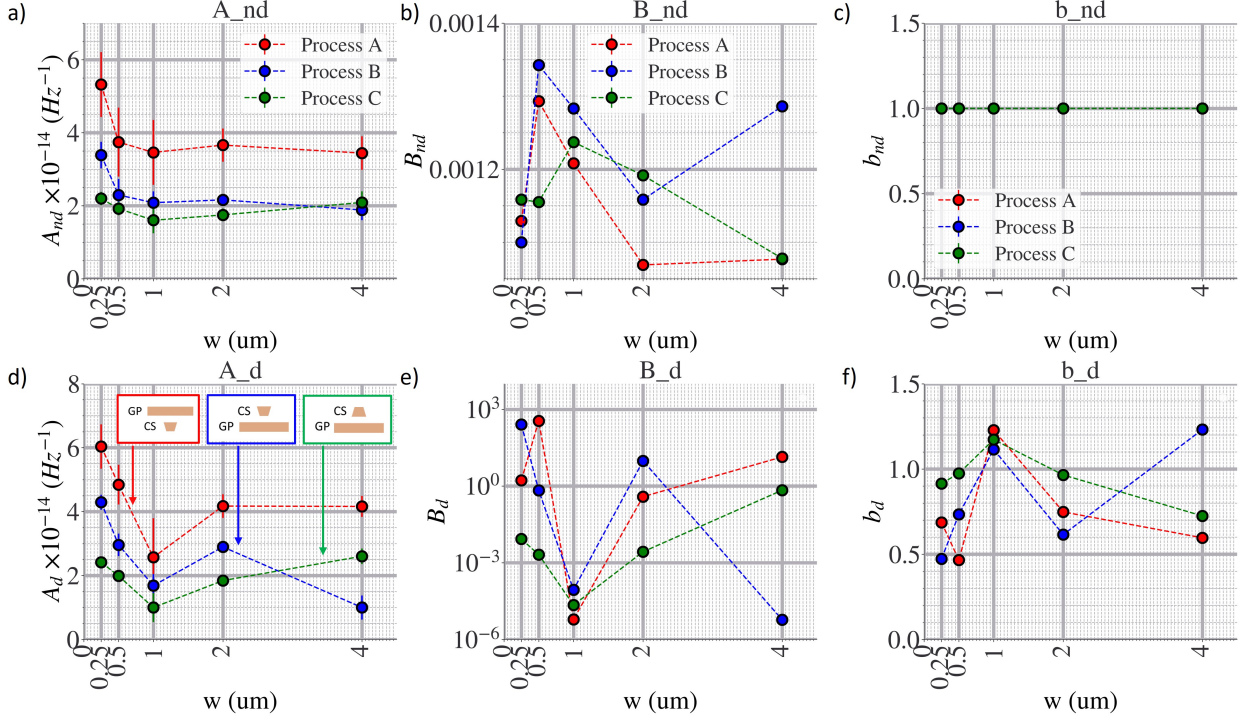
Figure 4.13: The top row are fitting parameters for non-dispersive $\tan\delta$ model assuming $b = 1$ (linear fits) shown in Fig. 4.5 and using Eq. 3.12. Width dependence of linear a) slope parameter A due to conductive loss, b) assumed non-dispersive loss tangent $B = \tan\delta$ where c) $b = 1$. The second row are fitting parameters for dispersive $\tan\delta$ model showing width dependence of free fitting parameters: d) slope A proportional to conductive loss e) pre-exponent term B f) and exponent term b. Diagrams of the MTL geometry for each process are shown in d) for convenience.

serves as a validation of the deconvolution method described here because 1) the R_s results are comparable to measured values found in literature, and 2) the $\tan\delta$ dispersive relationship and values agree with previous findings.

Aside from the $1\,\mu m$ MTLs and process B $4\,\mu m$ MTL, extracted R_{s0} and $\tan\delta$ assuming the dispersive model in Fig. 4.14 general agrees with the non-dispersive extraction method in Fig. 4.9. By general, i mean the R_{s0} magnitude is still in between 15-35 $\mu\Omega$ using the dispersive model and $\tan\delta$ is within 50% of values relative to non-dispersive fits. This is a very important result, regarding the R_{s0} values falling below BCS limit in Fig. 4.9(a) being suspect $R_{BCS} = 17\,\mu\Omega <$ R_{s0}. The minimal change in R_{s0} values using dispersive fits here only marginally increase and
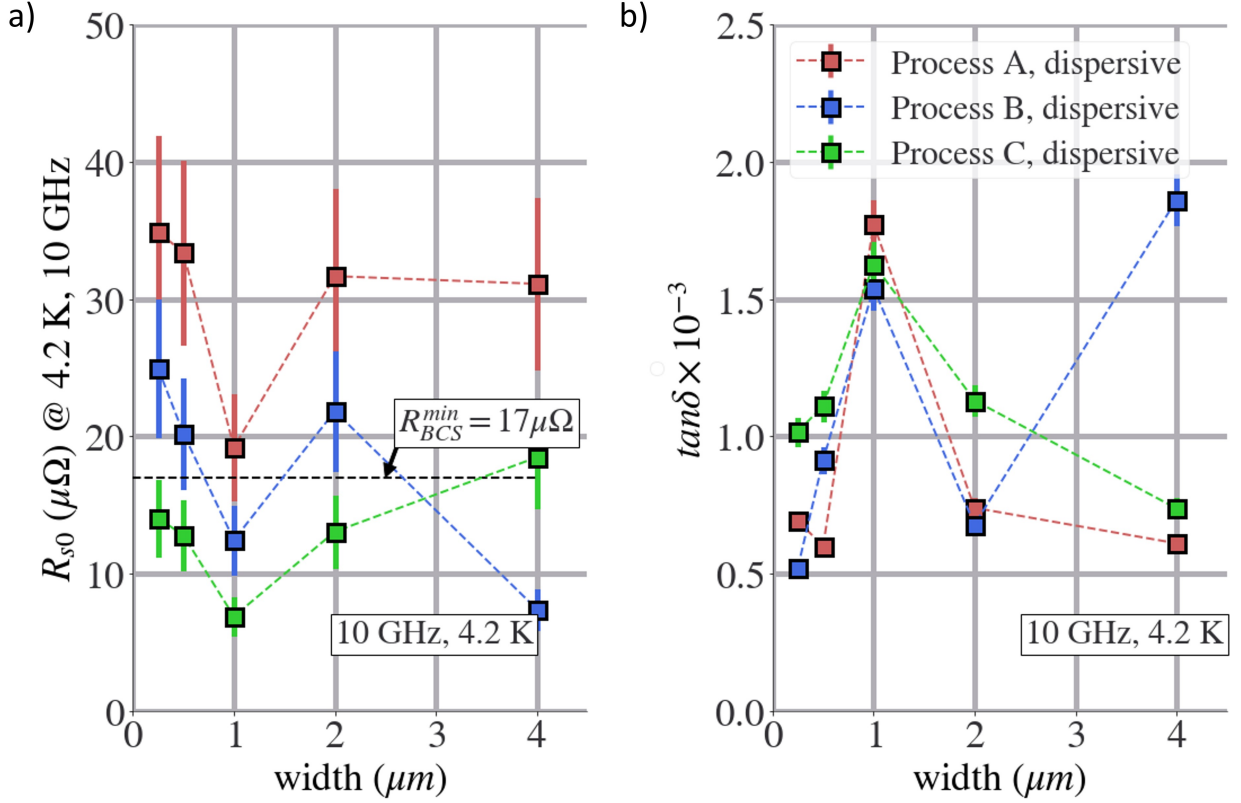
Figure 4.14: Extracted a) Intrinsic resistance R_s and b) $\tan\delta$ versus MTL width using dispersive $\tan\delta$ 3-parameter fit model

support results in Fig. 4.9(a). MTL width dependence is not discernible in Fig. 4.14 due to the noise, which is most likely due to the dispersive fitting model being close to over-determined with 3 fitting parameters and only 4 data points.

Ultimately, exploring the dispersive $\tan\delta$ model and fitting the data as a function of MTL width and different processes, varying in loss significantly as a function of frequency, offered the proposed gleaned information:

(1) TEOS $\tan\delta(\omega)$ extracted from process C Q_i data using the simple Q_c^{-1} subtractive method agrees with Kaiser *et al.* in both magnitude and frequency dependence for SiO_2

(2) TEOS $\tan\delta(\omega)$ extracted from a 3-parameter fit for the majority of data (process and MTL

width) also agrees with Kaiser *et al.* in both magnitude and frequency dependence for SiO_2

(3) Nb R_{s0} extracted from a dispersive 3-parameter fit give support of values measured below the results measured by Benvenuti *et al.* [64]

4.5   Discussion

The previous two sections have demonstrated the method to deconvolve the losses by assuming different models. In this discussion, we will focus on the results from Fig. 4.9, where a non-dispersive $\tan\delta$, homogeneous ($R_{s0GP} = R_{s0CS}$) MTL model was assumed. Models to explain the intrinsic resistance R_s difference as a function of (i) width dependence) and (ii) fabrication process (A,B,C) will be proposed relying on the morphology and chemical analysis in Section 3.2.

Up-turn of R_s at $0.25\ \mu m$

In reference to Fig. 3.3(a) and (c), the damascene process induces two grain orientations, sidewall horizontal grains and vertical trench grains, meeting along a diagonal line with approximate angle of 30 degrees. Here, we will call this the *sidewall grain intersection*. At these intersection, voiding (or lower metal concentrations) occur. The percentage of sidewall horizontal grain on both sides of the microstrip remain fairly constant in size with maximum length of 100 nm at the top of the microstrip. As the microstrip width decreases, the crossectional area fraction of the sidewall grains increases. Here, we will call this the *sidewall grain fraction*. For a $1\ \mu m$ microstrip, sidewall grain fraction is only about 20%, whereas for a $0.25\ \mu m$ microstrip the sidewall grain fraction is approximately 50%. This is a model that could contribute to the upturn in R_s of about 20-30% for $0.25\ \mu m$ MTL relative to $4\ \mu m$ for process A and B.

Another model that could attribute to the upturn in R_s is the presence of voids, or areas of lower Nb concentration (see Fig. 3.3). Voids become a more significant fraction as microstrip width decreases. The effect of voiding on microwave surface resistance has not been studied carefully. Although, there has been extensive studies on how Nb vacancies can facilitate Nb hydride precipitate formation [180]. Consequently, the Nb voids could be acting as hydride formation sites. In addition, Nb voids could have an effect on the electron mean free path, and in turn increasing both the magnetic penetration depth and microwave surface resistance (see Eqs. 2.20 and 2.8).

It is worth mentioning a model of the NbO_x layer as the mechanism causing the upturn in R_s at 0.25 μm. In reference to Fig. 3.13, the fringing magnet fields do not start start to sample (overlap) a significant percentage of the top of the microstrip until below 1 μm. In process B, the exact geometry shown in Fig. 3.13, the upturn in R_s does not happen until 0.25 μm. It is conceivable the R_s upturn here is due to NbO_x, but would have expected a more gradual increase in R_s. This argument is more unlikely when considering Process A, as the fields are sampling the NbO_x layer for all MTL widths of equal fraction, and is more likely to be a different mechanism. An upturn in R_s in Process C is not visible.

R_s versus MTL width offset

In process A, due to the orientation of the GP relative to the fill morphology (sidewall grain orientation), the magnetic field (current density) is more concentrated at the oxide layer. The current is also concentrated where voiding occurs. Whereas in process B, the damscened surface is not at a location of highest current density. In "morphology section" we also found from chemical mapping that the oxide layer is closer to NbO or Nb_2O_3, which is a bulk superconductor with T_c approximately 6 K, but at 5 nm thickness is most likely a normal metal. Therefore, the

oxide location relative to the current concentration is a model that can explain the R_s offset by approximately a factor of 2 between process A and B. Process C does not have a detectable oxide at the interface of highest current concentration, suggesting the offset of approximately 40% between process B and C $0.25\,\mu m$ microstrip. Surprisingly, due to the etch undercut process, the rough and irregular surface of the strip did induce R_s larger than damascene processes A and B.

4.6 Summary

In summary, microstrip transmission line (MTL) resonators were designed into an RQL fabrication process where the Q-factors associated to conductor and dielectric loss are comparable $Q_c \approx Q_d \approx 1000$. The comparable Q-factors are not compatible with established techniques to analyze the dissipative loss coming from the superconductor and dielectric separately. Using the methods and HFSS numerical modeling procedures described in Chapter 3, the intrinsic resistance R_s of Nb and loss tangent $\tan \delta$ of TEOS were extracted from measured intrinsic Q-factors as a function of frequency $Q_i(\omega)$ utilizing their unique dispersive relationships. The uncertainty in extracted R_{s0} was used from the HFSS sensitivity analysis in Section 3.7 with a worst case error of $\pm 20\%$. The overall uncertainty is dictated by the fabrication geometry where the microstrip and dielectric separation thicknesses have the most significant impact on geometric factor variation. The standard deviation from measured values of the internal Q-factor Q_i across a wafer was much less than $\pm 20\%$, suggesting a well controlled fabrication process where both the resonator geometry and the intrinsic surface resistances are not varying significantly across the wafer. Different dispersive models were proposed and analyzed to demonstrate and give validation to the R_s and $\tan \delta$ extraction method from a single measurement at 4.2 K. Three fabrication processes were analyzed using this method, and found that the cloisonné process C yields R_{s0} of Nb near theorical minimums down to $0.25 \ \mu m$ MTL widths. Near equivalent R_s values can be achieved in the damscene process B down to $0.25 \ \mu m$ MTL widths. A NbO_x layers in MTLs can induce an extrinsic increase in R_{s0}, and its location relative to current density concentration inside the conducting strip can exacerbate this issue. An Al capping layer has been shown to prevent NbO_x formation at the conducting strip interface, and suggests this aided in the

minimum and near width independent R_{s0} measured in cloisonné process C. For all fabrication processes and MTL widths measured here, TEOS loss tangent $\tan \delta$ is width independent, and the measured frequency dependence agrees with previous work on similar amorphous dielectrics.

The materials characterization done here informs the implications on power dissipation performance of RQL interconnect operating at 4.2 K and 10 GHz. The TEOS dissipative loss is geometry independent, and only dependent upon fabrication. If the TEOS could be deposited at temperatures higher than 150 C, then it is possible to reduce its dissipative loss 1-2 orders of magnitude ($Q_d \approx 10^4 - 10^5$). The Nb dissipative loss has arguably reached its theoretical minimum ($Q_c \approx 3 - 4 \times 10^3$). The current minimum energy efficiency is $\eta \approx 0.3$ of RQL resonator clocks relative to the power dissipated by the RQL logic $\eta = P_{logic}/(P_{logic} + P_{clock})$. The efficiency is proportional to the resonator internal Q-factor by $\eta \propto 1/(1 + Q_i^{-1})$, where the power dissipated in the clock is proportional to the Q-factor by $P_{diss} \propto Q_i^{-1}$ having nominal value $Q_i = 250$ at 4.2 K and 10 GHz. Taking a resonator composed of MTL interconnect down to $0.25 \, \mu m$ widths fabricated by process C, the efficiency would increase to $\eta \approx 0.6$. If the dielectric loss could be reduced by a factor of 10 and 100, the effieciency would increase to $\eta \approx 0.83$ and ≈ 0.86, respectively. This is an exceptional decrease in power dissipation relative to the logic at maximum operation (i.e. all logic units are active in the circuit), but it is important to note that the efficiency is at its limit and cannot be pushed further unless materials other than Nb and TEOS are used or changes in the transmission lines geometries are allowable.

At the current RQL clock efficiencies of $\eta \approx 0.3$, it can be estimated that the total power consumption of RQL at 4.2 K would be a factor of 90 less than equivalent CMOS circuits, which includes refrigeration costs [4]. For $\eta \approx 0.86$, RQL would consume approximately 260 times less than equivalent CMOS circuits. In the next chapter, temperature will be used as a knob to

explore further reduction in power dissipation in RQL interconnects. The determination of power

dissipation limits and an optimum temperature of operation will also be investigated.

Chapter 5: Temperature Dependent Characterization of Microwave Loss in RQL Interconnects

5.1 Overview

In the last chapter, I measured the internal Q-factor of microstrip transmission lines (MTLs) and delconvolved microwave losses of the superconductor and dielectric at 4.2 K. It was found that the theoretical minimum of Nb BCS intrinsic resistance $R_s \approx 17\,\mu\Omega$ was reached for *Process C* down to 0.25 μm widths at 4.2 K. The TEOS dielectric loss tangent was found to be $\tan\delta \approx 1 \times 10^{-3}$ at 4.2 K and is MTL geometry independent. It is known both R_s and $\tan\delta$ decrease with decreasing temperature. Hence, to maximize energy efficiency in RQL interconnects, the temperature could be lowered to reduce the RF losses. Although, refrigeration costs increase as the operation temperature is reduced. It takes approximately 3 times more power to reduce the operating temperature from 4.2 to 2 K [181].

As mentioned in the Chapter 2, the microwave loss of superconductors and dielectrics have different scalings with temperature. As temperature is decreased below 4.2 K, The bulk and thin film Nb R_s temperature and frequency scaling is well known as temperature is decreased below 4.2 K. For amorphous dielectrics like TEOS, the temperature (below 4 K) and frequency dependence strongly depend on the input power (electric field strength) and dominant mechanisms

of loss (e.g. classical dielectric relaxation, TLS tunneling relaxation, and TLS tunneling absorption). Furthermore, the dominant mechanism of dielectric loss in the dielectric can change rapidly as temperature is decreased. Up until the 1990s, there had been limited microwave dielectric measurements in the 1.5-4.2 K temperature regime, as most SCE communities operate at 4.2 K (SFQ) or at mK temperatures (Quantum Computing).

In this chapter, the dispersive loss deconvolution (DLD) method will be applied to temperature dependent measurements. In the 1.5-4 K temperature range, the extracted temperature dependence of $R_s(T) \propto e^{-1/T}$ and $\tan\delta(T) \propto T^3$ agree with expected behavior. The measurement sensitivity of this method will be discussed. Specifically at temperatures below 3 K, the frequency dependence of the Q_i is anomalous with non-monotic behavior increasing in magnitude as temperature is decreased. With only 4 modes in MTLs, it is difficult to draw conclusions for the Q_i frequency dependence. This warranted the design and measurement of multiplexed resonators in the subsequent section using process C to do further microwave spectroscopy from 1.5 - 4 K. In the temperature range 1.5-3 K, it is suggested the frequency and temperature dependence of $Q_i(T, \omega)^{-1} \propto \tan\delta(T, \omega)$ is due to two-level system loss, and is supported by changes in the dielectric constant (MTL phase velocity).

At the end of this chapter, a discussion of the temperature dependent superconductor and dielectric microwave loss, and concluding statements will be made on how this affects performance and power efficiency of resonator clocks.

5.2 Temperature Dependent Resonator Measurements

Temperature dependent measurements in this section were performed with the same test fixture described in Chapter 4, but retrofitted into a system similar to the Dry ICE 1.5 K Cryostat [182]. The cryostat base temperature is approximately 1.4 K and has temperature cryostat temperature stability of $\pm 10\,mK$ from 1.4 to 10 K. It is important to note, this is a dry system and cooling is accomplished by means of thermal conduction. See Appendix C for more information.

All temperature dependent measurements in this section were performed on MTL widths $0.25 - 4\,\mu m$ from process B. An example of the temperature dependent data for 4 μm MTL can be found below in Fig. 5.1 Four resonant modes from 3-12 GHz were analyzed extracting $Q_i(T), Q_e(T), f_n(T)$ using methods from Khalil *et al.* [177] (see sections 4.2, 4.3).
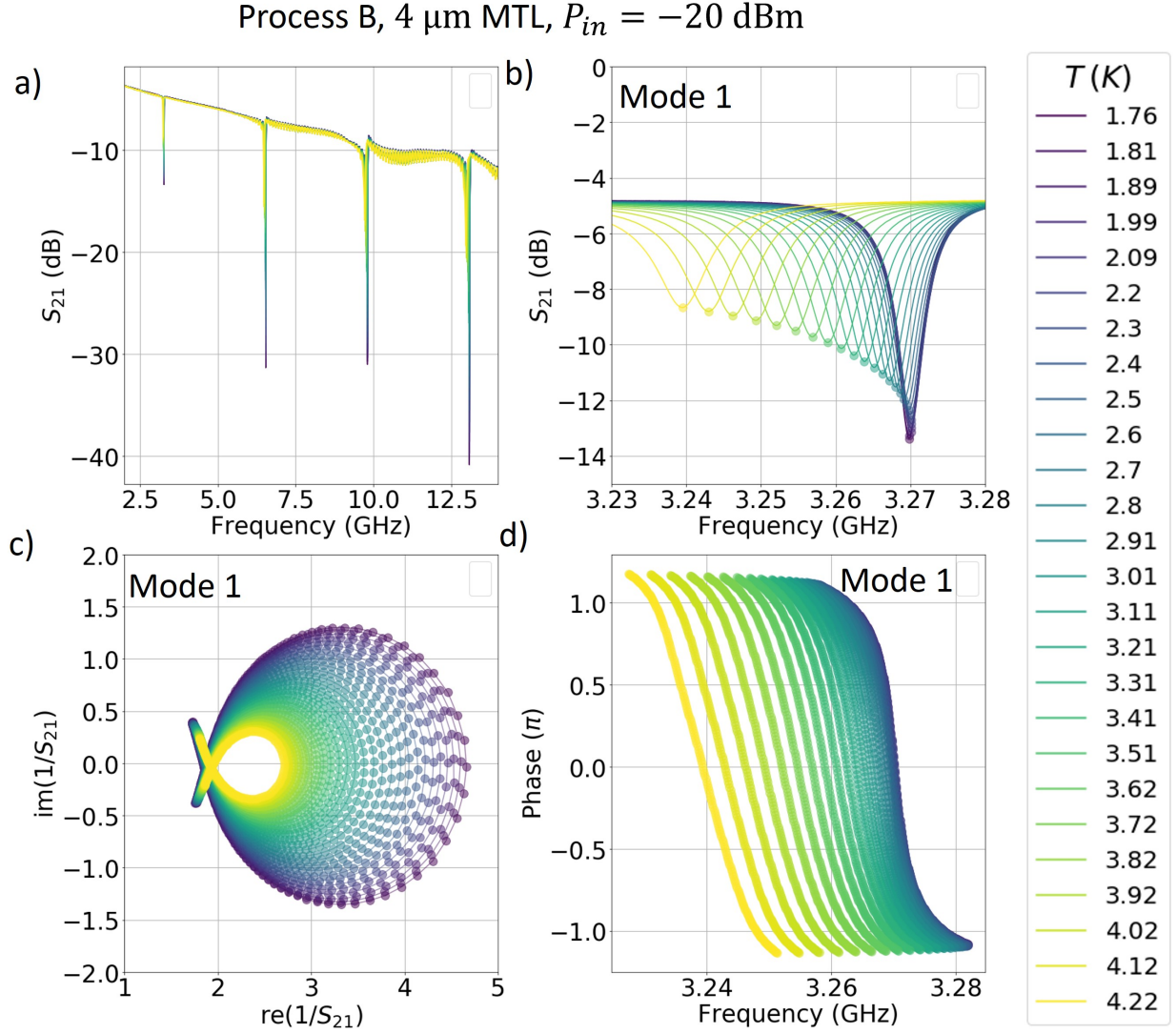
Figure 5.1: Temperature dependent measurements of $4\mu m$ MTL from process B using Dry ICE 1.5 K Cryostat equivalent [182] with ± 10 mK temperature control. S-Parameter measurements were with an input power of $P_{in} = -20\ dBm$. It will be shown this input power is too high and is shown only as an example that no non-linearities or bifurcation of resonant peak was found. Although, this relative high input power impacted the extracted internal Q-factors Q_i. a) S_{21} showing the temperature dependence of 4 modes were captured. b) Zoom in of mode one showing the resonant frequency shift and widening of 3 dB width as temperature is increased. c) The complex S_{21}^{-1}, which were fitted using [177]. d) The phase where with resonant frequency $\omega/2\pi$ at zero phase.

The nominal input power from the vector network analyzer (VNA) to the feedline is $P_{in} = -20 \ dBm = 10 \ \mu W$ at 4.2 K. It will be shown that -20 dBm is a relatively high power at 1.76 K. The effective power delivered to the resonator is dependent upon (i) the attenuation from the VNA to the feed-line on chip and (ii) the resonator coupling factor g. The coupling factor is dependent upon the resonator internal Q-factor Q_i and external (coupling) Q-factor Q_e by $g = Q_i/Q_e$ (see Eq. 4.2). Since Q-factors are temperature dependent, the coupling factor is also temperature dependent $g(T)$, and therefore the effective input power to the resonator is temperature dependent.

If it is desired to do temperature dependent measurements, the input power needs to be taken into consideration to prevent non-linear effects. Assuming the VNA is calibrated up to the shunt connection node, the incident power can be expressed in the following way by energy conservation [176]

$$P_{in} = P_r + P_t + P_d \tag{5.1}$$

where P_{in} is the incident power in Watts at the input of the resonator after cable attenuation (at the reference node in Fig. 5.2), P_r is the reflected power to the VNA, P_t is the transmitted power, and P_d is the power dissipated by the resonator.

The transmitted power P_t for a reactively coupled MTL can be calculated by [176]

$$P_t = P_{in}|S_{21}|^2 \tag{5.2}$$

where P_{in} is the incident power in Watts at the input of the resonator after cable attenuation, $|S_{21}|$
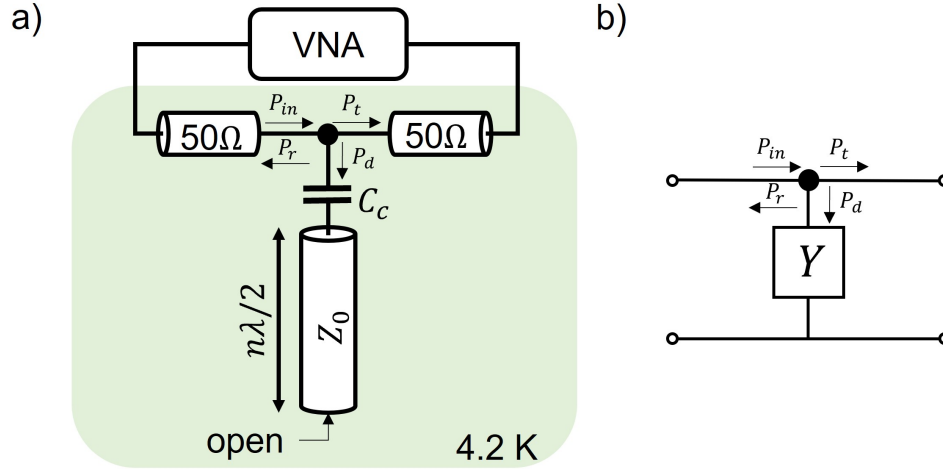
Figure 5.2: a) Representation diagram of the open ended MTL resonator. The reference point for the power conservation Eq. 5.1 is the node between the two 50 Ω lines and the coupling capacitor C_c. b) Block diagram showing the capacitively coupled $\lambda/2$ microstrip transmission line shown in a) is effectively an impedance inverter where Y is the shunt admittance. The node pointed out in a) is the same point in b) in reference to the power conservation Eq. 5.1

is the transmission coefficient magnitude related to the insertion loss IL in dB by $|S_{21}| = 10^{IL/20}$

at the resonant frequency $\omega/2\pi$. In this case of a reactively coupled microstrip resonator, the IL

is -6 dB for critical coupling $g \equiv 1$. Note, the typical insertion loss off resonance ranges from

-15 to -5 dB due to cable loss and impedance mismatch. This measurement is self calibrated in

the sense that $|S_{21}|$ is the size of the resonant dip relative to the baseline loss. For example, in

Fig. 5.3(b) the 3.3 GHz resonant mode has an insertion loss of $-8.5dB$ at 1.76 K. The transmitted

power to the resonator is $P_t \approx 14~\mu W$ for a -20 dBm input power. Assuming constant material

properties, the transmitted power can be tuned by varying the coupling capacitor C_c, temperature,

and geometry of the resonator (refer to chapter 4).

From the energy conservation law for microwave circuits [10, 176], the dissipated power

at resonance can be found regardless of the g value and calibration. The dissipated power can be

calculated by [10, 176]

$$P_d = 2P_{in}(|S_{21}| - |S_{21}|^2) \tag{5.3}$$

where P_d is the dissipated power in Watts. In Fig. 5.1(b) at a nominal $P_{in} \approx 10\ \mu W$, $IL \approx -8.5\ dB$ at 1.76 K yields a dissipated power of $P_d \approx 50\ \mu W$.

The circulating (stored) power in the resonator can now be calculated by

$$P_{st} = Q_i P_d = 2Q_i P_{in}(|S_{21}| - |S_{21}|^2) \tag{5.4}$$

where Q_i is the internal Q-factor at resonant frequency $\omega/2\pi$. Fitting the 3.3 GHz resonance at 1.76 K from Fig. 5.3(b) yields a $Q_i \approx 1.3 \times 10^3$. The stored power is then $P_{st} \approx 18\ mW$.

A superconductor becomes non-linear when RF current density comes close to the temperature dependent critical current density $J_c(T)$. In fabricated superconducting electronic circuits, the minimum critical current density at $T \leq 4.2\ K$ of Nb $0.35 - 0.5\ \mu m$ metal lines with $200\ nm$ thickness are typically $J_c \approx 20 MA/cm^2$ [32]. Considering a worst case for a $4\ \mu m$ and $0.25\ \mu m$, at nominal 200 nm thicknesses, the MTL minimum critical currents are approximately $160\ mA$ and $10\ mA$, respectively.

The peak RF current in the resonator I_{peak} can be compared to the expected critical current I_c to estimate onset of nonlinearity. It is also important to keep track of the peak voltage V_{peak} to monitor electromagnetic strengths in both the superconductor and dielectric. The temperature dependent magnitude of the peak current $I_{peak}(T)$ and voltage $V_{peak}(T)$ can be calculated by

$$I_{peak}(T) = \sqrt{\tfrac{16}{n\pi} \tfrac{P_{in}}{Z_0} P_d(T) Q_i(T)} \tag{5.5}$$

$$V_{peak}(T) = Z_0 I_{peak}(T) \tag{5.6}$$

where P_{in} is the input power, n is the mode index of the resonance, Z_0 is the characteristic impedance of the MTL assumed to be constant at $T \leq 4.2K$, and $Q_i(T)$ and $P_d(T)$ are the temperature dependent internal Q-factor and dissipated power, respectively. The rms peak current is $I_{rms} = \sqrt{2}I_{peak}$. Referring back to Fig. 5.3(b), assuming a characteristic impedance $Z_0 \approx 8\,\Omega$ for $4\,\mu m$ MTL, the peak current is $I_{peak} \approx 190\,mA$. This peak current of 190 mA exceeds the estimated $I_c \approx 160\,mA$.

For completeness, a $4\mu m$ MTL from Process B was measured at two input powers P_{in} of -20 dBm and -35 dBm and the temperature dependent results can be found below in Fig. 5.3. At 1.7 - 1.8 K, a clear difference in Q_i as a function of frequency can be seen. The 6 and 9 GHz modes at $T < 1.8K$ show almost equivalent Q_i^{-1} for -20 and -35 dBm, whereas the 3 GHz has a much higher loss with $P_{in} = -20dBm$. Surprisingly, the 12 GHz mode for the lower -35 dBm power shows a factor of two increase in Q_i^{-1} relative to the 12 GHz mode at -20 dBm. This will be revisited.

The non-monotonic behavior in Fig. 5.3 gives motivation to analyze the presence of non-linear effects. In Fig. 5.4, the peak current I_{peak} was calculated from data in Fig. 5.3. The peak current I_{peak} in the $4\,\mu m$ was calculated from Eqs. 5.5, 5.3 using measured $|S_{21}|$ and Q_i at each resonance and temperature T. It can be immediately seen that mode 1 (yellow) I_{peak} $0.5I_{c,min}$ for $P_{in} = -20dBm$ at the lowest temperatures. Mode 4 has peak current I_{peak} $0.15I_{c,min}$. For
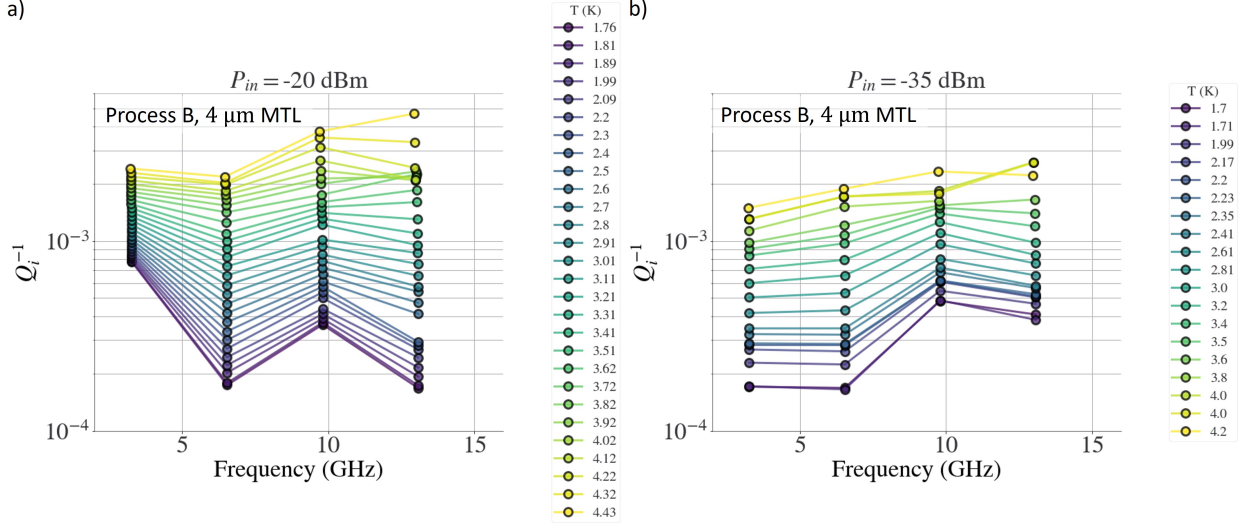
Figure 5.3: Extracted Q_i versus resonant frequency (mode index) as a function of temperature for a) $P_{in} = -20 \, dBm$ and b) $P_{in} = -35 \, dBm$. No visual bifurcation of the resonant peaks were witnessed. Although, particularly at 1.7-1.8 K, there is a clear different in extracted Q_i as a function of mode number

an $P_{in} = -35dBm$, the peak current drops to a factor of 10 and 20 lower for mode 1 and mode 4, respectively, relative to $I_{c,min}$. Note, looking vertically at each temperature, the peak currents in the resonator has an approximate monotonic dependence with mode index n, where n=1 is the 3.27 GHz mode. This is as expected and should go as $I_{peak} \propto n^{-1/2}$. Although, for $P_{in} = -35 \, dBm$, the mode 3 peak current relative to mode 2 decreases by $I_{rf,3} \approx 1.7 I_{rf,2}$ at 1.7 K, where a factor of 1.2 would be expected from mode dependence alone. Whereas the mode 4 decrease relative to mode 2 at 4.2 K is as expected with $I_{rf,3} \approx 1.7 I_{rf,2}$. Referring back to Fig. 5.3, the larger decrease in $I_{peak,3}$ for mode 3 seems to be coupled with a factor of 2 increase in $Q_{i,3}^{-1}$ relative to mode 2 at 1.7 K. With mode 2 and 3 peak currents more than an order of magnitude less than the critical current $I_{peak,3} < I_{peak,2} \ll I_c$ for $P_{in} = -35 \, dBm$, the non-monotonic mode dependence of Q_i^{-1} in Fig. 5.3(b) suggests it is related to the voltage amplitude or some other mechanism This will be revisited towards the end of the section.
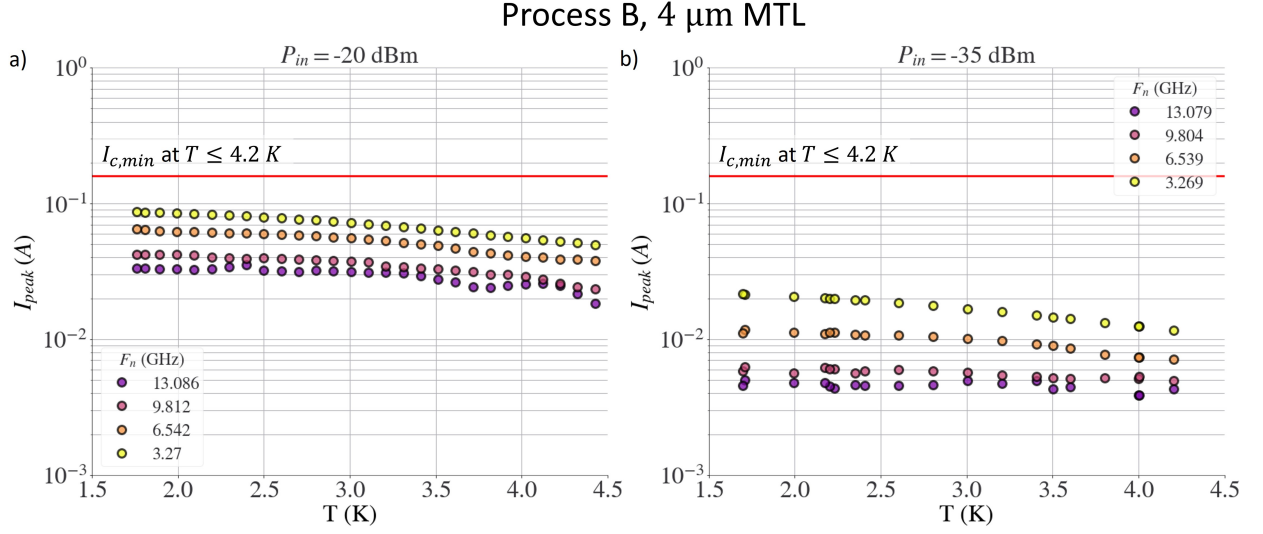
Figure 5.4: Calculated Peak currents in $4\,\mu m$ MTL as a function of temperature for 4 resonances at input powers (a) -20 dBm and (b) -35 dBm. The peak currents were calculated using Eqs. 5.5, 5.3, and measured transmission coefficient magnitude $|S_{21}|$ and Q_i for resonance at temperature T. The characteristic impedance was calculated to be $Z_0 = 8.2\,\Omega$ from HFSS measurements and known cross-sectional geometry. The red horizontal lines are a referenced expected minimum $I_c \approx 160\,mA$ estimated from $J_c \approx 20MA/cm^2$ [32].

It has now been established that the peak currents for all modes in $4\,\mu m$ MTL resonator at $P_{in} = -35dBm$ are much less than the critical current $I_{peak,n} \ll I_c$ for temperatures $T = 1.5 - 4.2\,K$. Fig. 5.5 below is a plot of the inverse internal Q-factor Q_i at 1.7 K for each mode index and MTLs 0.25 - 4 μm from process B. All mode 4 Q-factors $Q_{i,4}^{-1}$ have approximately the same magnitude for all MTL widths. Surprisingly, all mode 2 $Q_{i,2}^{-1}$ have the same magnitude. Conversely, modes 1 and 3 vary significantly by as much as a factor of 5. The same peak current and voltage analysis will be performed to determine if this is driven by an abnormal stimulus dependence.

Fig. 5.6 shows the Q_i as a function of calculated peak currents I_{peak} for process B 0.25 - 4 μm MTLs at 1.7 (a) and 4.2 K (b). At 4.2 K, all MTLs except 0.25 μm yield peak currents at least a factor of two less than I_c. This suggests that 0.25 μm MTLs should be measured with
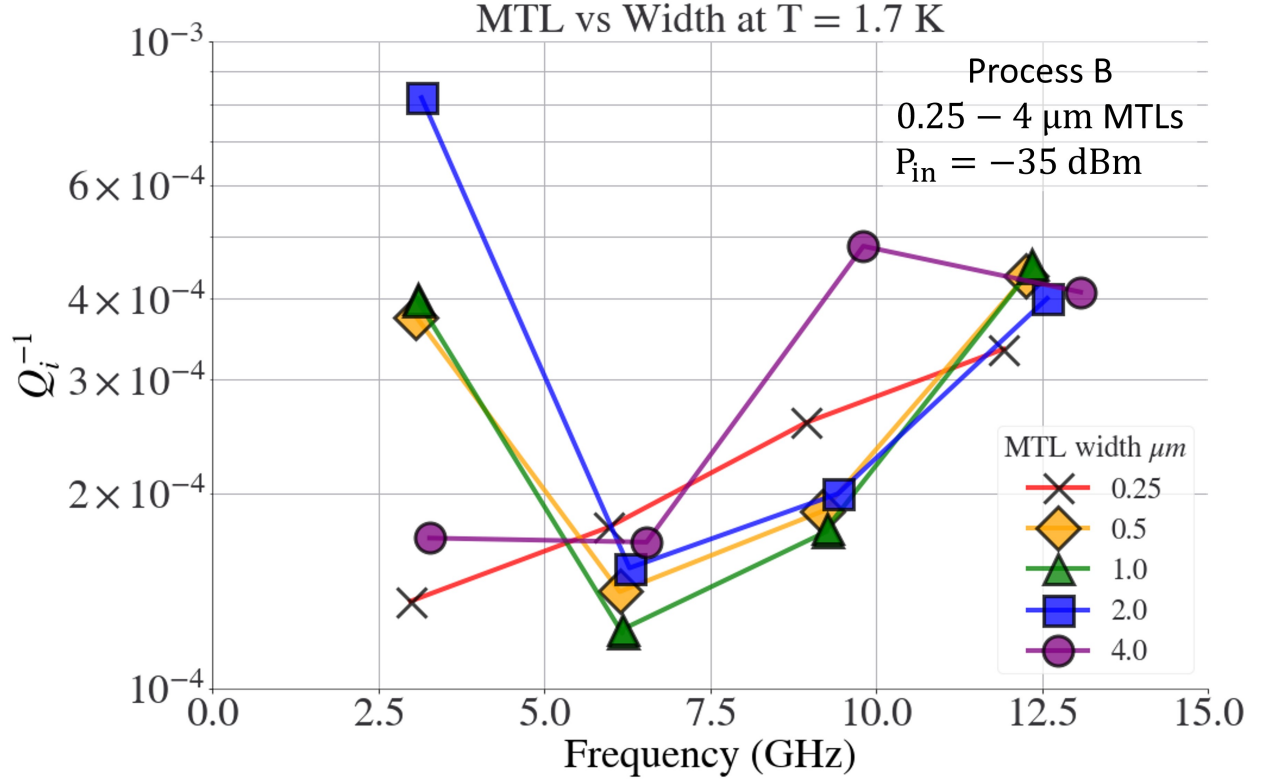
Figure 5.5: Q_i as a function of mode index at 1.7 K and $P_{in} = -35\ dBm$ for MTL widths $0.25 - 4\mu m$. Using fitting methods described reference [177], complex S_{21} fitting errors for Q_i, Q_e, and f_0 were less than 5% for all data shown here. Careful analysis of the raw data was performed, and no non-linear effects (e.g. resonant peak bifurcation) were found.

input powers $P_{in} \leq 35\,dBm$. At 1.7 K, the 4 and 2 μm MTLs have peak currents much less than the estimated critical current $I_{peak,1}, I_{peak,2} \ll I_c$. The 0.5 μm MTL peak currents come close and even cross over the estimated critical current, and could explain the decrease of the Q-factor for the fourth mode $Q_{i,0.5\mu m}^{-1} \approx 3 \times 10^{-3}$ and peak current $I_{peak} \approx 17\,mA$ Similarly, for the 1 μm MTL a similar increase in $Q_{i,1\mu m}^{-1}$ can be seen at the same $I_{peak} \approx 17\,mA$. This could also be explained by 1 μm I_{peak} within $< 2I_c$ of its critical current, inducing an additional loss due to some weak link at the peak current nodes in the resonator. Conversely, the 0.25 μm MTL resonant modes have peak currents residing up to $2I_c$, but the Q_i increases at increasing peak currents.

In summary, the high peak RF currents for all MTL resonator widths cannot explain the non-monotonic mode (frequency) dependence of Q_i alone. As briefly suggested, the peak currents occur at specific locations along the resonator, and could be exacerbating weak-links or material defects in the Nb wires or ground plane. This also goes for material defects in the TEOS dielectric. In light of this, the peak current/voltage technique and analysis could be used to accentuate nonlinear properties of the superconductor or dielectric losses due to spatially varying extrinsic material defects. Furthermore, the peak current analysis proved useful to determine an input power of -20 and -35 dBm was was too high to analyze the intrinsic superconductor and dielectric RF losses as a function of temperature and frequency with the current MTL resonator design. Regretfully so, these large input powers relative to the high coupling of the current MTL design was known, and measuring at lower powers posed difficulty in signal-to-noise in the current test fixture. This facilitated the design of a multi-plexed MTL design to further analyze RF losses in RQL interconnects at temperature $T = 1.7 - 4.2\,K$, and is the topic of the next section.
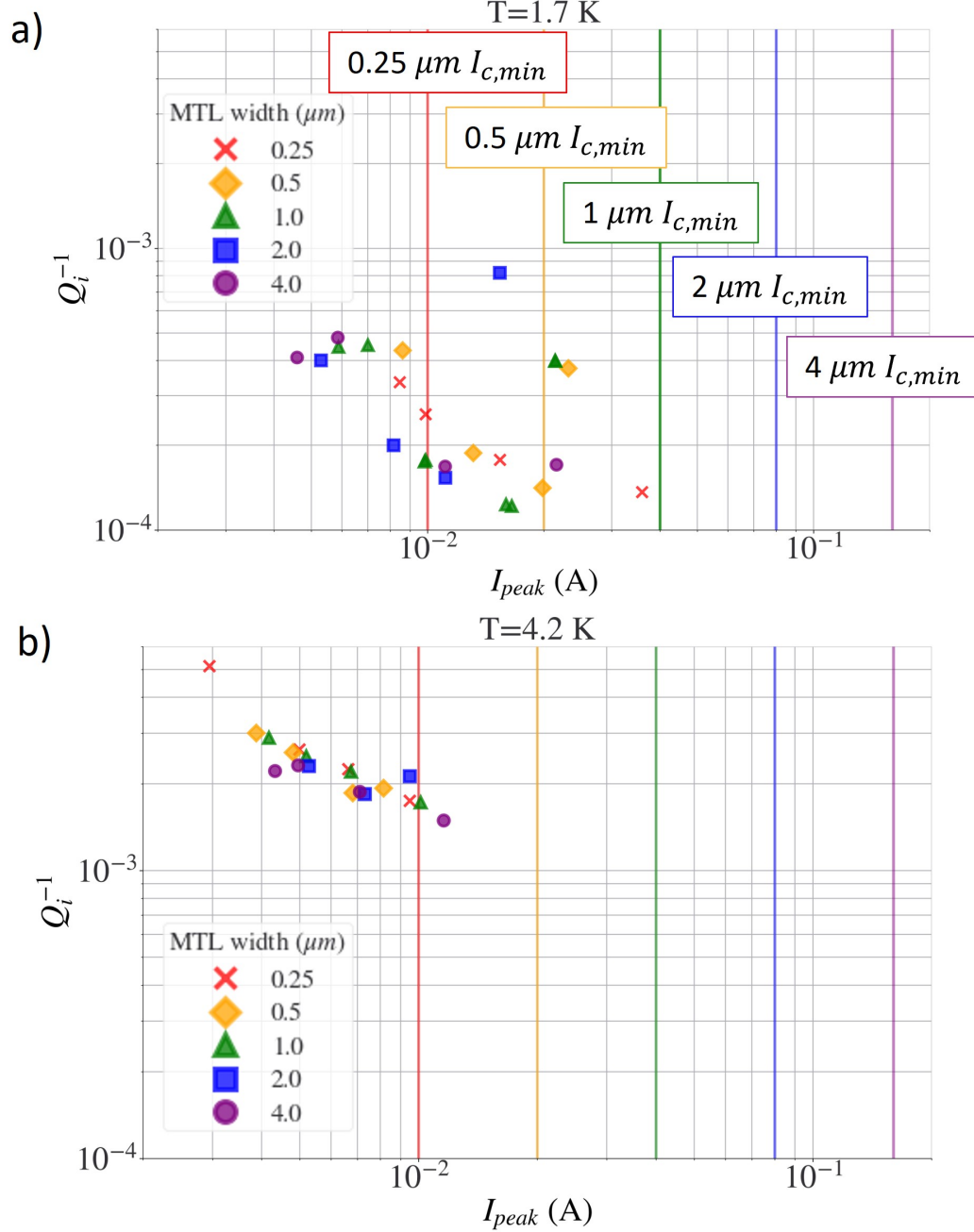
Figure 5.6: Calculated peak currents I_{peak} at (a) 1.7 K and (b) 4.2 K for MTL widths $0.25 - 4\,\mu m$ and mode indices 1-4 with respective $Q_i(\omega_n)$. The vertical lines are the assumed minimum critical currents I_c based on a critical current density $J_c = 20 MA/cm^2$ of superconducting Nb wires at 4.2 K [32]. The input power was $P_{in} = -35\,dBm$ for all measurements and data shown here.

5.3 Multiplexed Microstrip Transmission Line (MUX-MTL) Resonators

As seen in the last section, there was an anomalous mode dependence of the internal Q-factor Q_i. Especially at the lowest measured temperatures $T < 2\ K$. In this section, I will introduce a different resonator design with more resonances from 4-10 GHz to investigate the frequency and temperature dependence with better certainty.

Rather than measuring a single $\lambda/2$ resonator, the new design has many microstrip transmission line resonators that are capacitively coupled to a single feedline. This multi-plexed MTL resonator design will be termed MUX-MTL. Multiplexing resonators designs are typically used to measure many sensors at once, e.g. SQUID multiplexing [184, 185]. Here, the MUX-MTL is designed to measure the intrinsic RF losses in the Nb and TEOS. Conveniently, the frequency dependence of the material properties can be measured since each resonator needs to have a unique resonant frequency.

A layout of the MUX-MTL resonators can be found in Fig. 5.7. Here, the MUX-MTL highlighted in Fig. 5.7c will measured. These MTLs are coupled with coupling capacitors having the lowest value of $C_c \approx 25\ fF$. This yields a resonator coupling low enough to ensure (i) a high enough signal-to-noise (resonant peak size) at an input power of $-35\ dBm$ and (ii) transmitted powers to the resonator low enough to avoid peak current/voltage effects discussed in the last section. Fig. 5.7d shows a zoom in of a single MTL capacitively coupled (orange) to the MUX feedline (blue horizontal line running across the bottom). The feedline and MTL have a line width of $w = 0.75\ \mu m$. As opposed to MTLs in Chapter 4, each MTL here coupled to the MUX feedline are $\lambda/4$ resonators grounded at the end. A 7 mm $\lambda/4$ MTL has a fundamental mode of approximately 4 GHz. The grounding areas are enlarged to allow for current spreading.

Additionally, the feedline and $\lambda/4$ MTL have TEOS dielectric thicknesses of 500 nm with nominal 200 nm Nb ground plane and conductor strip thicknesses. A single MUX-MTL will be analyzed here and was fabricated using process C. The pertinent resonator information and results are summarized in Table 5.2.
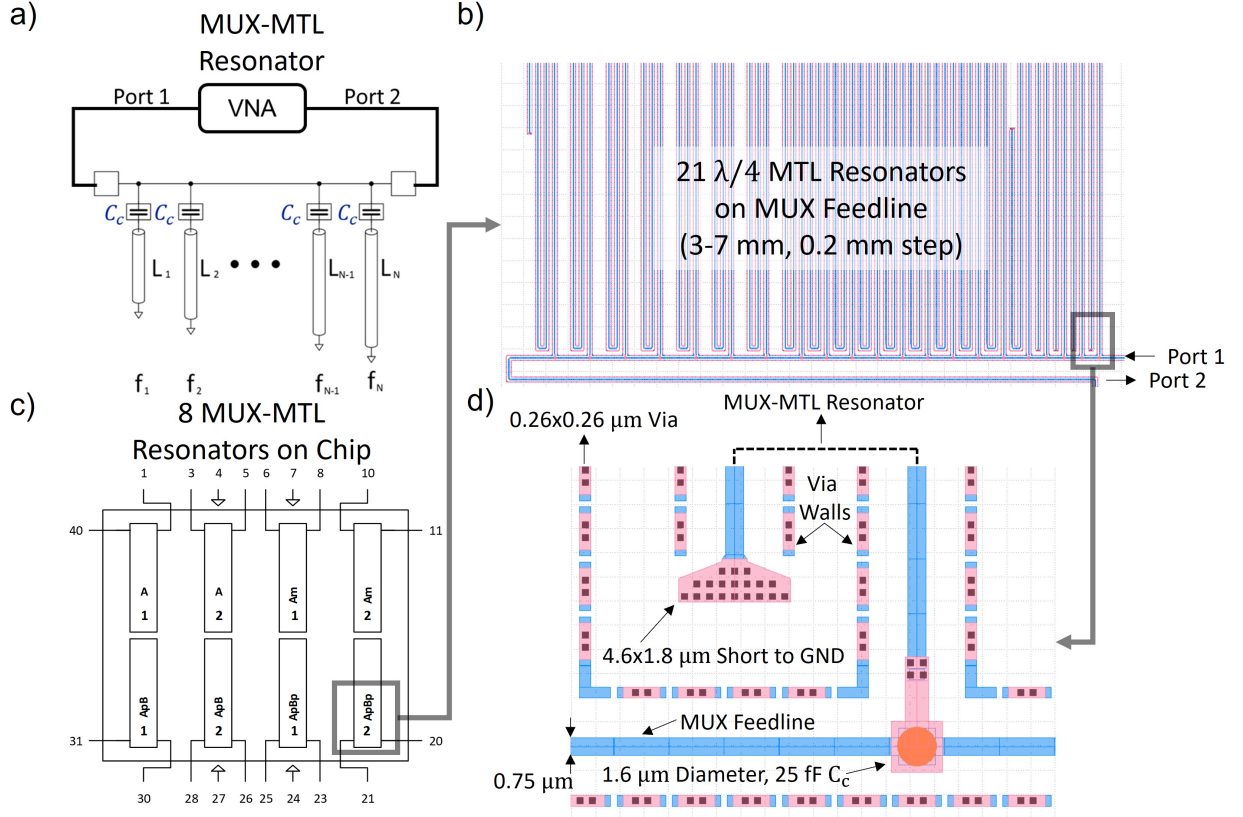
Figure 5.7: Physical design of a MUX-MTL resonator showing a) a diagram and the b) physical layout of a single MUX-MTL resonator. There are 21 $\lambda/4$ MTL resonators on a single MUX feedline with resonator lengths ranging from 3-7 mm with a 0.2 mm step. There are c) 8 MUX-Resonators designed on a single 5x5 mm chip. d) A zoom in of the first $\lambda/4$ MTL resonator connected to the MUX-Feedline coupled through a coupling capacitor with nominal capacitance of $C_c = 25fF$. The MTL and feedline width is 0.75 μm. The end of the MTL is shorted to GND with a wire fan out and many 0.25 μm vias to prevent the wire going normal at the current node. Via walls surround the feedline and MTL for isolation.

The MUX-MTL resonators were measured in the same way MTLs were measured and analyzed in Section 5.2. The resulting temperature dependent S-parameter measurements can be
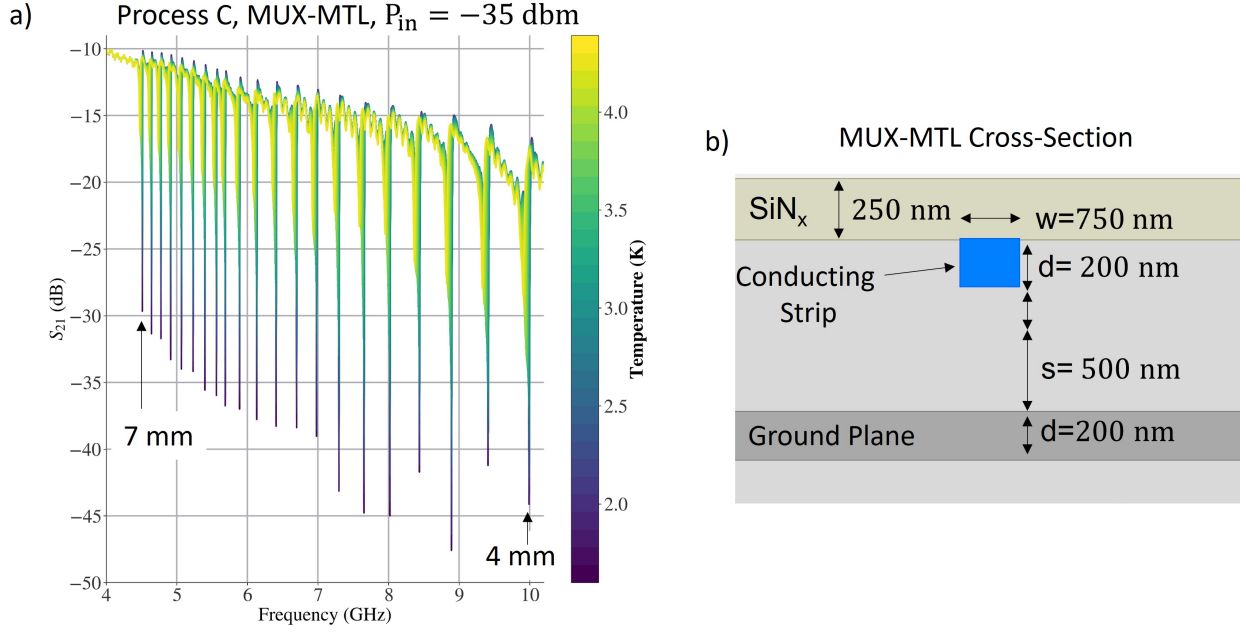
Figure 5.8: a) The measured S_{21} versus frequency as a function of temperature b) Cross-section diagram of the MUX-MTL geometry. The 21 resonances pertain are the fundamental modes of $\lambda/4$ MTLs with lengths ranging from 4-7 mm increasing in 0.2 mm increments.

found in fig. 5.8(a), and (b) is a cross section diagram of the MUX-MTL resonator.

All resonances in Fig. 5.8 were analyzed using an automated python script. The internal Q-factors Q_i, external (coupling) Q-factors Q_e, and resonant frequencies f_0 were extracted from a complex circle fitting script following the procedure in reference [177]

5.4 Using the Dispersive Deconvolution Method to Simultaneously Measure $\tan\delta(T)$ and $R_s(T)$

In this section, I will apply the dispersive loss deconvolution (DLD) method presented in Chapter 3 and applied in Chapter 4 to extract the temperature dependent loss tangent and intrinsic resistance simultaneously.

Fig. 5.9 shows the resulting fitted inverse internal Q-factors Q_{-1} of MUX-MTL $\lambda/4$ resonators

152
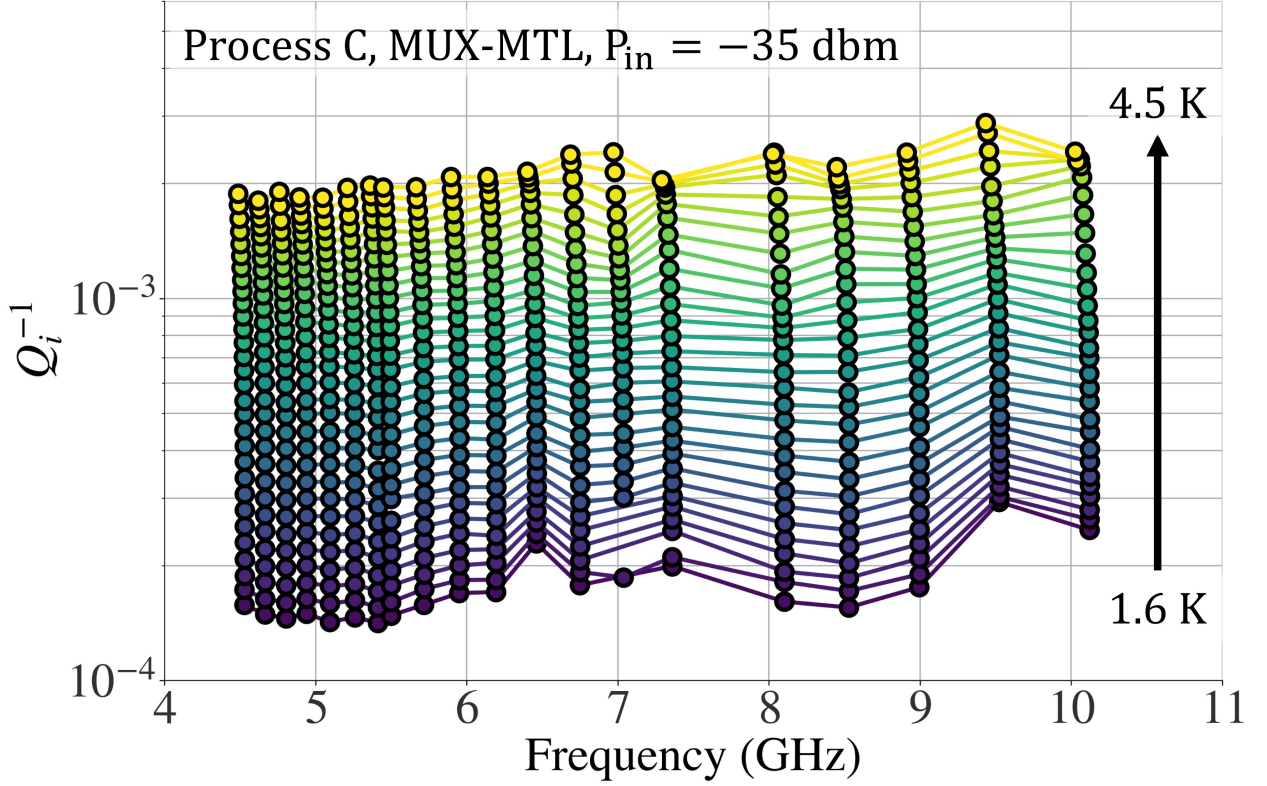
Figure 5.9: Frequency dependence of the inverse internal Q-factor Q_i at successive temperatures from 1.6-4.5 K at a constant input power of $P_{in} = -35\ dBm$. Complex S_{21} fitting procedure was performed on data from Fig. 5.8. The $0.75\ \mu m$ MUX-MTLs were fabricated using process C described in Chapters 3 and 4.

from S-Parameter measurements in Fig. 5.8. At 1.6 K, a non-monotonic frequency dependence

of Q_i^{-1} can be seen, and will be discussed in the next section.

It is important to first discuss the measurement sensitivity of the DLD method before fitting

the data in Fig. 5.9. For parallel plate resonator measurements, it was found by Taber *et al.* that

the measurement sensitivity of the intrinsic resistance was $R_{s0} \approx 5\ \mu\Omega$ [136], and he needed

to vary the resonator geometric factor to get accurate measurements of R_{s0}. To estimate the

DLD measurement sensitivity of R_{s0} and $\tan \delta$ using MTL resonators, Eqs. 3.12 and 3.13 from

Section 3.3 can be re-written as follows

$$Q_{i,nd}^{-1}(T) = \frac{R_{s0}(T)}{\Gamma_{c0}}(\omega/\omega_0) + \tan\delta_0(T) \tag{5.7}$$

$$Q_{i,d}^{-1}(T) = \frac{R_{s0}(T)}{\Gamma_{c0}}(\omega/\omega_0) + \tan\delta_0(T)(\omega/\omega_0)^{b-1} \tag{5.8}$$

$$R_{s0}^{lim}(T) \approx \Gamma_{c0}\tan\delta_0(T) \tag{5.9}$$

where ω is the measurement frequency, Γ_{c0} is partial geometric factor of the MTL, b is the free fitting power exponent assuming a dispersive loss tangent, and $R_{s0}(T)$ and $\tan\delta_0(T)$ are the intrinsic resistance and loss tangent at reference frequency ω_0 at temperature T, respectively. Eq. 5.7 can be used to fit data when a non-dispersive loss tangent can be assumed. Eq. 5.8 is used in this work to fit data assuming a dispersive loss tangent where $0 < b < 1$. Eq. 5.9 is an estimate of $R_{s0} = R_{s0}^{lim}$ measurement sensitivity at reference frequency ω_0 from reference [136]. Similarly, the approximate measurement sensitivity for the loss tangent is $\tan\delta_0^{lim} \approx R_{s0}/\Gamma_{c0}$ In other words, when the R_{s0} and $\tan\delta$ are comparable for a given resonator geometry, it is important to utilize the frequency dependence, temperature dependence, or some other means to deconvolve the two loss mechanisms. The latter case was demonstrated in the previous chapter.

In this section, S-parameter measurements are performed down to 1.6 K, and it is expected the Nb R_{s0} will exponentially decrease $R_{s0} \propto (1/T)exp(-1/T)$ (see Eq. 2.27). Assuming TLS relaxation proccesses dominate the dielectric loss below 4.2 K, the TEOS $\tan\delta_0$ is expected to decreases with $\approx T^3$ dependence (see Section 2.3). At 4.2 K, the TEOS loss tangent is $\tan\delta \approx 1 \times 10^{-3}$. The geometric factor for the $0.75\mu m$ MUX-MTL is approximately $17.3\ m\Omega$. The approximate sensitivity of R_{s0}^{lim} at ω_0 and 4.2 K is then $17\ \mu\Omega$. Taking advantage of the conductor

Q-factor frequency dependence $Q_c^{-1} \approx \omega$, the intrinsic resistance can still be deconvolved at 4.2 K using the DLD method, as the losses are still comparable. Although, at temperatures far below 4.2 K, the case $R_{s0}^{lim} \ll \Gamma_{c0} \tan \delta_0$ will yield $Q_i \approx \tan \delta$, and vice versa when temperature is much greater than 4.2 K $Q_i \approx \Gamma_{c0}/R_{s0}$.

The DLD method is applied to data in Fig. 5.9 and $R_{s0}(T)$ and $\tan \delta(T)$ are deconvolved and shown in Fig. 5.10(a) and Fig. 5.10(b), respectively. The x-axis in Fig. 5.9(a) is T_c/T where at superconducting critical temperature of $T_c = 9.2\ K$ was assumed. Both a disperive (black) and non-disperive (blue) $\tan \delta$ were assumed using Eq. 5.7 and 5.8, respectively. Note, the DLD method was only applied to the resonant peaks between 4.5-5.5 GHz and 8-10 GHz, ignoring the "loss peaks" at 6.5 and 9.5 GHz. These loss peaks will be discussed in the next sections.

The dashed lines in Fig. 5.9(a) are calculated using Eq. 5.9 and serve as a reference for the approximate measurement sensitivity of R_{s0} as a function of temperature. At $T_c/T = 3$ for the non-disperive data (blue), the R_{s0} is approximately a factor of two below the sensitivity limit $R_{s0} \approx 2R_{s0}^{lim,nd}$. Whereas the dispersive R_{s0} (black) is only about 10% below $R_{s0}^{lim,d}$ for non-dispersive (blue) dashed line and approximately a factor of 3 above the dispersive (black) dashed line. This suggests that $\tan \delta$ is frequency dependent and has a power exponent of $b \approx 0$ yielding $\tan \delta \propto \omega^{-1}$. Furthermore, the dispersive model is suggested to be more sensitive to R_{s0} in the approximate temperature range $T_c/T = 2-3$. The R_{s0} plateau at approximately $3\ \mu\Omega$ is an artifact of the measurement sensitivity, and is not a residual resistance. Typical residual resistance for Nb thin films are $R_{res} \approx 1-20\ n\Omega$ and do not exceed $100\ n\Omega$.

The expected temperature dependence of R_{s0} was fit to the dispersive data using Eq. 2.27 with fitted Nb superconducting gap of $\Delta = 19.5 \pm 2.2\ K$. Benvenuti *et al.* measured a superconducting gap of $\Delta = 19.6\ K$ for Nb thin films [64]. Assuming a superconducting critical

temperature of $T = 9.2\ K$, the gap ratio is estimated to be $\Delta/k_B T_c = 2.1 \pm 0.2$, and is within 10% of the expected gap ratio 1.97 for Nb [46]. Valente-Feliciano measures a slightly lower gap ratio of 1.89 for Nb thin films [71].

Fig. 5.9(b), the assumed dispersive (black) and non-dispersive (blue) $\tan\delta$ temperature dependence was fit to a power law expected when dielectric loss is dominated by TLS relaxation (see Eq. 2.37). Using the dispersive model fit to deconvolved TEOS $\tan\delta$, the power exponent is $n = 2.5$. Microwave dielectric measurements of amorphous silica have found $T^{2.4}$ from 2-8 K in the TLS relaxation regime at 10 GHz [84]. TEOS deposited at low temperatures of 150 C is considered amorphous [74]. This is the first indication that TLS relaxation processes are present in TEOS at temperatures below 3 K and will be discussed further in the next section.

In this section, I have demonstrated the DLD method is capable of deconvolve R_s and $\tan\delta$ as a function of temperature. From this, I estimated the the superconducting gap of the Nb in the MUX-MTL in good agreement with typical Nb thin films. Additionally, from the fitted temperature dependence i found that the TEOS $\tan\delta$ shows signs of TLS relaxation.
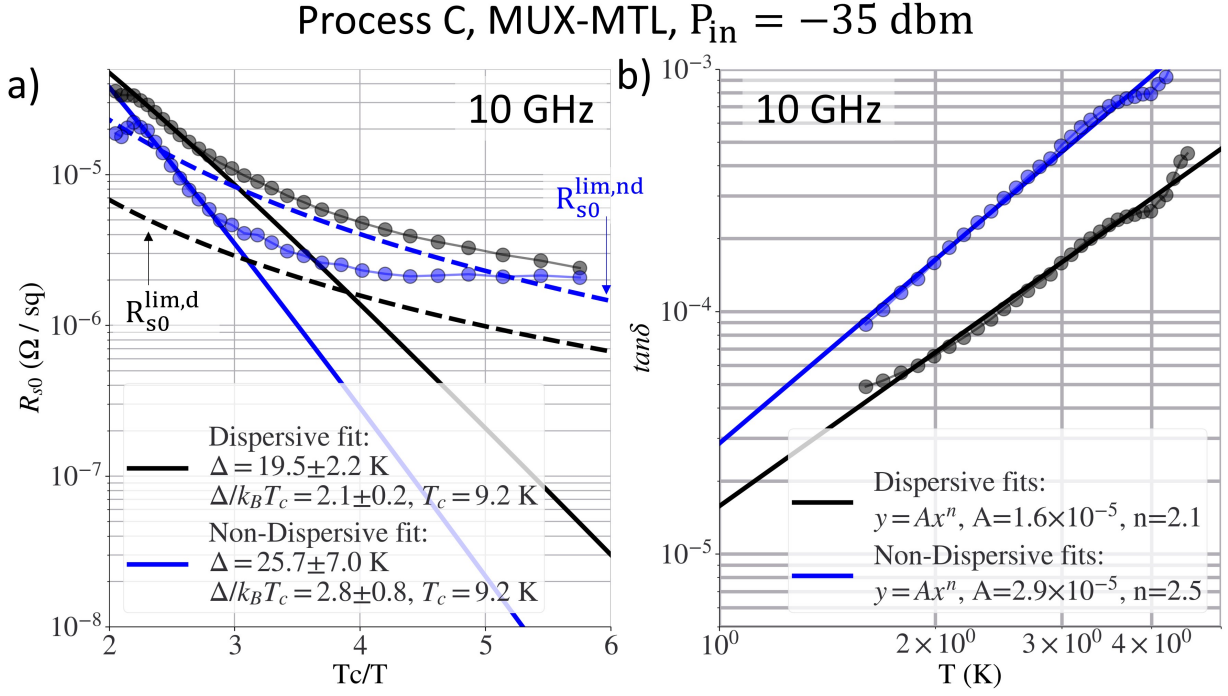
Figure 5.10: The deconvolved a) R_{s0} and b) $\tan\delta$ as a function of T_c/T using the DLD method at reference frequency $\omega_0/2\pi = 10 GHz$. The critical temperature is assumed to be $T_c = 9.2\ K$. Data from Fig. 5.9 were fit to Eq. 5.7 (2 parameter fit) and 5.8 (3 parameter fit) assuming a non-dispersive and dispersive (frequency dependent) loss tangent, respectively. The DLD method was only applied to the resonances between 4.5-5.5 GHz and 8-10 GHz, ignoring the "loss peaks" at 6.5 and 9.5 GHz. The dashed lines in a) are calculated using Eq. 5.9 showing the approximate sensitivity of the intrinsic resistance for the dispersive $R_{s0}^{lim,d}$ and non-disperive fits $R_{s0}^{lim,nd}$. The solid lines in a) are fits to the R_{s0} temperature dependence using Eq. 2.27 in the range $T_c/T = 2.2 - 2.5$. The solid lines in b) are fits to the $\tan\delta$ temperature dependence using Eq. 2.37 for the entire temperature range. In a) the R_{s0} plateau in at approximately $3\ \mu\Omega$ is an artifact of the measurement sensitivity, and is not a residual resistance.

5.5 TLS Absorption and Relaxation Microwave Loss in TEOS Above $1\,K$

In this section, I will claim signatures of TLS loss in TEOS at temperatures below 3 K supported by measurements of the the relative dielectric constant ε_r and dielectric loss tangent $\tan\delta$. Furthermore, as temperature is decreased, there is a clear transition from TLS relaxation to TLS absorption dominating the RF loss at approximately 2.25 K. This temperature transition as a non-monotonic frequency dependence. Below is a summary table for the resonant frequency dependent measurements and fitting to TLS models.

The electric perturbation of a two-level systems (TLSs) interacting with the phonon lattice is analogous to the acoustic case for [79, 83]. The Hamiltonian matrix $H = H_0 + H'$ describes the system where H_0 is TLS without perturbation and H' is due to the electric field. The magnitude of the diagonal and off-diagonal elements in H' are the permanent dipole moment μ and induced dipole moment μ', respectively. The permanent dipole moment describes the TLS relaxation process expressing the shift in energy splitting caused by the electric field and is characteristic of a TLS relaxation process. The induced dipole moment describes the resonant absorption of TLSs by the coupling between the TLSs and electric field. The latter TLS resonant absorption process can be saturated by strong electric fields and dominates at temperatures approximately below $1\,K$. Conversely, the former relaxation process cannot be saturated by an electric field and is the dominant process at temperature approximately above $1\,K$ [79]. Consequently, depending on the temperature, applied electric field, and the angular frequency ω, a non-monotonic dependence of the relative dielectric constant ε_r and loss tangent $\tan\delta$ can occur (see Fig. 2.4 in Chapter 2). Note, for a weak electric field as temperature is increased from $0\,K$, the cross over temperature will shift to increasing (decreasing) temperatures as ω is increased (decreased), reminiscent of

an increased (decreased) sampling of higher energy resonant absorption TLSs prior to relaxation dominating. Both the change in dielectric constant and loss tangent data will be fit assuming absorption and relaxation TLS processes.

The temperature dependent change in relative dielectric constant ε assuming the superposition of TLS absorption and relaxation contributions is typically written as [186]

$$\frac{\Delta\varepsilon(T)}{\varepsilon(T_0)} = \frac{\varepsilon(T) - \varepsilon(T_0)}{\varepsilon(T_0)} = \frac{\Delta\varepsilon_{abs} + \Delta\varepsilon_{rel}}{\varepsilon(T_0)} \tag{5.10}$$

where $\varepsilon(T)$ is the temperature dependent relative dielectric constant of the material, T_0 is typically the lowest measured temperature and is arbitrary, and $\Delta\varepsilon_{abs}$ and $\Delta\varepsilon_{rel}$ are the change in dielectric constant due to TLS resonant absorption and relaxation, respectively. The relative dielectric constant of TEOS is approximately $\varepsilon \approx 4.2$ [73] and agree with estimations from measured data in Section 4.2.

At low temperatures, the resonant absorption contribution to the change in dielectric constant can be fit to

$$\Delta\varepsilon_{abs}(T) = 4\pi \, n\mu'^2 \left[Re\Psi\left(\frac{1}{2} + \frac{\hbar\omega}{2\pi i k_B T}\right) - Re\Psi\left(\frac{1}{2} + \frac{\hbar\omega}{2\pi i k_B T_0}\right) - \ln\frac{T}{T_0} \right] \tag{5.11}$$

where $n\mu'^2$ is the induced dipole coupling of TLSs having a density of states n, T and T_0 are the measurement and lowest arbitrary reference temperature, respectively, k_B is the Boltzmann constant, $\hbar$ is the reduced Planck constant, and $Re\Psi$ represents the real part of the digamma function [187]. Note, the first and second terms in brackets dominant at temperature $\ll 1 \, K$ and a frequency dependence can be measured. For measurements here where $T > 1.5 \, K$,

the natural natural logorithmic temperature dependence dominates and can be assumed to be frequency independent.

Here, we assume the relaxation process is mediated by the so-called single-phonon assisted tunneling as the TLSs relax back to equilibrium. This is also commonly referred to as the one-phonon process and is in opposition to coherent unassisted tunneling motion[79]. Assuming a constant density of states n, the TLS relaxation process responsible for the change in dielectric constant can be modeled by

$$\Delta\varepsilon_{rel} = \frac{4\pi}{3}n\mu^2 \int_0^\infty \frac{df}{dU}\left(1 + \omega^2\tau^2\right)^{-1} dU \tag{5.12}$$

$$\tau^{-1} = a(Uk_BT)^3 \coth\left(U/2\right) \tag{5.13}$$

$$f = \left(e^U + 1\right)^{-1} \tag{5.14}$$

where $n\mu^2$ is the permanent dipole coupling, f is the Fermi function, ω is the measurement frequency under an applied electric field, and τ is the TLS relaxation time commonly referred to as the radiative lifetime of TLSs T_1 [79, 79]. Found from acoustic measurements the material constant a is

$$a = \frac{\bar{M}^2}{\rho v_a^5} \frac{1}{2\pi\hbar^4} \tag{5.15}$$

$$\bar{M}^2 = (M_l^2/c_l^5 + 2M_t^2/c_t^5)/(c_l^{-5} + 2c_t^{-5}) \tag{5.16}$$

where $\bar{M}$ is the average coupling energy [188], v_a is the average acoustic velocity of two transverse sound velocities and one longitudinal sound velocity, ρ is the mass density of the dielectric, and

subscripts l and t in Eq. 5.16 are the longitudinal and transverse components, respectively. For vitreous silica, $\bar{M}$ ranges from approximately $0.28 - 0.34 \, eV$ [188], $\rho \approx 2.2 \times 10^3 kg/m^3$, and $v_a \approx 4.7 \times 10^3 \, m/s$ averaging the transverse and longitudinal components. Pohl *et al.* gives a comprehensive review of these material constants for various glassy metals and dielectrics [93]. For glassy silicon oxides, ρ and $v_{t,l}$ can decrease by approximately an order of magnitude for high porosity.

The measured resonant frequency for reactively coupled microstrip transmission lines is proportional to the relative dielectric constant by $f_0 \propto \varepsilon^{-1/2}$. Using this relationship and Eq. 5.10, the temperature dependent resonant frequency data in Fig 5.9 can be converted by

$$\frac{\Delta\varepsilon(T)}{\varepsilon(T_0)} = \frac{f_0^2(T) - f_0^2(T_0)}{f_0^2(T_0)} \tag{5.17}$$

where $f_0^2(T)$ is the temperature dependent resonant frequency of each resonator in the MUX-MTL, and $f_0(T_0)$ resonant frequency at the lowest temperature measured T_0.

Fig. 5.11 shows the resulting fits to Eq. 5.10 to data from Fig 5.9. The data was fit with a Python script using the "Powell" minimization method in SciPy package [189]. The data was fit at each data power where the measured resonant frequency and temperature were inputs. The dielectric constant at T_0 was assumed to be $\varepsilon = 4.2$ [73] and the material constant in Eq. 5.15 was assumed to be $a = 2 \times 10^{75} \, J^{-3} s^{-1}$. The two fitting parameters were the permanent and induced dipole coupling constants $n\mu^2$ and $n\mu'^2$ in equations Eq. 5.11 and Eq. 5.12, respectively. The dip in the data is reminiscent of a transition from TLS resonant absorption to relaxation processes dominating the dielectric constant change as temperature is increased from T_0. The magnitude offset for the $7\,GHz$ (4.4 mm) resonator in the MUX-MTL is due to a slightly higher T_0. Because

of this, the fitted data for the $7\,GHz$ resonator will be ignored due to minimization fitting artifact. In this context, the maximum change in $\Delta\varepsilon(T)/\varepsilon(T_0)$ is negative showing a slight decrease of the dielectric constant of approximately 0.06%. Surprisingly, this value is in agreement with Schickus *et al.* of vitreous silica with 1000 ppm OH- concentration [186]. Although, his maximum change in dielectric constant occurs at a much higher temperature of approximately 7 K, whereas in Fig. 5.11 occurs at approximately 2.2 K. Starting from 3 K and decreasing in temperature and following the color scale, the relaxation regime shows almost a monomonic frequency dependence, where for increasing frequencies the dielectric constant is effectively decreasing. At and below the dip around 2.2 K, a non-monotonic frequency dependence of dielectric constant change is visible. This will be probed further in the fits of $n\mu^2$ and $n\mu'^2$.

Fig. 5.12 is a plot of the data fitting (solid lines) from Fig. 5.11. Again, the 7 GHz data here will be ignored due to a fitting artifact. Immediately it can be seen that the permanent dipole coupling is 3 orders of magnitude larger than the induce dipole coupling (notice scale bars on left and right y-axis). This is not understood and reported values for all permanent dipole coupling constants for glassy dielectrics do not exceed 1×10^{-3} [89, 93, 188]. Table 5.1 is a summary of measured permanent and induced dipole coupling for various materials. From this table, it can be seen that the permanent and induced diople coupling increases in vitreous silica by approximately an order of magnitude when the concentration of hydroxide concentration is increased. This is supported by the theory where hydroxide ions are the dominant TLS system coupling to phonons and the electromagnetic waves [186]. The TLS states in borosilicate glass have a higher permanent dipole coupling to phonons relative to vitreous silica [89]. Although predominantly a crystalline solid electrolyte, it is assumed that the existence of low-energy excitations in $\mathrm{Na} - \beta - \mathrm{Al_2O_3}$ is a consequence of a high degree of disorder in the $\mathrm{Na^+}$-sublattice
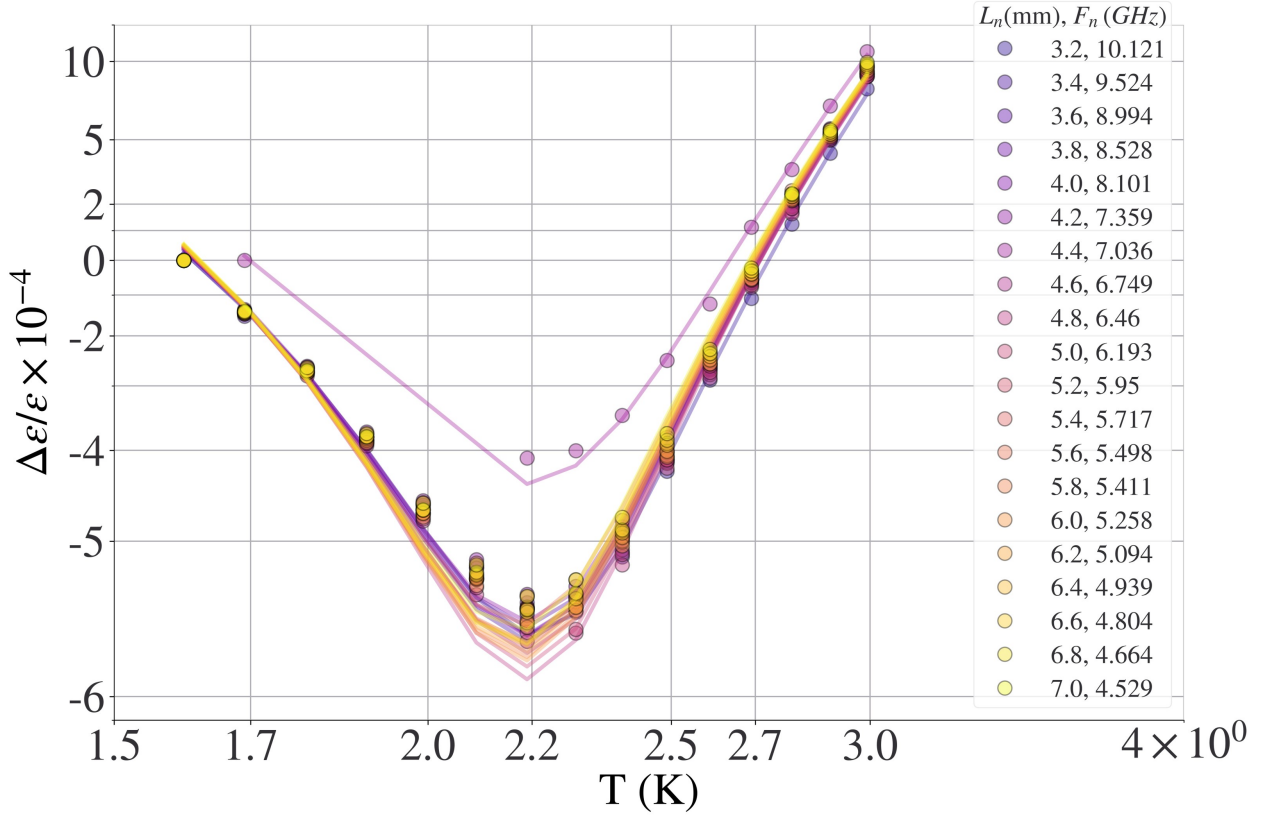
Figure 5.11: Temperature dependence of the dielectric constant ε for $0.75\mu m$ MUX-MTLs fabricated from process C at a constant VNA input power of $P_{in} = -35\ dBm$. The data from Fig 5.9 was converted into $\Delta\varepsilon = \varepsilon(T) - \varepsilon(T_0)/\varepsilon$ using Eq. 5.17. The data was fit using Eq.s 5.10, where the total change in dielectric constant is the superposition of the TLS absorption and TLS relaxation contributions using Eq.s 5.11 and 5.12, respectively. assuming material constant $a = 2 \times 10^{75} J^{-3} s^{-1}$ [186]. Refer to Summary Table 5.2

and is considered amorphous [94, 190]. Furthermore, $\mathrm{Na} - \beta - \mathrm{Al_2O_3}$ has the highest induced dipole coupling with the electromagnetic waves and most likely due to its ionic nature. $\mathrm{Li_3N}$ has a much lower induced dipole coupling and the TLS low energy excitations are suggested to be coming from hydrogen ions [190]. The permanent dipole coupling for $\mathrm{Na} - \beta - \mathrm{Al_2O_3}$ was not calculated, but based on the high induced dipole coupling, it is possible the permanent dipole coupling can be of order 10^{-2} but it is unlikely the coupling is as high as 10^{-1}, as seen by the extract values measured for TEOS in Fig. 5.12. Nevertheless, this can be further examined in future experiments at lower temperatures and power dependent measurements as performed by Schickfus *et al.* [84].

Table 5.1: A summary table of measured permanent dipole coupling $n\mu^2$ and induced dipole coupling $n\mu'^2$ in various materials at the respective measurement frequency. The values were taken from references [Schickfus1976] [186], [SchickfusThesis1977] [89], [Strom1978] [94], [Baumann1980] [190].

	Permanent Dipole Coupling $n\mu^2$	Induced Dipole Coupling $n\mu'^2$	Measurement Frequency (GHz)	Material Type
Vitreous Silica <100 OH$^-$ ppm by weight [Schickfus1976]	7×10^{-5}	1×10^{-5}	11	Glassy, dielectric
Vitreous Silica 1200 OH$^-$ ppm by weight [Schickfus1976]	3.4×10^{-4}	1.5×10^{-4}	11	Glassy, dielectric
Borosilicate glass [SchickfusThesis 1977]	6×10^{-3}	3×10^{-4}	11	Glassy, dielectric
Na-β-Al$_2$O$_3$ [Strom1978]	-	$1.5 - 1.7 \times 10^{-3}$	11.5	Crystalline, Solid electrolyte
Li$_3$N [Baumann1980]	-	3.4×10^{-6}	0.63	Crystalline, Ionic Conductor

Care was taken in the evaluation of the integral in Eq. 5.12, and the material constant a is not expected to change orders of magnitude. Furthermore, if this were real, the 3 orders of

magnitude increase would have to be comming from the permanent dipole moment, as the TLS density of states n cannot increase beyond approximately an order of magnitude.

Aside from the magnitude difference, the results in Fig. 5.12, the data can still be discussed qualitatively. The permanent dipole coupling increases with increasing frequency, which is in agreement with the notion that higher frequencies accesses higher energy insatiable TLS relaxation processes. The induced dipole moment decreases with increasing frequency, and is also in agreement with intuition of TLS absorption in that higher energy absorption processes contribute to the change in phase velocity (dielectric constant) in the resonator. Another way to describe the decrease in induced dipole coupling is that at higher frequency, it is expected that TLS absorption can dominate at higher temperatures [89].

The magnitude discrepancy for fitted values for $n\mu^2$ measured via temperature dependence resonant frequency will be investigated further and compared with temperature dependent data of the dielectric loss tangent.

5.6   Dielectric Loss Spectroscopy

In this section, the dielectric loss tangent will be fit to TLS resonant absorption and relaxation models to determine the frequency dependence of the permanent and induced dipole coupling constants $n\mu^2$ and $n\mu'^2$, respectively. The data fitting models will be introduced first, followed by a suggested explanation of the anomalous loss peaks in Fig. 5.9 at 6.5 and 9.5 GHz.

As a consequence of the TLS tunneling and relaxation process scattering phonons, a non-monotonic temperature dependence of the dielectric loss tangent $\tan\delta$ can be measured and depends on the microwave electric field strength [84].
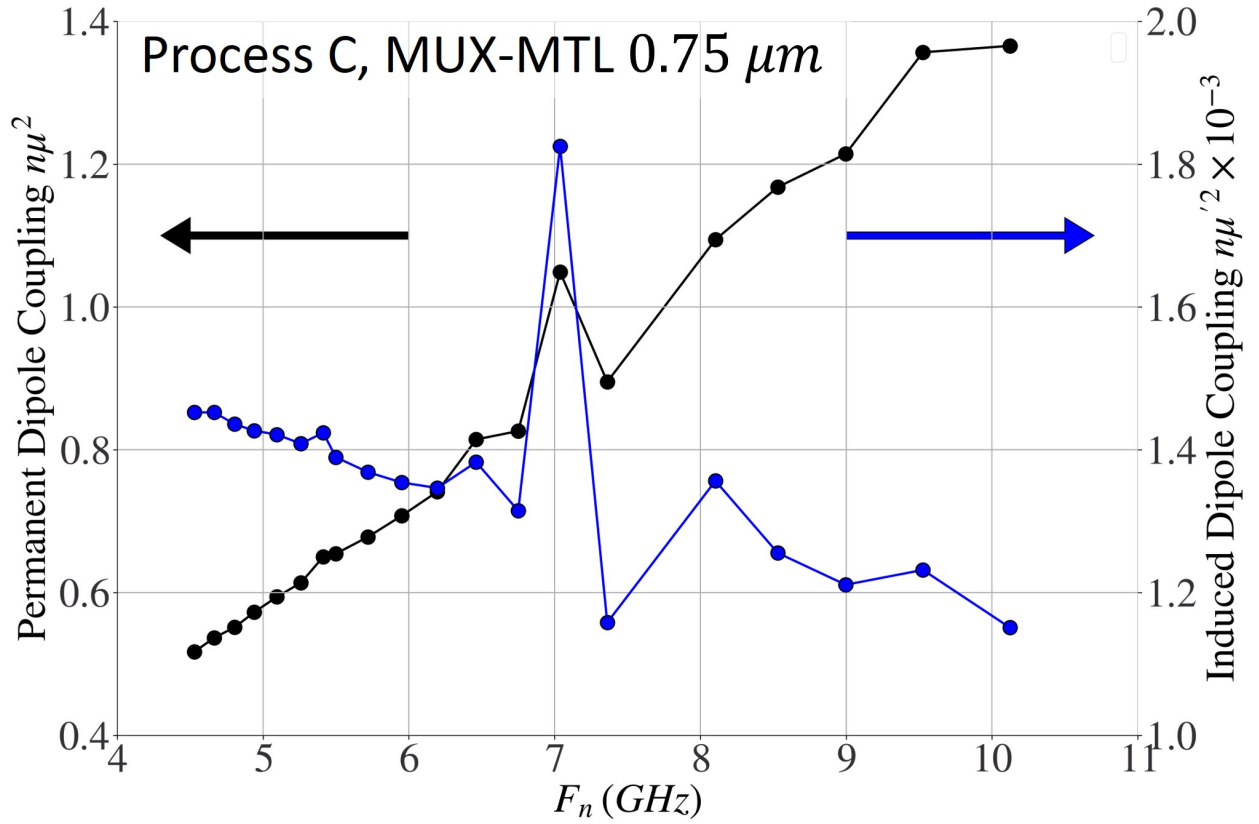
Figure 5.12: Frequency dependence of the permanent and induced dipole coupling from the data fits in Fig. 5.11. Refer to Summary Table 5.2 for assumed parameters and results comparison to $\tan \delta$ fits. MUX-MTL, *Process B*, $Q_i^{-1}(T)$

The superposition of TLS processes $\tan\delta$ can be written as

$$\tan\delta = \tan\delta_{abs} + \tan\delta_{rel} \tag{5.18}$$

where $\tan\delta_{abs}$ and $\tan\delta_{rel}$ are the resonant absorption and relaxation contributions, respectively, and here I am assuming these are the only processes involved in the microwave loss in the temperature range $T = 1.5 - 3\,K$ and frequency range $4 - 10\,GHz$.

The measured loss tangent from resonant absorption can be fit to the following

$$\tan\delta_{abs} = n{\mu'}^2 \frac{4\pi}{3} \frac{\tanh\frac{\hbar\omega}{2k_BT}}{(1 + J/J_c)^{1/2}} \tag{5.19}$$

where $n{\mu'}^2$ is the induced dipole coupling constant, J is the microwave energy intensity, and J_c is the critical energy intensity. For $J > J_c$, resonant TLSs undergoing resonant absorption are saturated and $\tan\delta_{abs}$ continually decreases as temperature is decreased. For $J < J_c$ TLS resonant absorption processes induce loss and an upturn in $\tan\delta$ is observed as temperature is decreased to absolute zero [84].

For microwave dielectric loss dominated by TLS relaxation, data can be fit to the following equation [89]

$$\tan\delta_{rel} = n\mu^2 \frac{T^3}{\omega} \left[\frac{\bar{M}^2}{\rho v_a^5} \frac{\zeta(4, 0.5)k_B^3}{8\pi\hbar^4} \right] \tag{5.20}$$

where $n\mu^2$ is the permanent dipole coupling constant, $\zeta(4, 0.5) = 97.8$ is the Riemann zeta function [89], ρ is the mass density of the dielectric, $\bar{M}^2$, v_a are the average coupling and acoustic velocity introduced in Eqs. 5.15-5.16, respectively.

167

Before fitting to the above models and extracting $n\mu^2$ and $n\mu'^2$, the power law fits to $\tan\delta$ data in Fig. 5.13 will be discussed. The resulting power law fits in Fig. 5.13(b) show the power exponent is close to 3, strongly suggesting the TEOS dielectric loss is dominated by TLS relaxation processes. The power exponent measured for vitrious silica is approximately 2.4 [84]. Power exponents below 3 are typical, as the curvature of the temperature dependence can change rapidly as a consquence of either TLS absorption at lower temperatures or classical relaxation processes at higher temperatures inducing the so called "plataeu" effect [93].

Using Eqs. 5.18-5.20 above and data in Fig. 5.13, the TEOS dielectric loss tangent is fit for MUX-MTL resonators and shown in Fig. 5.14. The fitting results of temperature dependence in $Q_i^{-1}(T)$ and resonant frequency $f_0(T)$ can be found in Summary Table 5.2.

Notice, the data (circles) and fits (solid lines) show non-monotonic frequency dependence looking vertically at a particular temperature below 2.5 K. Assuming an onset of TLS resonant absorption below 2.5 K, it can be inferred that different frequencies are coupling stronger to resonant TLSs. The converse argument is that each resonator is coupling non-monotonically to the feedline, inducing different power densities circulating in the resonator. The latter will be explored in the next graph followed by frequency dependence of dipole coupling constant fits from Fig. 5.14.

Fig. 5.15 shows the calculated stored power and peak currents in the MUX-MTL resonators. It can be seen quantitatively that the circulating power in the resonators scale monotonically with frequency at all temperatures. This is supporting the claim that the non-monotonic dependence in Fig. 5.14 is not an artifact of the variation in resonator coupling. Although, the peak currents in the resonator for the lowest frequency resonators are less than a factor of two away from the assumed worst case critical current for these lines. It is conceivable that this could induce non-
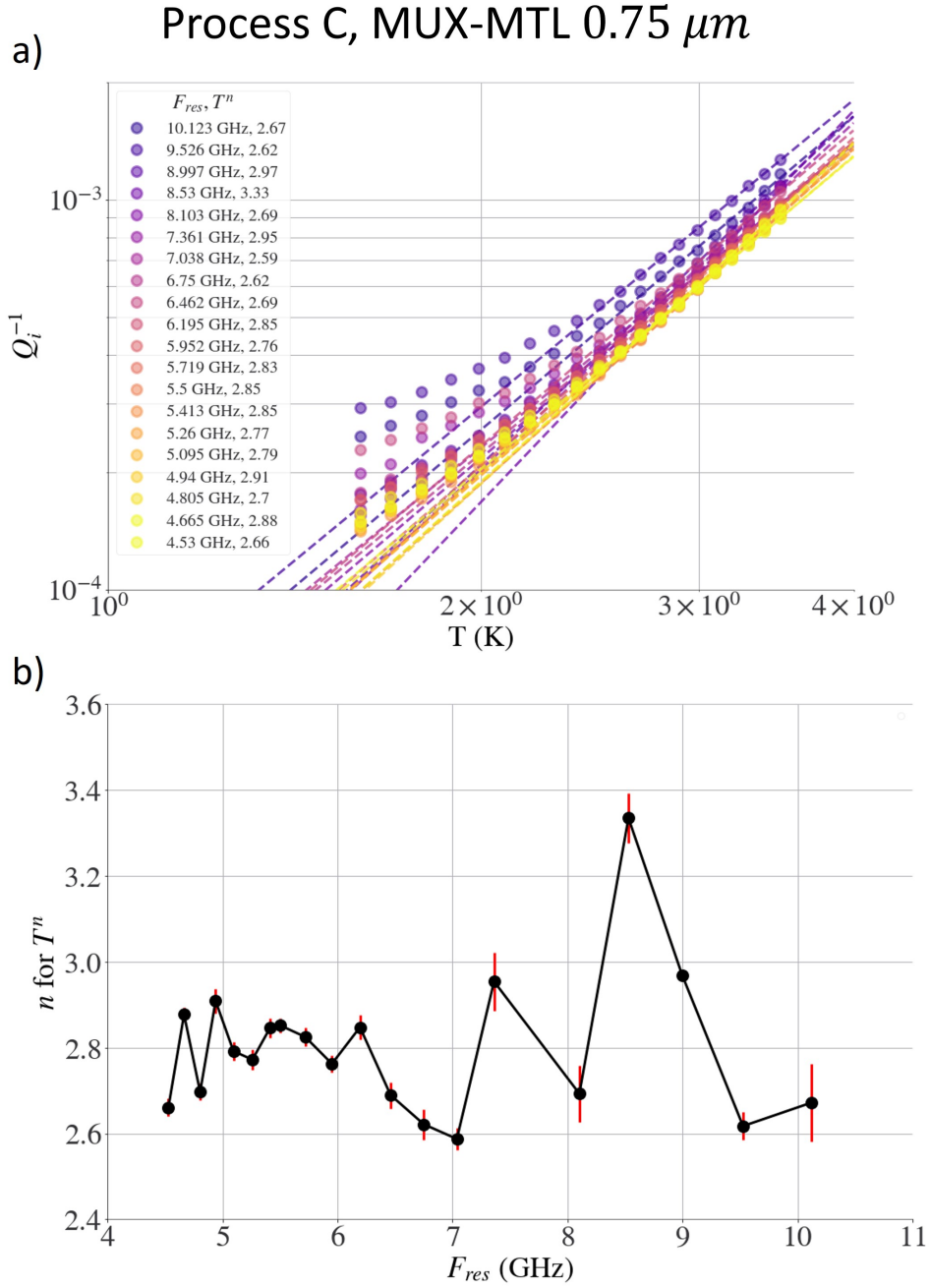
Figure 5.13: a) Temperature dependent inverse internal Q-factor of MUX-MTL resonators. At these temperatures, It is assumed that the Q-factor is dominated by the TEOS dielectric loss tangent by $Q_i^{-1} = \tan\delta$. Each color is a different resonator coupled to the MUX feedline with resonant frequency listed in the legend. The dashed lines are power law fits in the temperature range 2.5 to 3.5 K. b) Resulting power law fits for each resonator in the MUX-MTL including one sigma error bars for each fit. These resonators were fabricated using process C and constant VNA input power $P_{in} = -35\,dBm$. This is the same data from Fig 5.9.
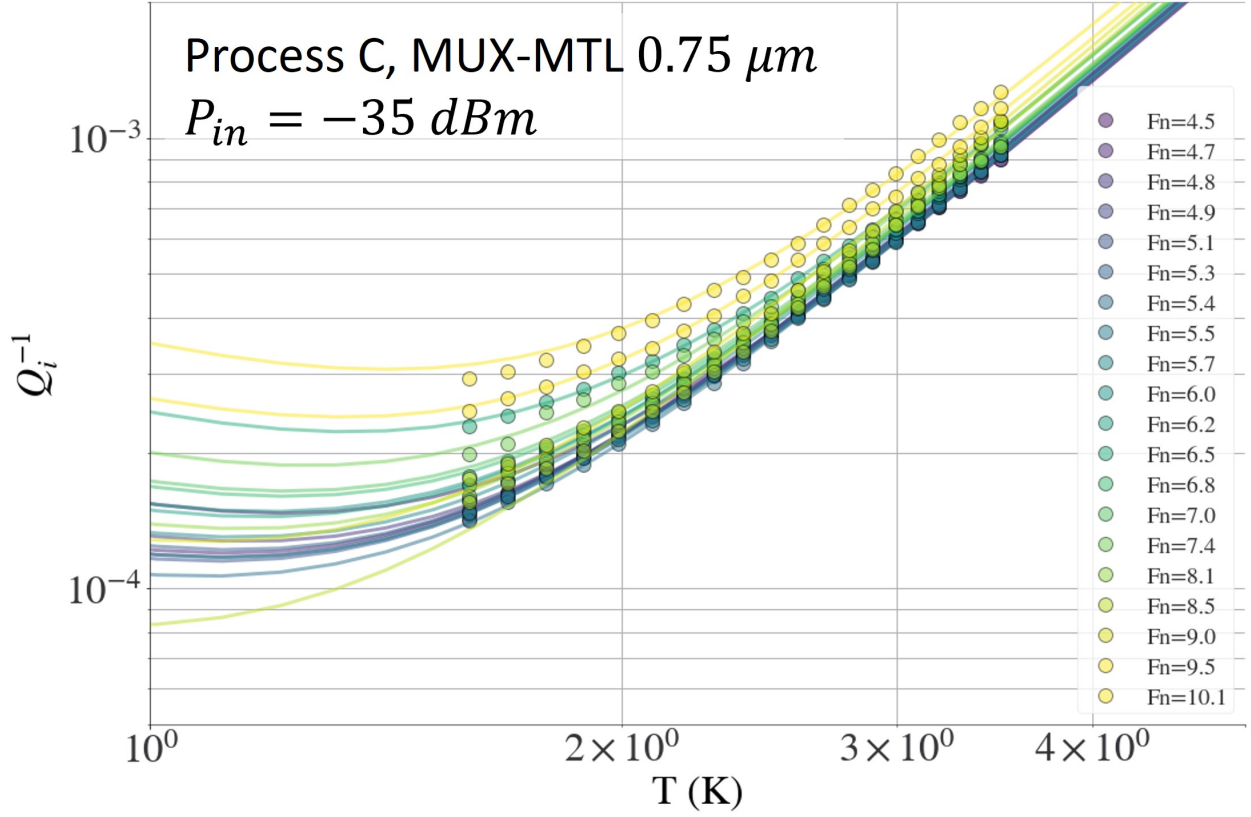
Figure 5.14: Temperature dependence of the inversive internal Q-factor Q_i^{-1} for each MUX-MTL resonator with unique fundamental resonant frequencies at a constant input power of $P_{in} = -35dBm$. At these temperatures, It is assumed that the Q-factor is dominated by the TEOS dielectric loss tangent by $Q_i^{-1} = \tan\delta$. The solid lines are fits to Eqs. 5.18-5.20 with $n\mu'^2$, $n\mu^2$, and J/J_c as free fitting parameters. A summary of results and assumed constants are listed in Summary Table 5.2.

Table 5.2: A summary table of temperature dependent fitting results to models of TLS absorption and relaxation. At these temperatures, It is assumed that the Q-factor is dominated by the TEOS dielectric loss tangent by $Q_i^{-1} = \tan\delta$. The $Q_i^{-1}(T)$ and $F_0(T)$ data were fit with 3 and 2 free fitting parameters to Eq.s 5.18 and 5.10, respectively. The constants were assumed from references [Kim2001] [72], [Pohl2002] [93], [Jackle1976] [188], [Rocha2004] [73], [Schickfus1976] [186]. The constant a assumed in $Q_i^{-1}(T)$ fits was calculated from the other assumed constants in the column using Eq. 5.15. Note, the extracted values of $n\mu^2$ from resonant frequency fits are 3 orders of magnitude larger than typical values of amorphous dielectrics [Phillips1981] [89]

		Q_i^{-1}(T) Fits $T = 1.5 - 3$ K	F_0(T) Fits $T = 1.5 - 3$ K
	Fab. Process	C	C
	Resonator Type	MUX-MTL	MUX-MTL
	microstrip width (μm)	0.75	0.75
Assumed Constants	ε_r	-	4.2 [Rocha2004]
	ρ (g/cm^2)	2.21 [Kim2001]	-
	v^a (cm/s)	4×10^5 [Pohl2002]	-
	$\overline{M}$	0.34 eV [Jackle1976]	-
	a (J^{-3}s^{-1})	2.5×10^{75}	2×10^{75} [Schickfus1976]
Fitted Parameters	Permanent Dipole Coupling $n\mu^2$	$2.4 - 6.6 \times 10^{-3}$	$0.5 - 1.4^*$
	Induced Dipole Coupling $n\mu'^2$	$0.4 - 0.8 \times 10^{-3}$	$3.6 - 7.0 \times 10^{-3}$
	J/J_c	3-41	-

$^*10^3$ higher than values measured for glassy dielectrics [Phillips1981]

linear enhancement of quasiparticle loss in the Nb. Although, the peak current qualitatively scales

mono-tonically with frequency, where the peak current is decreasing for increasing frequencies.

This suggests that a similar monotonic dependence would be seen in the internal Q-factor. This is by no means a rigorous argument and should be explored further by doing power dependent measurements. Although, it is also worth noting that since the peak voltage is linearly related to the peak current by $V_{peak} = Z_0 I_{peak}$ where $Z_0 \approx 50\ \Omega$ is the characteristic impedance of the MTL resonators. The reduction in peak voltage as frequency increased could be giving rise to the non-monotonic dependence of the loss tangent in the TEOS. This is postulated to be due to the expected increase in $\tan\delta$ when voltage is increased, characteristic of TLS resonant absorption processes. Admittedly, during the time of these measurements, it was not expected that TLS mechanisms would be present nor was the design peak current incorporated as a design parameter. The subject of the original design was to investigate the coupling capacitor values for the smallest capacitors, inadvertently producing weak enough coupling, and circulating power to see unsaturated TLS resonant absorption loss.

The resulting 3-parameter fits in Fig. 5.14 are plotted as a function of frequency in Fig. 5.16b and Fig. 5.16c. Fig. 5.16a is re-plotted data from Fig. 5.9 for convenience. The permanent dipole coupling constant $n\mu^2$ (black) increases for increasing frequencies by a factor of 3 from 4-10 GHz. This agrees qualitatively with values fitted from temperature dependent changes in the dielectric constant in Fig. 5.12. Although, the magnitude $n\mu^2 \approx 3 - 10 \times 10^{-3}$ in Fig. 5.16b is more agreeable with published data on various amorphous dielectrics. The values of $n\mu^2$ for TEOS measured here are of order values measured for borosilicate glass 6×10^{-3} [89], and approximately an order of magnitude higher than vitreous silica for the lowest concentrations of OH^- [186]. Similarly, the range of extracted induced dipole coupling $n\mu'^2 = 4 - 8 \times 10^{-4}$ in Fig. 5.16 also are in fairly good agreement with borosilicate glass having 3×10^{-4} found in Schickfus thesis reported in [89].

172
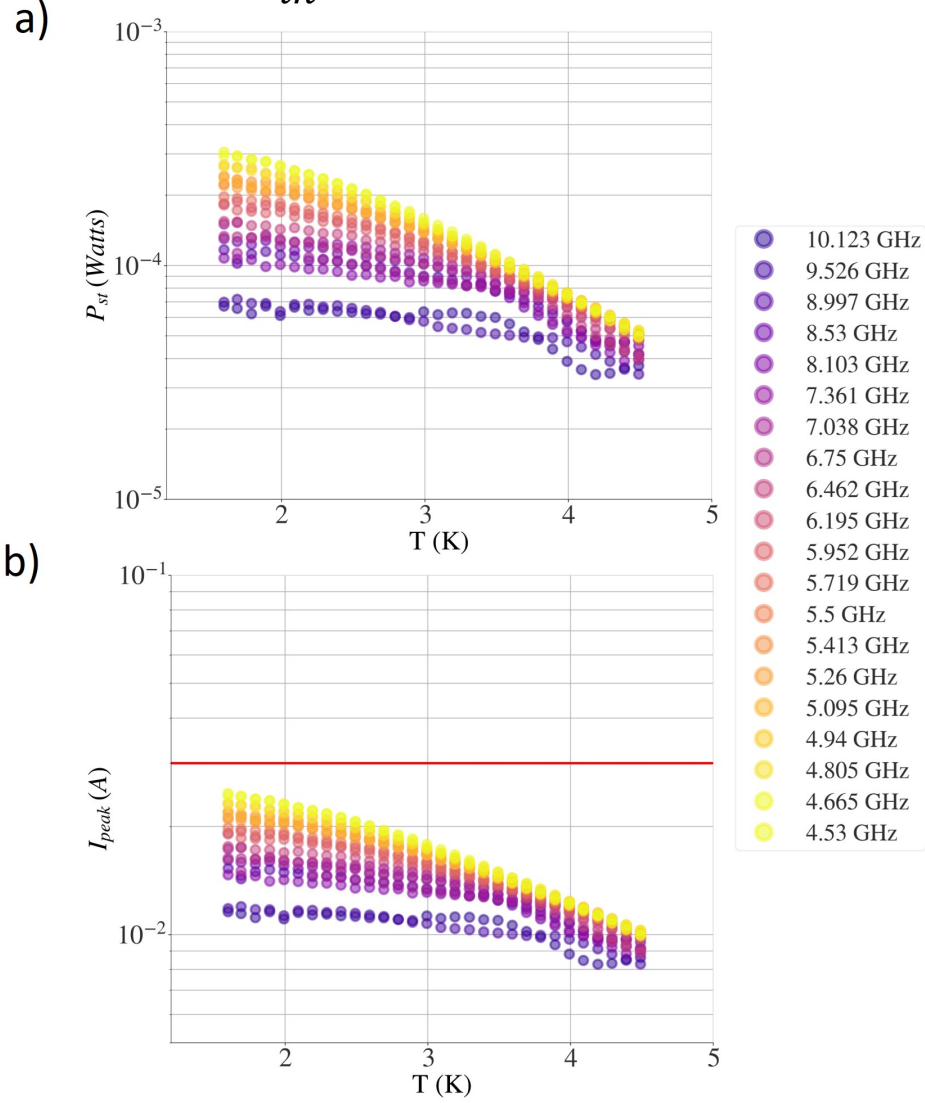
Figure 5.15: Temperature dependence of a) the stored circulating power P_{st} b) peak current I_{peak} in the MUX-MTL resonators for VNA input power of $P_{in} = -35\,dBm$. The stored power in each resonator and each temperature was calculated from Eq. 5.4. The peak currents were calculated using Eq. 5.5. The solid red line in b) is the minimum critical current I_c of a $0.75\,\mu m$ wide Nb wire with a 200 nm thickness assuming critical current density $J_c = 20\,MA/cm^2$ [32].

It is an important distinction to note that measured dipole moment coupling in microwave dielectric experiments are much more sensitive to impurities and the chemical composition of insulating glasses relative to acoustic measurements. Therefore, it is claimed that absolute values of $n\mu'^2$ and $n\mu^2$ plotted in Fig. 5.16 may be off by factors of 2-3 due to assumed constants in Table 5.2, but the the qualitative frequency variation $n\mu'^2$ is claimed here to be due to coupling of TLSs with the electric field at distinct frequencies. In other words, the peaks of $n\mu'^2$ at 6.5 and 9.5 GHz in Fig. 5.16a align with the loss peaks in Fig. 5.16b. Furthermore, these peaks align with relatively low J/J_c ratios in Fig. 5.16c, suggesting that the loss peaks are affiliated to enhanced TLS resonant absorption loss. The maximums of J/J_c at 8.5 GHz shows a saturation of circulating power to TLS resonant absorption, reducing Q_i^{-1}. An interesting data point is the 7 GHz point, where there is an increase in both the induced coupling to TLSs and the circulating power exhibiting an overall constant Q_i^{-1} relative to the neighboring frequencies.

This demonstration shows a new microwave loss spectroscopy method to probe TLS loss by relying on the frequency dependence. In future work, better care can be taken with the coupling design as well as systematic input power dependence to further explore this technique and the exhibited TLS character relative to the dielectric composition and impurities.

5.7   Temperature Dependence of the Power Dissipation in Nb and TEOS

The primary goal of this dissertation is to glean information on how to reduce intrinsic microwave losses in Nb and TEOS to reduce the power dissipation in RQL resonator clock networks. This chapter has focused on demonstrating techniques to better understand the dominate loss mechanisms coming from the superconductor and dielectric materials as temperature is
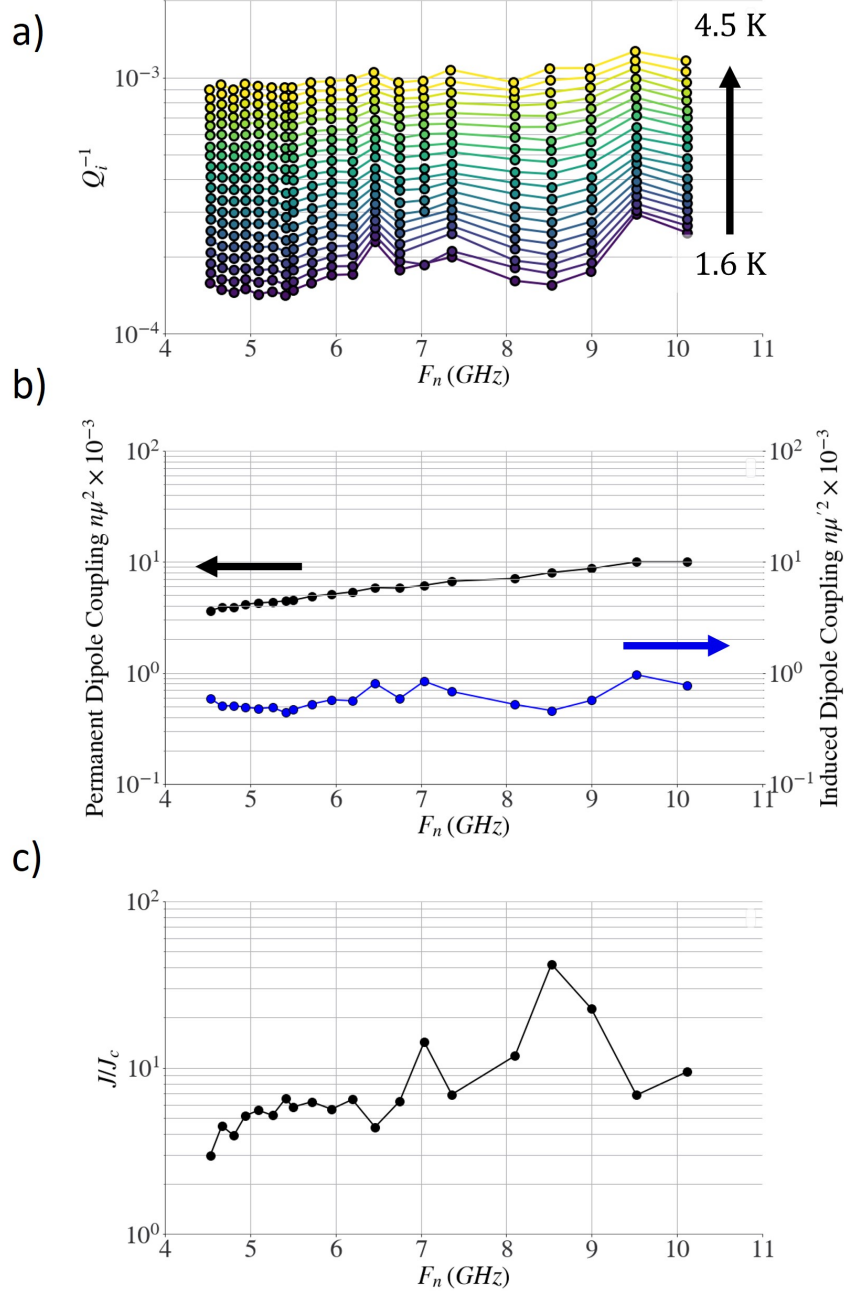
Figure 5.16: a) Frequency dependence of Q_i^{-1} for MUX MTL resonators for constant VNA input power $P_{in} = -35\,dBm$ in the temperature range $T = 1.6 - 4.5\,K$ (Re-plotted Fig. 5.9). b) Frequency dependence of the fitted permanent (black) and induced dipole (blue) coupling constants. c) Frequency dependence of the power density ratio J/J_c where J and J_c are the circulating input power density in the resonator and the critical power density for TLS resonant absorption saturation, respectively. The fitted parameters in b) and c) were fit to data in Fig. 5.14 using Eqs. 5.18. A summary of results and assumed constants are listed in Summary Table 5.2.

175

decreased below 4.2 K. This chapter will be concluded with direct measurements of power dissipation in MUX-MTL resonators that can be directly related to RQL interconnects having the same geometry and input power. Furthermore, estimates can be made from this data for arbitrary geometries and input power.

Strong *et al.* measured the dissipated power of meta-material zeroth-order resonators (ZORs) used in RQL clock networks and found a dissipated powers on the order of $20 \ \mu W$ [10]. Using Eq. 5.3, the temperature dependent dissipated power P_d of MUX-MTL resonators at $P_{in} = -35 \ dBm$ is plotted in Fig. 5.17.

In Fig. 5.17 at approximately 4-4.5 K, the dissipated power for all resonators (frequencies) is approximately $100-200 nW$ for VNA input power $P_{in} = -35 dBm$. For a nominal input power $P_{in} = -9 \ dBm$ used in ZOR resonators, the dissipated power in MUX-MTLs is approximated to be $60 \ \mu W$, and is within a factor of 3 of ZOR power dissipation. As temperature is decreased, the $4.5 \ GHz$ resonator reduces in dissipated power down to $P_d = 70 \ nW$ at 1.6 K. At 1.7 K, the dissipated power decreases as frequency is increased up to 10 GHz with a minimum dissipation of $P_d = 26 \ nW$. The frequency dependence of this dissipated power is due to the saturation of TLS resonant absorption loss at higher frequencies and discussed in the previous section. This is an expected and known result, and further supports the notion that the TEOS dielectric microwave loss dominates the ZOR resonator clock power dissipation for the temperature range 1.5-3.5 K. There is a subtle maximum power dissipation at low frequencies around 3.5 K where the Nb and TEOS microwave losses are comparable for this resonator geometry, and can shift depending on the material used and the RQL clock geometry. Overall, this has established the limits to power efficiency in resonator clocks due to material losses and demonstrates a method of characterization.
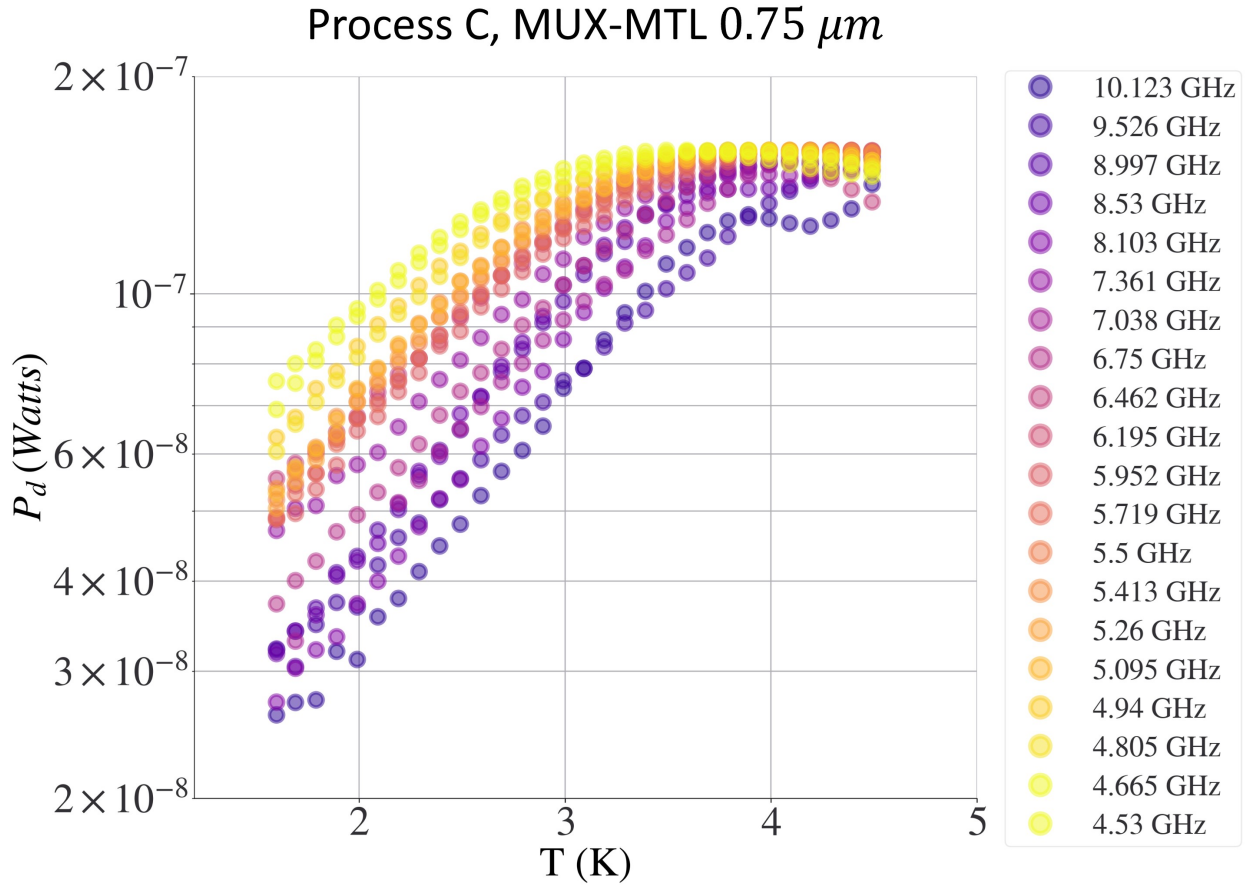
Figure 5.17: Temperature dependence of the dissipated power P_d in MUX-MTL resonators at a constant VNA input power $P_{in} = -35\ dBm$. The dissipated power was calculated from data in Figs. 5.15 and 5.8 using Eq. 5.3.

5.8 Summary

At the beginning of this chapter, the temperature dependence of the resonant frequency f_n and internal Q-factor Q_i in the range 1.5-4.5 K was measured for MTL widths $0.25 - 4\mu m$ from process B. The anomalous non-monotonic frequency dependence of Q_i^{-1} was ambiguous. Measurements of the peak currents in the resonator suggested enhancements of Q_i^{-1} when the currents in the resonator were close to the expected critical currents of the Nb strips Although, the model did not apply when currents were more than a magnitude below the critical current. This facilitated the design of multi-plexed microstrip resonators on a single feedline to have a higher density of frequency points to analyze.

In the next section, a design of multiplexed $0.75~\mu m$ MTL resonators was presented. In an approximate range of 3-4.2 K, I was able to deconvolve the R_s(T) and $\tan\delta(T)$ temperature dependence using the dispersive loss deconvolution (DLD) method. This was validated by fitting to the expected R_s and $\tan\delta(T)$ temperature dependence $e^{-\Delta/k_B T}$ and approximately T^3, respectively. From the extracted $\tan\delta$(T) going to temperatures below 3 K, I proposed that the change from T^3 dependence at approximately 2 K is due to a transition from TLS relaxation to TLS absorption mechanisms. This was supported by a decrease in ε_r of approximately 0.03-0.04% at 2 K from $f_n(T)$ measurements. Fits to the temperature change in resonant frequency were fit to TLS resonant absorption and relaxation models, but the fitted values for permanent dipole coupling were 3 orders of magnitude off from expected values and is not understood. Fits to the temperature dependence of Q_i^{-1} to TLS models had much better agreement to expected. From these fits, microwave loss spectroscopy analysis showed a non-monotonic dependence on the TLS induced dipole coupling. This non-monotonic dependence agrees with loss peaks in Q_i^{-1}

and is claimed to be a combination of saturation of TLS absorption processes and enhancements of specific TLSs coupled to impurities in the material resonant with the probed frequency. Although, this is speculative and not a rigorous analysis, and systematic power dependent measurement should be performed.

Aside from the anomalous behavior, the conclusions on temperature dependence power efficiency of RQL clock resonators can still be summarized and found in the last section. Similar to the conclusion drawn from the last chapter, $\tan\delta$ is the limiting loss dominating power dissipation in RQL resonators as temperature is reduced below 3 K. This is analogous to the dominant loss mechanism in superconducting Qubit systems. However, care needs to be taken on resonator clock input power requirements as temperature falls below 3 K. At high input powers, TLS resonant absorption processes are saturated, allowing for reduced power dissipation in the resonator clock. At increased powers, there are two additional considerations: (i) Input current (power) to the resonator needs to remain far below the critical current of the MTL to mitigate nonlinear effects and increased microwave loss from the superconducting wires and groundplanes. (ii) At temperatures below 3 K, especially mK temperatures, the heat lift in cryostat decreases, and heat dissipation designs may need to be implemented. At 2 K, the internal Q-factor Q_i of RQL interconnect increased by an order of magnitude, yielding an RQL interconnect efficiency of $\eta \approx 0.9$. Although, an order of magnitude increase of Q_i at 2 K comes at an added refrigeration cost by a factor of 3 relative to 4.2 K [181]. From this, it can be estimated that the total power consumption of RQL operating at 10 GHz is 100x less than equivalent CMOS circuits operating at 1-4 GHz (logic and interconnects) [4].

Chapter 6:   Summary and Conclusions

6.1   Summary

The work performed in this dissertation was aimed at performing materials characterization of microwave losses in Nb and TEOS to provide information on the limitations and mitigation strategies to reduce power dissipation in RQL clock interconnects. The superconductor and dielectric losses at temperature below 4.2 K and GHz frequencies have independent frequency and temperature scalings. On one hand this makes it difficult to design a system to optimize power efficiency performance. On the other hand, the unique frequency and temperature dependence presents the opportunity to deconvolve the loss mechanisms in a single measurement. In this dissertation I discussed the power efficiency limitations dictated by the Nb and TEOS supported by direct measurements of the microwave losses using the Dispersive Loss Deconvolution method (DLD). The DLD method confirmed the initially fabricated Nb material was of low quality, as opposed to the TEOS dielectric, and helped the fabrication team rapidly fine tune the process to yield the ultra-low loss Nb interconnect material.

At 4.2 K, the theoretical minimum of Nb microwave losses can be reached and heavily depends on the microstrip geometry and the fabrication process used. At temperatures below 4.2 K, the microwave losses in the superconductor become negligible and the dielectric losses dominate and is independent of the resonator geometry. It was found that TLS relaxation pro-

cesses dominate the dielectric loss in the temperature range 2.5 to 4.2 K. At temperatures below 2.5 K, TLS resonant absorption processes become comparable to the relaxation loss and has a significant input power dependence.

At 2 K, it was found that the RQL interconnect efficiency was estimated to be $\eta \approx 0.9$ relative to the logic. Accounting for the refrigeration costs, it can be estimated that the total power consumption of RQL operating at 10 GHz is 100x less than equivalent CMOS circuits operating at 1-4 GHz (logic and interconnects) [4]. Changing the operating temperature of RQL from 4.2 to 2 K would not create significant design changes since Nb inductance decreases by less than 20%, $Nb/AlO_x/Nb$ Josephson junction critical currents increase by less than 20%, and TEOS relative dielectric constant remains virtually constant.

RQL is a classical computing technology with notable energy efficiency advantages over CMOS with circuits that can operate over 100 GHz. Although, circuit density still remains as a significant limiting factor preventing the technology from competing with CMOS. Both the size of the Jospehson junctions and the interconnects need to be pushed to dimensions below 0.25 μm. Specifically for Nb interconnects, pushing the critical dimensions to be comparable with the magnetic penetration depth $\lambda \approx 90 \ nm$ imposes strict requirements on the fabrication process to produce low loss interconnects while increasing the processing window.

6.2 Future Work

The work performed in this dissertation was aimed at improving the energy efficiency of RQL superconducting interconnects and help provide a path for RQL to meet computing power demands. The power dissipation in RQL interconnects is inherently dependent on RF losses in

the superconductor and dielectric. Since resonator-based clock networks deliver power on the same order of the total dynamic power of the Josephson junction logic, the RF losses in the superconductor and dielectric can directly influence the efficiency and scaling of the technology. Considering the superconductor and dielectric RF losses are comparable in RQL interconnect due to the imposed transmission line geometry from the fabrication process, both RF loss channels need to be minimized.

In this dissertation, through the lens of material science, I discussed some of the essential work needed to improve the processing, properties, and performance of RQL interconnect. Furthermore, the novel Dispersive Loss Deconvolution (DLD) method and resonator designs described here serve as the groundwork for future groups interested in measuring RF losses in inseparable superconductor-dielectric systems. The outlook and possible research directions include:

Processing

(a) Further improvement of the metal damascene fabrication process down to and below 0.25-micron dimensions such as protective buffer and capping layers (thermal oxide diffusion barriers), and deposition parameters that yield uniform trench filling (eliminate voiding and facilitate conformal coverage).

(b) Tighter control of critical dimensions and material property variation across the wafer. The sensitivity analysis in Section 3.7 showed that $\tan \delta$ is geometry independent with a variation of approximately 20% across the wafer. Whereas the conductor Q-factor is both sensitive to the geometric factor Γ with worst case 20% variation, and the intrinsic surface resistance R_s, which seemed have a variation less than that (see Fig. 4.9).

(c) Increasing the thermal budget - (i) implement junction-on-top or more thermally resilient

182

Josephson junction barrier technologies, (ii) on wiring layers to promote ideal growth kinetics if a damascene process is needed. A damascene process is used in CMOS industry because it is difficult to etch Cu (as opposed to silicon dioxide). Nb is fairly easy to etch, so it is conceivable to rely on Nb etch processes to define the wires and CMP the dielectric, which yielded the lowest loss Nb reported in Chapter 4.

(d) Surveying different superconductor and dielectric materials with lower RF losses and/or more resilient to process variations. Candidate superconducting materials are NbN and NbTiN for their low RF loss properties and sputtering compatibility. On one hand, NbN and NbTiN have higher inductance and can reduce circuit sizes, but on the other hand this will decrease propagation speed relative to Nb and inductance uniformity needs to also be considered. Silicon nitride is a candidate dielectric material as it can have an order of magnitude lower loss than TEOS, but it is important to consider the change in propagation speed (relative dielectric constant difference). The relative dielectric constant for TEOS and silicon nitride are approximately 4.2 and 7.5, respectively. Therefore the propagation velocity would decrease by approximately 25% switching from TEOS to silicon nitride.

Properties

(a) Reduce the fundamental mode frequency of the microstrip transmission line used in Chapters 4 and 5 down to below 1 GHz to increase the frequency range to validate the superconducting frequency dependencies.

(b) Continue multi-plexed resonator technique to understand spatial distribution of properties (and critical dimensions) across a chip/wafer

(c) Incorporate the impact of nonlinear dynamics in FEM of superconducting interconnects, as I assumed the system displays linear response throughout this thesis, but is most likely not the case since electromagnetic field concentration at the edges and will only become exacerbated as dimensions are pushed below 0.25-microns and the input power will be pushed to its limits.

(d) Incorporate common nonlinear measurements (vs power, vs applied magnetic field (in-plane, out-of-plane).

(e) Physical characterization techniques with higher sensitivity to trace element contamination both in interconnect cross-section as well as spatially (e.g. atom probe tomagraphy, etc).

(f) Determine if there is a correlation between dielectric loss tangent $\tan \delta$ between 4.2 K and mK. Conceivably, rapid measurements at 4.2 K may be more advantageous to evaluate a superconducting interconnect.

(g) Use as a test vessel to measure vortex dynamic properties on wide microstrip MTLs with temerpature dependent measurements in perpendicular magnetic field [137].

Performance

(a) In the nominal configuration, RQL power dissipation is less of an issue at mK temperatures due to million level Q-factors (superconductor loss is negligible and TLSs saturate at RQL powers).

(c) Continue work on exploring cross-sectional RQL interconnect geometries to mitigate RF losses by engineering the geometric factor Γ.

(d) Further explore mK-K temperature range of superconducting-dielectric RF losses in conjuction with cooling costs to optimize energy efficient computing.

(e) Higher throughput test systems to get wafer statistics, a wafer prober can alleviate this [191].

Appendix A: FIB Cross Sections of Process A and B

To accurately calculate the geometric factor Γ of microstrip transmission line (MTL) resonators (see Chapter 3), exact measurements of the MTL geometries were measured using a similar instrument as the FEI Helios 660 Dual Beam FIB/SEM. The cross section of the MTLs were exposed using a focused ion beam (FIB) and then imaged using a scanning electron microscope (SEM).

Table A.1:   FIB Results Summary table for processes A and B measured in this work. All of these microstrip tranmission lines were measured using a similar instrument as the FEI Helios 660 Dual Beam FIB/SEM. Cross sections were taken at about the half way point along the meandor resonator ($\approx 7\ mm$). The second column are the nominal (designed) wire widths. Example FIB cross sections can be found in Figs A.1 and A.2. The third column are the measured mean widths averaged between the bottom and top of the wire. The $\pm$ values in the last three columns are the calculated one standard deviations taken from measurements of all 5 wire widths.

Process	Nominal wire width [μm]	Measured wire width [μm]	Ground Plane Thickness [nm]	Dielectric Thickness [nm]	Wire Thickness [nm]
A	0.25	0.27	169 ± 14	165 ± 3	218 ± 8
A	0.5	0.53	169 ± 14	165 ± 3	218 ± 8
A	1	1.01	169 ± 14	165 ± 3	218 ± 8
A	2	2.00	169 ± 14	165 ± 3	218 ± 8
A	4	3.97	169 ± 14	165 ± 3	218 ± 8
B	0.25	0.25	233 ± 9	147 ± 4	222 ± 10
B	0.5	0.48	233 ± 9	147 ± 4	222 ± 10
B	1	0.99	233 ± 9	147 ± 4	222 ± 10
B	2	1.98	233 ± 9	147 ± 4	222 ± 10
B	4	3.98	233 ± 9	147 ± 4	222 ± 10

Table A.1 is a summary of the measurements for MTLs made from process A and B. The

second column are the nominal (designed) wire widths. The third column are the measured mean

widths averaged between the bottom and top of the wire. The $\pm$ values in the last three columns

are the calculated one standard deviations taken from measurements of all 5 wire widths.
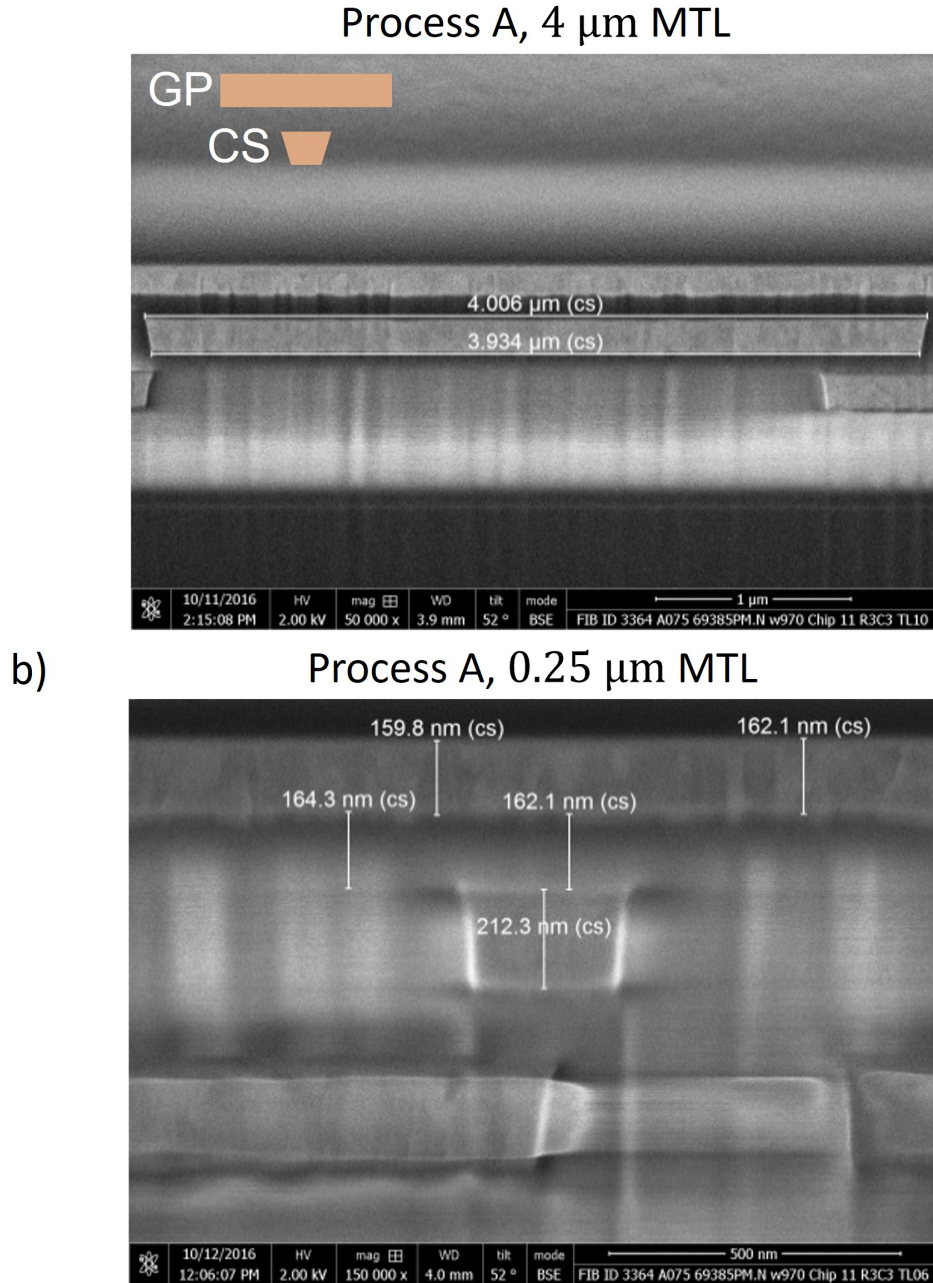
Figure A.1: Example cross sections and measurements of the microstrip tranmission line resonator geometry for the $0.25\mu m$ and $4\mu m$ wire widths fabricated using process A. In this process the conducting strip (CS) is below the ground plane (GP)
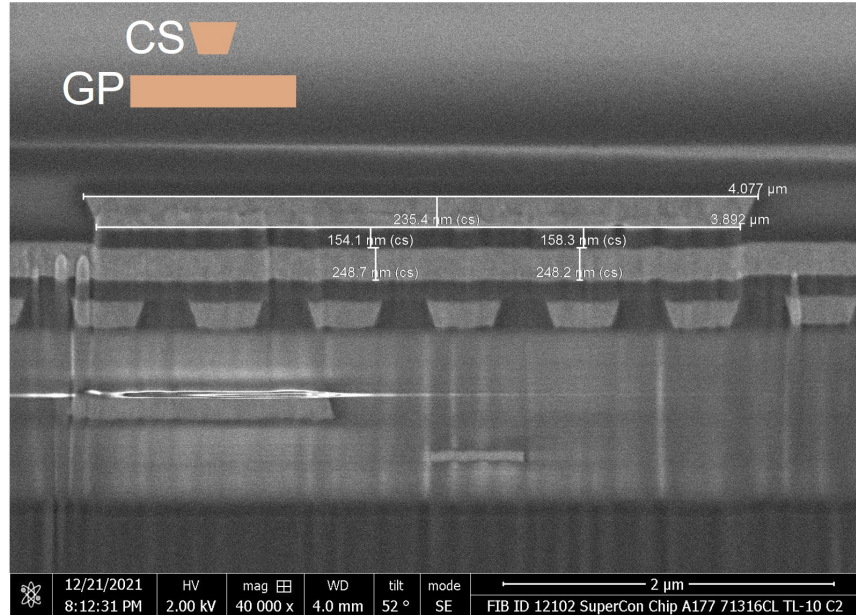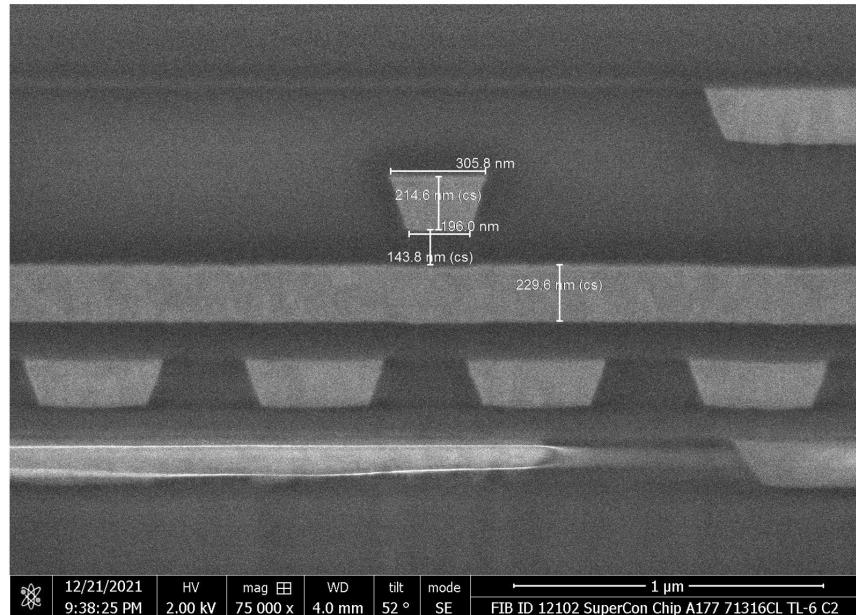
Figure A.2: Example cross sections and measurements of the microstrip tranmission line resonator geometry for the $0.25\mu m$ and $4\mu m$ wire widths fabricated using process B. In this process the conducting strip (CS) is above the ground plane (GP)

Example cross sections for $0.25\mu m$ and $4\mu m$ MTLs can be found in Fig. A.1 from process

A. In this process the conducting strip (wire) is below the ground plane.

Example cross sections for $0.25\mu m$ and $4\mu m$ MTLs can be found in Fig. A.2 from process B. In this process the conducting strip (wire) is above the ground plane.

Appendix B: Estimation of Radiation Q-Factor

The radiation Q-factor in general is the ratio of the energy stored in the resonator over the power radiated from the transmission line resonator, and can be estimated using the following equation from [163]

$$Q_{rad} = \frac{4\pi Z_0}{480(s\beta)^2 F(\varepsilon_{eff})} \tag{B.1}$$

$$F(\varepsilon_{eff}) = \frac{\varepsilon_{eff}+1}{\varepsilon_{eff}} - \frac{(\varepsilon_{eff}-1)^2}{2\varepsilon_{eff}^{3/2}} \ln\left(\frac{\varepsilon_{eff}^{1/2}+1}{\varepsilon_{eff}^{1/2}-1}\right) \tag{B.2}$$

where Z_0 is the characteristic impedance, s is the dielectric thickness, β is the phase constant, and ε_{eff}. For a $Z_0 = 55\,\Omega$ and $\beta = 670\,m^{-1}$ found using HFSS simulation with inputs $R_s = 20\,\mu\Omega$, $\lambda = 90\,nm$, $\varepsilon_{eff} = 4.5$, and geometry shown in Fig. 4.1, $Q_{rad} \approx 230 \times 10^6$. For internal Q-factor Q_i and external (or coupling) Q-factor Q_e on the order of 1×10^3, it is safe to ignore Q_{rad} using

the following relation of the loaded Q-factor $Q_L^{-1} = Q_i^{-1} + Q_e^{-1} + Q_{rad}^{-1}$.

Appendix C: Temperature Dependent Resonator Measurements

C.1   Measurements System

For high quality RF measurements (up to 12 GHz) with precise temperature control (1.5 – 9 K), I utilize a system similar to the Dry ICE 1.5 K Cryostat [182]. This system has a base temperature of 1.4 K and temperature can be set between 1.4-10 K with a temperature stability of $\pm 10\,mK$. The temperature is controlled using a Lakeshore 336 PID control [192] with a 25 Ω heater.

Figure C.1: I utilized a system similar to the Dry ICE 1.5 K Cryostat [182] for temperature control for the testing and results described in Chapter 5. The test fixture is similar to the RF dip probe outfitted with a 32 pin (contact pad) described in Chapter 4. The same test fixutre was used in previous works [35], [34], [36], [10]. To achieve RF signal integrity and avoid wire bonding for fast sample chip exchanges, a non-magnetic Cu/Au flip chip press contact technology is used. The fixture PCB connects the flip-chip bump pads to the probe .047 inch semi-rigid coaxial cables. The chip and roughly $30\ cm$ of the cables are cooled by the Dry ICE 1.5 K Cryostat during measurements. The temperature was monitored with a calibrated Lakeshore Cernox sensor. The resonators were measured by 2-port S-parameters using a Keysight N5222A vector network analyzer (VNA). The network analyzer was calibrated up to the top of the probe.

Appendix D: Relevant Equations for Parallel Plate Transmission Line Resonator

In the following equations in this appendix section, a parallel plate transmission line geometry is assumed. In this assumption with an infinitely wide ground plane, the microstrip width is much greater than the dielectric thickness $w \gg s$.

The complex propagation constant $\gamma = \alpha + i\beta$ is assumed here to be that of a Swihart wave and is a good approximation for a wide microstrip transmission line with the form [36, 59]

$$\alpha = \frac{\beta}{2} \left[\frac{2R_{eff}}{\omega\mu_0 s + 2(X_{eff} - R_{eff}\tan\delta)} + \tan\delta \right] \tag{D.1}$$

$$\beta = \omega\sqrt{\varepsilon_0 \varepsilon_r \mu_0}\sqrt{1 + \frac{2(X_{eff} - R_{eff}\tan\delta)}{\omega\mu_0 s}} \tag{D.2}$$

where R_{eff} is the effective surface resistance (see Eq. 2.24), X_{eff} is the effective surface reactance (see Eq. 2.25), s is the dielectric thickness between the microstrip and groundplane, ε_r is the relative dielectric constant of the dielectric, $\tan\delta$ is the loss tangent of the dielectric material, ε_0 is the permittivity of free space, and μ_0 is the permeability of free space.

Here, a PPW system has been enforced, and we are interested in the resulting quasi-transverse electromagnetic (quasi-TEM) mode propagating along the longitudinal length l in the x direction (see Fig. 3.10). The accuracy of HFSS solutions will be tested using the following equations for $RLGC$ by inserting the superconducting impedance definitions Eq. 2.24 and Eq. 2.25

into PPW analytical solutions [95]

$$R = \frac{2R_{eff}}{w} \tag{D.3}$$

$$L = \mu_0 \frac{s + 2\lambda \coth(d/\lambda)}{w} \tag{D.4}$$

$$G = \omega \varepsilon_0 \varepsilon_r \tan\delta \frac{w}{s} \tag{D.5}$$

$$C = \varepsilon_0 \varepsilon_r \frac{w}{s} \tag{D.6}$$

where μ_0 is the vacuum permeability, ε_0 is the vacuum permittivity, ω is the angular frequency, w is the PPW width, s is the plate separation dielectric thickness, R_{eff} is the effective resistance defined in Eq. 2.24, and $\tan\delta$ is the dielectric loss tangent. The $RLGC$ are the series resistance, series inductance, shunt conductance, and shunt capacitance per unit length of a generalized transmission line defined in Eq. 3.2-Eq. 3.5 in Section 3.3.

MTL resonators support a TM_{00n} [59] mode with the eigen frequency

$$f_n = \frac{n}{2l_{res}\sqrt{LC}} = \frac{nc}{2l_{res}\sqrt{\varepsilon_r}\sqrt{1 + 2\lambda \coth(d/\lambda)/s}} \tag{D.7}$$

where $n = 1, 2, 3\ldots$ is the mode index, l_{res} is the geometrical length of the resonator, and L and C are the conducting strip series inductance and shunt capacitance per unit length defined by Eq. 3.3 and 3.5. The right hand side in Eq. D.7 holds for a wide MTL where the width is much greater than the dielectric thickness ($w \gg s$) [70], where c is the speed of light, and ε_r is the dielectric constant.

Using Eqs. D.4 and D.6, the characteristic impedance can be calculated by

$$Z_0 = \sqrt{L/C} = \frac{s}{w}\sqrt{\frac{\mu_0}{\varepsilon_0\varepsilon_r}}\left(1 + 2\lambda_{eff}/s\right) \tag{D.8}$$

where $\lambda_{eff} = \lambda\coth(d/\lambda)$ is the effective magnetic penetration depth.

Using Eq. 3.1, the partial conductor and dielectric Q-factors for a parallel plate resonator, $Q_c = \omega L/R$ and $Q_d = \omega C/G$, respectively, are

$$Q_c = \omega\mu_0\frac{s+2\lambda\coth(d/\lambda)}{2R_{eff}} \tag{D.9}$$

$$Q_d = 1/\tan\delta \tag{D.10}$$

Notice, the PPW width w drops out in Q_c, and ω drops out in Q_d with no geometry dependence. Then, the only parameters needed to model the superconducting PPW, analytically and with HFSS impedance boundaries, are s, d, ω, λ, R_s, and $\tan\delta$.

To provide a simple analytical limiting case for Eq. 3.14 consider a resonator formed by a parallel-plate waveguide with identical superconducting plates of the width w and thickness d, separated by the dielectric layer of thickness s. This geometry approximates MTL with $w \gg s$. The geometric factor is

$$\Gamma_{PP}(\omega) = \omega\mu_0\frac{s + 2\lambda\coth(d/\lambda)}{2[\coth(d/\lambda) + (d/\lambda)\mathrm{csch}^2(d/\lambda)]} \tag{D.11}$$

utilizing the expression for the effective surface resistance of thin superconducting films, and by $R_{eff} \approx R_s[\coth(d/\lambda)+(d/\lambda)\mathrm{csch}^2(d/\lambda)]$ that ignores transmission loss through the superconducting

films [69]. In the thick film limit the geometric factor reduces to $\Gamma_{PP} = \frac{1}{2}\omega\mu_0(s + 2\lambda)$ and the geometric factor is no longer dependent on the superconductor plate thicknesses d. For the thin film limit where $\lambda \gg d$ the full expression needs to be used in Eq. D.11 and a term including the dielectric substrate impedance may be needed [70].

Bibliography

[1] John Shalf. The future of computing beyond moore's law. *Philosophical Transactions of the Royal Society A*, 378(2166):20190061, 2020.

[2] Martijn Koot and Fons Wijnhoven. Usage impact on data center electricity needs: A system dynamic forecasting model. *Applied Energy*, 291:116798, 2021.

[3] Mark Neisser. International roadmap for devices and systems lithography roadmap. *Journal of Micro/Nanopatterning, Materials, and Metrology*, 20(4):044601, 2021.

[4] Quentin P Herr, Anna Y Herr, Oliver T Oberg, and Alexander G Ioannidis. Ultra-low-power superconductor logic. *Journal of applied physics*, 109(10):103903, 2011.

[5] Quentin P Herr, Joshua Osborne, Micah JA Stoutimore, Harold Hearne, Ryan Selig, Jacob Vogel, Eileen Min, Vladimir V Talanov, and Anna Y Herr. Reproducible operating margins on a 72 800-device digital superconducting chip. *Superconductor Science and Technology*, 28(12):124003, 2015.

[6] Yuri Polyakov, Supradeep Narayana, and Vasili K Semenov. Flux trapping in superconducting circuits. *IEEE transactions on applied superconductivity*, 17(2):520–525, 2007.

[7] Vasili K Semenov, Yuri A Polyakov, and Sergey K Tolpygo. Ac-biased shift registers as fabrication process benchmark circuits and flux trapping diagnostic tool. *IEEE Transactions on Applied Superconductivity*, 27(4):1–9, 2017.

[8] Leland Chang, David J Frank, Robert K Montoye, Steven J Koester, Brian L Ji, Paul W Coteus, Robert H Dennard, and Wilfried Haensch. Practical strategies for power-efficient computing technologies. *Proceedings of the IEEE*, 98(2):215–236, 2010.

[9] Raj K Jana, Gregory L Snider, and Debdeep Jena. Energy-efficient clocking based on resonant switching for low-power computation. *IEEE Transactions on Circuits and Systems I: Regular Papers*, 61(5):1400–1408, 2014.

[10] J.A. Strong. A resonant metamaterial clock distribution network for superconducting logic. *Nat Electron*, 2022.

[11] Donald R Askeland and Wendelin J Wright. *Essentials of materials science and engineering*. Cengage Learning, 2018.

[12] Peidong Yang and Jean-Marie Tarascon. Towards systems materials engineering. *Nature materials*, 11(7):560–563, 2012.

[13] Brian David Josephson. Possible new effects in superconductive tunnelling. *Physics letters*, 1(7):251–253, 1962.

[14] Philip W Anderson and John M Rowell. Probable observation of the josephson superconducting tunneling effect. *Physical Review Letters*, 10(6):230, 1963.

[15] John M Rowell. Cryogenic supercurrent tunneling devices, October 25 1966. US Patent 3,281,609.

[16] M Gurvitch, MA Washington, and HA Huggins. High quality refractory josephson tunnel junctions utilizing thin aluminum layers. *Applied Physics Letters*, 42(5):472–474, 1983.

[17] Theodore Van Duzer and Charles W. Turner. *Principles of Superconductive Devices and Circuits - 2nd edition*. Prentice Hall, Inc., 1999.

[18] S Hasuo. Josephson microprocessors. In *The New Superconducting Electronics*, pages 363–399. Springer, 1993.

[19] Jay Fleischman, David Feld, Peter Xiao, and Theodore Van Duzer. Evaluation of flux-based logic schemes for high-t/sub c/applications. *IEEE transactions on magnetics*, 27(2):2769–2772, 1991.

[20] F Bedard, N Welker, GR Cotter, MA Escavage, and JT Pinkston. Superconducting technology assessment. *National Security Agency, Office of Corporate Assessments*, 2005.

[21] KK Likharev, OA Mukhanov, and VK Semenov. Resistive single flux quantum logic for the josephson-junction digital technology. *SQUID Journal*, 85:1103–1108, 1985.

[22] Konstantin K Likharev and Vasilii K Semenov. Rsfq logic/memory family: A new josephson-junction technology for sub-terahertz-clock-frequency digital systems. *IEEE Transactions on Applied Superconductivity*, 1(1):3–28, 1991.

[23] Mutsumi Hosoya, Willy Hioe, Juan Casas, Ryotaro Kamikawai, Yutaka Harada, Yasou Wada, Hideaki Nakane, Reiji Suda, and Eiichi Goto. Quantum flux parametron: a single quantum flux device for josephson supercomputer. *IEEE Transactions on Applied Superconductivity*, 1(2):77–89, 1991.

[24] Mark H Volkmann, Anubhav Sahu, Coenrad J Fourie, and Oleg A Mukhanov. Implementation of energy efficient single flux quantum digital circuits with sub-aj/bit operation. *Superconductor Science and Technology*, 26(1):015002, 2012.

[25] Naoki Takeuchi, Dan Ozawa, Yuki Yamanashi, and Nobuyuki Yoshikawa. An adiabatic quantum flux parametron as an ultra-low-power logic device. *Superconductor Science and Technology*, 26(3):035010, 2013.

[26] Sergey K Tolpygo, Diana Tolpygo, Richard T Hunt, Supradeep Narayana, Yuri A Polyakov, and Vasili K Semenov. Wafer bumping process and inter-chip connections for ultra-high data transfer rates in multi-chip modules with superconductor integrated circuits. *IEEE transactions on applied superconductivity*, 19(3):598–602, 2009.

[27] S Narayana, VK Semenov, YA Polyakov, V Dotsenko, and SK Tolpygo. Design and testing of high-speed interconnects for superconducting multi-chip modules. *Superconductor Science and Technology*, 25(10):105012, 2012.

[28] Micah Stoutimore, James Medford, Quentin Herr, Ofer Naaman, Harold Hearne, Joel Strand, Anthony Przybysz, Aaron Pesetski, and John Przybysz. Demonstrated control of a transmon using a reciprocal quantum logic digital circuit-part 1. In *APS March Meeting Abstracts*, volume 2015, pages J39–012, 2015.

[29] Micah Stoutimore, James Medford, Quentin Herr, Ofer Naaman, Harold Hearne, Joel Strand, Anthony Przybysz, Aaron Pesetski, and John Przybysz. Demonstrated control of a transmon using a reciprocal quantum logic digital circuit-part 1. In *APS March Meeting Abstracts*, volume 2015, pages J39–012, 2015.

[30] Swamit S Tannu, Zachary A Myers, Prashant J Nair, Douglas M Carmean, and Moinuddin K Qureshi. Taming the instruction bandwidth of quantum computers via hardware-managed error correction. In *Proceedings of the 50th Annual IEEE/ACM International Symposium on Microarchitecture*, pages 679–691, 2017.

[31] INTERNATIONAL ROADMAP FOR DEVICES and SYSTEMS. Cryogenic electronics and quantum information processing, 2020.

[32] Sergey K Tolpygo. Superconductor digital electronics: Scalability and energy efficiency issues. *Low Temperature Physics*, 42(5):361–379, 2016.

[33] Naveen Kumar Katam, Jamil Kawa, and Massoud Pedram. Challenges and the status of superconducting single flux quantum technology. In *2019 Design, Automation & Test in Europe Conference & Exhibition (DATE)*, pages 1781–1787. IEEE, 2019.

[34] Jonathan Egan, Max Nielsen, Joshua Strong, Vladimir V Talanov, Ed Rudman, Brainton Song, Quentin Herr, and Anna Herr. Synchronous chip-to-chip communication with a multi-chip resonator clock distribution network. *arXiv preprint arXiv:2109.00560*, 2021.

[35] Haitao Dai, Corey Kegerreis, Deepal Wehella Gamage, Jonathan Egan, Max Nielsen, Yuan Chen, David Tuckerman, Sherman Peek, Bhargav Yelamanchili, Michael Hamilton, et al. Isochronous data link across a superconducting nb flex cable with 5 femtojoules per bit. *Superconductor Science and Technology*, 2022.

[36] Vladimir Talanov, Derek Knee, David Harms, Kieran Perkins, Andrew Urbanas, Jonathan Egan, Quentin Herr, and Anna Y Herr. Propagation of picosecond pulses on superconducting transmission line interconnects. *Superconductor Science and Technology*, 2022.

[37] INTERNATIONAL ROADMAP FOR DEVICES and SYSTEMS. Cryogenic electronics and quantum information processing, 2020.

[38] H Kamerlingh Onnes. Comm. leiden nr. 108. In *Proc. Roy. Acad. Amsterdam*, volume 11, page 168, 1908.

[39] H Kamerlingh Onnes. The resistance of pure mercury at helium temperatures. *Commun. Phys. Lab. Univ. Leiden, b*, 120, 1911.

[40] Cornelis Jacobus Gorter and Hendrik Casimir. On supraconductivity i. *Physica*, 1(1-6):306–320, 1934.

[41] Pyotr Kapitza. Viscosity of liquid helium below the λ-point. *Nature*, 141(3558):74–74, 1938.

[42] John F Allen and AD Misener. Flow of liquid helium ii. *Nature*, 141(3558):75–75, 1938.

[43] Fritz London and Heinz London. The electromagnetic equations of the supraconductor. *Proceedings of the Royal Society of London. Series A-Mathematical and Physical Sciences*, 149(866):71–88, 1935.

[44] Werner Buckel and Reinhold Kleiner. *Superconductivity: fundamentals and applications*. John Wiley & Sons, 2008.

[45] J. Bardeen, L. N. Cooper, and J. R. Schrieffer. Theory of superconductivity. *Phys. Rev.*, 108:1175–1204, Dec 1957.

[46] B Mitrović, HG Zarate, and JP Carbotte. The ratio 2 δ 0 k b t c within eliashberg theory. *Physical Review B*, 29(1):184, 1984.

[47] Heinz London. The high-frequency resistance of superconducting tin. *Proceedings of the Royal Society of London. Series A. Mathematical and Physical Sciences*, 176(967):522–533, 1940.

[48] AB Pippard. The surface impedance of superconductors and normal metals at high frequencies i. resistance of superconducting tin and mercury at 1200 mcyc./sec. *Proceedings of the Royal Society of London. Series A. Mathematical and Physical Sciences*, 191(1026):370–384, 1947.

[49] Daniel C Mattis and John Bardeen. Theory of the anomalous skin effect in normal and superconducting metals. *Physical Review*, 111(2):412, 1958.

[50] Richard L Kautz. Picosecond pulses on superconducting striplines. *Journal of Applied Physics*, 49(1):308–314, 1978.

[51] Michael Tinkham. *Introduction to superconductivity*. Courier Corporation, 2004.

[52] Alfred Brian Pippard and William Lawrence Bragg. An experimental and theoretical study of the relation between magnetic field and current in a superconductor. *Proceedings of the Royal Society of London. Series A. Mathematical and Physical Sciences*, 216(1127):547–568, 1953.

[53] Nicola Pinto, S Javad Rezvani, Andrea Perali, Luca Flammia, Milorad V Milošević, Matteo Fretto, Cristina Cassiago, and Natascia De Leo. Dimensional crossover and incipient quantum size effects in superconducting niobium nanofilms. *Scientific reports*, 8(1):1–12, 2018.

[54] Sergey K Tolpygo, Evan B Golden, Terence J Weir, and Vladimir Bolkhovsky. Inductance of superconductor integrated circuit features with sizes down to 120 nm. *Superconductor Science and Technology*, 34(8):085005, 2021.

[55] Orest G Vendik, Irina B Vendik, and Dimitri I Kaparkov. Empirical model of the microwave properties of high-temperature superconductors. *IEEE transactions on microwave theory and techniques*, 46(5):469–478, 1998.

[56] Oliver Lodge. On lightning, lightning conductors, and lightning protectors. *Journal of the Institution of Electrical Engineers*, 18(80):386–430, 1889.

[57] Simon Ramo, John R Whinnery, and Theodore Van Duzer. *Fields and waves in communication electronics*. John Wiley & Sons, 1994.

[58] Julls Adams Stratton. Electromagnetic theory, mcgrow-hill book company. *Inc., New York, and London*, pages 205–207, 1941.

[59] James C Swihart. Field solution for a thin-film superconducting strip transmission line. *Journal of Applied Physics*, 32(3):461–469, 1961.

[60] Sergey V Yuferev and Nathan Ida. *Surface impedance boundary conditions: a comprehensive approach*. CRC press, 2018.

[61] Sergei A Schelkunoff. The impedance concept and its application to problems of reflection, refraction, shielding and power absorption. *Bell System Technical Journal*, 17(1):17–48, 1938.

[62] Nathan Newman and W Gregory Lyons. High-temperature superconducting microwave devices: fundamental issues in materials, physics, and engineering. *Journal of Superconductivity*, 6(3):119–160, 1993.

[63] JP Turneaure, J Halbritter, and HA Schwettman. The surface impedance of superconductors and normal conductors: The mattis-bardeen theory. *Journal of Superconductivity*, 4(5):341–355, 1991.

[64] Cristoforo Benvenuti, S Calatroni, IE Campisi, P Darriulat, MA Peck, R Russo, and A-M Valente. Study of the surface resistance of superconducting niobium films at 1.5 ghz. *Physica C: Superconductivity*, 316(3-4):153–188, 1999.

[65] InductEx, C J Fourie. *HFSS*. Stellenbosch Univ., Stellenbosch, South Africa, 2015.

[66] MA Leontovich. A new method to solve problems of em wave propagation over the earth surface. *USSR Academy of Sciences Trans., Physics Series*, 8(1):16–22, 1944.

[67] MA Leontovich. Approximate boundary conditions for the electromagnetic field on the surface of a good conductor. *Investigations on radiowave propagation*, 2:5–12, 1948.

[68] Aleksandr N Shchukin. Propagation of radio waves. *Svyazizdat, Moscow*, 1940.

[69] N Klein, H Chaloupka, G Müller, S Orbach, H Piel, B Roas, L Schultz, U Klein, and M Peiniger. The effective microwave surface impedance of high t c thin films. *Journal of Applied Physics*, 67(11):6940–6945, 1990.

[70] Vladimir V Talanov, Lucia V Mercaldo, Steven M Anlage, and John H Claassen. Measurement of the absolute penetration depth and surface resistance of superconductors and normal metals with the variable spacing parallel plate resonator. *Review of Scientific Instruments*, 71(5):2136–2146, 2000.

[71] Anne-Marie Valente-Feliciano. Superconducting rf materials other than bulk niobium: a review. *Superconductor Science and Technology*, 29(11):113002, 2016.

[72] Jin Yong Kim, Moo Sung Hwang, Yoon-Hae Kim, Hyeong Joon Kim, and Young Lee. Origin of low dielectric constant of carbon-incorporated silicon oxide film deposited by plasma enhanced chemical vapor deposition. *Journal of Applied Physics*, 90(5):2469–2473, 2001.

[73] OF Rocha, CE Viana, LCD Gonçalves, and NI Morimoto. Electrical characteristics of pecvd silicon oxide deposited with low teos contents at low temperatures. *Microelectronics Technology and Devices SBMICRO 2004*, pages 295–300, 2004.

[74] Babacar Diallo, Konstantina C Topka, Maxime Puyo, Charlotte Lebesgue, Cecile Genevois, Raphael Laloo, Diane Samelor, Helene Lecoq, Mathieu Allix, Hugues Vergnes, et al. Network hydration, ordering and composition interplay of chemical vapor deposited amorphous silica films from tetraethyl orthosilicate. *journal of materials research and technology*, 13:534–547, 2021.

[75] Corey Rae Harrington McRae, Haozhi Wang, Jiansong Gao, Michael R Vissers, Teresa Brecht, Andrew Dunsworth, David P Pappas, and Josh Mutus. Materials loss measurements using superconducting microwave resonators. *Review of Scientific Instruments*, 91(9):091101, 2020.

[76] Vera V Daniel. *Dielectric relaxation*. Academic press, 1967.

[77] RC Zeller and RO Pohl. Thermal conductivity and specific heat of noncrystalline solids. *Physical Review B*, 4(6):2029, 1971.

[78] Peter Debye. Zur theorie der spezifischen wärmen. *Annalen der Physik*, 344(14):789–839, 1912.

[79] William A Phillips. Two-level states in glasses. *Reports on Progress in Physics*, 50(12):1657, 1987.

[80] A Anderson. Topics in current physics (amorphous solids: Low temperature properties) vol. 24, 1981.

[81] OL Anderson and HE Bömmel. Ultrasonic absorption in fused silica at low temperatures and high frequencies. *Journal of the American Ceramic Society*, 38(4):125–131, 1955.

[82] P W Anderson, Bertrand I Halperin, and C M Varma. Anomalous low-temperature thermal properties of glasses and spin glasses. *Philosophical Magazine*, 25(1):1–9, 1972.

[83] William A Phillips. Tunneling states in amorphous solids. *Journal of Low Temperature Physics*, 7(3):351–360, 1972.

[84] M Von Schickfus and S Hunklinger. Saturation of the dielectric absorption of vitreous silica at low temperatures. *Physics Letters A*, 64(1):144–146, 1977.

[85] C Laermans, W Arnold, and S Hunklinger. Influence of an electromagnetic wave on the acoustic absorption of borosilicate glass at low temperatures. *Journal of Physics C: Solid State Physics*, 10(8):L161, 1977.

[86] Sonja Rau, Christian Enss, Siegfried Hunklinger, Peter Neu, and Alois Würger. Acoustic properties of oxide glasses at low temperatures. *Physical Review B*, 52(10):7179, 1995.

[87] M Sargent III. M. 0. scully, and we lamb, jr. *Laser Physics*, pages 144–155, 1974.

[88] CP Slichter. Principles of magnetic resonance springer-verlag, berlin. *Heidelberg, New York*, 1980.

[89] William Andrew Phillips and AC Anderson. *Amorphous solids: low-temperature properties*, volume 24. Springer, 1981.

[90] U Buchenau, Yu M Galperin, VL Gurevich, DA Parshin, MA Ramos, and HR Schober. Interaction of soft modes and sound waves in glasses. *Physical Review B*, 46(5):2798, 1992.

[91] DA Parshin. Soft potential model and universal properties of glasses. *Physica Scripta*, 1993(T49A):180, 1993.

[92] VG Karpov, I Klinger, and FN Ignat'Ev. Theory of the low-temperature anomalies in the thermal properties of amorphous structures. *Zh. Eksp. Teor. Fiz*, 84:775, 1983.

[93] Robert O Pohl, Xiao Liu, and EunJoo Thompson. Low-temperature thermal conductivity and acoustic attenuation in amorphous solids. *Reviews of Modern Physics*, 74(4):991, 2002.

[94] U Strom, M Von Schickfus, and S Hunklinger. Low-temperature anomalies in the microwave dielectric properties of na β-alumina. *Physical Review Letters*, 41(13):910, 1978.

[95] David M Pozar. *Microwave engineering*. John wiley & sons, 2011.

[96] M Pollak and To H Geballe. Low-frequency conductivity due to hopping processes in silicon. *Physical Review*, 122(6):1742, 1961.

[97] Andrew K Jonscher. The 'universal'dielectric response. *nature*, 267(5613):673–679, 1977.

[98] KL Ngai, AK Jonscher, and CT White. On the origin of the universal dielectric response in condensed matter. *Nature*, 277(5693):185–189, 1979.

[99] Christoph Kaiser. *High quality Nb/Al-AlOx/Nb Josephson junctions: technological development and macroscopic quantum experiments*, volume 4. KIT Scientific Publishing, 2011.

[100] David B Tuckerman, Michael C Hamilton, David J Reilly, Rujun Bai, George A Hernandez, John M Hornibrook, John A Sellers, and Charles D Ellis. Flexible superconducting nb transmission lines on thin film polyimide for quantum computing applications. *Superconductor Science and Technology*, 29(8):084007, 2016.

[101] Jiansong Gao. *The physics of superconducting microwave resonators*. California Institute of Technology, 2008.

[102] Thomas J Licata, Evan G Colgan, James ME Harper, and Stephen E Luce. Interconnect fabrication processes and the development of low-cost wiring for cmos products. *IBM Journal of Research and Development*, 39(4):419–435, 1995.

[103] M David Levenson. Extending optical lithography to the gigabit era. *Solid State Technology*, 38(2):57–63, 1995.

[104] Panayotis C Andricacos, Cyprian Uzoh, John O Dukovic, Jean Horkans, and Hariklia Deligianni. Damascene copper electroplating for chip interconnections. *IBM Journal of Research and Development*, 42(5):567–574, 1998.

[105] Thomas P Moffat, JE Bonevich, WH Huber, A Stanishevsky, DR Kelly, GR Stafford, and D Josell. Superconformal electrodeposition of copper in 500–90 nm features. *Journal of The Electrochemical Society*, 147(12):4524, 2000.

[106] Milan Paunovic and Mordechay Schlesinger. *Fundamentals of electrochemical deposition*. john wiley & sons, 2006.

[107] WD Van Driel. Facing the challenge of designing for cu/low-k reliability. *Microelectronics Reliability*, 47(12):1969–1974, 2007.

[108] Jivaan Kishore Jhothiraman and Rajesh Balachandran. Electroplating: Applications in the semiconductor industry. *Advances in Chemical Engineering and Science*, 9(2):239–261, 2019.

[109] Henry H Radamson, Huilong Zhu, Zhenhua Wu, Xiaobin He, Hongxiao Lin, Jinbiao Liu, Jinjuan Xiang, Zhenzhen Kong, Wenjuan Xiong, Junjie Li, et al. State of the art and future perspectives in advanced cmos technology. *Nanomaterials*, 10(8):1555, 2020.

[110] Daniel T Yohannes, Rick T Hunt, John A Vivalda, Denis Amparo, Alexander Cohen, Igor V Vernik, and Alex F Kirichenko. Planarized, extendible, multilayer fabrication process for superconducting electronics. *IEEE Transactions on Applied Superconductivity*, 25(3):1–5, 2014.

[111] SEEQC. The digital superconducting company, 2019.

[112] Patrick A Truitt, Aritoki Suzuki, Daniel Yohannes, Michael Kamkar, Christopher Raum, Benjamin Westbrook, Trevor Sasse, and Adrian Lee. Commercially fabricated low loss superconducting resonators integrated with detectors for frequency domain multiplexing readout of future cosmic microwave background experiments. *IEEE Transactions on Applied Superconductivity*, 29(5):1–4, 2019.

[113] Takumi Ando, Shuichi Nagasawa, Naoki Takeuchi, Naoki Tsuji, Fumihiro China, Mutsuo Hidaka, Yuki Yamanashi, and Nobuyuki Yoshikawa. Three-dimensional adiabatic quantum-flux-parametron fabricated using a double-active-layered niobium process. *Superconductor Science and Technology*, 30(7):075003, 2017.

[114] Mutsuo Hidaka and Shuichi Nagasawa. Fabrication process for superconducting digital circuits. *IEICE Transactions on Electronics*, 104(9):405–410, 2021.

[115] Sergey K Tolpygo, Vladimir Bolkhovsky, Ravi Rastogi, Scott Zarr, Alexandra L Day, Evan Golden, Terence J Weir, Alex Wynn, and Leonard M Johnson. Advanced fabrication processes for superconductor electronics: Current status and new developments. *IEEE Transactions on Applied Superconductivity*, 29(5):1–13, 2019.

[116] Lynn A Abelson and George L Kerber. Superconductor integrated circuit fabrication technology. *Proceedings of the IEEE*, 92(10):1517–1533, 2004.

[117] Carter Kaanta, William Cote, John Cronin, Karey Holland, Pei-Ing Lee, and Terry Wright. Submicron wiring technology with tungsten and planarization. In *1987 International Electron Devices Meeting*, pages 209–212. IEEE, 1987.

[118] William L Guthrie, William J Patrick, Ernest Levine, Harris C Jones, Ebrahim A Mehter, Thomas F Houghton, George T Chiu, and Michael A Fury. A four-level vlsi bipolar metallization design with chemical-mechanical planarization. *IBM journal of research and development*, 36(5):845–857, 1992.

[119] Mahadevaiyer Krishnan, Jakub W Nalaskowski, and Lee M Cook. Chemical mechanical planarization: slurry chemistry, materials, and mechanisms. *Chemical reviews*, 110(1):178–204, 2010.

[120] Abelaziz Ramzi, Serge A Charlebois, and Philip Krantz. Niobium and aluminum josephson junctions fabricated with a damascene cmp process. *Physics Procedia*, 36:211–216, 2012.

[121] David A Chan, Bogdan Swedek, Andreas Wiswesser, and Manush Birang. Process control and monitoring with laser interferometry based endpoint detection in chemical mechanical

planarization. In *IEEE/SEMI 1998 IEEE/SEMI Advanced Semiconductor Manufacturing Conference and Workshop (Cat. No. 98CH36168)*, pages 377–384. IEEE, 1998.

[122] Jeffrey David, B Bonner, T Osterheld, and R Jin. Advanced sti cmp solutions for new device technologies. In *Proceedings of SEMI Technology Symposium (STS)*, volume 99, pages 8–64, 1999.

[123] Applied Materials. Leader in materials engineering solutions used to produce virtually every new chip and advanced display in the world.., 1967.

[124] Ron Allen, Charles Chen, Tom Trikas, Kurt Lehman, Robert Shinagawa, Vijay Bhaskaran, B Stephenson, and D Watts. In-situ cmp copper endpoint control system. In *2001 IEEE International Symposium on Semiconductor Manufacturing. ISSM 2001. Conference Proceedings (Cat. No. 01CH37203)*, pages 391–394. IEEE, 2001.

[125] Prahalad K Rao, M Brij Bhushan, Satish TS Bukkapatnam, Zhenyu Kong, Sanjay Byalal, Omer F Beyca, Adam Fields, and Ranga Komanduri. Process-machine interaction (pmi) modeling and monitoring of chemical mechanical planarization (cmp) process using wireless vibration sensors. *IEEE Transactions on Semiconductor Manufacturing*, 27(1):1–15, 2013.

[126] Prahalad Krishna Rao. *Sensor-based monitoring and inspection of surface morphology in ultraprecision manufacturing processes*. Oklahoma State University, 2013.

[127] Donna R Cote, SV Nguyen, William J Cote, Scott L Pennington, Anthony K Stamper, and Dragan V Podlesnik. Low-temperature chemical vapor deposition processes and dielectrics for microelectronic circuit manufacturing at ibm. *IBM Journal of Research and Development*, 39(4):437–464, 1995.

[128] Peter F Cheng, SM Rossnagel, and David N Ruzic. Directional deposition of cu into semiconductor trench structures using ionized magnetron sputtering. *Journal of Vacuum Science & Technology B: Microelectronics and Nanometer Structures Processing, Measurement, and Phenomena*, 13(2):203–208, 1995.

[129] Shin-Pon Ju, Cheng-I Weng, Jee-Gong Chang, and Chi-Chuan Hwang. Molecular dynamics simulation of sputter trench-filling morphology in damascene process. *Journal of Vacuum Science & Technology B: Microelectronics and Nanometer Structures Processing, Measurement, and Phenomena*, 20(3):946–955, 2002.

[130] CC Koch, JO Scarbrough, and DM Kroeger. Effects of interstitial oxygen on the superconductivity of niobium. *Physical Review B*, 9(3):888, 1974.

[131] Matthias Hein. *High-temperature-superconductor thin films at microwave frequencies*, volume 155. Springer Science & Business Media, 1999.

[132] Jerzy Krupka, Krzysztof Derzakowski, Bill Riddle, and James Baker-Jarvis. A dielectric resonator for measurements of complex permittivity of low loss dielectric materials as a function of temperature. *Measurement Science and Technology*, 9(10):1751, 1998.

[133] Harold A Wheeler. Transmission-line properties of parallel strips separated by a dielectric sheet. *IEEE Transactions on Microwave Theory and Techniques*, 13(2):172–185, 1965.

[134] WH Chang. The inductance of a superconducting strip transmission line. *Journal of Applied Physics*, 50(12):8129–8134, 1979.

[135] H-Y Lee and Tatsuo Itoh. Phenomenological loss equivalence method for planar quasi-tem transmission lines with a thin normal conductor or superconductor. *IEEE Transactions on Microwave Theory and Techniques*, 37(12):1904–1909, 1989.

[136] RC Taber. A parallel plate resonator technique for microwave loss measurements on superconductors. *Review of scientific instruments*, 61(8):2200–2206, 1990.

[137] MS Pambianchi, DH Wu, L Ganapathi, and SM Anlage. Dc magnetic field dependence of the surface impedance in superconducting parallel plate transmission line resonators. *IEEE transactions on applied superconductivity*, 3(1):2774–2777, 1993.

[138] David M Sheen, Sami M Ali, Daniel E Oates, Richard S Withers, and J Kong. Current distribution, resistance, and inductance for superconducting strip transmission lines. *IEEE Transactions on Applied Superconductivity*, 1(2):108–115, 1991.

[139] AR Kerr. Surface impedance of superconductors and normal conductors in em simulators. *MMA Memo*, 21(245):1–17, 1999.

[140] Mohammad Hossein Amini and Alireza Mallahzadeh. Modeling of superconducting components in full-wave simulators. *Journal of Superconductivity and Novel Magnetism*, 34(3):675–681, 2021.

[141] Gianluca Piccinini and André Chatel. Simulation and modelling of interconnect networks for cmos quantum bit systems.

[142] Release 2021 R2. *HFSS*. ANSYS, Canonsburg, PA, 2021.

[143] S Wuensch, G Benz, E Crocoll, M Fitsilis, M Neuhaus, TA Scherer, and W Jutzi. Normal and superconductor coplanar waveguides with 100 nm line width. *IEEE transactions on applied superconductivity*, 11(1):115–118, 2001.

[144] W Jutzi, S Wuensch, E Crocoll, M Neuhaus, TA Scherer, T Weimann, and J Niemeyer. Microwave and dc properties of niobium coplanar waveguides with 50-nm linewidth on silicon substrates. *IEEE transactions on applied superconductivity*, 13(2):320–323, 2003.

[145] James Wenner, R Barends, RC Bialczak, Yu Chen, J Kelly, Erik Lucero, Matteo Mariantoni, A Megrant, PJJ O'Malley, D Sank, et al. Surface loss simulations of superconducting coplanar waveguide resonators. *Applied Physics Letters*, 99(11):113513, 2011.

[146] Greg Calusine, Alexander Melville, Wayne Woods, Rabindra Das, Corey Stull, Vlad Bolkhovsky, Danielle Braje, David Hover, David K Kim, Xhovalin Miloshi, et al. Analysis and mitigation of interface losses in trenched superconducting coplanar waveguide resonators. *Applied Physics Letters*, 112(6):062601, 2018.

[147] David B Williams and C Barry Carter. The transmission electron microscope. In *Transmission electron microscopy*, pages 3–17. Springer, 1996.

[148] PW Hawkes. Aberration correction past and present. *Philosophical Transactions of the Royal Society A: Mathematical, Physical and Engineering Sciences*, 367(1903):3637–3664, 2009.

[149] SD Findlay, Naoya Shibata, Hidetaka Sawada, E Okunishi, Yukihito Kondo, T Yamamoto, and Yuichi Ikuhara. Robust atomic resolution imaging of light elements using scanning transmission electron microscopy. *Applied Physics Letters*, 95(19):191913, 2009.

[150] Stephen J Pennycook and Peter D Nellist. *Scanning transmission electron microscopy: imaging and analysis*. Springer Science & Business Media, 2011.

[151] C Barry Carter and David B Williams. *Transmission electron microscopy: Diffraction, imaging, and spectrometry*. Springer, 2016.

[152] AJ d'Alfonso, B Freitag, D Klenov, and LJ Allen. Atomic-resolution chemical mapping using energy-dispersive x-ray spectroscopy. *Physical Review B*, 81(10):100101, 2010.

[153] M-W Chu, SC Liou, C-P Chang, F-S Choa, and CH Chen. Emergent chemical mapping at atomic-column resolution by energy-dispersive x-ray spectroscopy in an aberration-corrected electron microscope. *Physical review letters*, 104(19):196101, 2010.

[154] Leslie J Allen, Adrian J D'Alfonso, Bert Freitag, and Dmitri O Klenov. Chemical mapping at atomic resolution using energy-dispersive x-ray spectroscopy. *MRS bulletin*, 37(1):47–52, 2012.

[155] LABS. *EAG*. EAG, www.eag.com, 2022.

[156] Lucille A Giannuzzi and Frederick A Stevie. A review of focused ion beam milling techniques for tem specimen preparation. *Micron*, 30(3):197–204, 1999.

[157] Joachim Mayer, Lucille A Giannuzzi, Takeo Kamino, and Joseph Michael. Tem sample preparation and fib-induced damage. *MRS bulletin*, 32(5):400–407, 2007.

[158] Eiji Okunishi, Isamu Ishikawa, Hidetaka Sawada, Fumio Hosokawa, Madoka Hori, and Yukihito Kondo. Visualization of light elements at ultrahigh resolution by stem annular bright field microscopy. *Microscopy and Microanalysis*, 15(S2):164–165, 2009.

[159] M Varela, Andrew R Lupini, K van Benthem, Albina Y Borisevich, Matthew F Chisholm, Naoya Shibata, E Abe, and Stephen J Pennycook. Materials characterization in the aberration-corrected scanning transmission electron microscope. *Annu. Rev. Mater. Res.*, 35:539–569, 2005.

[160] KA Mkhoyan, PE Batson, J Cha, WJ Schaff, and J Silcox. Direct determination of local lattice polarity in crystals. *Science*, 312(5778):1354–1354, 2006.

[161] Peter F Cheng, SM Rossnagel, and David N Ruzic. Directional deposition of cu into semiconductor trench structures using ionized magnetron sputtering. *Journal of Vacuum Science & Technology B: Microelectronics and Nanometer Structures Processing, Measurement, and Phenomena*, 13(2):203–208, 1995.

[162] JK Hulm, CK Jones, RA Hein, and JW Gibson. Superconductivity in the tio and nbo systems. *Journal of Low Temperature Physics*, 7(3):291–307, 1972.

[163] E Belohoubek and E Denlinger. Loss considerations for microstrip resonators (short papers). *IEEE Transactions on Microwave Theory and Techniques*, 23(6):522–526, 1975.

[164] AR Sass and WC Stewart. Self and mutual inductances of superconducting structures. *Journal of Applied Physics*, 39(4):1956–1963, 1968.

[165] William M Fairbank. High frequency surface resistivity of tin in the normal and superconducting states. *Physical Review*, 76(8):1106, 1949.

[166] SJ Fiedziuszko and PD Heidmann. Dielectric resonator used as a probe for high t/sub c/superconductor measurements. In *IEEE MTT-S International Microwave Symposium Digest*, pages 555–558. IEEE, 1989.

[167] Victor Belitsky, C Risacher, Miroslav Pantaleev, and Vessen Vassilev. Superconducting microstrip line model studies at millimetre and sub-millimetre waves. *International journal of infrared and millimeter waves*, 27(6):809–834, 2006.

[168] U-Yen Kongpop, Karwan Rostem, and Edward J Wollack. Modeling strategies for superconducting microstrip transmission line structures. *IEEE Transactions on Applied Superconductivity*, 28(6):1–5, 2018.

[169] Ansoft. *HFSSv10UserGuide*. Ansoft, http://anlage.umd.edu/HFSSv10UserGuide.pdf, 2005.

[170] Kenneth K Mei and G-C Liang. Electromagnetics of superconductors. *IEEE transactions on microwave theory and techniques*, 39(9):1545–1552, 1991.

[171] in high-T_c superconductors the c-axis plasmon can be below the gap frequency Although in conventional low-T_c superconductors ω_p lays above the superconducting gap frequency. .see t. m. mishonov, phys. rev. b 44, 12033. 1991.

[172] RE Glover III and Ms Tinkham. Conductivity of superconducting films for photon energies between 0.3 and 4 0 k t c. *Physical Review*, 108(2):243, 1957.

[173] Jerzy Krupka, Jonathan Breeze, Anthony Centeno, Neil Alford, Thomas Claussen, and Leif Jensen. Measurements of permittivity, dielectric loss tangent, and resistivity of float-zone silicon at microwave frequencies. *IEEE Transactions on microwave theory and techniques*, 54(11):3995–4001, 2006.

[174] Daniel E Oates, Sergey K Tolpygo, and Vladimir Bolkhovsky. Submicron nb microwave transmission lines and components for single-flux-quantum and analog large-scale superconducting integrated circuits. *IEEE Transactions on Applied Superconductivity*, 27(4):1–5, 2017.

[175] E Maxwell, PM Marcus, and John Clarke Slater. Surface impedance of normal and superconductors at 24,000 megacycles per second. *Physical Review*, 76(9):1332, 1949.

[176] APS Khanna and Y Garault. Determination of loaded, unloaded, and external quality factors of a dielectric resonator coupled to a microstrip line. *IEEE Transactions on Microwave Theory and Techniques*, 31(3):261–264, 1983.

[177] M Stoutimore Khalil, MJA Stoutimore, FC Wellstood, and KD Osborn. An analysis method for asymmetric resonator transmission applied to superconducting devices. *Journal of Applied Physics*, 111(5):054510, 2012.

[178] Anthony Megrant, Charles Neill, Rami Barends, Ben Chiaro, Yu Chen, Ludwig Feigl, Julian Kelly, Erik Lucero, Matteo Mariantoni, Peter JJ O'Malley, et al. Planar superconducting resonators with internal quality factors above one million. *Applied Physics Letters*, 100(11):113510, 2012.

[179] Liepe Research Group. *SRIMP*. Cornell Univ., https://www.classe.cornell.edu/ liepe/webpage/researchsrimp.html, 2012.

[180] A Romanenko, CJ Edwardson, PG Coleman, and PJ Simpson. The effect of vacancies on the microwave surface resistance of niobium revealed by positron annihilation spectroscopy. *Applied Physics Letters*, 102(23):232601, 2013.

[181] V Ganni. Helium refrigeration systems for super-conducting accelerators. In *AIP Conference Proceedings*, volume 1687, page 040001. AIP Publishing LLC, 2015.

[182] ICEoxford. Design and manufacture specialist of ultra low temperature (ult) and high magnetic field equipment for cryogenic research community, 2004.

[183] DE Oates, Alfredo C Anderson, and PM Mankiewich. Measurement of the surface resistance of yba2cu3o7- x thin films using stripline resonators. *Journal of Superconductivity*, 3(3):251–259, 1990.

[184] Kent D Irwin and Konrad W Lehnert. Microwave squid multiplexer. *Applied physics letters*, 85(11):2107–2109, 2004.

[185] John Arthur Benson Mates. The microwave squid multiplexer. *University of Colorado Boulder*, 2011.

[186] M Von Schickfus and S Hunklinger. The dielectric coupling of low-energy excitations in vitreous silica to electromagnetic waves. *Journal of Physics C: Solid State Physics*, 9(16):L439, 1976.

[187] Milton Abramowitz and Irene A Stegun. *Handbook of mathematical functions with formulas, graphs, and mathematical tables*, volume 55. US Government printing office, 1964.

[188] J Jäckle, L Piché, W Arnold, and S Hunklinger. Elastic effects of structural relaxation in glasses at low temperatures. *Journal of Non-Crystalline Solids*, 20(3):365–391, 1976.

[189] SciPy. minimize(method='powell'), 2020 [Online].

[190] T Baumann, MV Schickfus, S Hunklinger, and J Jäckle. "glassy" properties of crystalline li3n at low temperatures. *Solid State Communications*, 35(8):587–590, 1980.

[191] Joshua T West, Arthur Kurlej, Alex Wynn, Chad Rogers, Mark A Gouker, and Sergey K Tolpygo. Wafer-scale characterization of a superconductor integrated circuit process, using a cryogenic wafer prober. *arXiv preprint arXiv:2112.00705*, 2021.

[192] Lake Shore Cryotronics. Supporting advanced scientific research, lake shore is a leading global innovator in measurement and control solutions., 1968.